Chemical templates

Edited by Sigurd Höger

Imprint

Chemical templates

Sigurd Höger

When a single object is created from its constituents, a step-by-step assembly strategy is a modus operandi which allows the control of success and sometimes even an error correction after each sequential step. Moreover, it guarantees the uniqueness of the fabricated object. However, the fabrication of several identical objects by assembly or by shaping its constituents is much more effective if a mold or template can be used. All this holds true for the macroscopic as well as for the microscopic world.

A chemical template controls a reaction in such a way that from a multitude of possible products a specific one is preferentially or even exclusively formed. The template can influence the reaction in a stoichiometric or a catalytic way, it can be reused or remain in the product as an integral part.

Template effects in chemistry are commonly associated with the formation of (macro)cycles, or covalent bond formation in general. However, chemical templates can also exert a variety of other effects. They can influence the formation of non-covalent bonds or they can control the positioning of objects in one, two or three dimensions. For example, a functionalized linear template strand leads to the generation of a complementary functionalized product strand. A two-dimensional template, often a planar substrate with a specific structure and composition, determines the respective pattern formation on its surface.

And three-dimensional templates are a unique and versatile tool for providing well-designed volume structures, often decorated with useful functionality. Not surprisingly, the annual publication activity of scientific articles in the chemical community containing the concept "template" has doubled within the last decade and is expected to increase further.

Remarkable breakthroughs in synthetic, spectroscopic and microscopic as well as theoretical methods facilitate a closer investigation and more detailed understanding of template effects in all areas of chemistry. It will also lead to the identification of new template effects and new methodologies for the adaptation of existing binding motifs into functional chemical matrices. The articles in this Thematic Series represent a snapshot of the current activities in template-directed reactions. This selection from a broad variety of different fields of chemistry will hopefully be inspiring for the reader, thus leading to new exciting discoveries in template chemistry and attract new audience to this field.

Sigurd Höger

Bonn, June 2014

Novel supramolecular affinity materials based on (−)-isosteviol as molecular templates

Christina Lohoelter, Malte Brutschy, Daniel Lubczyk
and Siegfried R. Waldvogel[*]

Abstract

The readily available ex-chiral-pool building block (−)-isosteviol was combined with the C_3-symmetric platforms hexahydroxytriphenylene and hexaaminotriptycene providing large and rigid molecular architectures. Because of the persistent cavities these scaffolds are very potent supramolecular affinity materials for head space analysis by quartz crystal microbalances. The scaffolds serve in particular as templates for tracing air-borne arenes at low concentration. The affinities of the synthesized materials towards different air-borne arenes were determined by 200 MHz quartz crystal microbalances.

Introduction

Divalent building blocks with a well-defined geometry play a significant role in the construction of highly potent supramolecular structures [1-5]. The rigid nature of such architectures limits the degrees of freedom and guarantees a good preorganization [1,2,6-10]. Particular interest was given to C_3-symmetric structures, serving e.g. as templates in asymmetric catalysis or molecular recognition [11-14].

A specific but potent subclass of such C_3-symmetric architectures is represented by triphenylene ketals [15]. They have found significant application as receptors and chemical sensors in the detection of aromatic compounds [16-20]. Thus, the first

artificial receptor for caffeine had been established [21,22]. The introduction of chiral information onto a supramolecular entity gave rise for enantiofacial differentiation of a single substrate [23,24]. Due to the concave arrangement of both functional groups, exhibiting a distance of the two carbonyl carbon atoms of about 7 Å, naturally occurring diterpene (−)-isosteviol **1** [25] came into focus as building block for the construction of such receptor geometries (Figure 1) [26].

(−)-Isosteviol **1** can be easily obtained on large scale by acidic treatment of stevioside [27,28]. This stevioside is a commercially available natural sweetener which is isolated from *stevia*

Figure 1: Unique structural features of (−)-isosteviol.
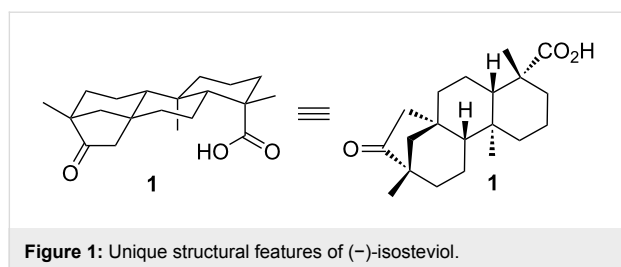
rebaudiana by alcoholic extraction [29,30]. In addition to their cytotoxic activities [31-34], compounds based on (−)-isosteviol have found application in various fields of synthetic chemistry [35], including the construction of tweezer-like supramolecular transporters for amino acids [36], chiral organocatalysts in aldol reactions [37], or the complex formation with aromatic compounds [38,39], Within in a nine-step synthesis triphenylene ketals based on (−)-isosteviol were prepared [40]. Receptor structures **2** equipped with amino or sulfonylamido functionalities were obtained (Figure 2).

all-*syn*-**2a:** R = H
all-*syn*-**2b:** R = SO$_2$Me

Figure 2: Triphenylene ketal based on (−)-isosteviol.
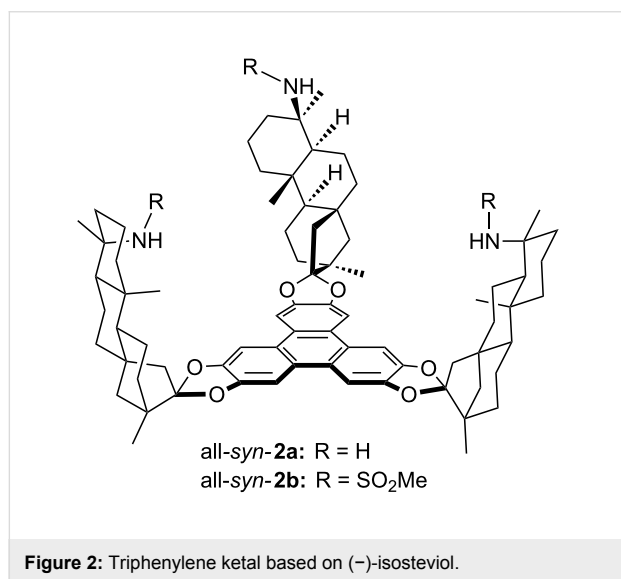
In addition to triphenylene ketals, triptycene-based structures also exhibit the geometrical requirements for the formation of C_3-symmetric architectures with extended cavities. Due to their structural features, triptycenes have found widespread application in organic synthesis: Ranging from polymer sciences [41], materials for gas storage [42-50], (organo)catalysis [51,52], molecular machinery [53,54] and supramolecular host–guest chemistry [55,56]. With an angle of 120° between its aromatic moieties, it exhibits a rigid geometry with a defined alignment of functional groups (Figure 3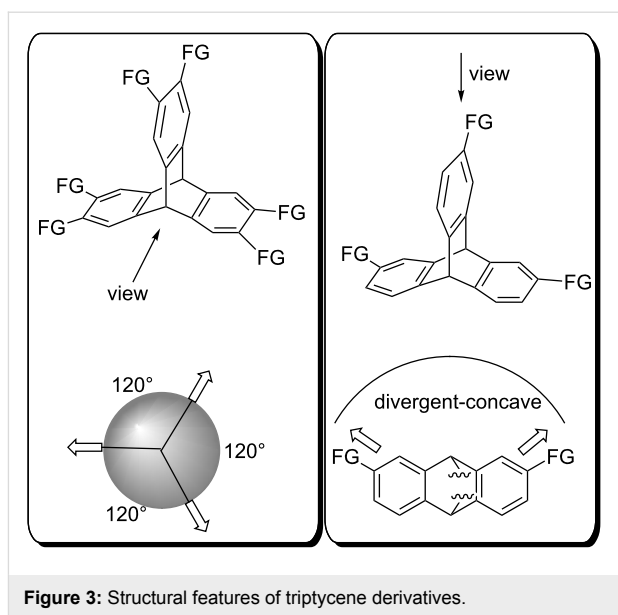, left). Next to classical convergent–concave structures, architectures with a divergent–concave arrangement of functionalities can be obtained upon installation of building blocks with a linear geometry (Figure 3, right).

Figure 3: Structural features of triptycene derivatives.

Here, the functionalization of (−)-isosteviol-based triphenylene ketal all-*syn*-**2a** as well as the combination of (−)-isosteviol with the triptycene platform is reported. The application of these novel architectures as supramolecular affinity materials was studied.

The investigations of these possible affinity materials were carried out with 200 MHz high fundamental frequency quartz crystal microbalances (HFF-QCMs) via gravimetric sensing of the adsorbed analytes. The advantage of HFF-QCMs is the low detection limit and the fast, highly reproducible and easy to apply electro spray protocol for the coating of such devices [57-59]. Almost all organic materials which show at least a certain solubility in tetrahydrofuran or other volatile organic solvents allow application of this versatile coating protocol. For such studies only small amounts of affinity material in the sub mg-range are required.

The frequency shifts of the coated QCMs were determined for different analyte concentrations. Subsequently, the constants of the Langmuir isotherm are obtained by fitting the frequency shifts over concentration. The affinity of an affinity material to an analyte is calculated by multiplication of these constants. Details about the experimental setup and the determination of the affinities are given in Supporting Information File 1.

Results and Discussion
Triphenylene ketals
The high hydrogen bonding donor capability of sulfonamides made this class of functional groups highly attractive for supramolecular affinity materials [60]. The installation of larger substituents at the sulfonyl moiety should provide suitable prop-

erties for the processing on the quartz crystal microbalances. Based on the reported triamine all-*syn*-**2a** [40], **2a** was brought to reaction with *para*-toluenesulfonyl chloride in order to equip the receptor scaffold with sulfonamide binding sites (Scheme 1).

Scheme 1: Functionalization of triphenylene ketal **2a**.
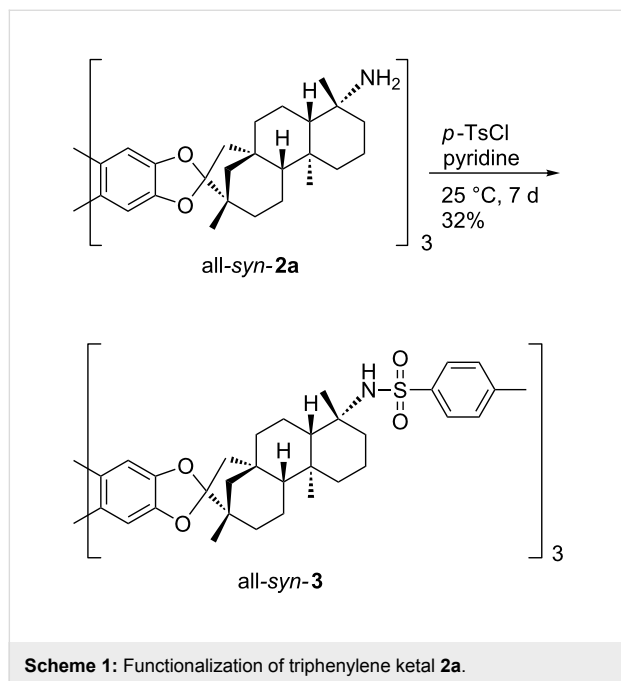
The reaction proceeds with a moderate yield of 32% under very mild reaction conditions. The high steric demand in vicinity of the amino functions requires these prolonged reaction times. Unfortunately, more drastic reaction conditions lead to degradation of the substrate.

Triptycenes

Recently, the synthesis of hexaammoniumtriptycene hexachloride **4** (Figure 4) was reported by Mastalerz et al. [61]. Further, (−)-isosteviol and its esters can be converted into the corresponding 1,2-diketones **5a–c** via Riley oxidation [62-66]. The linkage of the two building blocks by condensation reaction of the keto with the amino functionalities presents a promising route for the construction of novel (−)-isosteviol-based C_3-symmetric scaffolds.

Figure 4: Hexaammoniumtriptycene hexachloride **4** and 15-oxo-derivatives **5a–c** of (−)-isosteviol.

For the elaboration of optimal condensation conditions to form quinoxalines and to obtain model compounds representing subunits for the triptycene architectures *o*-phe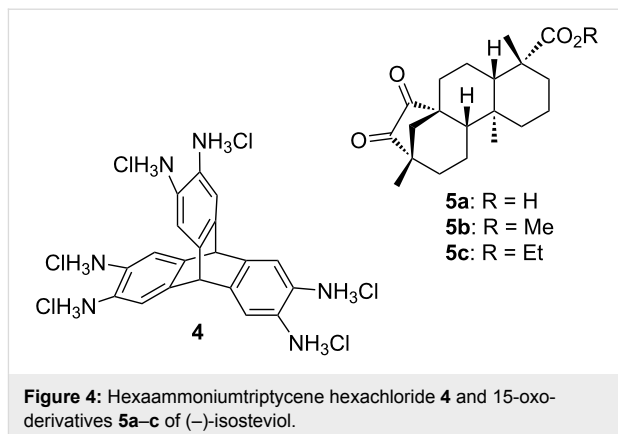nylenediamines were employed (Scheme 2). It turned out that **5b** forms the corresponding quinoxaline derivatives **6** and **7** in acceptable yields of 41% and 60%, respectively, when refluxing in glacial acetic acid.

The established reaction conditions failed on the C_3-symmetric platform due to the poor solubility of the starting materials. Switching to a protocol with sodium acetate as additional base and operation in a sealed tube provided a satisfactory yield of **8** (Scheme 3) [61]. By molecular modelling the structural features can be visualized (Figure 5). A relatively closed C_3-symmetric cleft is formed by all-*syn*-**8** (Figure 5a), whereas the less symmetric *anti,anti,syn*-**8** (Figure 5b) provides an open side to access the concave regime.

As anticipated, two stereoisomers are formed in this condensation reaction of **5b** with **4**. After separation via column chromatography, these products were identified as the all-*syn*- and *anti,anti,syn*-isomers of the desired product **8**, which were obtained in a total yield of 59%. Due to very similar polarity of both isomers, the separation turned out to be tedious. Thus, pure *anti,anti,syn*-**8** and all-*syn*-**8** were isolated in yields of only 25% and 3%, respectively, with the remaining 31% as mixture of isomers. In order to facilitate the separation of isomers the ester moiety of (−)-isosteviol was converted into nitrobenzylic esters.

Scheme 2: Quinoxalines based on diketone **5b**.
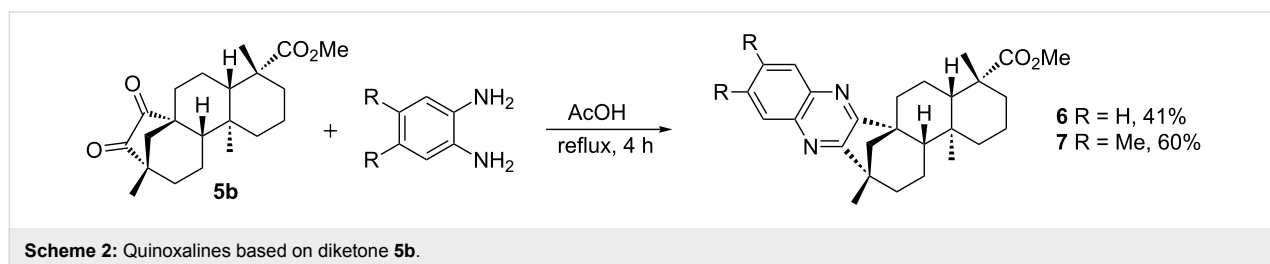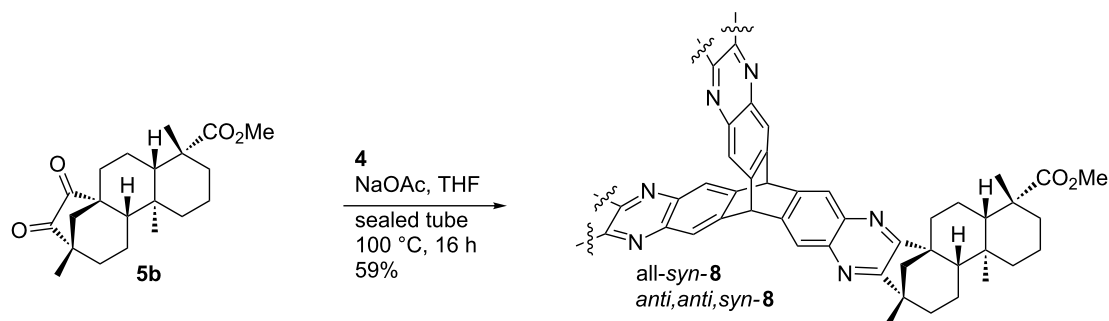
Scheme 3: Condensation of **5b** with hexaammoniumtriptycene hexachloride.
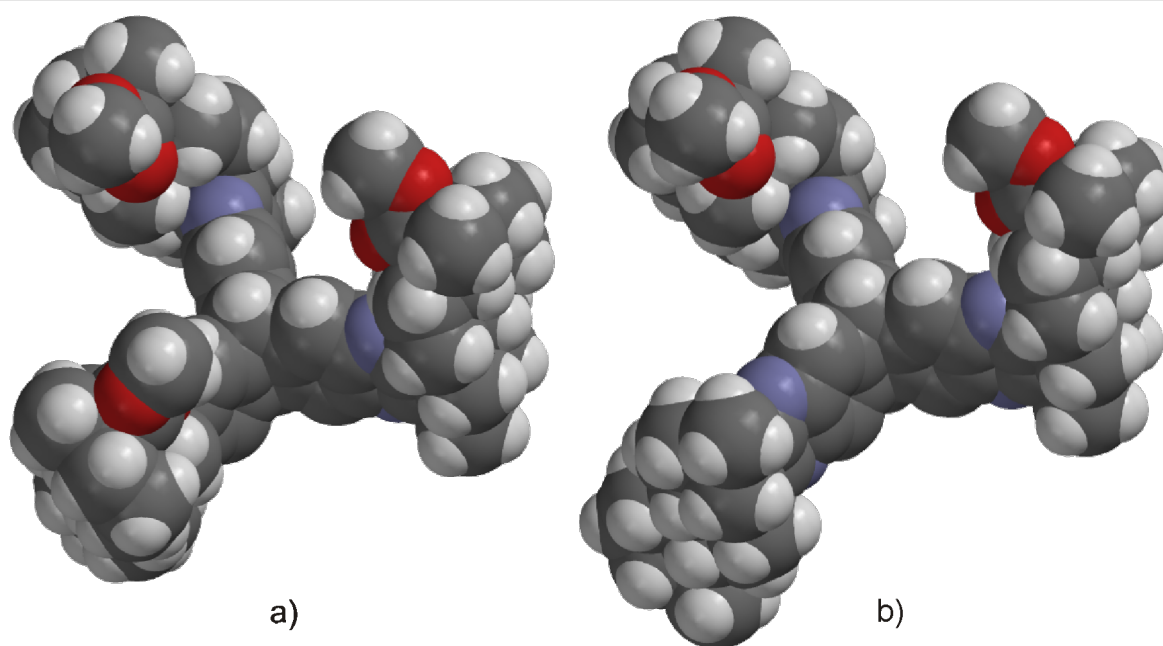
Figure 5: Molecular modelling structures (Spartan '08 V1.0.0) of (a) all-*syn*-**8** and (b) *anti,anti,syn*-**8**.

The highly polar nitro groups at the periphery of the resulting triptycene isomers should provide the desired difference in polarity. Another feature of the employment of benzyl derivatives is the facile cleavage under reductive conditions representing a versatile precursor for further modifications. Starting from (−)-isosteviol **1**, there are two ways of obtaining the diketo building blocks **10** and **11**, bearing a dinitrobenzylic (DNB) and a *p*-nitrobenzylic (PNB) ester moiety, respectively (Scheme 4).

Following path **A**, (−)-isosteviol can be oxidized under Riley conditions (Table 1, reaction conditions **a**: selenium dioxide/ xylene) [62,63] to give the corresponding diketone **9** [66]. Subsequent esterification with 3,5-dinitrobenzylic chloride under basic conditions (Table 1, reaction conditions **b** for R = DNB) [67] proceeds with a yield of 57% and leads to the formation of **10** with an overall yield of 46%. Alternatively,

protection of the carboxylic acid function of (−)-isosteviol can be carried out first (path **B**), yielding dinitrobenzyl ester **12**. Subsequent Riley-oxidation renders the desired product **10** in an overall yield of 48%. Since path **A** and path **B** both proceed with almost identical yields, either pathway is suitable for the preparation of such protected 1,2-diketones. Apart from applying 3,5-dinitrobenzyl chloride in the reaction sequence, the conversion of the carboxylic acids **1** and **9** with 4-nitrobenzyl (PNB) chloride was carried out (Scheme 4). Again, both paths **A** and **B** lead to the formation of the desired PNB protected diketone **11**. Esterification was achieved by reaction with 4-nitrobenzyl chloride and cesium carbonate in DMF (Table 1, reaction conditions **b** for R = PNB) [68]. Both sequences **A** and **B** proceed with similar overall yields as well, rendering **11** in 54% and 57%, respectively. Upon employing 4-nitrobenzyl chloride, both reaction paths result in slightly
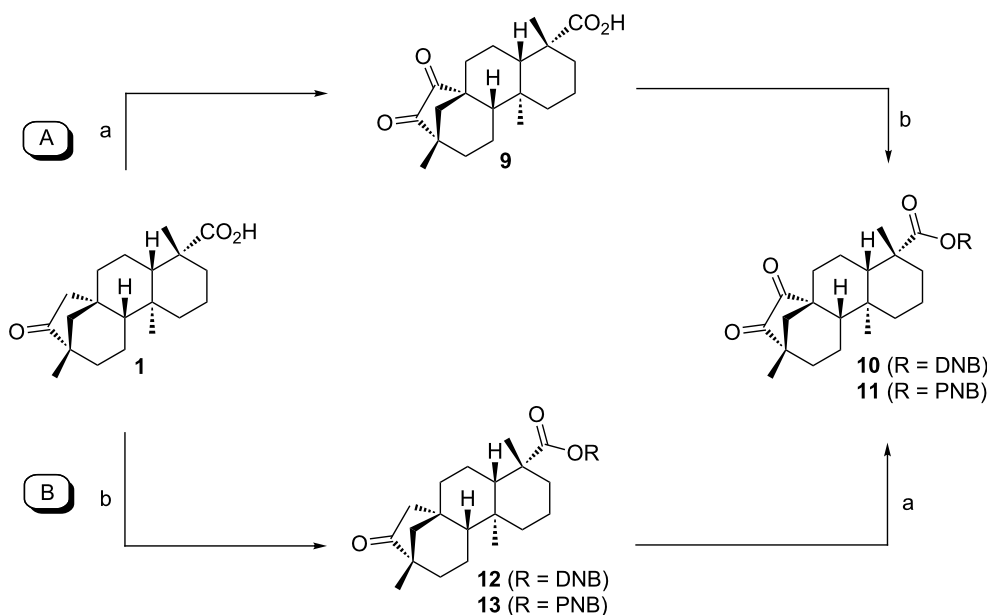
Scheme 4: Synthesis of nitrobenzylic ester derivatives **10** and **11**, starting from (−)-isosteviol **1**.

Table 1: Oxidation and esterification sequence of **1**.

R =	Reaction conditions	Yield	Overall yield a + b
DNB NO_2 NO_2	a: SeO$_2$, xylenes, 145 °C, 2 d	**9**: 80% **10**: 78%	Path **A**: 46%
	b: 3,5-dinitrobenzyl chloride, NEt$_3$, DMF, 25 °C, 16 h	**12**: 61% **10**: 57%	Path **B**: 48%
PNB NO_2	a: SeO$_2$, xylenes, 145 °C, 2 d	**9**: 80% **11**: 74%	Path **A**: 54%
	b: 4-nitrobenzyl chloride, Cs$_2$CO$_3$, DMF, 25 °C, 5 h	**13**: 77% **11**: 68%	Path **B**: 57%

higher yields than the analogous reactions with 3,5-dinitrobenzyl chloride. Diketones **10** and **11** were then brought to condensation with hexaammoniumtriptycene hexachloride **4**, following the protocol mentioned above (Scheme 5). Reaction of the 3,5-dinitrobenzyl ester **10** with **4** renders the corresponding triptycene structure **14** as a mixture of isomers in a good total yield of 86%. However, the impact of the nitro groups at the periphery of the molecule on the polarity of the isomers was far less than anticipated. After twofold column chromatography, the *anti,anti,syn*-isomer was isolated in a yield of 48% while the *all-syn*-isomer was obtained in 17% yield, again leaving the rest as a mixture of isomers.

Reaction of 4-nitrobenzyl ester **11** with **4** leads to the formation of the corresponding triptycenes *anti,anti,syn*-**15** and all-*syn*-**15**

in an excellent total yield of 95%. Separation of the isomers results in the isolation of 34% of the *anti,anti,syn*-isomer and 12% of the all-*syn*-isomer, leaving the remaining 49% as a mixture of isomers.

The benzyl ester moiety of all-*syn*-**15** was subsequently cleaved by hydrogenolysis using standard conditions (Scheme 6) [69]. The tricarboxylic acid all-*syn*-**16** was isolated in almost quantitative yield. In this protocol the heterogeneous catalyst did not affect the quinoxaline moieties by over-reduction.

With this versatile precursor all-*syn*-**16** in hands and the need for organic materials with pronounced cavities as potent affinity materials we envisioned the synthesis of a capsule-type architecture. Therefore, all-*syn*-**16** was *O*-alkylated by treatment with
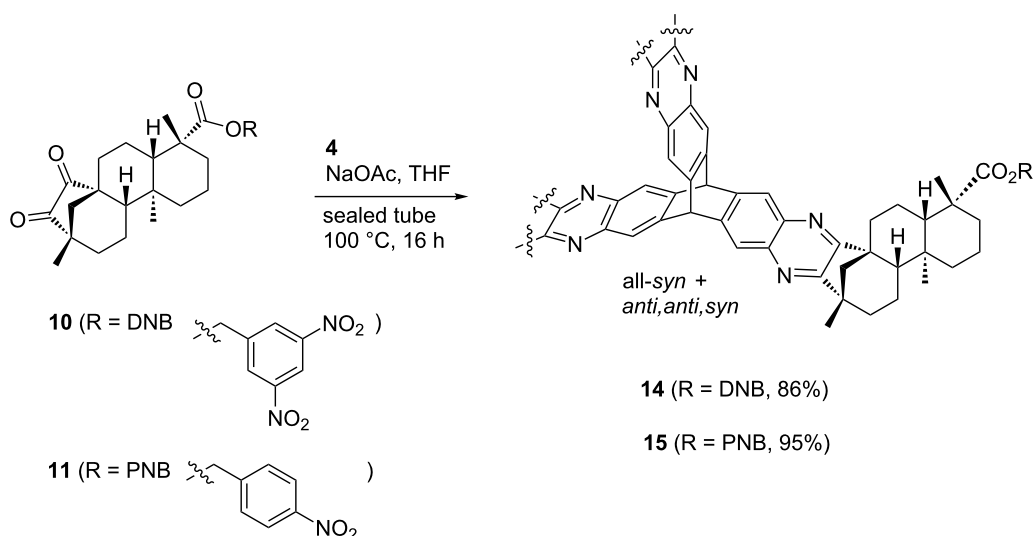
Scheme 5: Condensation of the nitrobenzyl esters **10** and **11** with hexaammoniumtriptycene hexachloride **4**.
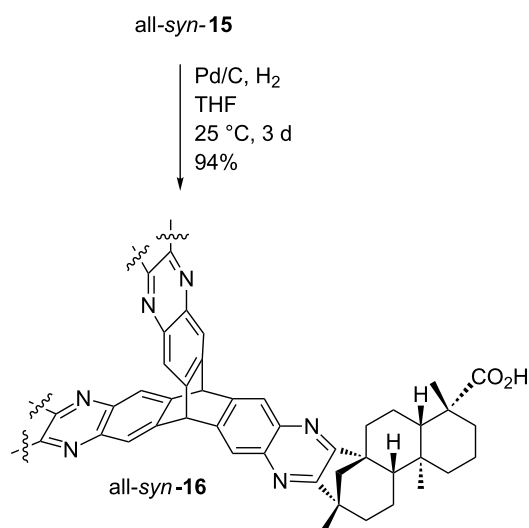
Scheme 6: Hydrogenolysis to tricarboxylic acid all-*syn*-**16**.
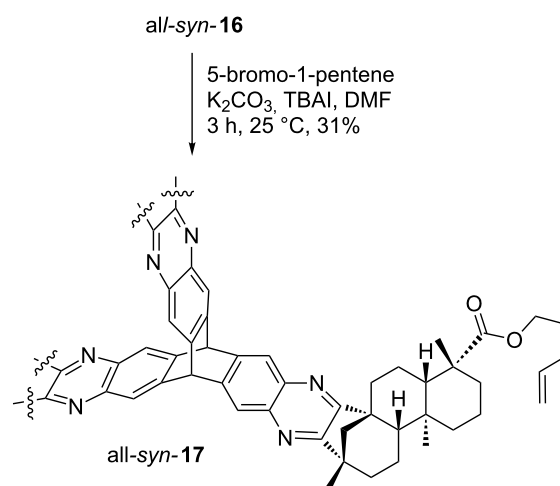
Scheme 7: Alkylation of all-*syn*-**16** renders terminal alkene all-*syn*-**17**.

5-bromo-1-pentene using standard conditions [70] to yield the corresponding triptycene derivative all-*syn*-**17** (Scheme 7). Alkylation proceeded with a moderate yield of 31%. Equipped with three terminal alkenes all-*syn*-**17** seems to be a suitable precursor for subsequent olefin metathesis to form a capsule-like structure.

The structure of all-*syn*-**17** was confirmed via X-ray analysis of a suitable single crystal. The molecular structure clearly reveals the spatial arrangement of the terminal alkene moieties. The side view of all-*syn*-**17** (Figure 6b) unequivocally shows the cavity which is formed, its size ranging approximately to the quinoxaline-nitrogen atoms of the triptycene core which exhibit

a mutual distance of 8.1 Å, 8.8 Å and 8.9 Å, whereas the carboxylic carbon atoms exhibit a distance of about 12 Å. The cavity of all-*syn*-**17** is "roofed" by the alkyl chains of the (−)-isosteviol units (Figure 6a), whose terminal carbon atoms show a mutual distance in the range of 4.2–5.2 Å.

Since the introduction of nitrobenzyl esters as protecting groups for the (−)-isosteviol carboxylic acid moiety obviously does not have an enhanced effect on the polarity of the two isomers and, as a consequence, the chromatographic separation procedure does not correlate with the nature of the ester substituent, the detour via protecting groups in the synthesis of alkylated triptycene **17** was subsequently avoided. Therefore, alkylated diketone **18** was synthesized, starting from (−)-isosteviol
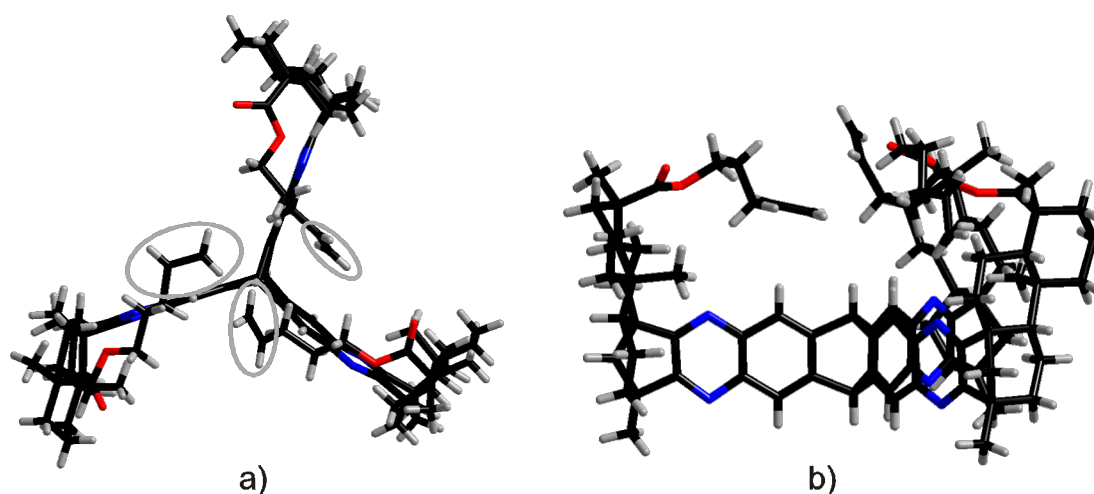
Figure 6: (a) Top view on the molecular structure of all-*syn*-**17** with the terminal alkene fragments labelled in grey; (b) side view of all-*syn*-**17**.
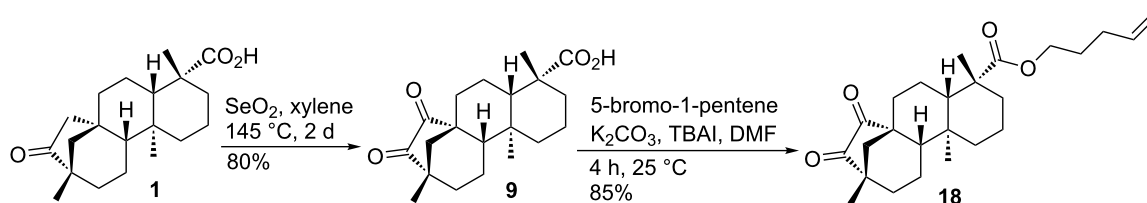
Scheme 8: Alkylation of (−)-isosteviol diketone **9** with 5-bromo-1-pentene.

(Scheme 8). Since alkenes are known to participate in Riley oxidations as well, rendering allylic alcohols, there is only one route to **18**. After Riley oxidation of **1**, alkylation was carried out under the same reaction conditions as before, providing the desired product in a yield of 85% [70].

18 was then brought to reaction with hexaammoniumtriptycene hexachloride **4** (Scheme 9). The corresponding all-*syn*- and *anti,anti,syn*-isomers of **17** were obtained in an overall yield of 67%.

After twofold column chromatography, complete separation of the isomers was achieved. The *anti,anti,syn*-derivative was isolated in a yield of 44% whereas the all-*syn*-derivative was obtained in 23% yield. The molecular structure of all-*syn*-**17** depicted in Figure 6 provides the rationale for the ameliorated separation of the isomers. The protection of one side with alkenyl esters blocks the access of the quinoxaline moieties from one side. The all-*syn* derivatives will show a better interaction with the stationary phase. The combination of entire isomer separation and shortcut in the reaction sequence (three steps instead of five, starting from (−)-isosteviol) makes this a highly attractive route for the construction of the desired
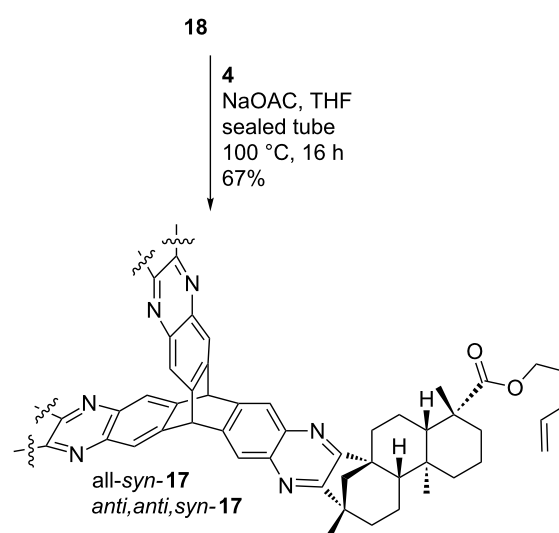
Scheme 9: Direct synthesis of alkylated triptycene **17** by condensation of **18** with hexaammoniumtriptycene hexachloride **4**.

triptycene derivatives. All-*syn*-**17** was then brought to reaction in an olefin metathesis (Scheme 10), employing the 2nd generation Grubbs catalyst in refluxing dichloromethane.
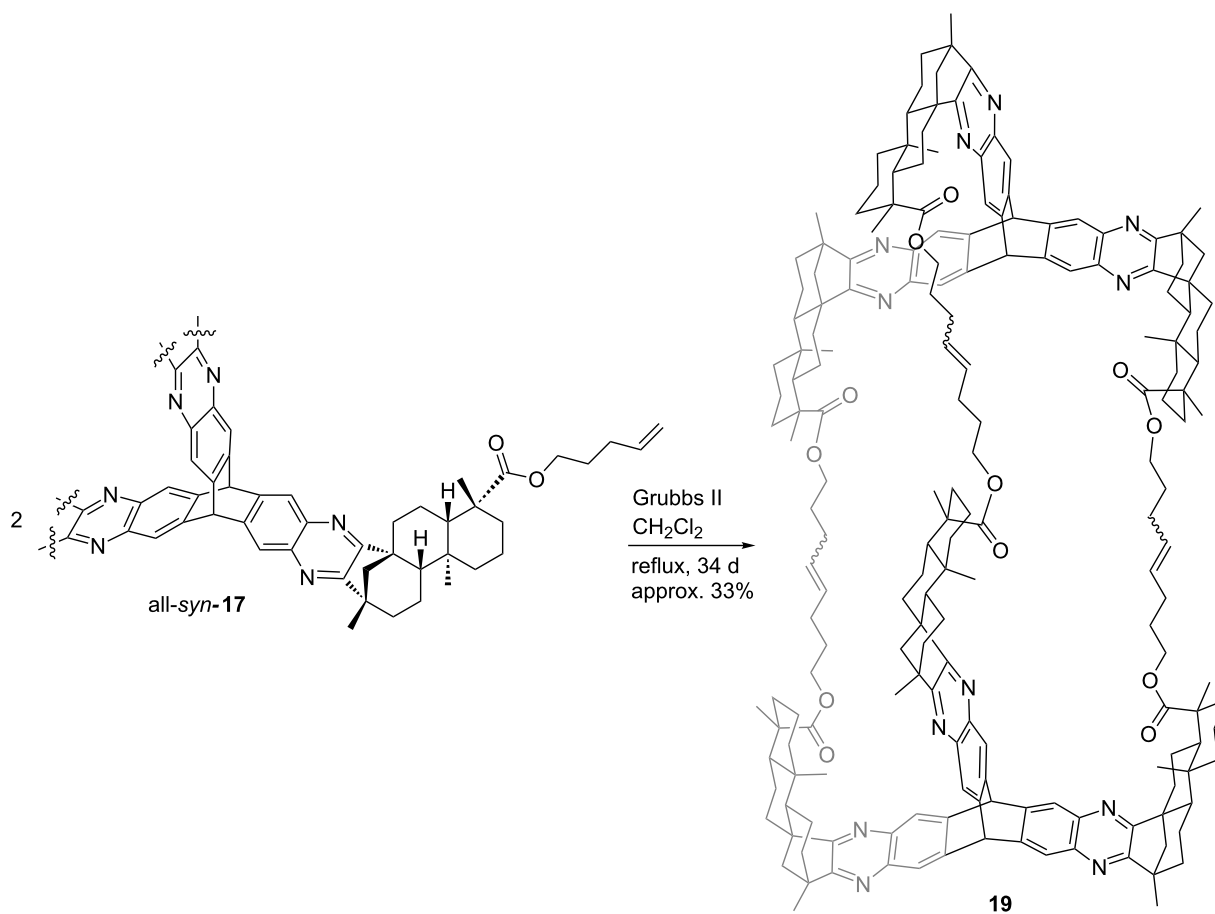
Scheme 10: Olefin metathesis of all-*syn*-**17**.

Even after prolonged reaction times, complete conversion of the starting material could not be achieved. However, the formation of a sole product was observed. Upon chromatographic separation, the product was obtained, exhibiting a molecular weight corresponding to the cage-like structure **19**. Comparison of according sections from the carbon NMR spectra of starting material and product shows that the signal which corresponds to the terminal carbon atom in the starting material (Figure 7, grey) is not existent in the product spectrum. Furthermore, a new set of signals (Figure 7, green) can be seen in the product spectrum which show typical shifts of 1,2-disubstituted alkenes.

Since the obtained analytical data strongly indicate the existence of cage compound **19**, molecular modelling calculations (Figure 8, MacroModel 9.3.5) indicate a "collapsed" structure in which the triptycene units are twisted by 60° and approaching each other, prohibiting the formation of significant voids for intercalation of analytes.

Results of the gravimetric measurements with HFF-QCMs

Triphenylene ketal **3** and the triptycene derivatives **8**, **14**, **15**, **17**, **19** and the model compound **7** were subjected to QCM measurements in order to evaluate their properties to serve as affinity materials in the tracing of volatile aromatic compounds. For this purpose, a collection of chemically related aromatic analytes were screened. The analytes range from benzene to pseudocumene, exhibiting similar electronic properties but differing in their size. This allows a probing of cavity size of the individual affinity materials.

Triptycene based material *anti,anti,syn*-**8** shows the highest affinity towards aromatic analytes, which can be rationalized with a more facile access of the analyte to the void created by the *anti,anti,syn*-isomer (Figure 9).

This remarkable effect can already be observed when plotting the primary data (Figure 10).
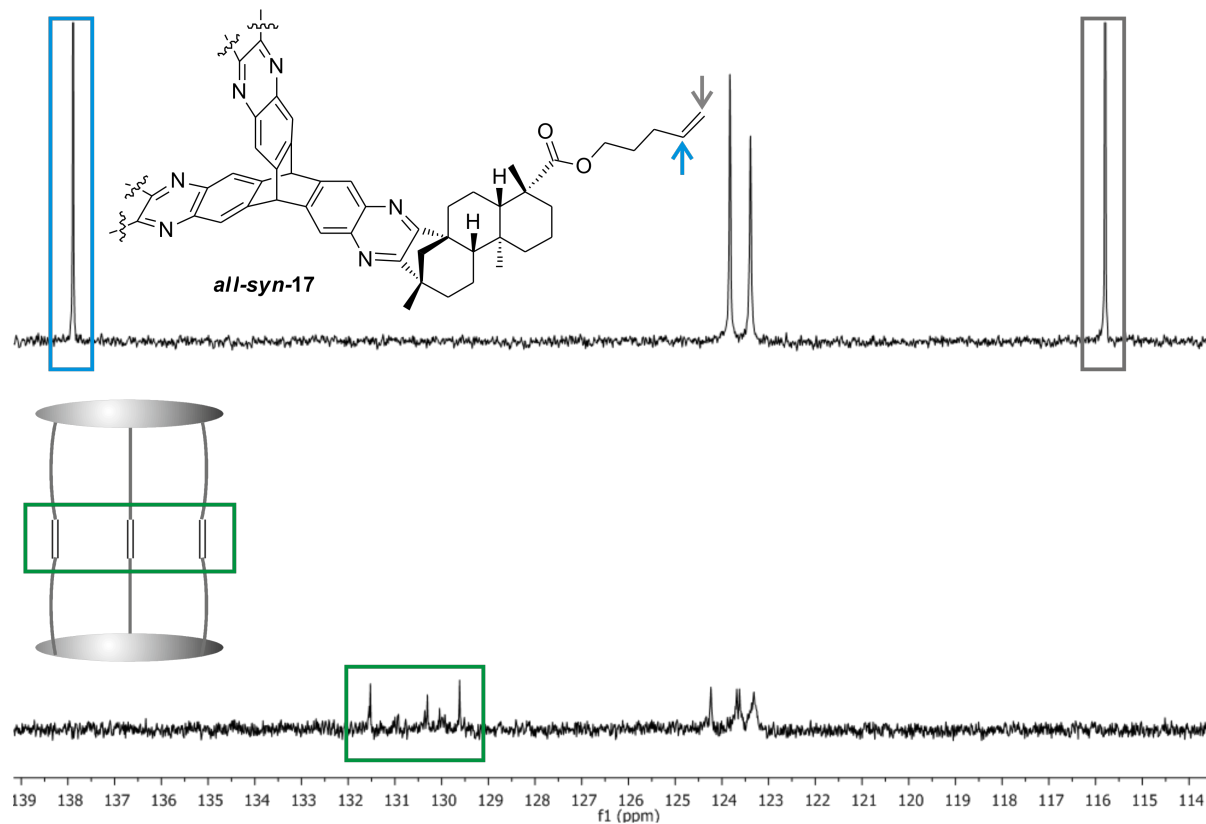
Figure 7: Extracts of the ^{13}C NMR spectra of starting material and product.
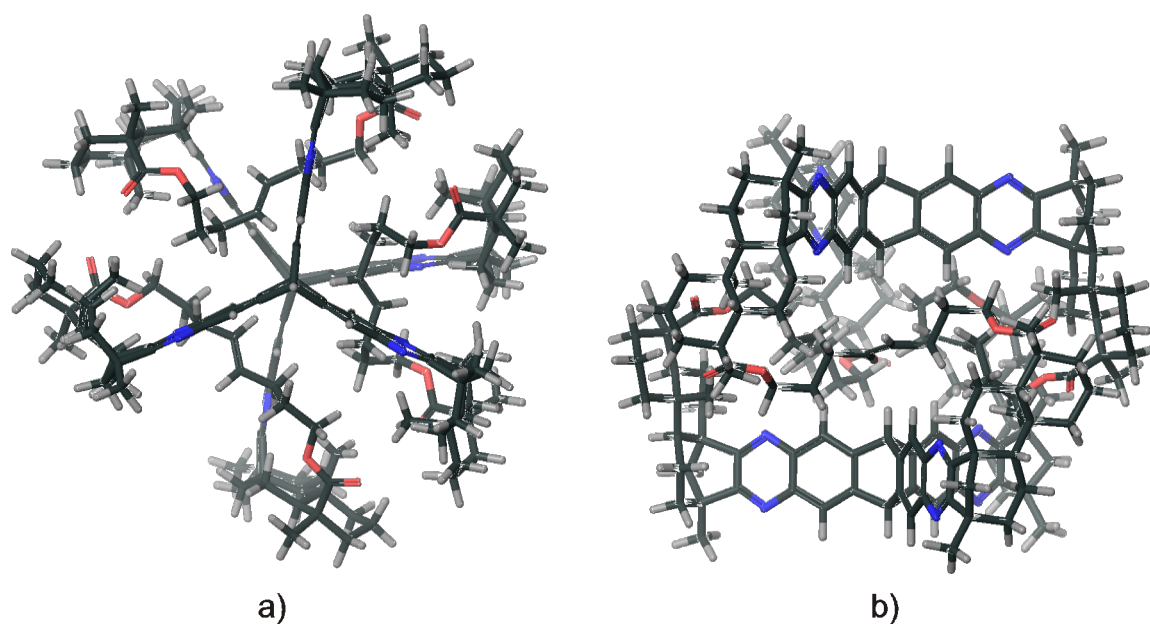
Figure 8: Molecular modelling structure (MacroModel 9.3.5) of collapsed **19**, (a) top view; (b) side view.
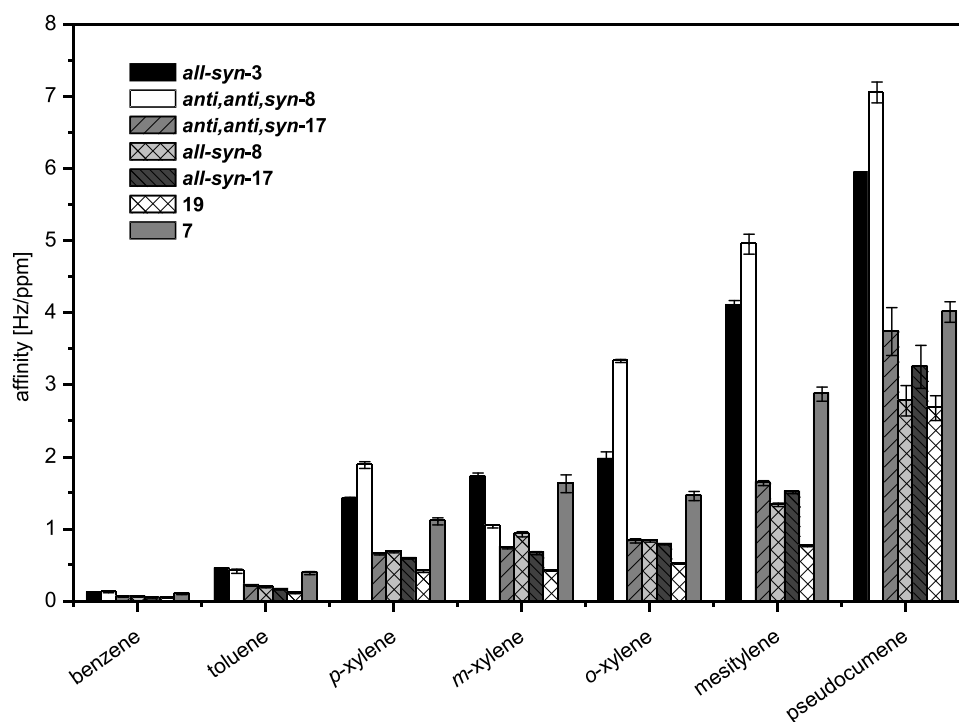
Figure 9: Screening of aromatic analytes with affinity materials **3**, **7**, **8**, **17** and **19**.
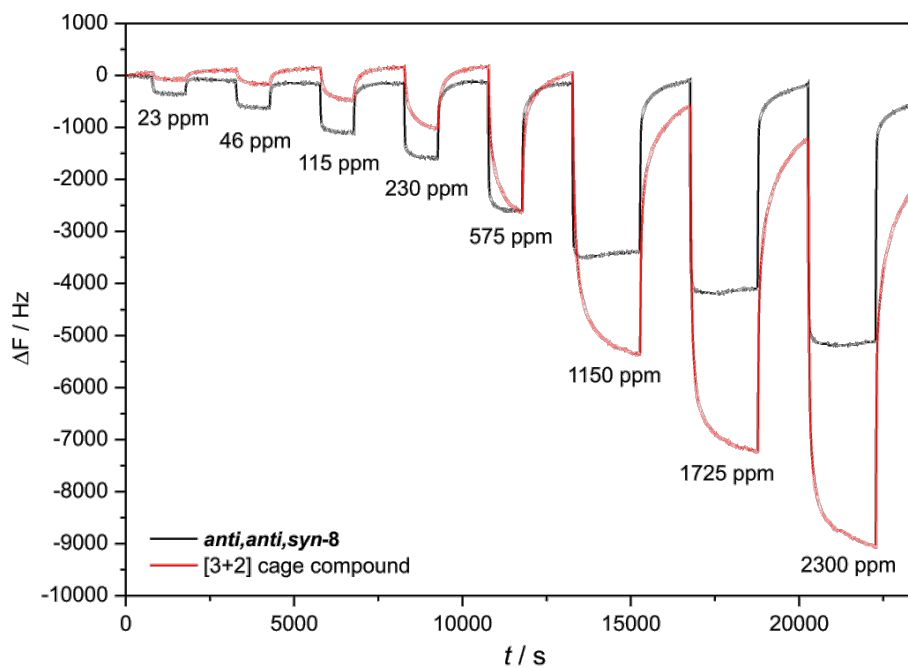
Figure 10: Primary data of *anti,anti,syn*-**8** and a [3 + 2] cage compound (increasing pseudocumene concentrations and recovery times between each step, for details see Supporting Information File 1).

For comparison, we included the primary data of an organic cage compound (for structure see Supporting Information File 1) which was published recently [71]. At small concentrations which are relevant for tracing, *anti,anti,syn*-**8** is creating unusual large signals which indicates a high affinity of the material for this analyte. For high concentrations, other materials like the [3 + 2] cage compound get ahead in means of signal depth, indicating more places for adsorption on/in the film. This behavior of *anti,anti,syn*-**8** is exclusively observed for the aromatic analytes. Our triptycene-based cage compound **19** exhibits only moderate affinities, which is in accordance with the calculated collapsed structure (Figure 8).

For protic analytes, *anti,anti,syn*-**8** is comparable or even inferior to other triptycene based materials (Figure 11). Therefore, *anti,anti,syn*-**8** is a very promising substance for the application as affinity material in a sensor array for the tracing of air-borne aromatic compounds at high dilution. Besides *anti,anti,syn*-**8**, the triphenylene based architecture all-*syn*-**3** also exhibits excellent affinities towards the aromatic analytes as well as very inferior affinities to protic analytes (Figure 11).

The affinities of triptycene derivatives with different protecting groups on the carboxylic acid function to protic analytes were then compared (Figure 11). While the adsorption of aromatic analytes is dominated by the cavity size, the nature of the protection group dominates the adsorption of the protic analytes

via hydrogen bonding [72]. A clear dependency on the number of nitro groups in the molecule, ascending from **8** with no nitro group to **14** with six nitro groups per molecule, is observed, indicating a strong influence of hydrogen bonding interactions between analyte and affinity material.

Conclusion

Architectures based on triptycenes and (−)-isosteviol create molecular voids which can accommodate guest molecules. These molecular templates are the basis for powerful affinity materials of quartz crystal microbalances (QCM). In particular, the combination of 15-oxoisosteviol methyl ester with hexa-aminotriptycene provides upon condensation reaction the statistically prone *anti,anti,syn*-derivative which shows unique properties as affinity material in QCM studies with aromatic analytes. Although this affinity material exhibits moderate performance at high analyte concentrations unusual strong signals are found at low concentrations of the analytes. This powerful and unique performance in the low ppm range is an essential prerequisite for latter tracing applications, e.g. gravimetric sensing. This superior property is attributed to well accessible molecular voids. As soon as such structures are allowed to collapse the outstanding affinity is not observed anymore.

Experimental

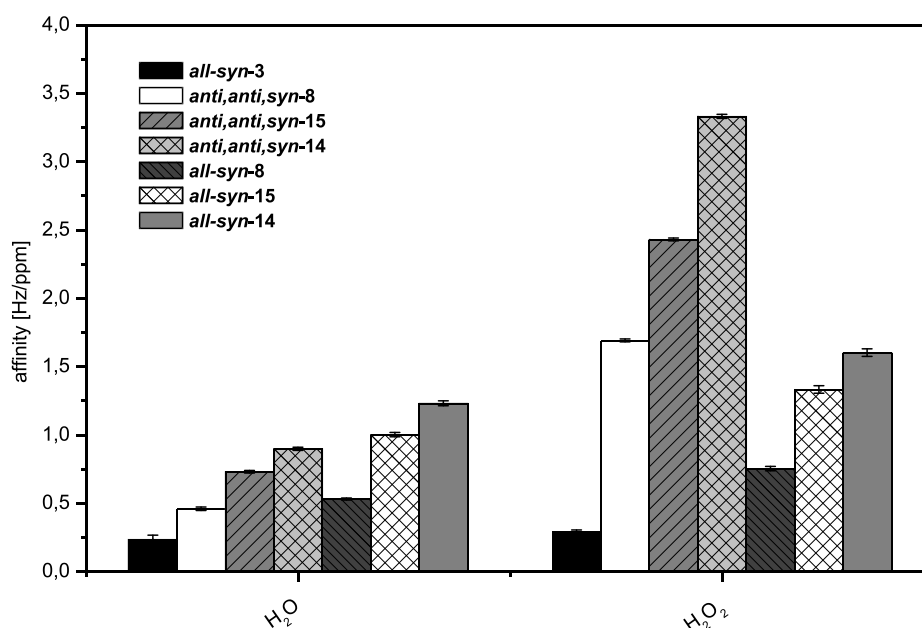For preparation and characterization of the compounds, see Supporting Information File 1.

Figure 11: Screening of protic analytes with affinity materials **3**, **8**, **14** and **15**.

Supporting Information

Supporting Information File 1
Characterization data, spectra of synthesized compounds, QCM set up, and QCM screening details.
[http://www.beilstein-journals.org/bjoc/content/supplementary/1860-5397-9-317-S1.pdf]

Acknowledgements

References

1. Steed, J. W.; Turner, D. R.; Wallace, K. J. *Core Concepts in Supramolecular Chemistry and Nanochemistry,* 1st ed.; John Wiley & Sons: Chichester, 2007.
2. Steed, J. W.; Atwood, J. L. *Supramolecular Chemistry,* 2nd ed.; John Wiley & Sons: Chichester, 2009.
3. Lehn, J.-M. *Supramolecular Chemistry. Concepts and Perspectives;* VCH: Weinheim, 1995.
4. Kim, J.; McHugh, S. K.; Swager, T. M. *Macromolecules* **1999,** *32,* 1500–1507. doi:10.1021/ma981774r
5. Weilandt, T.; Troff, R. W.; Saxell, H.; Rissanen, K.; Schalley, C. A. *Inorg. Chem.* **2008,** *47,* 7588–7598. doi:10.1021/ic800334k
6. Diederich, F.; Stang, P. J.; Tykwinski, R. R., Eds. *Modern Supramolecular Chemistry. Strategies for Macrocycle Synthesis,* 1st ed.; Wiley-VCH: Weinheim, 2008. doi:10.1002/9783527621484
7. Raatikainen, K.; Beyeh, N. K.; Rissanen, K. *Chem.–Eur. J.* **2010,** *16,* 14554–14564. doi:10.1002/chem.201001695
8. Cram, D. J. *Science* **1988,** *240,* 760–767. doi:10.1126/science.3283937
9. Hou, Z.; Sunderland, C. J.; Nishio, T.; Raymond, K. N. *J. Am. Chem. Soc.* **1996,** *118,* 5148–5149. doi:10.1021/ja9600946
10. Fiedler, D.; Leung, D. H.; Bergman, R. G.; Raymond, K. N. *Acc. Chem. Res.* **2005,** *38,* 349–358. doi:10.1021/ar040152p
11. Moberg, C. *Angew. Chem.* **1998,** *110,* 260–281. doi:10.1002/(SICI)1521-3757(19980202)110:3<260::AID-ANGE260>3.0.CO;2-6
Angew. Chem., Int. Ed. **1998,** *37,* 248–268. doi:10.1002/(SICI)1521-3773(19980216)37:3<248::AID-ANIE248>3.0.CO;2-5
12. Moberg, C. *Angew. Chem.* **2006,** *118,* 4838–4840. doi:10.1002/ange.200601214
Angew. Chem., Int. Ed. **2006,** *45,* 4721–4723. doi:10.1002/anie.200601214
13. Rebek, J., Jr. *Angew. Chem.* **1990,** *102,* 261–272. doi:10.1002/ange.19901020306
Angew. Chem., Int. Ed. Engl. **1990,** *29,* 245–255. doi:10.1002/anie.199002451
14. Gibson, S. E.; Castaldi, M. P. *Chem. Commun.* **2006,** 3045–3062. doi:10.1039/b602237e
15. Waldvogel, S. R.; Wartini, A. R.; Rasmussen, P. H.; Rebek, J., Jr. *Tetrahedron Lett.* **1999,** *40,* 3515–3518. doi:10.1016/S0040-4039(99)00545-6
16. Orghici, R.; Lützow, P.; Burgmeier, J.; Koch, J.; Heidrich, H.; Schade, W.; Welschoff, N.; Waldvogel, S. R. *Sensors* **2010,** *10,* 6788–6795. doi:10.3390/s100706788
17. Börner, S.; Orghici, R.; Waldvogel, S. R.; Willer, U.; Schade, W. *Appl. Opt.* **2009,** *48,* B183–B189. doi:10.1364/AO.48.00B183
18. Siering, C.; Kerschbaumer, H.; Nieger, M.; Waldvogel, S. R. *Org. Lett.* **2006,** *8,* 1471–1474. doi:10.1021/ol0603110
19. Bomkamp, M.; Siering, C.; Landrock, K.; Stephan, H.; Fröhlich, R.; Waldvogel, S. R. *Chem.–Eur. J.* **2007,** *13,* 3724–3732. doi:10.1002/chem.200601231
20. Siering, C.; Beermann, B.; Waldvogel, S. R. *Supramol. Chem.* **2006,** *18,* 23–27. doi:10.1080/10610270500310479
21. Waldvogel, S. R.; Fröhlich, R.; Schalley, C. A. *Angew. Chem.* **2000,** *112,* 2580–2583. doi:10.1002/1521-3757(20000717)112:14<2580::AID-ANGE2580>3.0.CO;2-D
Angew. Chem., Int. Ed. **2000,** *39,* 2472–2475. doi:10.1002/1521-3773(20000717)39:14<2472::AID-ANIE2472>3.0.CO;2-F
22. Schopohl, M. C.; Faust, A.; Mirk, D.; Fröhlich, R.; Kataeva, O.; Waldvogel, S. R. *Eur. J. Org. Chem.* **2005,** 2987–2999. doi:10.1002/ejoc.200500108
23. Schopohl, M. C.; Siering, C.; Kataeva, O.; Waldvogel, S. R. *Angew. Chem.* **2003,** *115,* 2724–2727. doi:10.1002/ange.200351102
Angew. Chem., Int. Ed. **2003,** *42,* 2620–2623. doi:10.1002/anie.200351102
24. Siering, C.; Grimme, S.; Waldvogel, S. R. *Chem.–Eur. J.* **2005,** *11,* 1877–1888. doi:10.1002/chem.200401002
25. Bridel, M.; Lavieille, R. B. *Soc. Chim. Biol.* **1931,** 781–796.
26. Lohoelter, C. Supramolekulare Affinitätsmaterialien basierend auf (–)-Isosteviol. Ph.D. Thesis, Johannes Gutenberg-Universität, Mainz, Germany, 2013.
The synthetic work presented in this manuscript is part of the Ph.D. thesis.
27. Mosettig, E.; Nes, W. R. *J. Org. Chem.* **1955,** *20,* 884–899. doi:10.1021/jo01125a013
28. Roy, A.; Roberts, F. G.; Wilderman, P. R.; Zhou, K.; Peters, R. J.; Coates, R. M. *J. Am. Chem. Soc.* **2007,** *129,* 12453–12460. doi:10.1021/ja072447e
29. Mosettig, E.; Beglinger, U.; Dolder, F.; Lichti, H.; Quitt, P.; Waters, J. A. *J. Am. Chem. Soc.* **1963,** *85,* 2305–2309. doi:10.1021/ja00898a025
30. Wood, H. B.; Allerton, R.; Diehl, H. W.; Fletcher, H. G. *J. Org. Chem.* **1955,** *20,* 875–883. doi:10.1021/jo01125a012
31. Wu, Y.; Dai, G.-F.; Yang, J.-H.; Zhang, Y.-X.; Zhu, Y.; Tao, J.-C. *Bioorg. Med. Chem. Lett.* **2009,** *19,* 1818–1821. doi:10.1016/j.bmcl.2008.12.101
32. Wu, Y.; Liu, C.-J.; Liu, X.; Dai, G.-F.; Do, J.-Y.; Tao, J.-C. *Helv. Chim. Acta* **2010,** *93,* 2052–2069. doi:10.1002/hlca.201000046
33. Lin, L.-H.; Lee, L.-W.; Sheu, S.-Y.; Lin, P.-Y. *Chem. Pharm. Bull.* **2004,** *52,* 1117–1122. doi:10.1248/cpb.52.1117
34. Chatsudthipong, V.; Muanprasat, C. *Pharmacol. Ther.* **2009,** *121,* 41–54. doi:10.1016/j.pharmthera.2008.09.007
35. Lohoelter, C.; Weckbecker, M.; Waldvogel, S. R. *Eur. J. Org. Chem.* **2013,** 5539–5554. doi:10.1002/ejoc.201300447
36. Kataev, V. E.; Strobykina, I. Yu.; Militsina, O. I.; Korochkina, M. G.; Fedorova, O. V.; Ovchinnikova, I. G.; Valova, M. S.; Rusinov, G. L. *Tetrahedron Lett.* **2006,** *47,* 2137–2139. doi:10.1016/j.tetlet.2006.01.126

37. An, Y.-J.; Zhang, Y.-X.; Wu, Y.; Liu, Z.-M.; Pi, C.; Tao, J.-C. *Tetrahedron: Asymmetry* **2010,** *21,* 688–694. doi:10.1016/j.tetasy.2010.04.019

38. Al'fonsov, V. A.; Andreeva, O. V.; Bakaleinik, G. A.; Beskrovnyi, D. V.; Gubaidullin, A. T.; Kataev, V. E.; Kovylyaeva, G. I.; Konovalov, A. I.; Korochkina, M. G.; Litvinov, I. A.; Militsina, O. I.; Strobykina, I. Yu. *Russ. J. Gen. Chem.* **2003,** *73,* 1255–1260. doi:10.1023/B:RUGC.0000007651.53262.a5

39. Andreeva, O. V.; Garifullin, B. F.; Gubaidullin, A. T.; Al'fonsov, V. A.; Kataev, V. E.; Ryzhikov, D. V. *J. Struct. Chem.* **2007,** *48,* 540–546. doi:10.1007/s10947-007-0081-1

40. Bomkamp, M.; Artiukhov, A.; Kataeva, O.; Waldvogel, S. R. *Synthesis* **2007,** 1107–1114. doi:10.1055/s-2007-965986

41. Swager, T. M. *Acc. Chem. Res.* **2008,** *41,* 1181–1189. doi:10.1021/ar800107v

42. Zhang, C.; Liu, Y.; Li, B.; Tan, B.; Chen, C.-F.; Xu, H.-B.; Yang, X.-L. *ACS Macro Lett.* **2012,** *1,* 190–193. doi:10.1021/mz200076c

43. Chong, J. H.; Ardakani, S. J.; Smith, K. J.; MacLachlan, M. J. *Chem.–Eur. J.* **2009,** *15,* 11824–11828. doi:10.1002/chem.200902188

44. McKeown, N. B.; Budd, P. M.; Book, D. *Macromol. Rapid Commun.* **2007,** *28,* 995–1002. doi:10.1002/marc.200700054

45. Mastalerz, M.; Oppel, I. M. *Angew. Chem.* **2012,** *124,* 5345–5348. doi:10.1002/ange.201201174 *Angew. Chem., Int. Ed.* **2012,** *51,* 5252–5255. doi:10.1002/anie.201201174

46. Zhao, Y.-C.; Cheng, Q.-Y.; Zhou, D.; Wang, T.; Han, B.-H. *J. Mater. Chem.* **2012,** *22,* 11509–11514. doi:10.1039/c2jm31187a

47. Hashem, M.; Grazia Bezzu, C.; Kariuki, B. M.; McKeown, N. B. *Polym. Chem.* **2011,** *2,* 2190–2192. doi:10.1039/c1py00288k

48. Ghanem, B. S. *Polym. Chem.* **2012,** *3,* 96–98. doi:10.1039/c1py00423a

49. Schneider, M. W.; Oppel, I. M.; Ott, H.; Lechner, L. G.; Hauswald, H.-J. S.; Stoll, R.; Mastalerz, M. *Chem.–Eur. J.* **2012,** *18,* 836–847. doi:10.1002/chem.201102857

50. Rabbani, M. G.; Reich, T. E.; Kassab, R. M.; Jackson, K. T.; El-Kaderi, H. M. *Chem. Commun.* **2012,** *48,* 1141–1143. doi:10.1039/c2cc16986j

51. Tauchert, M. E.; Warth, D. C. M.; Braun, S. M.; Gruber, I.; Ziesak, A.; Rominger, F.; Hofmann, P. *Organometallics* **2011,** *30,* 2790–2809. doi:10.1021/om200164f

52. Li, Y.; Wilson, J. J.; Do, L. H.; Apfel, U.-P.; Lippard, S. J. *Dalton Trans.* **2012,** *41,* 9272–9275. doi:10.1039/c2dt31260c

53. Frantz, D. K.; Linden, A.; Baldridge, K. K.; Siegel, J. S. *J. Am. Chem. Soc.* **2012,** *134,* 1528–1535. doi:10.1021/ja2063346

54. Jacquot de Rouville, H.-P.; Garbage, R.; Cook, R. E.; Pujol, A. R.; Sirven, A. M.; Rapenne, G. *Chem.–Eur. J.* **2012,** *18,* 3023–3031. doi:10.1002/chem.201102893

55. Chong, J. H.; MacLachlan, M. J. *Chem. Soc. Rev.* **2009,** *38,* 3301–3315. doi:10.1039/b900754g

56. Jiang, Y.; Chen, C.-F. *Eur. J. Org. Chem.* **2011,** 6377–6403. doi:10.1002/ejoc.201100684

57. Lubczyk, D.; Siering, C.; Lörgen, J.; Shifrina, Z. B.; Müllen, K.; Waldvogel, S. R. *Sens. Actuators, B* **2010,** *143,* 561–566. doi:10.1016/j.snb.2009.09.061

58. Fenn, J. B. *Angew. Chem.* **2003,** *115,* 3999–4024. doi:10.1002/ange.200300605 *Angew. Chem., Int. Ed.* **2003,** *42,* 3871–3894. doi:10.1002/anie.200300605

59. Rapp, M.; Bender, F.; Lubert, K.-H.; Voigt, A.; Bargon, J.; Wächter, L.; Klesper, G.; Klesper, H.; Fusshöller, G. Vorrichtung zum Aufbringen von Elektrospraybeschichtungen auf elektrisch nicht leitfähigen Oberflächen. Ger. Pat. 103,44,135 A1, May 4, 2005.

60. Martin, T.; Obst, U.; Rebek, J., Jr. *Science* **1998,** *281,* 1842–1845. doi:10.1126/science.281.5384.1842

61. Mastalerz, M.; Sieste, S.; Cenić, M.; Oppel, I. M. *J. Org. Chem.* **2011,** *76,* 6389–6393. doi:10.1021/jo200843v

62. Riley, H. L.; Morley, J. F.; Friend, N. A. C. *J. Chem. Soc.* **1932,** 1875–1883. doi:10.1039/jr9320001875

63. Waitkins, G. R.; Clark, C. W. *Chem. Rev.* **1945,** *36,* 235–289. doi:10.1021/cr60115a001

64. Bomkamp, M.; Gottfried, K.; Kataeva, O.; Waldvogel, S. R. *Synthesis* **2008,** 1443–1447. doi:10.1055/s-2008-1072533

65. Coates, R. M.; Kang, H. Y. *J. Org. Chem.* **1987,** *52,* 2065–2074. doi:10.1021/jo00386a031

66. Kovylyaeva, G. I.; Sharipova, R. R.; Strobykina, I. Yu.; Militsina, O. I.; Musin, R. Z.; Beskrovnyi, D. V.; Gubaidullin, A. T.; Al'fonsov, V. A.; Kataev, V. E. *Russ. J. Gen. Chem.* **2009,** *79,* 2663–2667. doi:10.1134/S1070363209120184

67. Hiroaki, S. H. M. Process for synthesizing cyclic peptide compound. Eur. Pat. 2,141,175 A1, March 26, 2010.

68. Merski, M.; Townsend, C. A. *J. Am. Chem. Soc.* **2007,** *129,* 15750–15751. doi:10.1021/ja076704r

69. Misner, J. W.; Fisher, J. W.; Gardner, J. P.; Pedersen, S. W.; Trinkle, K. L.; Jackson, B. G.; Zhang, T. Y. *Tetrahedron Lett.* **2003,** *44,* 5991–5993. doi:10.1016/S0040-4039(03)01483-7

70. Muthusamy, S.; Gnanaprakasam, B.; Suresh, E. *J. Org. Chem.* **2007,** *72,* 1495–1498. doi:10.1021/jo062043p

71. Brutschy, M.; Schneider, M. W.; Mastalerz, M.; Waldvogel, S. R. *Adv. Mater.* **2012,** *24,* 6049–6052. doi:10.1002/adma.201202786

72. Brutschy, M.; Schneider, M. W.; Mastalerz, M.; Waldvogel, S. R. *Chem. Commun.* **2013,** *49,* 8398–8400. doi:10.1039/c3cc43829e

Self-assembly of metallosupramolecular rhombi from chiral concave 9,9'-spirobifluorene-derived bis(pyridine) ligands

Rainer Hovorka[1], Sophie Hytteballe[1], Torsten Piehler[1],
Georg Meyer-Eppler[1], Filip Topić[2], Kari Rissanen[2], Marianne Engeser[1]
and Arne Lützen[*1]

Full Research Paper

Address:
[1]University of Bonn, Kekulé-Institute of Organic Chemistry and
Biochemistry, Gerhard-Domagk-Str. 1, D-53121 Bonn, Germany and
[2]Department of Chemistry, Nanoscience Center, University of
Jyväskylä, P.O. Box 35, 40014 Jyväskylä, Finland

Email:
Arne Lützen[*] - arne.luetzen@uni-bonn.de

* Corresponding author

Abstract

Two new 9,9'-spirobifluorene-based bis(4-pyridines) were synthesised in enantiopure and one also in racemic form. These ligands act as concave templates and form metallosupramolecular $[(dppp)_2M_2L_2]$ rhombi with *cis*-protected $[(dppp)Pd]^{2+}$ and $[(dppp)Pt]^{2+}$ ions. The self-assembly process of the racemic ligand preferably occurs in a narcissistic self-recognising manner. Hence, a mixture of all three possible stereoisomers $[(dppp)_2M_2\{(R)-L\}_2](OTf)_4$, $[(dppp)_2M_2\{(S)-L\}_2](OTf)_4$, and $[(dppp)_2M_2\{(R)-L\}\{(S)-L\}](OTf)_4$ was obtained in an approximate 1.5:1.5:1 ratio which corresponds to an amplification of the homochiral assemblies by a factor of approximately three as evidenced by NMR spectroscopy and mass spectrometry. The racemic homochiral assemblies could also be characterised by single crystal X-ray diffraction.

Introduction

Concave templates are versatile tools to achieve self-sorting behaviour in the self-assembly of defined aggregates from multicomponent mixtures in a social self-discrimination or a narcissistic self-recognition manner [1-3]. Usually, geometrical size and shape complementarity are employed to ensure such self-sorting. However, these factors do not account in self-

sorting processes where enantiomers are involved whose shape and size does not vary but only their relative spatial orientation. Hence, chiral self-sorting is a truly challenging task and high-fidelity chiral self-sorting processes have been observed in a rather limited number of examples for the formation of stereo-chemically defined metallosupramolecular aggregates from

racemic ligands in a self-recognising [4-18] or a self-discriminating manner [19-27].

As part of our ongoing programme to develop general guidelines for the diastereoselective self-assembly of metallosupramolecular aggregates, we have recently started a systematic study on the influence of rigid concave building blocks on the outcome of the self-assembly of bis(pyridine) ligands into dinuclear metallosupramolecular rhombi upon coordination to *cis*-protected [(dppp)Pd(OTf)$_2$] or [(dppp)Pt(OTf)$_2$] (dppp = 1,3-bis(diphenylphosphino)propane) complexes [27,28]. So far we have studied templates based on the Tröger's base [27] and the 2,2'-dihydroxybinaphthyl (BINOL) [28] scaffold and identified the bend angle of these V-shaped compounds to be a critical factor for the degree of self-sorting that can be achieved [9,15-18,25-28].

The 9,9'-spirobifluorene scaffold is another very interesting concave structure that offers the possibility to orient functional groups in a defined manner [29]. Hence, we were wondering how V-shaped bis(pyridine) ligands based on this chiral skeleton would behave upon coordination to [(dppp)Pd(OTf)$_2$] or [(dppp)Pt(OTf)$_2$] in order to learn more about the underlying principles of chiral self-sorting in metallosupramolecular chemistry.

Results and Discussion
Synthesis
The synthesis of the spirobifluorene-based templates is shown in Scheme 1. It started from 2-aminobiphenyl following the established procedures of J. M. Tour [30], M. Gomberg [31], and V. Prelog [32,33] leading to (*rac*)-2,2'-dihydroxy-9,9'-spirobifluorene ((*rac*)-**1**) in six consecutive steps. This sequence involved a Sandmeyer-like iodination, followed by a Grignard reaction with fluorenone to furnish the corresponding tertiary alcohol. This alcohol was subjected to an acid-mediated condensation to give the 9,9'-spirobifluorene. Friedel–Crafts acylation with acetyl chloride gave rise to the racemic 2,2'-diketone which was transformed to the racemic diester in a Baeyer–Villiger oxidation. Saponification of the ester functions then afforded (*rac*)-**1**. One part of the racemic material was transformed into the corresponding racemic ditriflate (*rac*)-**2** which was reacted with a 4-pyridylboronic acid ester in a Suzuki cross-coupling to afford the desired racemic bis(pyridine) ligand (*rac*)-**3**. (Please note that (*rac*)-**3** has been prepared before, however, on a different way [34].)

The other part of the racemic diol (*rac*)-**1** was resolved via clathrate formation with (*R*,*R*)-2,3-dimethoxy-*N*,*N*,*N'*,*N'*-tetra-cyclohexylsuccindiamide to obtain enantiomerically pure (*R*)-**1** and (*S*)-**1** [35,36] which were subsequently converted into the optically pure ditriflates (*R*)-**2** and (*S*)-**2**. (*R*)-**2** was then subjected to a two-fold Suzuki reaction to obtain the enantiomerically pure bis(pyridine) ligand (*R*)-**3**. (Please note, that the conditions used to elaborate the enantiomerically pure 9,9'-spirobifluorene derivatives were demonstrated not to affect the optical purity of these compounds in our previous work (see [35]).)

(*S*)-**1**, however, was reacted in a nickel-catalysed Kumada cross-coupling reaction to furnish 2,2'-dimethylated spirobifluorene (*S*)-**4** which was then brominated twice to afford tetra-functionalised spirobifluorene (*S*)-**5**. Finally, (*S*)-**5** could be transformed into the second bis(pyridine) ligand (*S*)-**6** in a two-fold Suzuki reaction.

Metal coordination
After the successful synthesis we mixed solutions of ligands **3** and **6** and [(dppp)Pd(OTf)$_2$] or [(dppp)Pt(OTf)$_2$] and characterised the resulting complexes by ^{1}H, ^{31}P, ^{1}H 2D-DOSY NMR, ESI-MS, and single crystal X-ray diffraction to investigate if the desired rhomboid complexes are formed and whether we can observe any degree of self-sorting in the self-assembly processes of the racemic samples.

The ESI-MS spectra recorded from the complex solutions showed the successful formation of the expected dinuclear [(dppp)$_2$M$_2$(L)$_2$] aggregates with different numbers of counter ions both from the enantiomerically pure (*R*)-**3** and the racemic ligand (*rac*)-**3** and the enantiomerically pure template (*S*)-**6**, and hence, proved the selectivity of the self-assembly processes in terms of aggregate stoichiometry (Figure 1 and Supporting Information File 1). (Please note, that we investigated our complexes in a number of different solvents (acetone, acetonitrile, mixtures of dichloromethane and acetonitrile) and in all cases we observed the expected dinuclear [(dppp)$_2$M$_2$(L)$_2$]-complexes as the dominating species.)

Next we measured ^{1}H NMR spectra of the aggregates and the free ligands. All complexes of the enantiomerically pure ligands gave rise to NMR spectra with sharp but significantly shifted signals compared to the ones of the free ligands, which supports the formation of discrete metallosupramolecular species (Figure 2b,c). This could be further confirmed by 2D ^{1}H DOSY NMR spectra (see Supporting Information File 1) of the aggregates as well as of the free ligands. In all cases the relative size of the aggregates was a little more than twice as large as that of the respective concave template. (Please note, that we could only determine relative sizes or ratios of sizes from the DOSY experiments because the spectra were recorded in a 3:1 mixture of dichloromethane and acetonitrile of unknown viscosity which does not allowed us to calculate hydrodynamic radii.)
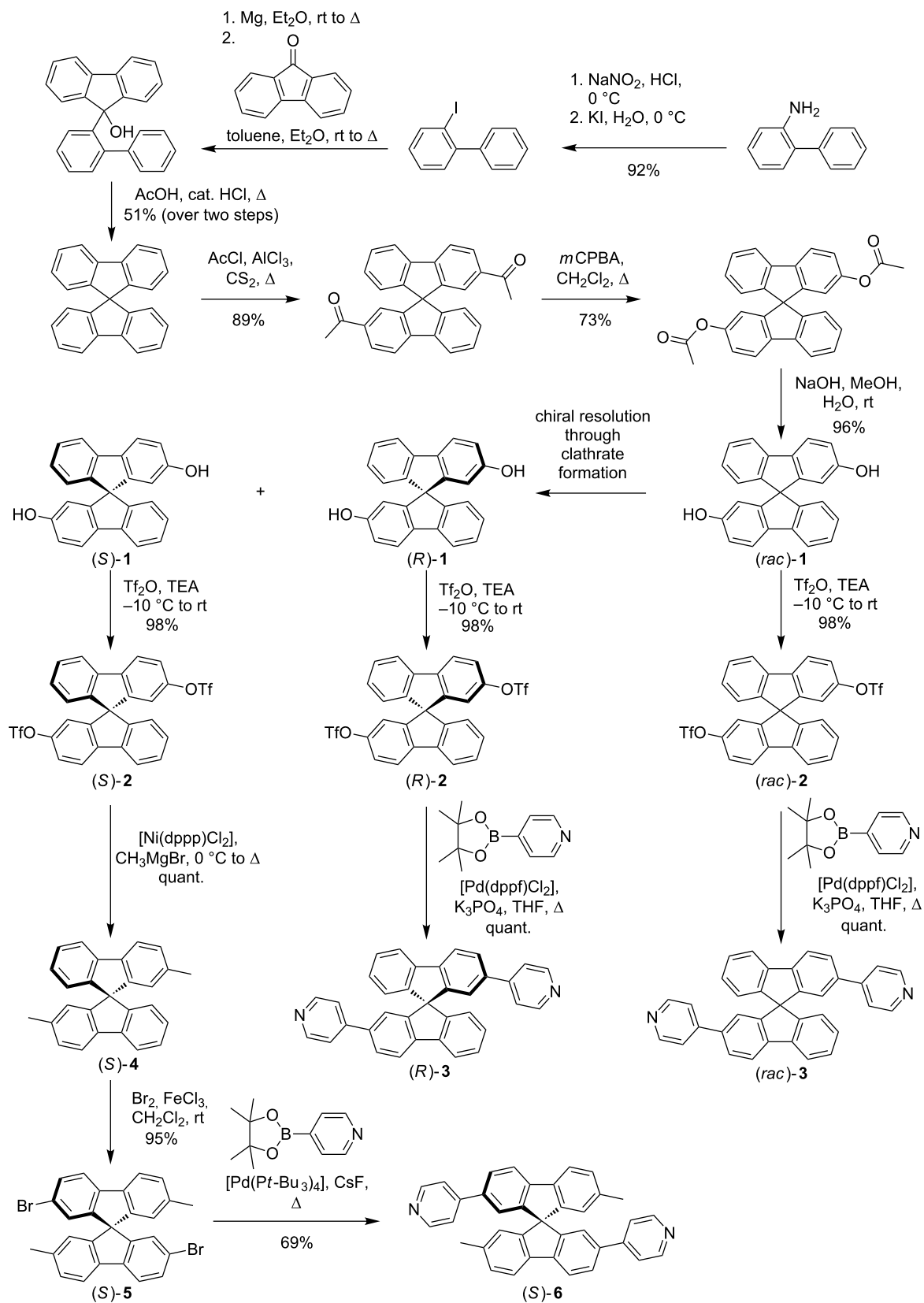
Scheme 1: Synthesis of ligands **3** and **6**.
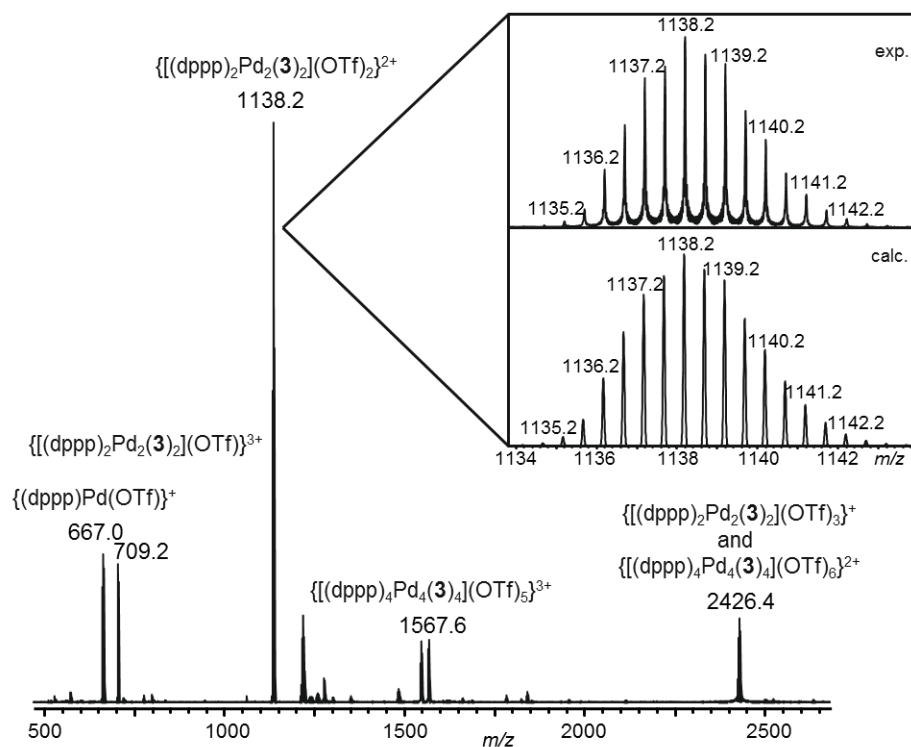
Figure 1: ESI mass spectrum (positive mode) of an 1:1 mixture of (*R*)-**3** and [(dppp)Pd(OTf)$_2$] in acetone.
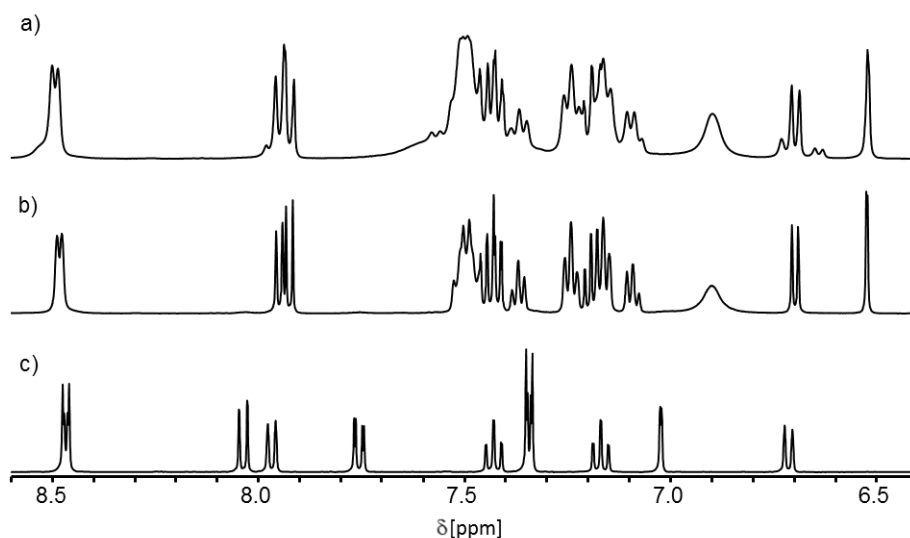
Figure 2: ^{1}H NMR spectra (500.1 MHz, in CD$_2$Cl$_2$/CD$_3$CN 3:1 at 298 K) of a) a 1:1 mixture of [Pd(dppp)]OTf$_2$ and (*rac*)-**3**, b) a 1:1 mixture of [Pd(dppp)]OTf$_2$ and (*R*)-**3**, and c) (*R*)-**3**.

Therefore, these NMR-spectroscopic results nicely complement the results from mass spectrometry with regard to the assemblies' composition.

Comparison of the ^{1}H NMR spectra of the homochiral complexes of (*R*)-**3** with the spectra of the complexes obtained from the racemic ligand (*rac*)-**3** then allowed us to obtain infor-

mation about the stereoselectivity of the self-assembly processes (Figure 2a,b). In principle, three stereoisomers of the dinuclear metallosupramolecular rhombi can form from racemic ligands upon coordination to [(dppp)Pd(OTf)$_2$] or [(dppp)Pt(OTf)$_2$] – a racemic mixture of two enantiomeric homochiral assemblies and an achiral heterochiral complex. These are expected to form in a 1:1:2 ratio if the assembly would occur in a completely non-selective purely statistical manner. Any deviation from this ratio would either mean an amplification of the racemic homochiral assemblies in the sense of self-recognition or an amplification of the heterochiral assembly in the sense of self-discrimination.

Analysis of the ^{1}H NMR spectra provides versatile information: first, the self-assembly is not completely diastereoselective, since a number of additional signals are visible in the spectrum of the aggregates obtained from (*rac*)-**3**. Second, the self-assembly does not happen in a completely statistical fashion but rather proceeds with a preference for forming homochiral

complexes for both palladium (Figure 2a,b) and platinum ions since the intensity of the signals of the homochiral assemblies is larger than expected from statistics. However, both diastereomers were found to give very similar NMR spectra resulting in strong signal overlap. Hence, we wanted to obtain further proof by recording ^{31}P NMR spectra in which signal overlap should be considerably less problematic due to the much broader spectral width.

As shown in Figure 3 the ^{31}P NMR spectra indeed confirm the conclusions drawn from the ^{1}H NMR spectra. Two individual peaks for the two diastereomers can be detected when (*rac*)-**3** is employed for complexation and the intensities of the signals of the racemic homochiral diastereomer are approximately three times as large as those of the signals of the heterochiral one in both cases – the palladium and the platinum complexes and independent of the solvents we used. This corresponds to an amplification of the homochiral stereoisomers via self-recognition by a factor of approximately three.
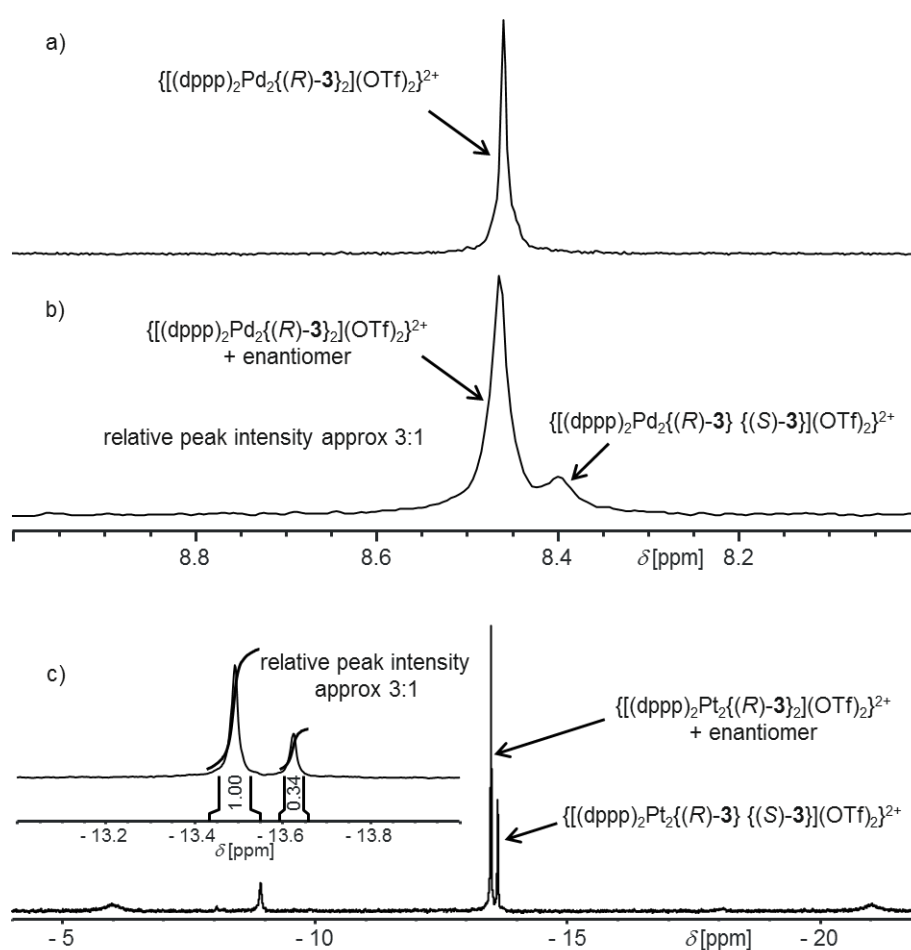
Figure 3: ^{31}P NMR spectra of a) a 1:1 mixture of [Pd(dppp)]OTf$_2$ and (*R*)-**3**, b) a 1:1 mixture of [Pd(dppp)]OTf$_2$ and (*rac*)-**3** (both recorded at 162.0 MHz in CD$_2$Cl$_2$/CD$_3$CN 3:1 at 293 K), and c) of a 1:1 mixture of [Pt(dppp)]OTf$_2$ and (*rac*)-**3** (202.5 MHz, in CD$_2$Cl$_2$ at 298 K).

Although these NMR spectra already provide a very good proof for the stereoselectivity of the self-assembly process we wanted to get additional independent evidence by another analytical method. Standard mass spectrometry, however, cannot distinguish between different stereoisomers. In order to employ this technique for this purpose, we therefore used a 1:1 mixture of ligands (*R*)-**3** and (*S*)-**6** as a *pseudo*-racemate in which the two methyl groups of **6** in the outer periphery of the ligand structure serve as a kind of mass label. These labels then allowed us to identify the three possible different complexes due to their different number of methyl groups, and hence, different *m/z* values. Equimolar amounts of the enantiomerically pure ligands (*R*)-**3** and (*S*)-**6** and two equivalents of the respective metal corner were mixed. The ESI mass spectrum of the diluted solution (Figure 4) nicely corroborates the results obtained by the NMR experiments as it shows the presence of ions derived from all three complexes $[(dppp)_2M_2\{(R)\text{-}\mathbf{3}\}_2](OTf)_4$, $[(dppp)_2M_2\{(R)\text{-}\mathbf{3}\}\{(S)\text{-}\mathbf{6}\}](OTf)_4$, and $[(dppp)_2M_2\{(S)\text{-}\mathbf{6}\}_2](OTf)_4$. Furthermore the peak ratios of the signals of these ions differ from the statistically expected 1:2:1 ratio. Although these peak ratios suggest a slightly lower amplification of the homochiral assemblies by a factor of only two to three, this still reinforces our analysis – especially, if one takes into account that mass labelling in the periphery might cause differences in the ESI response factors that can cause slight deviations in the

relative quantification of different components compared to the ratios obtained by other techniques, e.g. NMR spectroscopy, as we have recently reported [28].

Finally, we were able to grow single crystals of the dinuclear palladium complexes derived from the racemic ligands from a 3:1 mixture of dichloromethane and acetonitrile using ethyl acetate as anti-solvent and characterise them by X-ray diffraction. Interestingly, we only obtained single crystals of the racemic mixture of homochiral complexes although the solution obviously contains both diastereomers. Figure 5 shows both of the homochiral complexes $\{[(dppp)_2Pd_2\{(R)\text{-}\mathbf{3}\}_2](OTf)_4$ and $\{[(dppp)_2Pd_2\{(S)\text{-}\mathbf{3}\}_2](OTf)_4$ as they were found in the crystal structure. Again, this indicates the preferred formation of the homochiral complexes in the sense of a self-recognition because in most of the cases where both the achiral heterochiral and the chiral homochiral assemblies are present in solution the heterochiral aggregates tend to crystallise more readily. (The reason for the usually preferred crystallization of the achiral assembly (compared to the corresponding diastereomeric homochiral assembly) is not yet completely clear. It might be due to the fact that nature often tries to achieve the highest possible symmetry in crystalline matter. There is also some evidence that in most cases the achiral assemblies can pack more efficiently in the solid state than the chiral ones.) Hence, selec-
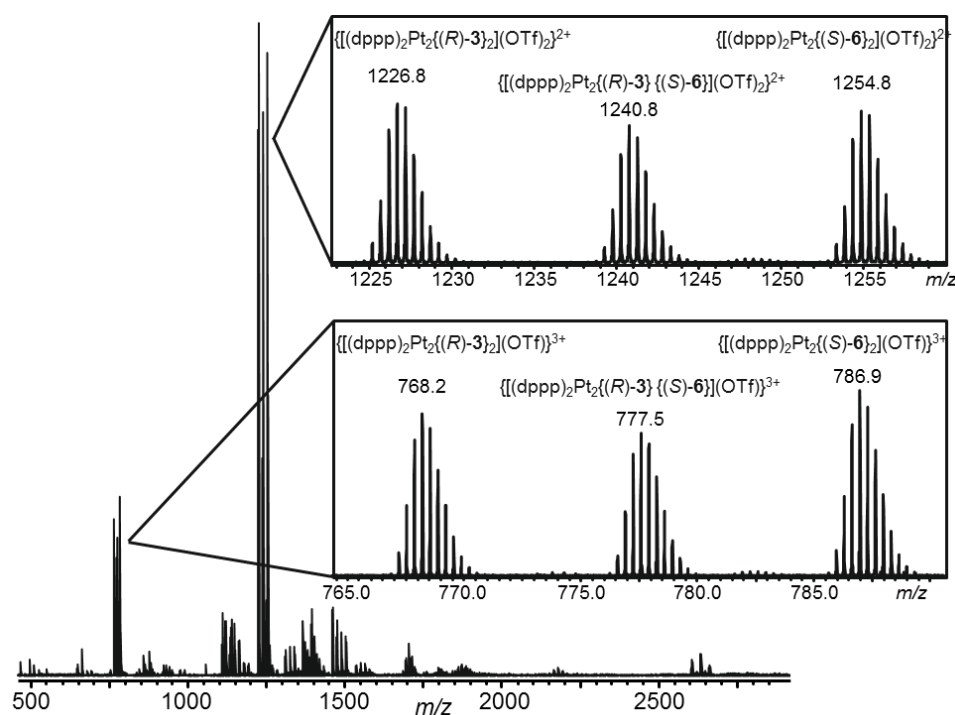
Figure 4: ESI mass spectrum (positive mode) of an 1:1:2 mixture of (*R*)-**3**, (*S*)-**6**, and [(dppp)Pt(OTf)$_2$] in acetonitrile.
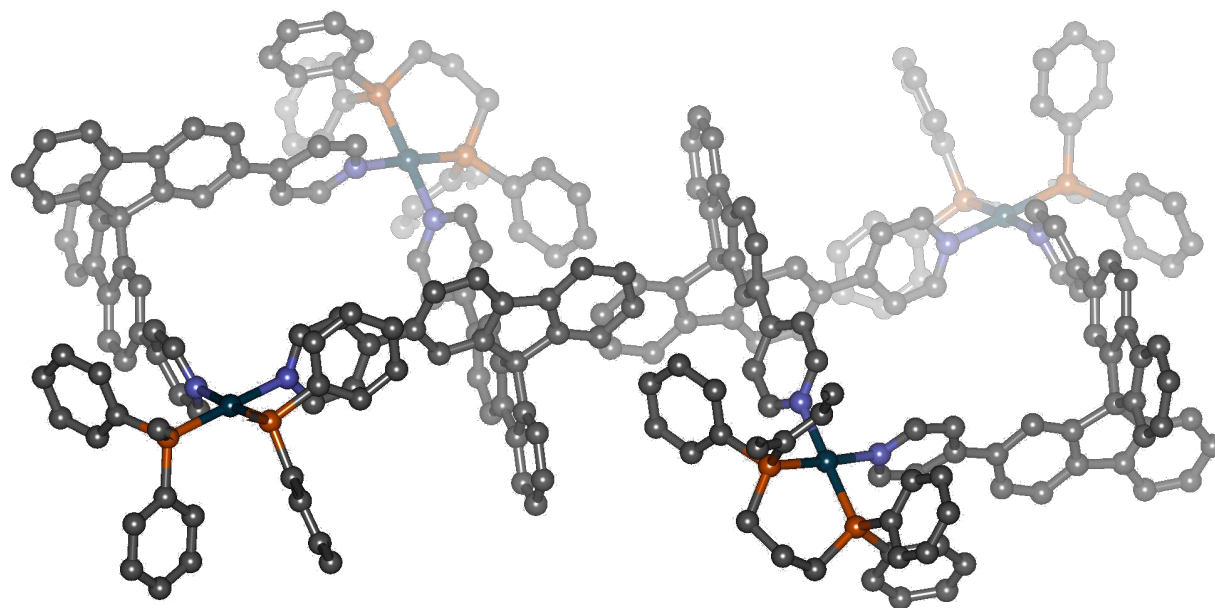
Figure 5: Single crystal X-ray structure analysis of [(dppp)₂Pd₂{(*R*)-**3**}₂][(dppp)₂Pd₂{(*S*)-**3**}₂](OTf)₈ obtained from a 1:1 mixture of (*rac*)-**3** and [(dppp)Pd(OTf)₂]. (Counterions and solvent molecules within the crystal packing, and hydrogen atoms are omitted, colour code: petrol – palladium, grey – carbon, blue – nitrogen, orange – phosphorous).

tive crystallisation of the homochiral aggregate can be interpreted as another hint for its thermodynamic more favourable formation. It is important to note, however, that dissolving the crystals again very quickly led to a mixture of homo- and heterochiral assemblies in the same ratio as observed before.

Conclusion

In summary, we were able to synthesise dissymmetric bis(4-pyridyl) ligands (*R*)- and (*rac*)-**3** based on the 9,9'-spirobi-fluorene scaffold in racemic and optically pure form and a closely related mass-labelled dimethylated derivative (*S*)-**6**. These ligands self-assemble into dinuclear metallosupramolecular [(dppp)₂M₂(L)₂](OTf)₄ rhombi upon coordination to [(dppp)Pt(OTf)₂] or [(dppp)Pd(OTf)₂], respectively. Interestingly, these self-assembly processes proceed with significant diastereoselective self-sorting via preferred narcissistic self-recognition amplifying the formation of the homochiral assemblies by a factor of approximately three. Together with the results obtained for further bis(pyridine) ligands derived from other rigid scaffolds such as Tröger's bases or 2,2'-dihydroxy-1,1'-binaphthyls this suggests that the bend angle of the V-shaped ligands seems to be a crucial general factor that has to be adjusted carefully to obtain (high-fidelity) self-sorting. Angles of more than 105° cause an unfavourable preorganisation of the ligands' structure thus leading to non-selective self-assembly processes whereas smaller angles of about 90–105° lead to chiral self-sorting. The current study of the ligands **3** and

6 provides further evidence that angles at the lower end of this range do lead to a preferred self-recognition.

Experimental

Reactions under inert gas atmosphere were performed under argon using standard Schlenk techniques and oven-dried glassware prior to use. Thin-layer chromatography was performed on aluminum TLC plates silica gel 60F₂₅₄ from Merck. Detection was carried out under UV light (254 and 366 nm). Products were purified by column chromatography on silica gel 60 (70–230 mesh) from Merck. The ¹H and ¹³C NMR spectra were recorded on a Bruker Avance 500 spectrometer at 298 K, at 500.1 and 125.8 MHz, or a Bruker AM 400 at 293 K, at 400.1 MHz and 100.6 MHz, respectively. ³¹P NMR spectra were recorded at 293 K at 162.0 MHz or at 298 K at 202.0 MHz. The ¹H NMR chemical shifts are reported on the δ scale (ppm) relative to residual non-deuterated solvent as the internal standard. The ¹³C NMR chemical shifts are reported on the δ scale (ppm) relative to deuterated solvent as the internal standard. ³¹P NMR chemical shifts are reported on the δ scale (ppm) relative to 85% H₃PO₄ as the external standard. Signals were assigned on the basis of ¹H, ¹³C, HMQC, and HMBC NMR experiments (for the numbering of the individual nuclei see Supporting Information). Mass spectra were recorded at a microOTOF-Q or an Apex IV FT-ICR from Bruker. Most solvents were dried, distilled, and stored under argon according to standard procedures. 4-Pyridylboronic acid pinacol ester and

2-aminobiphenyl were used as received from commercial sources. 2-Iodobiphenyl [30], 9,9'-spirobifluorene [31], (*rac*)-2,2'-diacetyl-9,9'-spirobifluorene [32], (*rac*)-2,2'-diacetoxy-9,9'-spirobifluorene [33], (*rac*)-, (*S*)-, and (*R*)-2,2'-dihydroxy-9,9'-spirobifluorene {(*rac*)-, (*S*)-, and (*R*)-**1**} [33,36], (*rac*)-, (*S*)-, and (*R*)-2,2'-bis(trifluoromethylsulfonyloxy)-9,9'-spirobifluorene {(*rac*)-, (*S*)-, and (*R*)-**2**} [36], (*S*)-2,2'-dimethyl-9,9'-spirobifluorene {(*S*)-**4**} [36], (*S*)-2,2'-dibromo-7,7'-dimethyl-9,9'-spirobifluorene {(*S*)-**5**} [36], and (dppp)M(OTf)$_2$ (M = Pd^{II}, Pt^{II}) [37,38] were prepared according to literature known procedures.

(*R*)-2,2'-Bis(4-pyridyl)-9,9'-spirobifluorene ((*R*)-3): (*R*)-**2** (339 mg, 0.55 mmol), K$_3$PO$_4$ (476 mg, 2.24 mmol), 4-pyridylboronic acid pinacol ester (551 mg, 2.69 mmol), [Pd(dppf)Cl$_2$] (25 mg, 0.031 mmol), and dppf (22 mg, 0.040 mmol) were added to a round-bottomed flask. Dry THF (10 mL) was added and the mixture was heated to 65 °C and stirred overnight resulting in a brown solution. After that the reaction mixture was cooled to rt and quenched with a sat. solution of NaHCO$_3$. The aqueous phase was extracted three times with dichloromethane and the collected organic phase was washed with water and brine and dried with MgSO$_4$. The solvent was removed in vacuo. The crude product was purified by column chromatography on silica gel using MeOH/ethyl acetate (1:1) as eluent. The solvents were evaporated and the residue extracted with dichloromethane to get rid of previously dissolved silica gel. After evaporation of the dichloromethane the product was obtained as a brown oil (262 mg, 100%). ^{1}H NMR (500.1 MHz, CDCl$_3$) δ 8.50 (d, $J_{15,16}$ = 5.4 Hz, 4H, H-16), 7.97 (d, $J_{3,4}$ = 7.9 Hz, 2H, H-4), 7.91 (d, $J_{5,6}$ = 7.5 Hz, 2H, H-5), 7.68 (dd, $J_{3,4}$ = 7.9 Hz, $J_{1,3}$ = 1.0 Hz, 2H, H-3), 7.41 (dd, $J_{5,6}$ = 7.5 Hz, $J_{6,7}$ = 7.3 Hz, 2H, H-6), 7.33 (d, $J_{15,16}$ = 5.4 Hz, 4H, H-15), 7.15 (dd, $J_{6,7}$ = 7.3 Hz, $J_{7,8}$ = 7.5 Hz, 2H, H-7), 7.00 (s, 2H, H-1), 6.77 (d, $J_{7,8}$ = 7.5 Hz, 2H, H-8) ppm; ^{13}C NMR (125.8 MHz, CDCl$_3$) δ 150.0 (C-16), 149.4 (C-10), 148.9 (C-13), 148.0 (C-14), 142.9 (C-11), 140.9 (C-12), 137.8 (C-2), 128.6 (C-7), 128.2 (C-6), 127.1 (C-3), 124.2 (C-8), 122.5 (C-1), 121.5 (C-14), 120.8 (C-4), 120.5 (C-5), 66.0 (C-9) ppm; HRMS-ESI (*m/z*): [M + H]$^+$ calcd for [C$_{35}$H$_{23}$N$_2$]$^+$, 471.1856; found, 471.1861; [α]$_D^{25}$ +280.7° (*c* 0.385, CHCl$_3$).

(*S*)-2,2'-Bis(4-pyridyl)-7,7'-dimethyl-9,9'-spirobifluorene ((*S*)-6): CsF (602 mg, 3.96 mmol) was dried under vacuum. After flushing with argon (*S*)-**5** (300 mg, 0.60 mmol), 4-pyridylboronic acid pinacol ester (148 mg, 0.72 mmol), and [Pd(P*t*-Bu$_3$)$_2$] (15 mg, 5 mol %) were added and the reaction flask was evacuated twice. Next dry THF (10 mL) was added and the reaction was heated to 65 °C overnight. After that the reaction mixture was cooled to rt and diluted with dichloromethane. The organic phase was washed with a saturated solu-

tion of Na$_2$CO$_3$ and the aqueous phase was repeatedly extracted with dichloromethane. The collected organic phases were washed with a diluted hydrochloric acid (5%) and the resulting aqueous phase was extracted thoroughly with CH$_2$Cl$_2$. The aqueous phase was brought to pH 14 with 2 N NaOH and extracted thoroughly with CH$_2$Cl$_2$. The collected organic phases were washed with water and brine and subsequently dried with MgSO$_4$. The solvents were removed in vacuo. The crude product was purified by column chromatography on silica gel using petrol ether/ethyl acetate/triethylamine (5:1:1) as eluent resulting in a yellow solid (207 mg, 69%). ^{1}H NMR (500.1 MHz, CDCl$_3$) δ 8.50 (d, $J_{15,16}$ = 5.6 Hz, 4H, H-16), 7.91 (d, $J_{3,4}$ = 7.9 Hz, 2H, H-4), 7.78 (d, $J_{6,5}$ = 7.8 Hz, 2H, H-6), 7.67 (dd, $J_{3,4}$ = 7.9 Hz, $J_{1,3}$ = 1.6 Hz, 2H, H-3), 7.33 (m, 4H, H-15), 7.22 (d, $J_{5,6}$ = 7.8 Hz, 2H, H-6), 6.99–6.98 (d, $J_{1,3}$ = 1.6 Hz, 2H, H-1), 6.56 (s, 2H, H-8), 2.23 (s, 6H, H-17) ppm; ^{13}C NMR (125.8 MHz, CDCl$_3$) δ 149.7 (C-16)*, 149.5 (C-10)*, 149.2 (C-13), 147.9 (C-14), 143.0 (C-11), 138.6 (C-7), 138.2 (C-12), 137.1 (C-2), 129.0 (C-6), 126.9 (C-3), 124.7 (C-8), 122.4 (C-1), 121.3 (C-15), 120.3 (C-5)*, 120.2 (C-4)*, 65.7 (C-9), 24.8 (C-17) ppm (* signal assignment might be interchanged); HRMS-ESI (*m/z*): [M + H]$^+$ calcd for [C$_{37}$H$_{27}$N$_2$]$^+$, 499.2169; found, 499.2160. [α]$_D^{24}$ −128.1° (*c* 0.39, CHCl$_3$).

Preparation and characterisation of the metal complexes: Approximately 10 μmol of a ligand and an equimolar amount of [(dppp)Pt(OTf)$_2$] or [(dppp)Pd(OTf)$_2$], respectively, were dissolved in 0.6 mL of CD$_2$Cl$_2$ and 0.2 mL of CD$_3$CN. The resulting solution was characterised by NMR. For the ESI-MS studies ca. 10 μmol of a ligand and an equimolar amount of [(dppp)Pt(OTf)$_2$] or [(dppp)Pd(OTf)$_2$], respectively, were dissolved in 1 mL of solvent (acetone, acetonitrile, mixtures of dichloromethane and acetonitrile). An aliquot of this solution was then diluted with the same solvent to give 1 mL of a 300 μmolar solution of the complex.

[(dppp)$_2$Pd$_2${(*R*)-3}$_2$](OTf)$_4$: ^{1}H NMR (500 MHz, CD$_3$CN/CD$_2$Cl$_2$ 1:1) δ 8.48 (d, $J_{15,16}$ = 5.8 Hz, 4H, H-16), 7.94 (d, $J_{5,6}$ = 7.7 Hz, 2H, H-5), 7.92 (d, $J_{3,4}$ = 8.0 Hz, 2H, H-4), 7.53–7.46 (m, 8H, H-dppp), 7.44 (dd, $J_{5,6}$ = 7.7 Hz, $J_{6,7}$ = 7.7 Hz, 2H, H-6), 7.41 (dd, $J_{3,4}$ = 8.1 Hz, $J_{1,3}$ = 1.5 Hz, 2H, H-3), 7.36 (dd, J = 7.5 Hz, J = 7.5 Hz, 2H, H-dppp), 7.24 (dd, J = 7.4 Hz, 4H, H-dppp), 7.21–7.14 (m, 6H, H-7, H-dppp), 7.09 (dd, J = 7.3 Hz, J = 7.3 Hz, 2H, H-dppp), 6.90 (s, 6H, H15), 6.69 (dd, J$_{7,8}$ = 7.5 Hz, 2H, H-8), 6.52 (d, $J_{1,3}$ = 1.5 Hz, 2H, H-1), 3.10–3.00 (m, 4H, H-dppp), 2.23–2.06 (m, 2H, H-dppp); ^{13}C NMR (125.8 MHz, CD$_3$CN/CD$_2$Cl$_2$ 1:1) δ 150.1, 149.9, 149.5, 148.4, 144.1, 140.8, 134.8, 133.1, 132.9, 132.3, 132.0, 129.4, 129.1, 128.5, 127.1, 125.9, 125.4, 125.4, 125.0, 123.9, 123.3, 122.4, 122.1, 121.3, 121.2, 119.9, 65.7, 21.4, 17.5; MS (ESI, positive mode, acetone) *m/z*: 667.0 {(dppp)Pd(OTf)}$^+$, 709.2

$\{[(dppp)_2Pd_2\{(R)\text{-}3\}_2](OTf)\}^{3+}$, 1138.2 $\{[(dppp)_2Pd_2\{(R)\text{-}3\}_2](OTf)_2\}^{2+}$, 1567.6 $\{[(dppp)_4Pd_4\{(R)\text{-}3\}_4](OTf)_5\}^{3+}$, 2426.4 $\{[(dppp)_2Pd_2\{(R)\text{-}3\}_2](OTf)_3\}^+$ and $\{[(dppp)_4Pd_4\{(R)\text{-}3\}_4](OTf)_6\}^{2+}$.

[(dppp)$_2$Pd$_2${(S)-6}$_2$](OTf)$_4$: ^{1}H NMR (500.1 MHz, CD$_3$CN/ CD$_2$Cl$_2$ 1:1) δ 8.47 (d, $J_{15,16}$ = 5.5 Hz, 4H, H-16), 7.86 (d, $J_{3,4}$ = 7.9 Hz, 2H, H-4), 7.82 (d, $J_{5,6}$ = 7.9 Hz, 2H, H-5), 7.54–7.45 (m, 9H, H-dppp), 7.39 (dd, $J_{3,4}$ = 7.9 Hz, $J_{1,3}$ = 1.6 Hz, 2H, H-3), 7.36 (d, J = 7.5 Hz, 2H, H-dppp), 7.28–7.21 (m, 6H, H-6, H-dppp), 7.16 (dd, J = 7.1 Hz, J = 7.1 Hz, 4H, H-dppp), 7.08 (dd, J = 7.3 Hz, J = 7.3 Hz, 2H, H-dppp), 6.89 (s, 3H, H-15), 6.52 (s, 2H, H-8), 6.49 (d, $J_{1,3}$ =1.6 Hz, 2H, H-1), 3.09–3.01 (m, 4H, H-dppp), 2.19 (s, 6H, H-17); ^{13}C NMR (125.8 MHz, CD$_3$CN/CD$_2$Cl$_2$ 1:1) δ 150.1, 149.9, 149.6, 148.8, 144.3, 139.4, 138.1, 134.2, 133.2, 133.0, 132.3, 131.9, 129.4, 126.0, 125.9, 125.5, 125.4, 125.0, 124.5, 123.3, 122.4, 122.1, 120.9, 119.9, 65.4, 21.5, 21.1, 17.5; MS (ESI, positive mode, acetone) m/z: 667.0 $\{(dppp)Pd(OTf)\}^+$, 1166.3 $\{[(dppp)_2Pd_2\{(S)\text{-}6\}_2](OTf)_2\}^{2+}$, 2482.5 $\{[(dppp)_2Pd_2\{(S)\text{-}6\}_2](OTf)_3\}^+$ and $\{[(dppp)_4Pd_4\{(S)\text{-}6\}_4](OTf)_6\}^{2+}$.

Crystal structure determination: Data for the X-ray crystallographic analysis of $[(dppp)_2Pd_2\{(R)\text{-}3\}_2][(dppp)_2Pd_2\{(S)\text{-}3\}_2](OTf)_8$ derived from (*rac*)-**3** and $[(dppp)Pd(OTf)_2]$ were collected on a SuperNova Dual Source diffractometer equipped with an Atlas detector using mirror monochromated Mo K$_a$ radiation (λ = 0.71073 Å). CrysAlisPro software [39] was used for data measurement and processing as well as to apply the numerical absorption correction. The structures were solved by direct methods (SIR97 [40]) and refined by full-matrix least squares on F^2 (SHELXL-2013 [41]). All non-hydrogen atoms were refined anisotropically. The SQUEEZE routine of PLATON [42] was used to calculate the contributions of the disordered solvent regions to the structure factors in the form of FAB files which were then used in refinement in SHELXL-2013. The hydrogen atoms at carbon were placed in calculated positions and refined isotropically using a riding model. Selected data: Crystal dimensions 0.63 × 0.29 × 0.25 mm^3, colourless prism, C$_{144}$H$_{128}$F$_{12}$N$_4$O$_{20}$P$_4$Pd$_2$S$_4$, M = 2927.42, monoclinic, space group $C\,2/c$ (no. 15), a = 18.8830(5), b = 23.7387(5), c = 35.9013(8) Å, α = 90, β = 101.585(2), γ = 90°, V = 15765.2(6) Å^3, Z = 4, ρ = 1.233 g cm^{-3}, μ = 0.395 mm^{-1}, F(000) = 6016, 27330 reflections ($2\theta_{max}$ = 50.50°) measured (14210 unique, R_{int} = 0.0193, completeness = 99.4%), R (I > $2\sigma(I)$) = 0.0505, wR_2 (all data) = 0.1399. GOF = 1.061 for 942 parameters and 669 restraints, largest diff. peak and hole 1.548/−0.653 e Å^3.

CCDC-971933 contains the supplementary data for this structure. These data can be obtained free of charge via http:// www.ccdc.cam.ac.uk/data_request/cif, or by emailing data_request@ccdc.cam.ac.uk, or by contacting The Cambridge Crystallographic Data Centre, 12, Union Road, Cambridge CB2 1EZ, UK; fax: +44 1223 336033.

Supporting Information

Supporting Information File 1

NMR and ESI mass spectra of ligands **3** and **6** and their metal complexes.
[http://www.beilstein-journals.org/bjoc/content/ supplementary/1860-5397-10-40-S1.pdf]

Acknowledgements

References

1. Osowska, K.; Miljanić, O. Š. *Synlett* **2011,** 1643–1648. doi:10.1055/s-0030-1260815
2. Safont-Sempere, M. M.; Fernández, G.; Würthner, F. *Chem. Rev.* **2011,** *111,* 5784–5814. doi:10.1021/cr100357h
3. Saha, M. L.; Schmittel, M. *Org. Biomol. Chem.* **2012,** *10,* 4651–4684. doi:10.1039/c2ob25098e
4. Krämer, R.; Lehn, J.-M.; Marquis-Rigault, A. *Proc. Natl. Acad. Sci. U. S. A.* **1993,** *90,* 5394–5398. doi:10.1073/pnas.90.12.5394
5. Caulder, D. L.; Raymond, K. N. *Angew. Chem.* **1997,** *109,* 1508–1510. doi:10.1002/ange.19971091309 *Angew. Chem., Int. Ed. Engl.* **1997,** *36,* 1440–1442. doi:10.1002/anie.199714401
6. Masood, M. A.; Enemark, E. J.; Stack, T. D. P. *Angew. Chem.* **1998,** *110,* 973–977. doi:10.1002/(SICI)1521-3757(19980403)110:7<973::AID-ANGE973>3. 0.CO;2-T *Angew. Chem., Int. Ed.* **1998,** *37,* 928–932. doi:10.1002/(SICI)1521-3773(19980420)37:7<928::AID-ANIE928>3.0. CO;2-T
7. Albrecht, M.; Schneider, M.; Röttele, H. *Angew. Chem.* **1999,** *111,* 512–515. doi:10.1002/(SICI)1521-3757(19990215)111:4<512::AID-ANGE512>3. 0.CO;2-Y *Angew. Chem., Int. Ed.* **1999,** *38,* 557–559. doi:10.1002/(SICI)1521-3773(19990215)38:4<557::AID-ANIE557>3.0. CO;2-S
8. Vincent, J.-M.; Philouze, C.; Pianet, I.; Verlhac, J.-B. *Chem.–Eur. J.* **2000,** *6,* 3595–3599. doi:10.1002/1521-3765(20001002)6:19<3595::AID-CHEM3595>3.0.C O;2-W

9. Lützen, A.; Hapke, M.; Griep-Raming, J.; Haase, D.; Saak, W. *Angew. Chem.* **2002,** *114,* 2190–2194. doi:10.1002/1521-3757(20020617)114:12<2190::AID-ANGE2190>3.0. CO;2-S *Angew. Chem., Int. Ed.* **2002,** *41,* 2086–2089. doi:10.1002/1521-3773(20020617)41:12<2086::AID-ANIE2086>3.0.CO ;2-0

10. Hwang, I.-W.; Kamada, T.; Ahn, T. K.; Ko, D. M.; Nakamura, T.; Tsuda, A.; Osuka, A.; Kim, D. *J. Am. Chem. Soc.* **2004,** *126,* 16187–16198. doi:10.1021/ja046241e

11. Kamada, T.; Aratani, N.; Ikeda, T.; Shibata, N.; Higuchi, Y.; Wakamiya, A.; Yamaguchi, S.; Kim, K. S.; Yoon, Z. S.; Kim, D.; Osuka, A. *J. Am. Chem. Soc.* **2006,** *128,* 7670–7678. doi:10.1021/ja0611137

12. Burchell, T. J.; Puddephatt, R. J. *Inorg. Chem.* **2006,** *45,* 650–659. doi:10.1021/ic051365t

13. Albrecht, M.; Fröhlich, R. *Bull. Chem. Soc. Jpn.* **2007,** *80,* 797–808. doi:10.1246/bcsj.80.797

14. Maeda, C.; Kamada, T.; Aratani, N.; Osuka, A. *Coord. Chem. Rev.* **2007,** *251,* 2743–2752. doi:10.1016/j.ccr.2007.02.017

15. Kiehne, U.; Weilandt, T.; Lützen, A. *Org. Lett.* **2007,** *9,* 1283–1286. doi:10.1021/ol070048i

16. Kiehne, U.; Weilandt, T.; Lützen, A. *Eur. J. Org. Chem.* **2008,** 2056–2064. doi:10.1002/ejoc.200701215

17. Bunzen, J.; Bruhn, T.; Bringmann, G.; Lützen, A. *J. Am. Chem. Soc.* **2009,** *131,* 3621–3630. doi:10.1021/ja807780j

18. Gütz, C.; Hovorka, R.; Schnakenburg, G.; Lützen, A. *Chem.–Eur. J.* **2013,** *19,* 10890–10894. doi:10.1002/chem.201301499

19. Kitamura, M.; Okada, S.; Suga, S.; Noyori, R. *J. Am. Chem. Soc.* **1989,** *111,* 4028–4036. doi:10.1021/ja00193a040

20. Hasenknopf, B.; Lehn, J.-M.; Baum, G.; Fenske, D. *Proc. Natl. Acad. Sci. U. S. A.* **1996,** *93,* 1397–1400. doi:10.1073/pnas.93.4.1397

21. Kim, T. W.; Lah, M. S.; Hong, J.-I. *Chem. Commun.* **2001,** 743–744. doi:10.1039/b100329l

22. Wang, R.; Hong, M.; Yuan, D.; Sun, Y.; Xu, L.; Luo, J.; Cao, R.; Chan, A. S. C. *Eur. J. Inorg. Chem.* **2004,** 37–43. doi:10.1002/ejic.200300375

23. Burchell, T. J.; Puddephatt, R. J. *Inorg. Chem.* **2005,** *44,* 3718–3730. doi:10.1021/ic050097w

24. Mizumura, M.; Shinokubo, H.; Osuka, A. *Angew. Chem., Int. Ed.* **2008,** *120,* 5458–5461. doi:10.1002/ange.200801269 *Angew. Chem., Int. Ed.* **2008,** *47,* 5378–5381. doi:10.1002/anie.200801269

25. Weilandt, T.; Kiehne, U.; Schnakenburg, G.; Lützen, A. *Chem. Commun.* **2009,** 2320–2322. doi:10.1039/b819335e

26. Troff, R. W.; Hovorka, R.; Weilandt, T.; Lützen, A.; Cetina, M.; Nieger, M.; Lentz, D.; Rissanen, K.; Schalley, C. A. *Dalton Trans.* **2012,** *41,* 8410–8420. doi:10.1039/c2dt30190c

27. Weilandt, T.; Kiehne, U.; Bunzen, J.; Schnakenburg, G.; Lützen, A. *Chem.–Eur. J.* **2010,** *16,* 2418–2426. doi:10.1002/chem.200902993

28. Gütz, C.; Hovorka, R.; Stobe, C.; Struch, N.; Topić, F.; Schnakenburg, G.; Rissanen, K.; Lützen, A. *Eur. J. Org. Chem.* **2014,** 206–216. doi:10.1002/ejoc.201301314

29. Saragi, T. P. I.; Spehr, T.; Siebert, A.; Fuhrmann-Lieker, T.; Salbeck, J. *Chem. Rev.* **2007,** *107,* 1011–1065. doi:10.1021/cr0501341

30. Tour, J. M.; Wu, R.; Schumm, J. S. *J. Am. Chem. Soc.* **1990,** *112,* 5662–5663. doi:10.1021/ja00170a053

31. Clarkson, R. G.; Gomberg, M. *J. Am. Chem. Soc.* **1930,** *52,* 2881–2891. doi:10.1021/ja01370a048

32. Haas, G.; Prelog, V. *Helv. Chim. Acta* **1969,** *52,* 1202–1218. doi:10.1002/hlca.19690520505

33. Prelog, V.; Bedeković, D. *Helv. Chim. Acta* **1979,** *62,* 2285–2302. doi:10.1002/hlca.19790620725

34. Wong, K.-T.; Liao, Y.-L.; Peng, Y. C.; Wang, C.-C.; Lin, S.-Y.; Yang, C.-H.; Tseng, S.-M.; Lee, G.-H.; Peng, S.-M. *Cryst. Growth Des.* **2005,** *5,* 667–671. doi:10.1021/cg049822o

35. Toda, F.; Tanaka, K. *J. Org. Chem.* **1988,** *53,* 3607–3609. doi:10.1021/jo00250a037

36. Thiemann, F.; Piehler, T.; Haase, D.; Saak, W.; Lützen, A. *Eur. J. Org. Chem.* **2005,** 1991–2001. doi:10.1002/ejoc.200400796

37. Appleton, T. G.; Bennett, M. A.; Tomkins, I. B. *J. Chem. Soc., Dalton Trans.* **1976,** 439–446. doi:10.1039/dt9760000439

38. Stang, P. J.; Cao, D. H.; Saito, S.; Arif, A. M. *J. Am. Chem. Soc.* **1995,** *117,* 6273–6283. doi:10.1021/ja00128a015

39. *CrysAlisPro 1.171.36.28;* Agilent Technologies Ltd.: Yarton, Oxfordshire, UK, 2013.

40. Altomare, A.; Burla, M. C.; Camalli, M.; Cascarano, G. L.; Giacovazzo, C.; Guagliardi, A.; Moliterni, A. G. G.; Polidori, G.; Spagna, R. *J. Appl. Crystallogr.* **1999,** *32,* 115–119. doi:10.1107/S0021889898007717

41. Sheldrick, G. *Acta Crystallogr., Sect. A* **2008,** *64,* 112–122. doi:10.1107/S0108767307043930

42. Spek, A. L. *Acta Crystallogr., Sect. D* **2009,** *65,* 148–155. doi:10.1107/S090744490804362X

License and Terms

Towards allosteric receptors – synthesis of β-cyclodextrin-functionalised 2,2'-bipyridines and their metal complexes

Christopher Kremer[1], Gregor Schnakenburg[2] and Arne Lützen[*1]

Full Research Paper

Open Access

Address:
[1]University of Bonn, Kekulé-Institute of Organic Chemistry and Biochemistry, Gerhard-Domagk-Str. 1, D-53121 Bonn, Germany and [2]University of Bonn, Institute of Inorganic Chemistry, Gerhard-Domagk-Str. 1, D-53121 Bonn, Germany

Email:
Arne Lützen[*] - arne.luetzen@uni-bonn.de

* Corresponding author

Abstract

Herein, we present three new 2,2'-bipyridines that carry two β-cyclodextrin moieties in different substitution patterns. When co-ordinated by zinc(II) or copper(I) ions (or their complexes), these compounds undergo conformational changes and switch between "open" and "closed" forms and thereby bringing together or separating the cyclodextrin moieties from each other.

Introduction

In biological systems, recognition events play a major role to guarantee the selectivity of essential processes. Multivalent [1,2] and cooperative binding [3-5] are two of the major concepts to ensure and control the efficiency in those events and the associated complex biochemical cascades following. In order to regulate several of their metabolical functions, a process named "allosteric regulation" is used by enzymes and proteins [6], which stands for cooperative effects in the binding of more than one substrate to different sites of a receptor. After binding of the first substrate (the effector), the receptor changes its conformation, and by this enhancing (positive allosteric cooperativity) or hampering (negative allosteric cooperativity) the binding of another substrate at a second binding site.

This powerful regulatory concept has become quite interesting in supramolecular chemistry, and the development of artificial receptor systems which can be controlled by allosteric effects comes out of it [7-14].

2,2'-Bipyridines have been demonstrated to be excellent artificial allosteric centres due to their well-known ability to switch between *syn-* and *anti*-conformations as an answer to an external stimulus [15]. This switching process can be controlled either by adding or removing suitable transition metal ions or their complexes [16] or by adjusting the pH value [17-19]. The latter, however, is not as secure as using metal ions because of three possible protonation states (not protonated: *anti*, protonated once: *syn*, protonated twice: *anti*) instead of two states

using metal ions (not coordinated: *anti*, coordinated: *syn*) and was not used in our work for this reason.

Some time ago we developed a series of 2,2'-bipyridine-based allosteric analogues [20-22] of the well-known resorcinarene-based hemicarcerands [23,24]. However, these possess only rather shallow binding sites that bind non-polar substrates via dispersive interactions. Hence, we wanted to take this approach one step further by using β-cyclodextrins as another class of macrocyclic compounds that are very well-known for their excellent recognition properties towards non-polar substrates [25]. Depending on the substitution pattern for the central 2,2'-bipyridines, three conceptually different types of allosteric receptors can be obtained: 4,4'- or 6,6'-substitution, both leading to positive allosteric receptors, meaning that they adopt an open *anti*-conformation in the free state where the two cyclodextrins cannot interact with a substrate in a cooperative fashion (*off*-state) but change their conformation to a closed *syn*-conformation (*on*-state) upon binding of a suitable transition metal ion or complex as an effector. This is shown schematically for a 4,4'-substituted bipyridine-based receptor in Scheme 1.

However, these two scenarios differ in the fact that the effector is bound close to the substrate in case of a 6,6'-substitution whereas it is bound in a remote place in case of a 4,4'-substitution. In contrast, a 4,6'-substitution leads to a negative allosteric system which adopts the closed *on*-state in the absence of the effector and changes its conformation to the open *off*-state upon binding of it. In this article we present the synthesis of three new cyclodextrin-functionalised 2,2'-bipyridines **1–3** differing in the bipyridine's substitution pattern (Scheme 2) and their metal complexes.

Results and Discussion
Synthesis
The synthesis of **1–3** requires the three different 2,2'-bipyridines that carry isothiocyanate functions and a monoami-

nated β-cyclodextrin that could be coupled with each other via two-fold nucleophilic addition.

Symmetrically 4,4'- and 6,6'-disubstituted 2,2'-bipyridines were prepared starting from commercially available 4-amino-2-chloropyridine (**4**) and 2-amino-6-bromopyridine (**5**), respectively. After protection of the amino functions as 2,5-dimethylpyrroles, pyridines **6** and **7** were transformed into the corresponding 2,2'-bipyridines **8** and **9** via a nickel-catalysed homo-coupling reaction in excellent yields [26]. The non-symmetric 4,6'-disubstituted bipyridine **10** was obtained in good yield from a Negishi cross-coupling of **6** and **7** [27]. Cleavage of the pyrrole protecting groups of **8–10** with hydroxylamine provided the corresponding diamines **11–13** [26] in satisfying to excellent yields which were finally reacted with thiophosgene to give rise to the desired diisothiocyanates **14–16** (Scheme 3) [28].

β-Cyclodextrin (**17**) was monotosylated by the reaction with tosyl chloride to give **18** in moderate yield [29]. Nucleophilic substitution of the sulfonate against an azide then furnished **19** [30] which could by peracetylated into **20** [31] using acetic acid anhydride both in decent yields. Staudinger reduction of the azide group of **20** then afforded the desired monoaminated cyclodextrin **21** (Scheme 4).

Finally, nucleophilic addition of **21** to the diisothiocyanato-2,2'-bipyridines **14–16** was found to proceed smoothly in dry dichloromethane at room temperature to furnish the desired bis(cyclodextrin)-functionalised 2,2'-bipyridines **1**, **2**, and **3** in very good yields of 92, 93, and 86% yield, respectively (Scheme 5).

Metal coordination – effector binding
With our three cyclodextrin-functionalised bipyridines in hands, we then examined their coordination behaviour towards different transition metal ions (or their complexes) to see whether these could act as effectors. In our previous work,

Scheme 1: *Off*- (open) and *on*- (closed) states of a ditopic positive allosteric receptor based on a 4,4'-functionalised 2,2'-bipyridine.
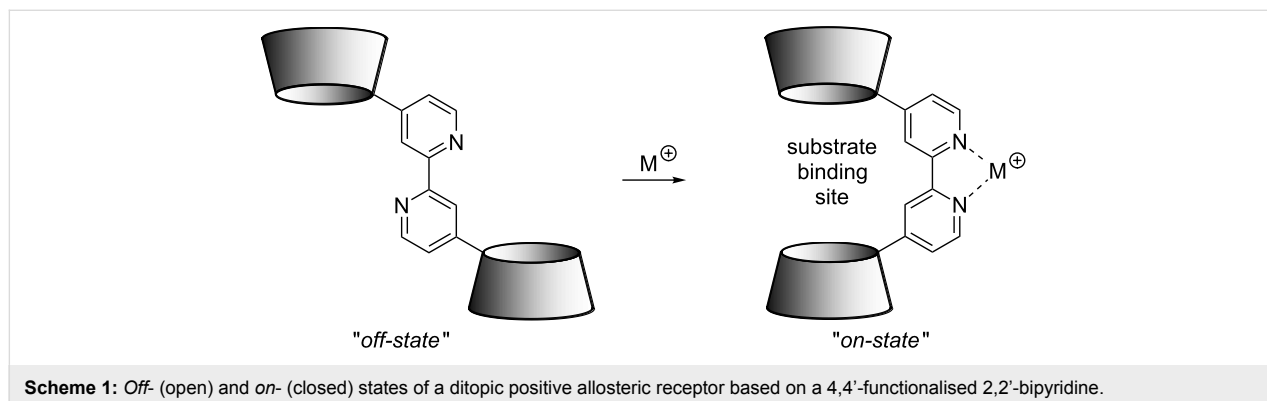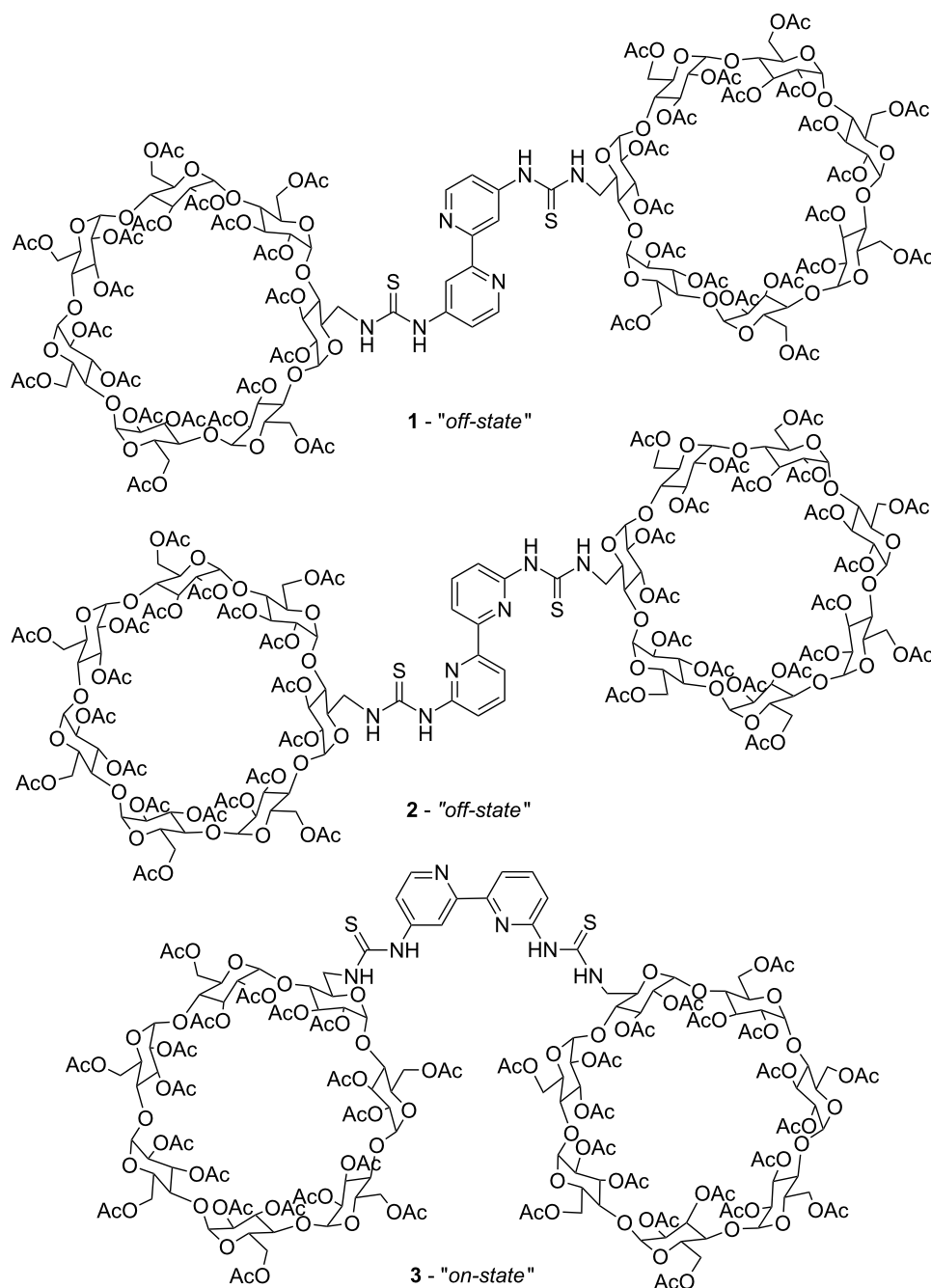
Scheme 2: Bis(β-cyclodextrin)-functionalised 2,2'-bipyridines **1–3**.

silver(I) and copper(I) salts as well as pentacarbonylrhenium(I) chloride proved to be good effectors for our allosteric receptors [20-22]. Hence, we also started with these here. Unfortunately, silver(I) ions turned out to be not effective in this case. Although, they seem to form complexes with compounds **1–3**, we did not observe any of the characteristic shifts of the signals assigned to the protons of the bipyridine moiety that would indicate successful binding of the silver(I) ions to the nitrogen

atoms. Thus, we conclude that the soft silver(I) ions rather bind to one of the sulfur atoms of the thiourea groups. This, however, does not cause the necessary conformational change of the bipyridine structure to potentially affect the binding of another substrate.

Rhenium(I), on the other hand, obviously prefers coordination to nitrogen compared to sulfur as we could demonstrate by
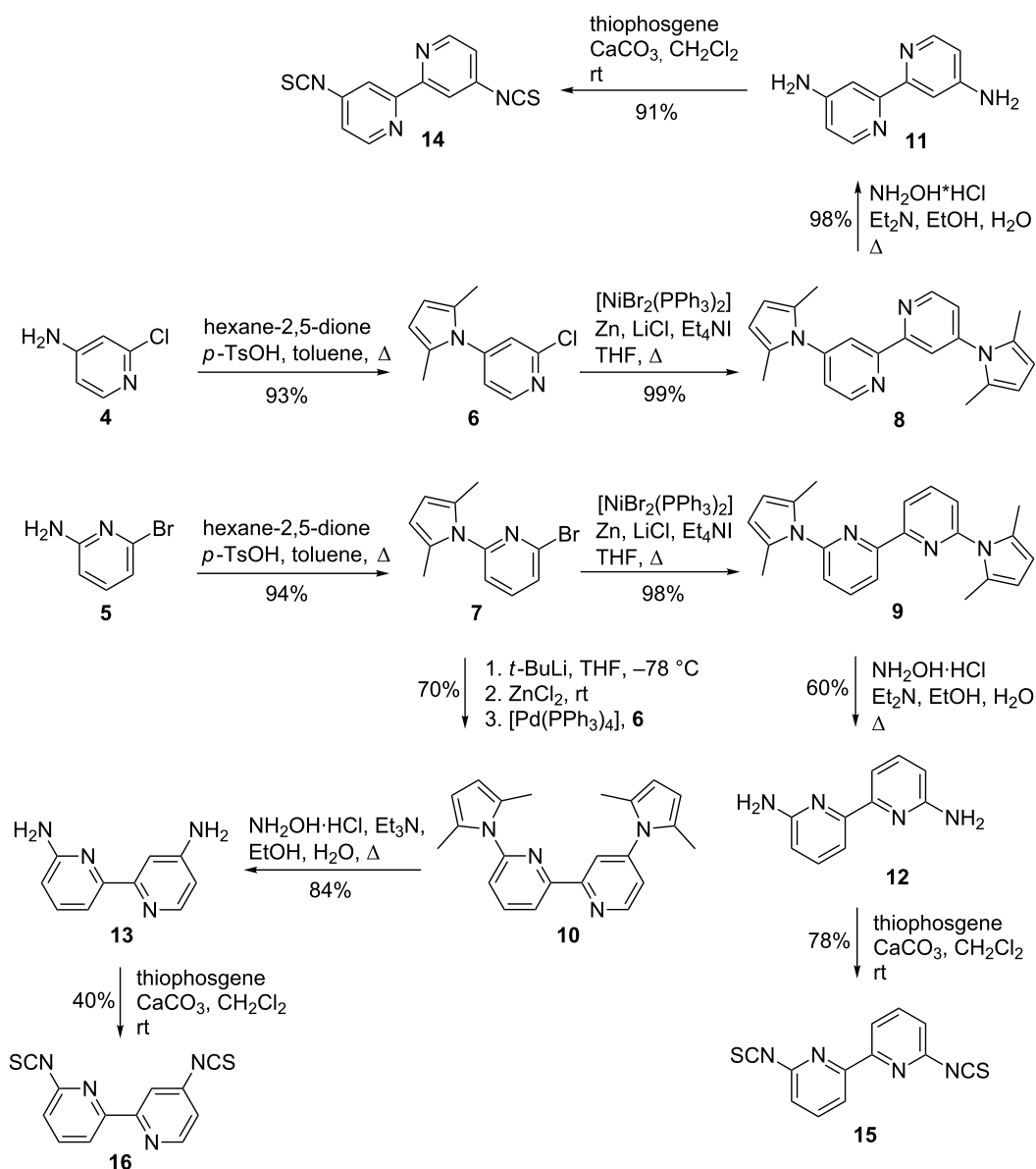
Scheme 3: Synthesis of diisothiocyanato-2,2'-bipyridines **14–16**.

coordinating 4,4'-dithioisocyanato-2,2'-bipyridine (**14**) to it. Figure 1 shows the molecular structure of this [(CO)$_3$Re(**14**)Cl] complex obtained by X-ray diffraction analysis.

Unfortunately, we were neither able to coordinate rhenium(I) to our bipyridines **1–3** nor did we succeed to prepare the rhenium complex [(CO)$_3$Re(**1**)Cl] by using [(CO)$_3$Re(**14**)Cl] and reacting it with aminocyclodextrin **21**.

Next, we tried copper(I) ions as effectors. Copper(I) ions indeed form complexes very fast. However, the complexes of **1** and **3** are obviously prone to rapid oxidation to copper(II) species.

These are paramagnetic complexes which cannot be analysed by NMR spectroscopy. Since this technique would be our preferred analytical tool to study the host–guest chemistry of these systems in the future, however, we did not investigate these further. Interestingly, the copper(I) complexes of **2** were much less sensitive to oxidation. This might be a consequence of the steric crowding caused by the 6,6'-disubstitution of the bipyridine which was found to give well-defined 1:1 [Cu(**2**)]$^+$ complexes in this case (Figure 2).

We then turned our attention to zinc(II) ions. These proved to be capable to act as effectors in the desired manner. We
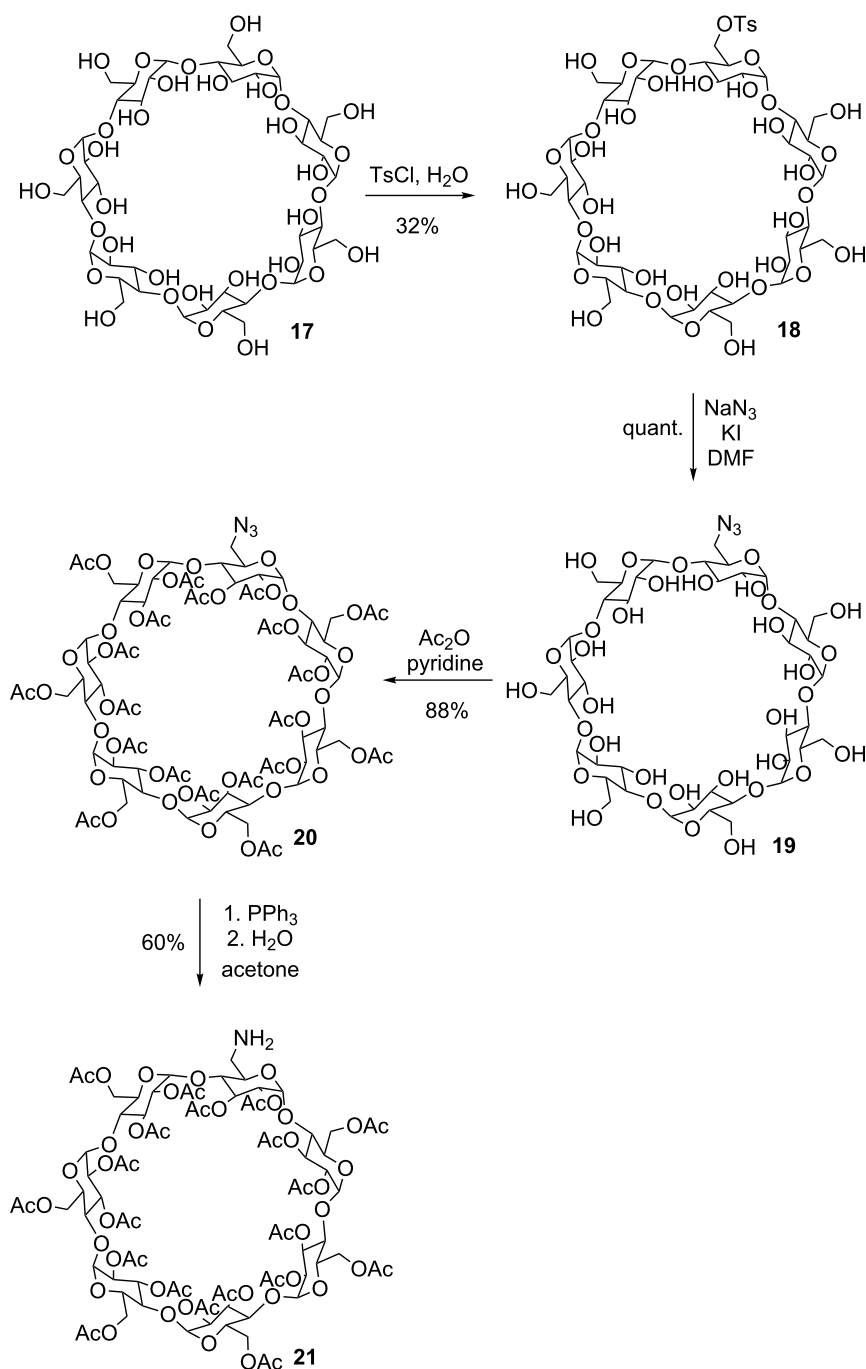
Scheme 4: Synthesis of peracetylated cyclodextrin **21**.

observed sharp signals in the NMR when we mixed the Zn(BF₄)₂ and ligands **1** (Figure 3) and **3** in a 1:2 ratio.

However, in the latter case, the expected [Zn(**3**)₂] or [Zn(**3**)] complexes could not be identified by mass spectrometry. Hence, we hesitate to claim that zinc(II) ions are reliable effectors for ligand **3**. In the case of **1**, however, we were able to find

signals corresponding to the expected well defined [Zn(**1**)₂] complexes which, together with the NMR data, proof that zinc(II) ions are suitable to act as an effector for **1**.

Changing the substitution pattern to 6,6' like in ligand **2**, however, makes it impossible to form a 1:2 complex due to the steric crowding around the metal binding site. In this case we
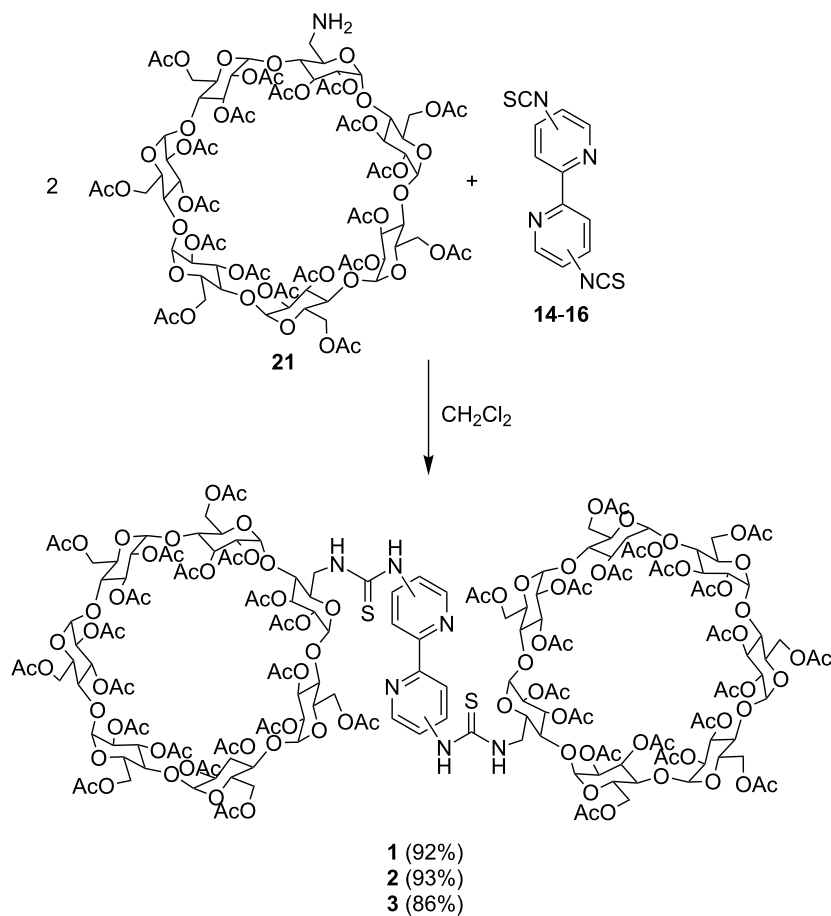
Scheme 5: Synthesis of receptors **1–3**.
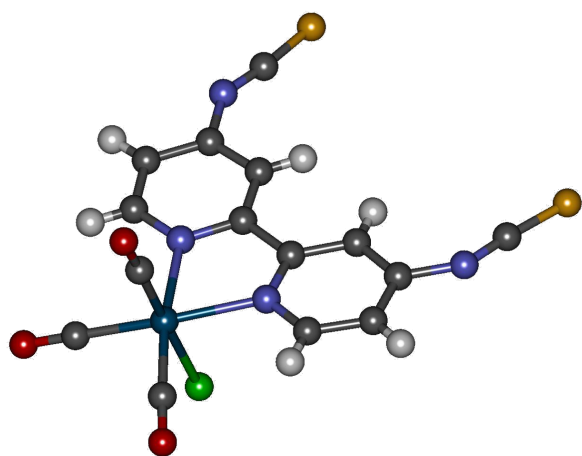
Figure 1: X-ray crystal structure analysis of [(CO)₃Re(**14**)Cl] (colour code: petrol: rhenium, grey: carbon, red: oxygen, blue: nitrogen, yellow: sulfur, white: hydrogen).
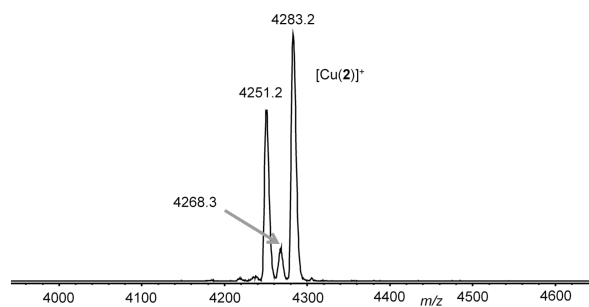
Figure 2: MALDI mass spectrum (sample prepared from a 1:1 mixture of CuPF₆ and **2** in benzene/acetonitrile (1:1) using DCTB (*trans*-2-[3-(4-*tert*-butylphenyl)-2-methyl-2-propenylidene]malononitrile) as matrix).

again observed only a 1:1 complex which probably coordinates solvent molecules to saturate the metal ion's coordination sphere as we did already in the case of copper(I) ions (Figure 4). Thus, copper(I) and zinc(II) ions can both act as effectors for **2**.
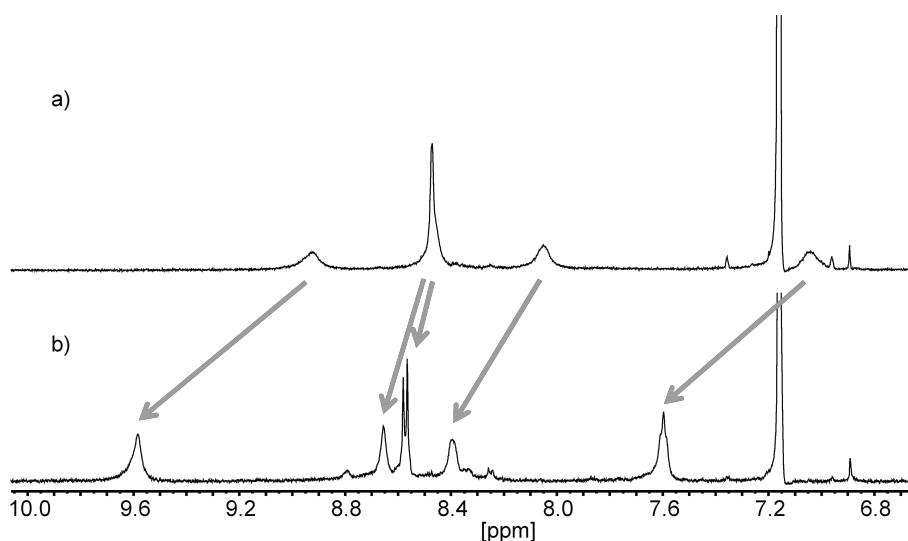
Figure 3: Aromatic region of the ^{1}H NMR spectra (400.1 MHz, 293 K, benzene-d_6/acetonitrile-d_3 1:1) of a) **1** and b) [Zn(**1**)$_2$](OTf)$_2$. Arrows indicate coordination-induced shifts of the individual signals.
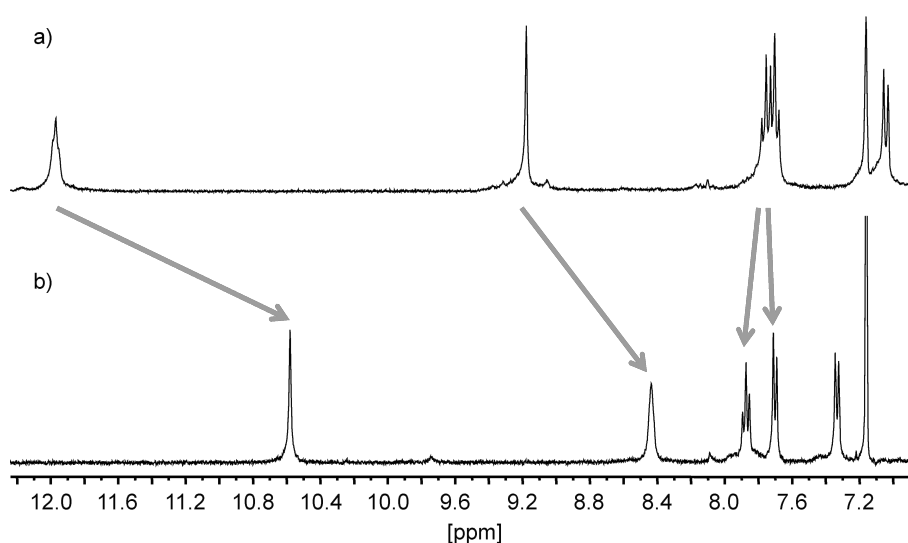
Figure 4: Aromatic region of the ^{1}H NMR spectra (400.1 MHz, 293 K, benzene-d_6/acetonitrile-d_3 1:1) of a) **2** and b) [Zn(**2**)](OTf)$_2$. Arrows indicate coordination-induced shifts of the individual signals.

In order to investigate the metal complexes' host–guest chemistry at a later stage in a quantitative manner, however, a 1:2 metal-to-ligand stoichiometry like in the [Zn(**1**)$_2$]-complexes is not very easy to study because one has to deal with a very complicated equilibrium between 1:2:2, 1:2:1, 1:2:0 and even more complicated metal-to-ligand-to-substrate assemblies which would be very difficult to handle. Thus, we wanted to restrict our systems to a 1:1 stoichiometry of metal-to-ligand complexes also with ligands **1** and **3**. This can be achieved by blocking parts of the coordination sphere of a metal ion by a kinetically and thermodynamically stable binding ligand. In this

way one can make sure that just one single other chelating ligand like a 2,2'-bipyridine can be bound to this metal complex fragment. Sterically hindered 1,10-phenanthrolines and their copper(I) complexes have been proven to be perfectly suited for this purpose [21,32-35]. Thus, we chose to prepare 2,9-bis[2,6-dimethoxyphenyl]-1,10-phenanthroline (**22**) as such a sterically congested ligand (Scheme 6) [36].

22 was synthesised starting from 1,10-phenanthroline via *N,N'*-dialkylation to dibromide **23** in very good yield [37]. Oxidation of **23** with potassium hexacyanoferrate then afforded diamide
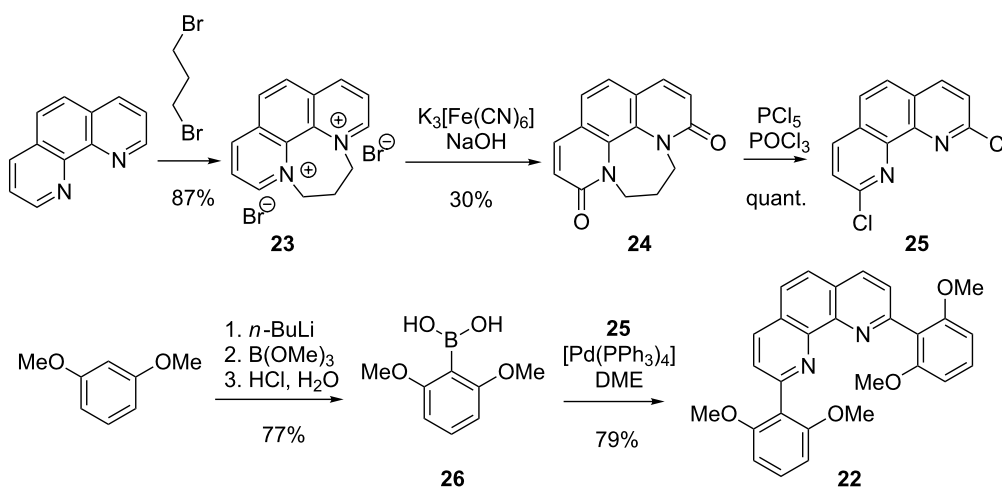
Scheme 6: Synthesis of ligand **22**.

24 in moderate yield [38]. Its subsequent chlorination with a mixture of phosphorous pentachloride and phosphoryl chloride furnished dichloride **25** in quantitative yield [38]. Finally, two-fold Suzuki cross-coupling of **25** with 2,6-dimethoxyphenyl-boronic acid (**26**) derived from 1,3-dimethoxybenzene via lithiation and borylation [39] afforded **22** in very good yield [40-42].

22 forms the 1:1 complex [Cu(**22**)([H$_3$CCN)$_2$]BF$_4$ upon coordination to copper(I) ions. Zinc(II) ions were found to form the dimeric complex [Zn(**22**)$_2$](OTf)$_2$ with an excess of **22** if no other ligand is available, as described before (Figure 5) [43].

Unfortunately, the strategy to prepare 1:1 complexes [Zn(**22**)]$^{2+}$ and [Cu(**22**)]$^+$ first and then let them react with **3** did not result in the formation of the desired heteroleptic complexes. Obviously, the complex fragments are just too large to fit into the sterically congested metal binding site of **3**. Hence, we have to conclude that, unfortunately, we have not succeeded in finding a suitable effector for this ligand yet.

Mixing of preformed complexes [Zn(**22**)]$^{2+}$ and [Cu(**22**)]$^+$ with **1** in a 1:1 ratio, however, afforded the desired heteroleptic complexes [Cu(**22**)(**1**)]PF$_6$, and [Zn(**22**)(**1**)](OTf)$_2$ as evidenced by MALDI mass spectrometry and NMR spectroscopy (Figure 6 and Figure 7).
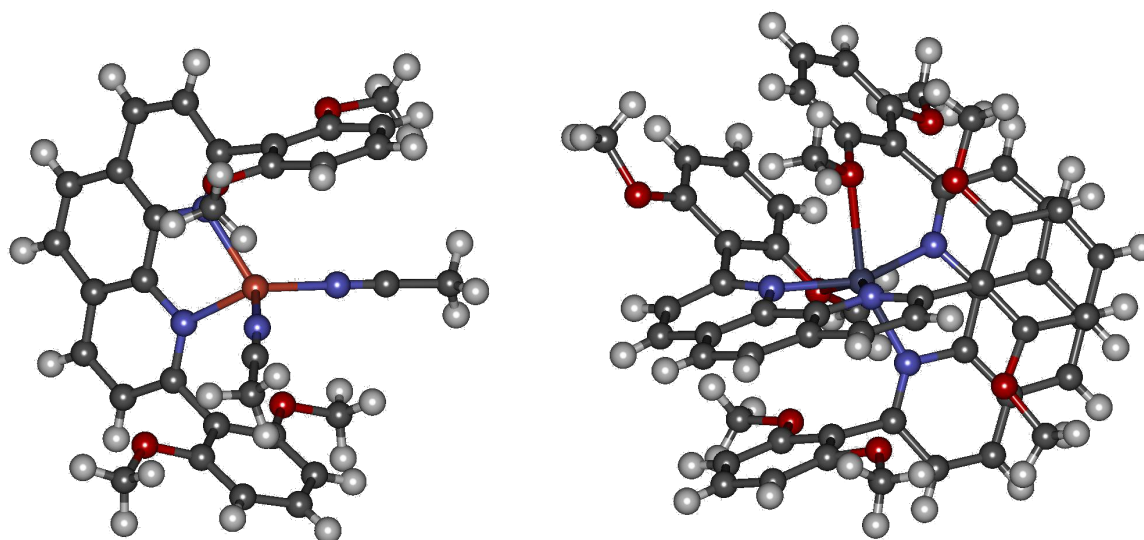
Figure 5: X-ray crystal structure analysis of [Cu(H$_3$CCN)$_2$(**22**)]BF$_4$ and [Zn(**22**)$_2$](OTf)$_2$ (counterions are omitted, colour code: orange: copper, petrol: zinc, grey: carbon, red: oxygen, blue: nitrogen, white: hydrogen).
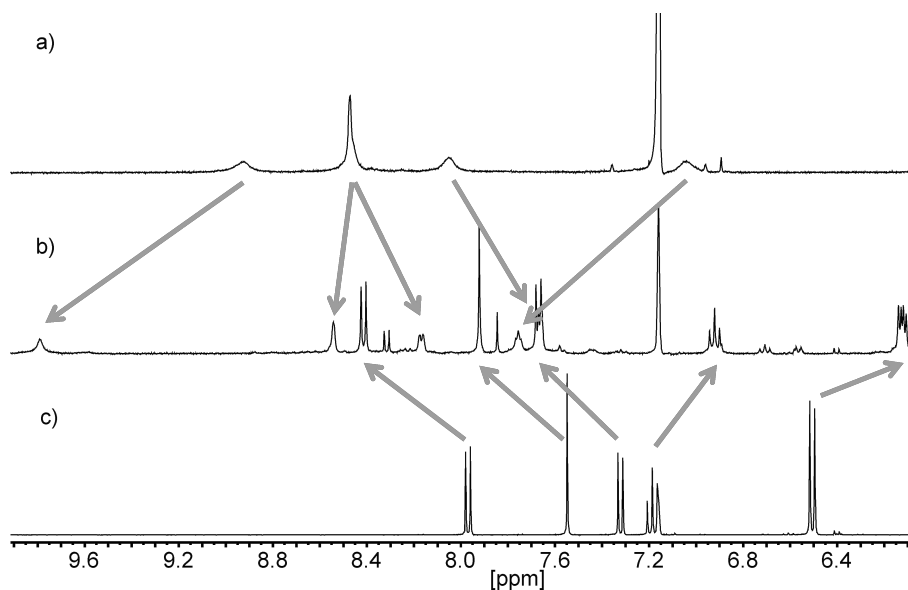
Figure 6: Aromatic region of the ^{1}H NMR spectra (400.1 MHz, 293 K, benzene-d_6/acetonitrile-d_3 1:1) of a) **1**, b) [Zn(**22**)(**1**)](OTf)$_2$, and c) **22**. Arrows indicate signal shifts upon formation of the heteroleptic complex.
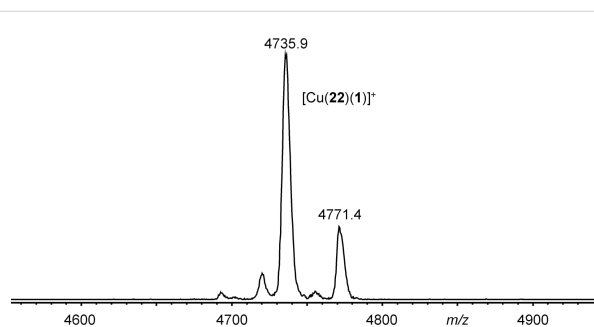

Figure 7: MALDI–TOF mass spectrum (sample prepared from of a 1:1:1 mixture of CuPF$_6$, **22**, and **1** in benzene/acetonitrile (1:1) using DCTB as matrix).

Hence, zinc(II) ions or their complexes with a single, sterically demanding phenanthroline ligand like **22** as well as a similar [Cu(**22**)]$^+$ complex were all found to be good effectors for ligand **1** forming either 1:2 or 1:1 effector:ligand complexes.

Conclusion

We have synthesised three new β-cyclodextrin-functionalised 2,2'-bipyridines and their complexation behaviour towards several metal salts or their complexes was investigated. Among those (pentacarbonyl)rhenium chloride and silver(I) ions proved to be ineffective to cause the desired long-range conformational changes. Unfortunately, we have also not yet succeeded in finding a suitable metal ion or a complex fragment that can efficiently bind to 4,6'-disubstituted bipyridine **3**, and hence, act as an effector to cause switching from the closed "*on*"-state to the open "*off*"-state. The sterically crowded 6,6'-

disubtituted bipyridine **2**, however, readily formed 1:1 complexes with both zinc(II) and copper(I) ions, and hence, can be switched between a closed "*on*"-state to an open "*off*"-state. Zinc(II) ions do also form the expected dimeric complexes with 4,4'-disubstituted bipyridine **1**. However, such a 1:2 effector–bipyridine ratio could lead to a difficult-to-handle host–guest chemistry when it comes to binding of additional guest molecules due to very complicated equilibria between 1:2:2, 1:2:1, 1:2:0 and even more complicated metal-to-ligand-to-substrate assemblies. Zinc(II) or copper(I) phenanthroline complexes with sterically very demanding phenanthrolines were found to be effective to achieve a 1:1 effector–receptor stoichiometry. This makes these ligands promising candidates that could act as potential allosteric receptors whose recognition behaviour can be largely influenced by those effectors. We are currently evaluating the host–guest chemistry of these compounds and their metal complexes which will be reported in near future.

Supporting Information

Experimental data of all new compounds, NMR and ESI mass spectra of compounds **1–3**, **14**, **21**, and **22** and their metal complexes.

Supporting Information File 1
Experimental data, NMR and ESI mass spectra.
[http://www.beilstein-journals.org/bjoc/content/supplementary/1860-5397-10-77-S1.pdf]

Acknowledgements

References

1. Mammen, M.; Choi, S.-K.; Whitesides, G. M. *Angew. Chem.* **1998,** *110,* 2908–2953.
   doi:10.1002/(SICI)1521-3757(19981016)110:20<2908::AID-ANGE2908>3.0.CO;2-2
   Angew. Chem., Int. Ed. **1998,** *37,* 2754–2794.
   doi:10.1002/(SICI)1521-3773(19981102)37:20<2754::AID-ANIE2754>3.0.CO;2-3
2. Fasting, C.; Schalley, C. A.; Weber, M.; Seitz, O.; Hecht, S.; Koksch, B.; Dernedde, J.; Graf, C.; Knapp, E.-W.; Haag, R. *Angew. Chem.* **2012,** *124,* 10622–10650. doi:10.1002/ange.201201114
   Angew. Chem., Int. Ed. **2012,** *51,* 10472–10498.
   doi:10.1002/anie.201201114
3. Whitty, A. *Nat. Chem. Biol.* **2008,** *4,* 435–439.
   doi:10.1038/nchembio0808-435
4. Hunter, C. A.; Anderson, H. L. *Angew. Chem.* **2009,** *121,* 7624–7636.
   doi:10.1002/ange.200902490
   Angew. Chem., Int. Ed. **2009,** *48,* 7488–7499.
   doi:10.1002/anie.200902490
5. Ercolani, G.; Schiaffino, L. *Angew. Chem.* **2011,** *123,* 1800–1807.
   doi:10.1002/ange.201004201
   Angew. Chem., Int. Ed. **2011,** *50,* 1762–1768.
   doi:10.1002/anie.201004201
6. Traut, T. *Allosteric Regulatory Enzymes;* Springer: New York, 2008.
   doi:10.1007/978-0-387-72891-9
7. Rebek, J., Jr. *Acc. Chem. Res.* **1984,** *17,* 258–264.
   doi:10.1021/ar00103a006
8. Tabushi, I. *Pure Appl. Chem.* **1988,** *60,* 581–586.
   doi:10.1351/pac198860040581
9. Nabeshima, T. *Coord. Chem. Rev.* **1996,** *148,* 151–169.
   doi:10.1016/0010-8545(95)01164-1
10. Shinkai, S.; Ikeda, M.; Sugasaki, A.; Takeuchi, M. *Acc. Chem. Res.* **2001,** *34,* 494–503. doi:10.1021/ar000177y
11. Takeuchi, M.; Ikeda, M.; Sugasaki, A.; Shinkai, S. *Acc. Chem. Res.* **2001,** *34,* 865–873. doi:10.1021/ar0000410
12. Kovbasyuk, L.; Krämer, R. *Chem. Rev.* **2004,** *104,* 3161–3188.
   doi:10.1021/cr030673a
13. Zhu, L.; Anslyn, E. V. *Angew. Chem.* **2006,** *118,* 1208–1215.
   doi:10.1002/ange.200501476
   Angew. Chem., Int. Ed. **2006,** *45,* 1190–1196.
   doi:10.1002/anie.200501476
14. Kremer, C.; Lützen, A. *Chem.–Eur. J.* **2013,** *19,* 6162–6196.
   doi:10.1002/chem.201203814
15. Zahn, S.; Reckien, W.; Kirchner, B.; Staats, H.; Matthey, J.; Lützen, A. *Chem.–Eur. J.* **2009,** *15,* 2572–2580. doi:10.1002/chem.200801374
16. For a more comprehensive list of references using 2,2'-bipyridines as allosteric centres, see references 6–26 in ref. [22] and the examples listed in ref. [14].
17. Howard, S. T. *J. Am. Chem. Soc.* **1996,** *118,* 10269–10274.
   doi:10.1021/ja960932w
18. Pan, J.-F.; Chen, Z.-K.; Chua, S.-J.; Huang, W. *J. Phys. Chem. A* **2001,** *105,* 8775–8781. doi:10.1021/jp010356c
19. Lehtonen, O.; Ikkala, O.; Pietilä, L.-O. *J. Mol. Struct.: THEOCHEM* **2003,** *663,* 91–100. doi:10.1016/j.theochem.2003.08.065
20. Lützen, A.; Haß, O.; Bruhn, T. *Tetrahedron Lett.* **2002,** *43,* 1807–1811.
   doi:10.1016/S0040-4039(02)00086-2
21. Staats, H.; Eggers, F.; Haß, O.; Fahrenkrug, F.; Matthey, J.; Lüning, U.; Lützen, A. *Eur. J. Org. Chem.* **2009,** 4777–4792.
   doi:10.1002/ejoc.200900642
22. Staats, H.; Lützen, A. *Beilstein J. Org. Chem.* **2010,** *6,* No. 10.
   doi:10.3762/bjoc.6.10
23. Cram, D. J.; Cram, M. J. *Container Molecules and Their Guests;* Royal Society of Chemistry: Cambridge, 1994.
24. Sherman, J. C. *Tetrahedron* **1995,** *51,* 3395–3422.
   doi:10.1016/0040-4020(94)01072-8
25. Dodziuk, H. *Cyclodextrins and Their Complexes;* Wiley-VCH: Weinheim, 2006. doi:10.1002/3527608982
26. Kiehne, U.; Bunzen, J.; Staats, H.; Lützen, A. *Synthesis* **2007,** 1061–1069. doi:10.1055/s-2007-965952
27. Hapke, M.; Staats, H.; Wallmann, I.; Lützen, A. *Synthesis* **2007,** 2711–2719. doi:10.1055/s-2007-983824
28. Kremer, C.; Lützen, A. *Synthesis* **2011,** 210–212.
   doi:10.1055/s-0030-1258342
29. Lee, T.; Lim, J.; Chung, I.; Kim, I.; Ha, C.-S. *Macromol. Res.* **2010,** *18,* 120–128. doi:10.1007/s13233-009-0120-1
30. Hbaieb, S.; Kalfat, R.; Chevalier, Y.; Amdouni, N.; Parrot-Lopez, H. *Mater. Sci. Eng., C* **2008,** *28,* 697–704.
   doi:10.1016/j.msec.2007.10.013
31. Sallas, F.; Marsura, A.; Petot, V.; Pintér, I.; Kovács, J.; Jicsinszky, L. *Helv. Chim. Acta* **1998,** *81,* 632–645. doi:10.1002/hlca.19980810314
32. Schmittel, M.; Lüning, U.; Meder, M.; Ganz, A.; Michel, C.; Hederich, M. *Heterocycl. Commun.* **1997,** *3,* 493–498. doi:10.1515/HC.1997.3.6.493
33. Schmittel, M.; Ganz, A. *Synlett* **1997,** 710–712.
   doi:10.1055/s-1997-3243
34. Schmittel, M.; Ganz, A. *Chem. Commun.* **1997,** 999–1000.
   doi:10.1039/a701509g
35. De, S.; Mahate, K.; Schmittel, M. *Chem. Soc. Rev.* **2010,** *39,* 1555–1575. doi:10.1039/b922293f
36. Lüning, U.; Müller, M. *Chem. Ber.* **1990,** *123,* 643–645.
   doi:10.1002/cber.19901230335
37. Yamada, M.; Nakamura, Y.; Kuroda, S.; Shimao, I. *Bull. Chem. Soc. Jpn.* **1990,** *63,* 2710–2712. doi:10.1246/bcsj.63.2710
38. Frey, J.; Kraus, T.; Heitz, V.; Sauvage, J.-P. *Chem.–Eur. J.* **2007,** *13,* 7584–7594. doi:10.1002/chem.200700671
39. Nishimura, N.; Yoza, K.; Kobayashi, K. *J. Am. Chem. Soc.* **2010,** *132,* 777–790. doi:10.1021/ja9084918
40. Lüning, U.; Abbass, M.; Fahrenkrug, F. *Eur. J. Org. Chem.* **2002,** 3294–3303.
   doi:10.1002/1099-0690(200210)2002:19<3294::AID-EJOC3294>3.0.CO;2-Z
41. Cacciapaglia, R.; Di Stefano, S.; Fahrenkrug, F.; Lüning, U.; Mandolini, L. *J. Phys. Org. Chem.* **2004,** *17,* 350–355.
   doi:10.1002/poc.735
42. Lüning, U.; Fahrenkrug, F. *Eur. J. Org. Chem.* **2004,** 3119–3127.
   doi:10.1002/ejoc.200400068
43. Schmittel, M.; Ganz, A.; Fenske, D.; Herderich, M. *J. Chem. Soc., Dalton Trans.* **2000,** 353–359. doi:10.1039/a907545c

Molecular recognition of isomeric protonated amino acid esters monitored by ESI-mass spectrometry

Andrea Liesenfeld and Arne Lützen[*]

Abstract

Two new 9,9'-spirobifluorene-derived crown ethers were prepared and used to recognise constitutionally isomeric amino acid derivatives. The performance of the receptors was evaluated by ESI-mass spectrometry using the isomer labelled guest method (ILGM). This method revealed the preferred binding of L-norleucine and L-leucine compared to L-isoleucine for both receptors. Furthermore, non-covalent isotope effects demonstrate the relevance of dispersive interactions for the overall binding event. These effects also provide hints for the relative spatial orientation of the guest molecules within the host–guest complex, and thereby prove the importance of the spirobifluorene moiety for the observed binding of the protonated amino acid esters.

Introduction

The separation of constitutionally isomeric amino acids is of practical interest. This is particularly true for leucine (Leu), isoleucine (Ile), and norleucine (Nle), especially since the first two are both proteinogenic amino acids (Figure 1). However, it is a great challenge to separate molecules that have the same molecular mass and do not differ significantly in structure. Hence, the chemical and physical properties are very similar, and the isomers leucine, isoleucine, and norleucine are difficult to separate employing commonly used analytical methods like crystallization, enzymatic separation methods, or modified thin-layer chromatography [1-5].

Figure 1: L-Norleucine, L-isoleucine, and L-leucine.
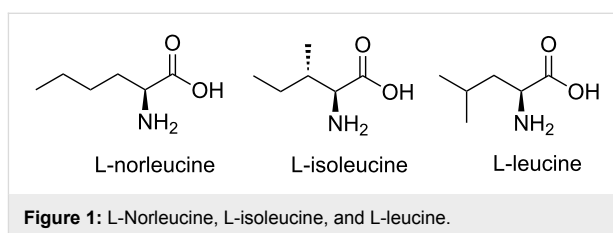
Therefore, we thought to look for a supramolecular approach to achieve amino acid recognition by an artificial host [6-11] with regard to isomer separation upon isomer-selective molecular

recognition by a concave template acting as a host, thereby avoiding the necessity to establish or break additional covalent chemical bonds. Hence, we have prepared two new templates based on a 9,9'-spirobifluorene core and tested them with regard to their ability to recognize the three isomeric amino acids in form of their protonated methyl esters. We decided to use ESI-mass spectrometry for these tests since this technique is fast to perform, consumes only trace amounts of material, and can be used to explore competitive experiments that are difficult to perform using UV–vis or NMR spectroscopy.

Results and Discussion
Design and synthesis of the concave templates

Ammonium ions exhibit strong binding affinity towards crown ether moieties. Hence, we decided to use this motif to achieve binding of the leucine isomers as their protonated ester derivatives. This provides the major part of the overall binding energy. However, to distinguish the three isomers the receptors need to provide further elements that either provide additional binding sites for the non-polar parts of the substrates, e.g., via attractive dispersive interactions, or provide steric hindrance

that prevents substrates of a certain shape to be accommodated in the concave binding site of the templates. Since the 9,9'-spirobifluorene moiety provides such a rigid concave, non-polar scaffold that has been demonstrated to be a valuable part of some receptors [12,13], we decided to employ this motif. Therefore, we designed the two compounds **1** and **2** shown in Figure 2 that differ only in the bridging element between the crown ether group and the spirobifluorene.

The synthesis of **1** and **2** started from 1-bromo-4-methoxybenzene which was transferred into 2-bromo-4'-methoxybiphenyl (**3**) in 92% yield via lithiation with *t*-BuLi, transmetallation with zinc(II) bromide, and subsequent Negishi cross-coupling reaction with 1-bromo-2-iodobenzene [14,15]. **3** was then transformed into the corresponding Grignard reagent which was reacted with 9-fluorenone to afford tertiary alcohol **4** in 55% yield. Adopting a protocol of Tour et al. [16] led to 2-methoxy-9,9'-spirobifluorene (**5**) in 95% yield via acidic condensation of **4**. Next, the methoxy group was cleaved quantitatively by reaction with boron tribromide, followed by hydrolysis to afford phenol **6** which was finally transferred into the corresponding triflate **7** in 64% yield (Scheme 1).
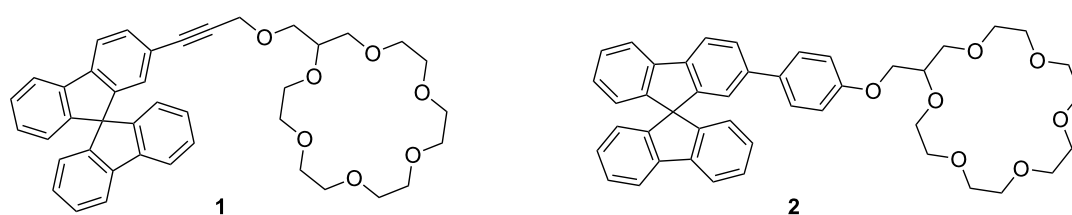
Figure 2: Concave templates **1** and **2**.
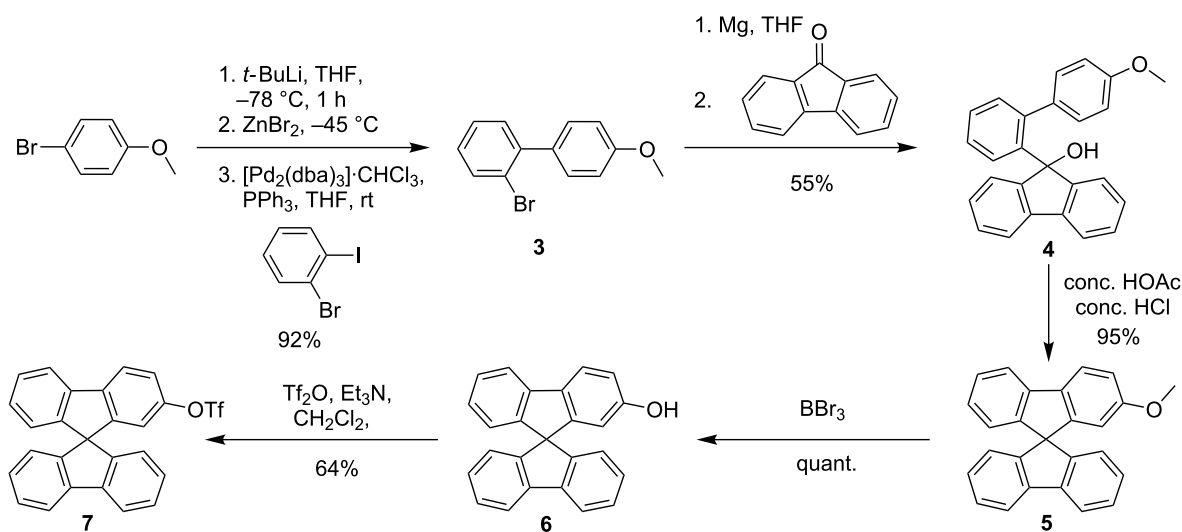
Scheme 1: Syntheses of the 2-(9,9'-spirobifluorene-2-yl)trifluoromethansulfonate (**7**).

Triflate **7** was then subjected to a Sonogashira cross-coupling reaction and a Suzuki cross-coupling reaction followed by treatment with boron tribromide to obtain the ethynylated and arylated alcohols **8** in 95% yield and **9** in 87% yield over both steps, respectively. Finally, deprotonation by sodium hydride and reaction with tosylated 18-crown-6 derivative **10** [17,18] derived from commercially available (1,4,7,10,13,16-hexaoxa-cyclooctadecan-2-yl)methanol afforded the desired target compounds **1** and **2** in moderate yields (Scheme 2).

Molecular recognition studies

With our crown ether derivatives **1** and **2** in hands we studied their recognition behaviour towards the L-leucine isomers. Usually, spectroscopic techniques like NMR or UV–vis spectroscopy are used for this purpose. However, mass spectrometry has become a major analytical tool in supramolecular chemistry in recent years [19-21] and seemed to be perfectly suited in this case, since we were planning to recognise the amino acid derivatives in form of their protonated alkyl esters

anyway. Thus, the host–guest complexes would be charged and supposedly easy to detect by mass spectrometry if they can be separated from the counter-ions.

Nevertheless, it still sounds kind of paradox to use mass spectrometry to study isomeric complexes due to their identical mass/charge ratio. This problem can be circumvented by the use of isotopically labelled substrates in the sense of an isomer labelled guest method (ILGM) (Figure 3) which is closely related to the enantiomer labelled guest method (ELGM) introduced by Sawada [22].

Here, a competitive recognition experiment using a non-labelled substrate and a mass-labelled *quasi*-isomer is performed to reveal the relative affinity of a receptor towards the different isomers. In this way, the mass spectrometric analysis easily allows direct identification of the individual host–guest complexes. This is usually more complicated with other techniques such as, e.g., NMR spectroscopy because it is more diffi-
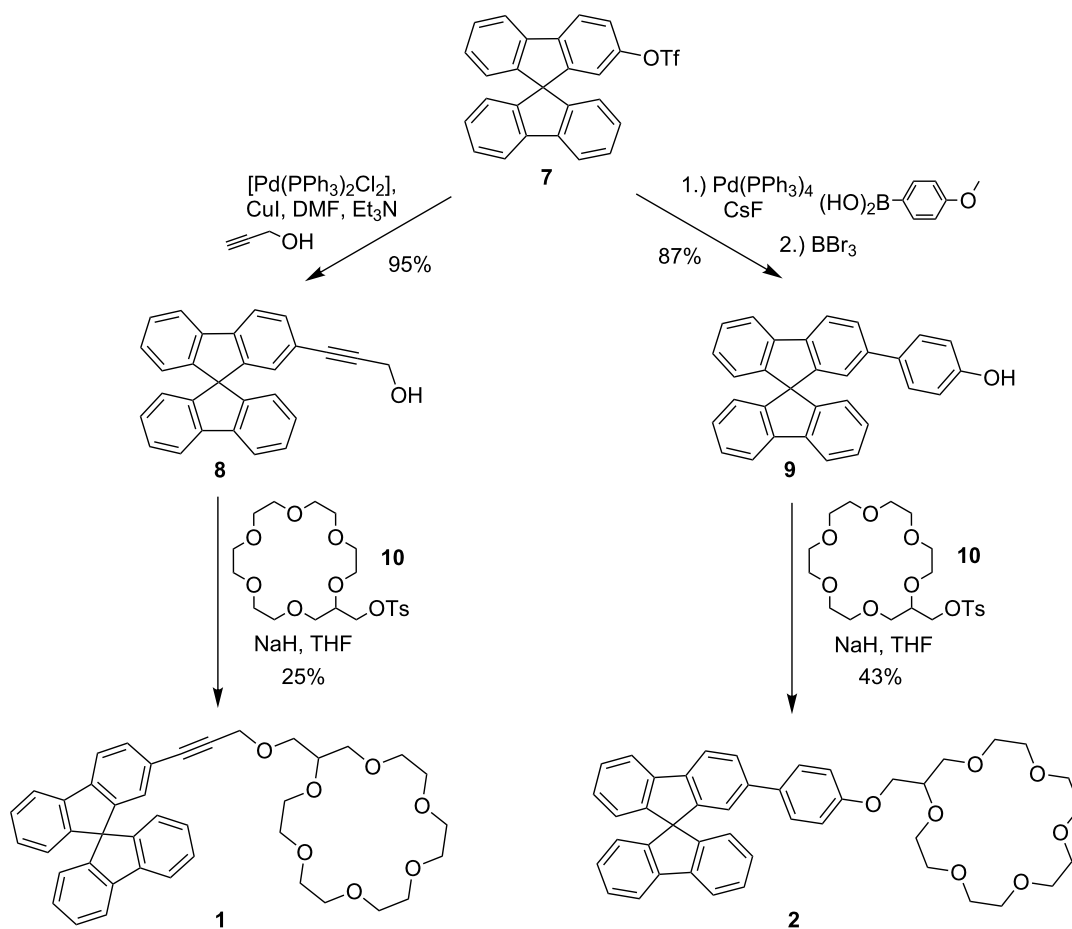
Scheme 2: Synthesis of the two receptors **1** and **2**.

Figure 3: Schematic presentation of the isomer labelled guest method (ILGM).
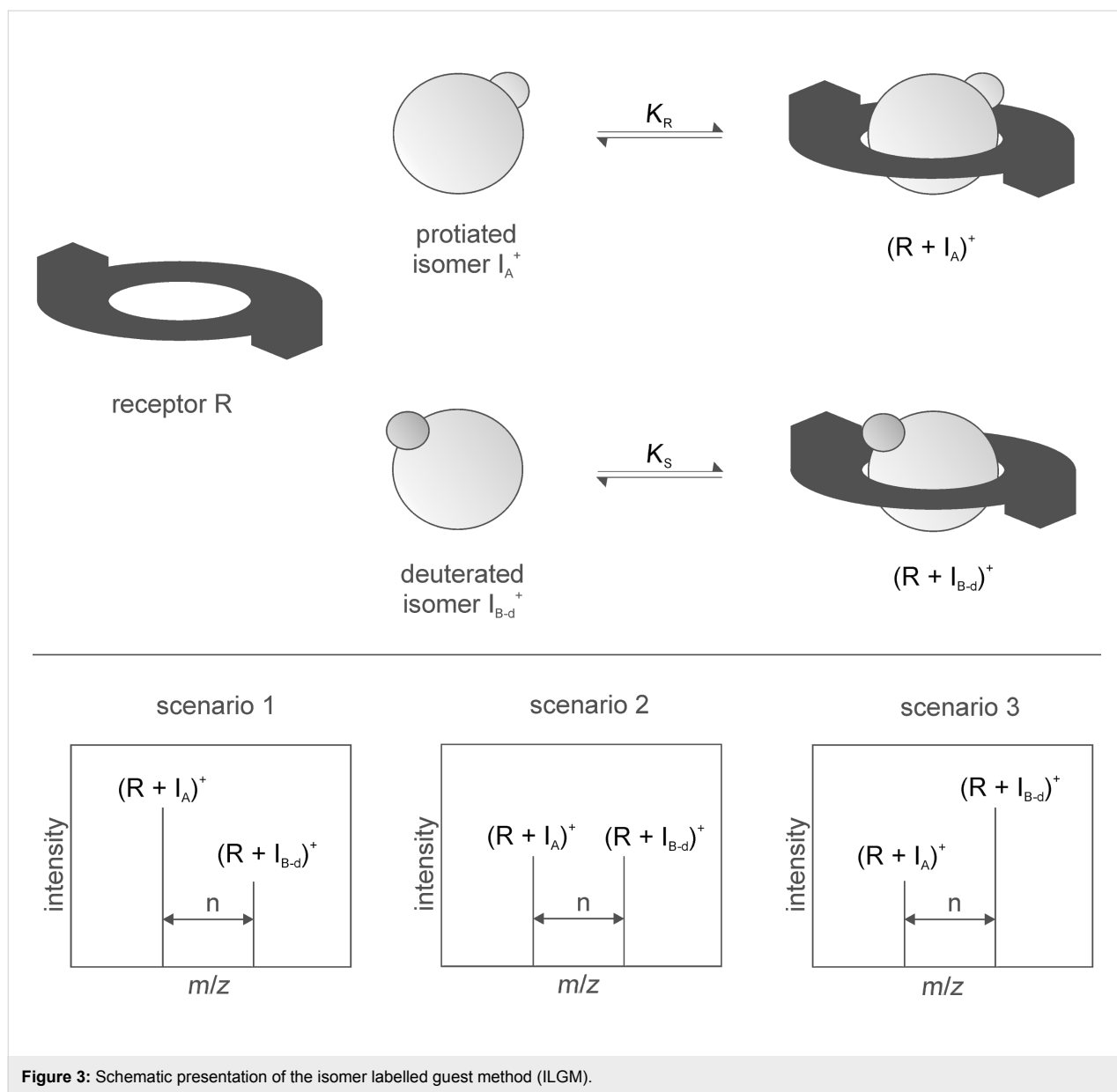
cult to assign the signals to the individual host–guest complexes and the analysis might be additionally hindered or even be impossible due to severe signal overlapping.

In our case, we used the methyl groups of the ester function as the mass label by employing either the normal protiated methyl group or a trideuteromethyl group as the labelled one. To test the relative affinity of a receptor towards two isomeric substrates we prepared solutions that contain 1:1:1 mixtures of the receptor, a non-labelled guest, and an isotopically-labelled guest. These solutions were analysed by ESI-mass spectrometry (Figure 4). The intensity ratios of the signals of the host–guest complexes can then be used to conclude which guest is bound stronger since the mass difference is large enough to

allow an individual detection but also small enough not to cause any problems due to mass discrimination phenomena.

It is important to note that these measurements are obviously not biased by, e.g., different solvation energies of the structural isomers which could cause different ESI response factors because we did not observe different intensity ratios when we changed the overall concentration of our samples. Another important point that has to be mentioned here, however, is that intensity differences of the complexes might also be the result of differences in the tendency to dissociate under the conditions of the ESI–MS experiment. Unfortunately, the low mass of the leucine derivatives investigated here did not allow to study this phenomenon directly because the FTICR spectrometer we used
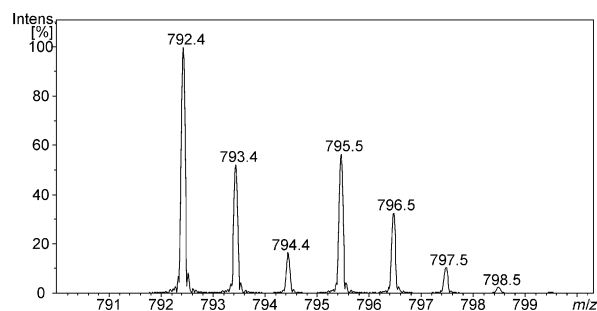
Figure 4: ESI-mass spectrum (positive mode) of a 1:1:1 mixture of **1**, protonated L-leucine methyl ester (LeuOMe), and protonated L-isoleucine trideuteromethyl ester (IleOMe-d_3) in a 1:1 mixture of CH$_2$Cl$_2$/MeOH (*m/z* = 792.4 LeuOMe–**1**, *m/z* = 795.5 IleOMe-d_3–**1**).

is tuned in a way that it does not allow detection of such low molecular mass ions with the necessary accuracy. Hence, we optimized our ESI conditions using larger and well-detectable protonated amino acid esters like protonated phenylalanine benzyl ester to make sure that the conditions are mild enough not to cause dissociation.

Having made sure that the method is in principle suitable to study the recognition of protonated amino acid derivatives in a competitive fashion there is still one more factor that has to be taken into account: non-covalent isotope effects [23] might also cause significant differences of the signals' intensities. Therefore, every experiment has to be repeated with the different order of isotope labelling and in addition one should measure the same isomer in both forms – non-labelled and labelled – in order to quantify this effect (Figure 5).
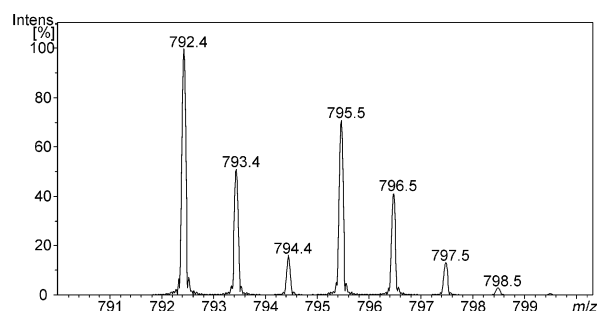
Figure 5: ESI-mass spectrum (positive mode) of a 1:1:1 mixture of **1**, protonated L-leucine methyl ester (LeuOMe), and protonated L-leucine trideuteromethyl ester (LeuOMe-d_3) in a 1:1 mixture of CH$_2$Cl$_2$/MeOH (*m/z* = 792.4 LeuOMe–**1**, *m/z* = 795.5 LeuOMe-d_3–**1**).

Table 1 lists the results of the ILGM measurements with regard to the affinity of templates **1** and **2** towards L-norleucine,

L-isoleucine, and L-leucine that were calculated according to Equation 1.

$$\frac{I_{\text{NleOMe}-d_3}}{I_{\text{LeuOMe}}} \Big/ \frac{I_{\text{NleOMe}-d_3}}{I_{\text{NleOMe}}} = \frac{\boldsymbol{I}_{\text{NleOMe}}}{\boldsymbol{I}_{\text{LeuOMe}}} =$$

$$\frac{I_{\text{NleOMe}}}{I_{\text{LeuOMe}-d_3}} * \frac{I_{\text{LeuOMe}-d_3}}{I_{\text{LeuOMe}}} = \text{ILGM-value} \qquad (1)$$

Table 1: ILGM ratios for the recognition of the three pairs of L-leucine isomers by templates **1** and **2**.

pair of isomers	**1**	**2**
L-NleOMe/L-IleOMe	1.5	1.2
L-IleOMe/L-LeuOMe	0.7	0.8
L-NleOMe/L-LeuOMe	1.0	0.9

These ratios translate into the following relative affinities of our receptors:

Receptor **1**: L-NleOMe ≈ L-LeuOMe > L-IleOMe

Receptor **2**: L-LeuOMe ≥ L-NleOMe > L-IleOMe

Interestingly, isoleucine methyl ester is the worst guest in both cases although the effect is not large enough yet to think about an application for the separation of the isomers on a larger scale via supramolecular transport, for instance. However, these results are still promising with regard to the development of a template that allows the efficient separation of isoleucine and leucine which is obviously the most interesting challenge. The non-covalent isotope effects clearly demonstrate that the ester group of the amino acid derivative must interact with our templates, and therefore, these effects tell us something about the relative spatial orientation of the template and the substrate within the host–guest complexes (Figure 6).

In fact, the deuterated guests were always bound less good than the protiated guests. This can be rationalized by assuming attractive dispersive interaction to play a significant role during the recognition event. The deuterated group is on average slightly smaller than the protiated group [14-26] which causes a smaller van der Waals volume of the deuterated group [27-32]. In a first approximation, however, the dispersive interactions get stronger with an increasing size of the volume and consequently the contact area, and hence, the deuterated compounds ability to interact via those interactions is weaker [33-35]. This observation perfectly agrees with the conclusion that the ester group gets into close contact with the non-polar parts of the

Figure 6: Two different motifs for the binding of substrates to the templates.
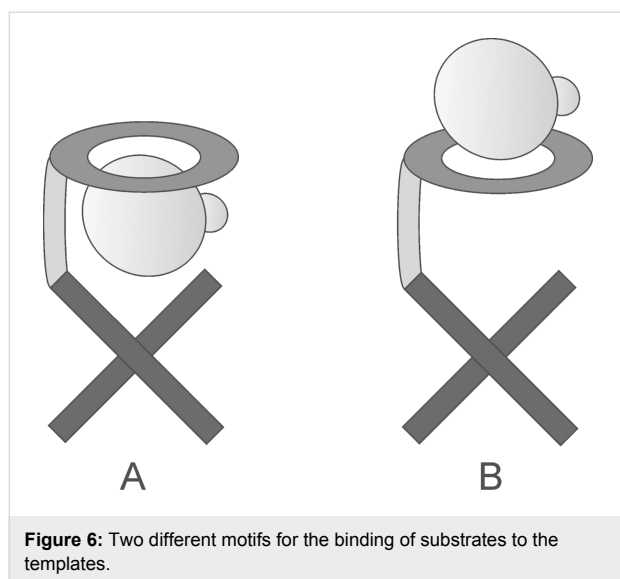
templates, and thereby, contribute to the binding affinity by attractive dispersive interactions.

Hence, we can conclude that the binding of the amino acid derivatives occurs in a way that puts the substrates in close contact to the crown ether and the spirobifluorene backbone as depicted in motif A in Figure 6 rather than placing them in a more remote position where only the ammonium group can interact with the crown ether moiety which would largely rule out any isotope effect (motif B in Figure 6).

Conclusion

We have synthesised two new functionalized crown ethers **1** and **2** both bearing a 9,9'-spirobifluorene moiety and studied their ability to differentiate between the constitutional isomers L-leucine, L-norleucine, and L-isoleucine. ESI-mass spectrometry measurements using the isomer labelled guest method (ILGM) were used for this purpose. This technique proved to be a quick method that needs only trace amounts of material and allows easily studying relative affinities in competitive experiments. Interestingly, L-isoleucine was found to be the worst guest for both of our templates, whereas L-leucine and L-norleucine turned out to be almost equally good guests. The occurrence of significant non-covalent isotope effects allowed us to obtain information on the relative spatial orientation of the substrates within the concave host structure. Obviously, the spirobifluorene part of **1** and **2** provides a possibility to undergo attractive dispersive interactions with non-polar parts of the substrates. Nevertheless, however, it also provides enough rigidity to differentiate between different substitutions in the β-position of the amino acid derivative at the same time. Hence, we think it is not fallacious that **1** and **2** might serve as kind of lead structures to develop even better templates in the future.

Supporting Information

Experimental data of all new compounds and of the ESI mass spectrometric experiments.

Supporting Information File 1

Experimental data, ESI-mass spectrometric experiments.
[http://www.beilstein-journals.org/bjoc/content/supplementary/1860-5397-10-78-S1.pdf]

References

1. Stein, W. H.; Moore, S.; Stamm, G.; Chou, C.-Y.; Bergmann, M. *J. Biol. Chem.* **1942,** *143,* 121–129.
2. Hongo, C.; Yoshioka, R.; Yamada, S.; Chibata, I. *J. Chem. Technol. Biotechnol.* **1979,** *29,* 145–148. doi:10.1002/jctb.503290304
3. Martens, J.; Weigel, H. *Liebigs Ann. Chem.* **1983,** *1983,* 2052–2054. doi:10.1002/jlac.198319831124
4. Stoddard, M. P.; Dunn, M. S. *J. Biol. Chem.* **1942,** *142,* 329–343.
5. McBride, R. W.; Jolly, D. W.; Kadis, B. M.; Nelson, T. E., Jr. *J. Chromatogr., A* **1979,** *168,* 290–291. doi:10.1016/S0021-9673(00)80728-1
6. Collins, B. E.; Wright, A. T.; Anslyn, E. V. *Top. Curr. Chem.* **2007,** *277,* 181–218. doi:10.1007/128_2007_114
7. Kraus, T. *Curr. Org. Chem.* **2011,** *15,* 802–814. doi:10.2174/138527211794518907
8. Mutihac, L.; Lee, J. H.; Kim, J. S.; Vicens, J. *Chem. Soc. Rev.* **2011,** *40,* 2777–2796. doi:10.1039/c0cs00005a
9. Joseph, R.; Rao, C. P. *Chem. Rev.* **2011,** *111,* 4658–4702. doi:10.1021/cr1004524
10. Urbach, A. R.; Ramalingam, V. *Isr. J. Chem.* **2011,** *51,* 664–678. doi:10.1002/ijch.201100035
11. Schneider, H.-J.; Agrawal, P.; Yatsimirski, A. K. *Chem. Soc. Rev.* **2013,** *42,* 6777–6800. doi:10.1039/c3cs60069f
12. Das, G.; Hamilton, A. D. *Tetrahedron Lett.* **1997,** *38,* 3675–3678. doi:10.1016/S0040-4039(97)00725-9
13. Cuntze, J.; Diederich, F. *Helv. Chim. Acta* **1997,** *80,* 897–911. doi:10.1002/hlca.19970800323
14. Li, C.-W.; Wang, C.-I.; Liao, H.-Y.; Chaudhuri, R.; Liu, R.-S. *J. Org. Chem.* **2007,** *72,* 9203–9207. doi:10.1021/jo701504m
15. Varela, J. A.; Peña, D.; Goldfuss, B.; Denisenko, D.; Kulhanek, J.; Polborn, K.; Knochel, P. *Chem.–Eur. J.* **2004,** *10,* 4252–4264. doi:10.1002/chem.200400023
16. Tour, J. M.; Wu, R.; Schumm, J. S. *J. Am. Chem. Soc.* **1990,** *112,* 5662–5663. doi:10.1021/ja00170a053
17. Czech, B.; Son, B.; Bartsch, R. A. *Tetrahedron Lett.* **1983,** *24,* 2923–2926. doi:10.1016/S0040-4039(00)88059-4
18. Dishong, D. M.; Diamond, C. J.; Cinoman, M. I.; Gokel, G. W. *J. Am. Chem. Soc.* **1983,** *105,* 586–593. doi:10.1021/ja00341a045
19. Schalley, C. A. *Mass Spectrom. Rev.* **2001,** *20,* 253–309. doi:10.1002/mas.10009

20. Schalley, C. A.; Springer, A. *Mass Spectrometry and Gas Phase Chemistry of Non-Covalent Complexes;* Wiley: Hoboken, 2009.
21. Zehnacker, A., Ed. *Chiral Recognition in the Gas Phase;* CRC Press, Taylor & Francis Group: Boca Raton, 2010.
22. Sawada, M. *Mass Spectrom. Rev.* **1997,** *16,* 73–90. doi:10.1002/(SICI)1098-2787(1997)16:2<73::AID-MAS2>3.0.CO;2-6
23. Wade, D. *Chem.-Biol. Interact.* **1999,** *117,* 191–217. doi:10.1016/S0009-2797(98)00097-0
24. Kuchitsu, K.; Bartell, L. S. *J. Chem. Phys.* **1962,** *36,* 2470–2481. doi:10.1063/1.1732910
25. Pulay, P.; Meyer, W.; Boggs, J. E. *J. Chem. Phys.* **1978,** *68,* 5077–5085. doi:10.1063/1.435626
26. Lacks, D. J. *J. Chem. Phys.* **1995,** *103,* 5085–5090. doi:10.1063/1.470595
27. Felder, T.; Schalley, C. A. *Angew. Chem.* **2003,** *115,* 2360–2363. doi:10.1002/ange.200350903
    Angew. Chem., Int. Ed. **2003,** *42,* 2258–2260. doi:10.1002/anie.200350903
28. Rechavi, D.; Scarso, A.; Rebek, J., Jr. *J. Am. Chem. Soc.* **2004,** *126,* 7738–7739. doi:10.1021/ja048366p
29. Liu, Y.; Warmuth, R. *Angew. Chem.* **2005,** *117,* 7269–7272. doi:10.1002/ange.200501840
    Angew. Chem., Int. Ed. **2005,** *44,* 7107–7110. doi:10.1002/anie.200501840
30. Mugridge, J. S.; Bergman, R. G.; Raymond, K. N. *J. Am. Chem. Soc.* **2010,** *132,* 1182–1183. doi:10.1021/ja905170x
31. Mugridge, J. S.; Bergman, R. G.; Raymond, K. N. *Angew. Chem.* **2010,** *122,* 3717–3719. doi:10.1002/ange.200906569
    Angew. Chem., Int. Ed. **2010,** *49,* 3635–3637. doi:10.1002/anie.200906569
32. Mugridge, J. S.; Bergman, R. G.; Raymond, K. N. *J. Am. Chem. Soc.* **2012,** *134,* 2057–2066. doi:10.1021/ja2067324
33. Matucha, M.; Jockisch, W.; Verner, P.; Anders, G. *J. Chromatogr.* **1991,** *588,* 251–258. doi:10.1016/0021-9673(91)85030-J
34. Turowski, M.; Yamakawa, N.; Meller, J.; Kimata, K.; Ikegami, T.; Hosoya, K.; Tanaka, N.; Thornton, E. R. *J. Am. Chem. Soc.* **2003,** *125,* 13836–13849. doi:10.1021/ja036006g
35. Schmarr, H.-G.; Slabizki, P.; Müntnich, S.; Metzger, C.; Garcia-Moreno, E. *J. Chromatogr., A* **2012,** *1270,* 310–317. doi:10.1016/j.chroma.2012.11.010

The influence of intraannular templates on the liquid crystallinity of shape-persistent macrocycles

Joscha Vollmeyer[1], Ute Baumeister[*2] and Sigurd Höger[*1]

Full Research Paper

Address:
[1]Kekulé-Institut für Organische Chemie und Biochemie, Rheinische Friedrich-Wilhelms-Universität Bonn, Gerhard-Domagk-Str. 1, 53121 Bonn, Germany and [2]Institut für Chemie, Physikalische Chemie, Martin-Luther-Universität Halle-Wittenberg, Von-Danckelmann-Platz 4, 06120 Halle (Saale), Germany

Email:
Ute Baumeister[*] - ute.baumeister@chemie.uni-halle.de;
Sigurd Höger[*] - hoeger@uni-bonn.de

* Corresponding author

Abstract

A series of shape-persistent phenylene–ethynylene–naphthylene–butadiynylene macrocycles with different extraannular alkyl groups and intraannular bridges is synthesized by oxidative Glaser-coupling of the appropriate precursors. The intraannular bridges serve in this case as templates that reduce the oligomerization even when the reaction is not performed under pseudo high-dilution conditions. The extraannular as well as the intraannular substituents have a strong influence on the thermal behavior of the compounds. With branched alkyl chains at the periphery, the macrocycles exhibit liquid crystalline (lc) phases when the interior is empty or when the length of the alkyl bridge is just right to cross the ring. With a longer alkyl or an oligoethylene oxide bridge no lc phase is observed, most probably because the mesogene is no longer planar.

Introduction

The supramolecular chemistry of shape-persistent macrocycles has enormously expanded during the past several years [1-6]. It covers the non-covalent interaction between the compound molecules and also the interaction between the macrocycles and appropriate partners. For example, the 2D organization of shape-persistent macrocycles at suitable surfaces leads to long-range ordered patterns with nanoscale lattice parameters and, moreover, even to the epitaxial absorption of appropriate guest molecules on this macrocycle template [7-10]. In solution, shape-persistent macrocycles aggregate into defined dimers or up to μm long fibers that can form gels (in solution) or can be casted to yield efficient sensor materials [11-23]. Amphiphilic macrocycles in aqueous solution have been shown to be able to form vesicles [24,25]. In the bulk state, most of the macrocycles crystallize and some could be explored by single-crystal X-ray analysis [26-28]. Heating crystalline macrocycles above

the melting point does not always lead immediately to an isotropic melt, but thermotropic mesophases are observed when the macrocycles have an appropriately substituted rim [29-35]. If the macrocycles pack on top of each other, hexagonal columnar or rectangular columnar phases can be observed in which the (empty) interior is able to accommodate small guest molecules [36-39]. In some cases, however, macrocycles with a filled interior seem to exhibit more stable mesophases compared to the compounds alike but with an empty interior [40]. Moreover, it has also been observed that even macrocycles with a flexible interior only, lacking the flexible rim, can form stable mesophases (macrocycles with an inverse structure) [41-43].

Recently, we presented a series of gel forming macrocycles that have an identical periphery but bear different intraannular substituents [11]. We were able to show that these substituents influence the thermal stability of the gel. As pointed out before, the ring interior can also have a dramatic effect on the mesophase stability of thermotropic liquid crystalline shape-persistent macrocycles [40,43-45]. However, more detailed studies on that issue are still scarcely found in the literature. Here, we designed and synthesized macrocycles **1–4** with flexible extraannular alkyl groups and a fixed intraannular chain that crosses the ring interior (Figure 1) and acts during the synthesis as a template. We studied the influence of the extra- and intraannular substituents on the molecule's ability to form liquid crystalline phases. The macrocycles are based on a phenylene–ethynylene–naphthylene–butadiynylene backbone. Naphthylene units at the four corners are expected to have a higher mesomorphic tendency compared with compounds

Figure 1: Shape-persistent macrocycles with different peripheral side groups and intraannular templates.
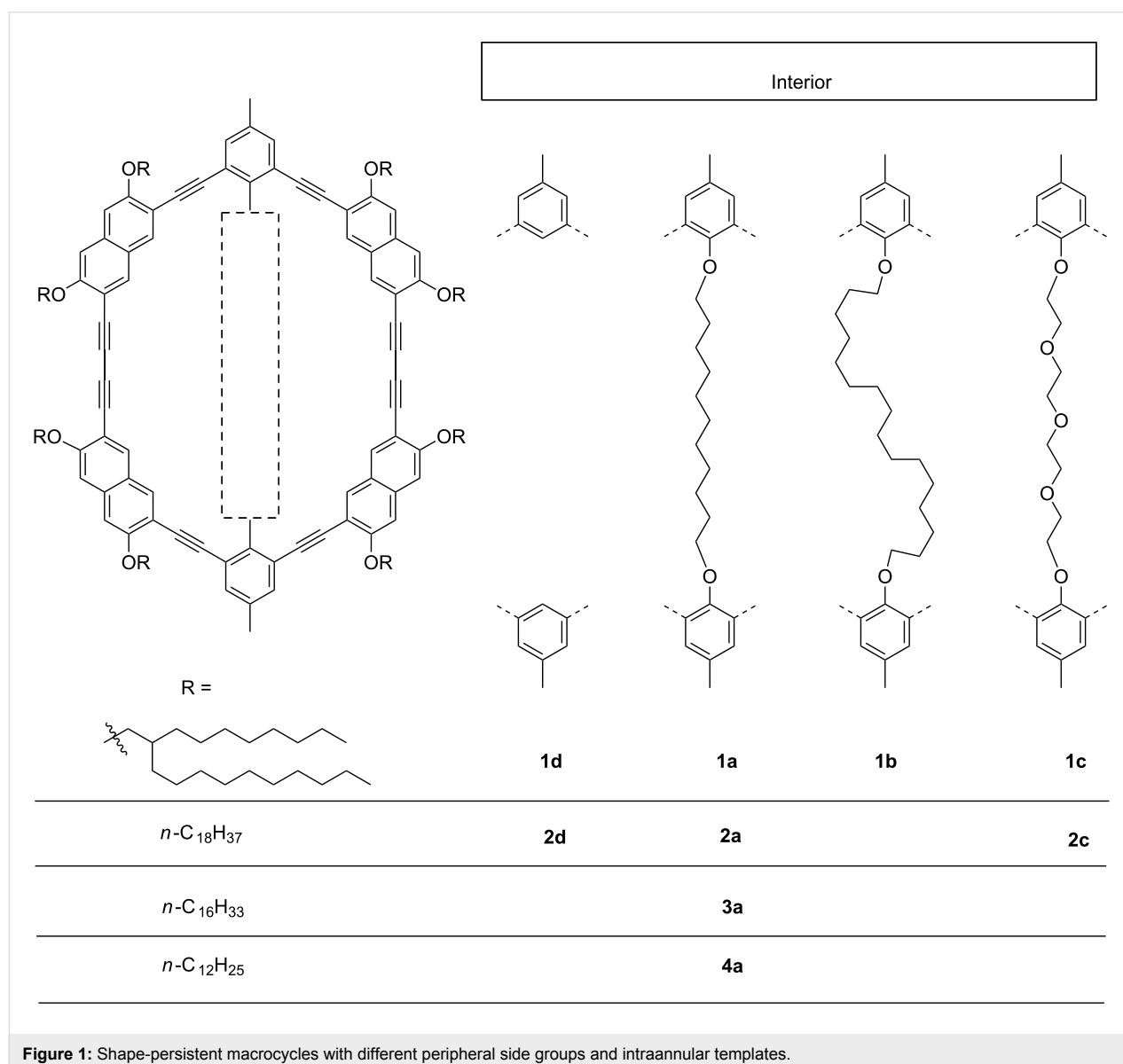
solely based on phenylene units [46]. Moreover, the naphthylene corners allow an efficient surrounding of the macrocycles with an alkyl fringe, according to the general design principle for discotic liquid crystals [47]. In addition to the macrocycles with intraannular bridges, we also synthesized and investigated a corresponding compound with an empty interior (**1d**).

Results and Discussion
Synthesis
Template-based macrocycles

The synthesis of the macrocycle **1** follows our often used strategy to dimerize appropriate rigid bisacetylenes oxidatively [48]. This coupling reaction can be performed statistically or template supported, where the latter is either non-covalently or covalently bound to the bisacetylenes [45,49,50]. The template does not necessarily only support the desired cyclization, it can also take over an active function in the final target structure. Covalently attached templates have the advantage over most of the supramolecular templates of being robust against solvent or temperature changes and will still be applicable at elevated temperatures. The bisacetylenes can be prepared independently and attached to the template just prior to the cyclization reaction or, and this is done here, the (template bound) oligoacetylene is prepared at the template [51].

Scheme 1 shows the general synthetic approach towards the macrocycles with an intraannular flexible bridge. The tetraiodide **5**, which contains the two phenylene ring corners and the

Scheme 1: Synthesis of macrocycle **1a** with an intraannular undecanedioxy bridge. a: Pd(PPh$_3$)$_2$Cl$_2$, PPh$_3$, CuI, piperidine, 84%; b: TBAF, THF, 94%; c: Pd(PPh$_3$)$_2$Cl$_2$, CuI, 1,4-benzoquinone, piperidine, THF, 49%.
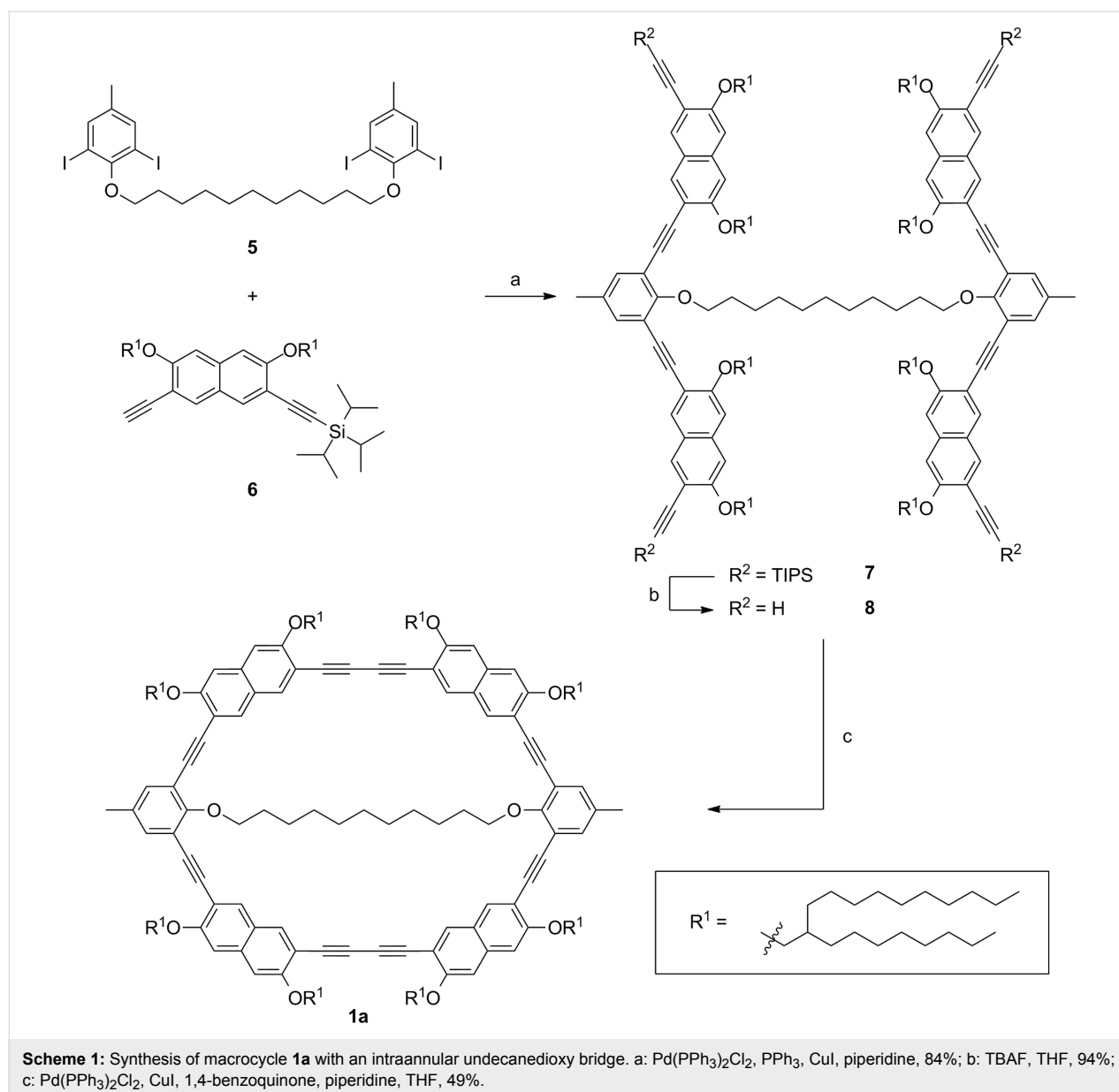
flexible alkyl template, as well as the naphthylene units **6** are synthesized independently (see Supporting Information File 1). Then **6** is attached to **5** in a fourfold Sonogashira–Hagihara reaction. To compensate the acetylene dimerization side reaction, the acetylene is added in 25% excess. Fluoride-induced removal of the silyl protecting groups yields the precursor **7**. With Pd(PPh$_3$)$_2$Cl$_2$ and CuI as catalysts and 1,4-benzoquinone as oxidant, the precursor is finally intramolecular cyclized in THF/piperidine under high-dilution conditions by slowly adding (48 hours) a solution of the tetraacetylene to the reaction media.

Gel permeation chromatography (GPC) analysis of the crude product indicates that only few oligomeric byproducts are formed (Figure 2). With the aid of recycling GPC (recGPC) these impurities could be removed and **1a** is obtained in 49% yield. Following this synthetic route we synthesized the macrocycles **1a–c** as well as the macrocycles **3a** and **4a** with different side chains (Figure 1, see Supporting Information File 1 for experimental details and reference [11] for the preparation of **2a–d**).

Statistical macrocycle synthesis

Macrocycle **1d** without intraannular substituents is obtained via statistical dimerization of the halfring **10** (Scheme 2). The half ring synthesis follows the above described approach and precursor **10** is cyclized under the same conditions as described
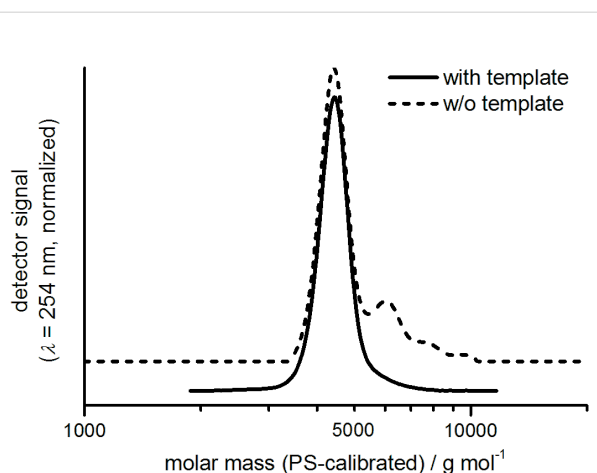
Figure 2: GPC elugrams of the crude product of the cyclization reaction of **1a** (—) and **1d** (- - -), respectively. For a better view the curves are vertically shifted.

for the template-mediated reaction. The GPC trace of the crude product shows significant amounts of oligomeric byproducts (Figure 2). Nevertheless, after purification by means of recGPC, macrocycle **1d** is obtained in a yield of 57%.

The comparison of the GPC traces of the crude products of **1a** and **1d** shows that in the intramolecular reaction less oligomers

Scheme 2: Synthesis of the template free macrocycle **1d**. a: Pd(PPh$_3$)$_2$Cl$_2$, PPh$_3$, CuI, piperidine, 98%; b: TBAF, THF, quant.; c: Pd(PPh$_3$)$_2$Cl$_2$, CuI, 1,4-benzoquinone, piperidine, THF, 50 °C, 57%.
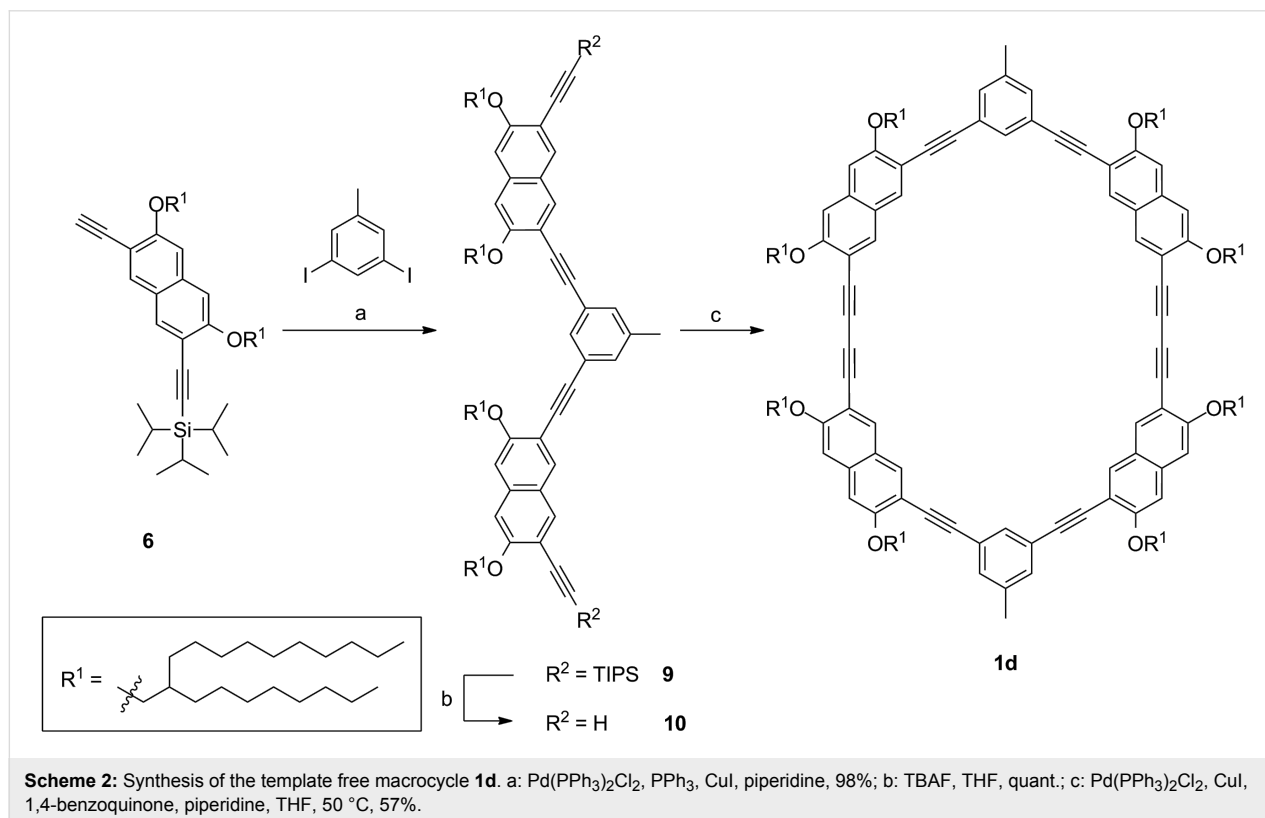
are formed than in the intermolecular reaction. However, the yields of the cyclization reactions do not differ significantly. That indicates that in the template-mediated cyclization side reactions cannot be completely suppressed. In the statistical half ring dimerization, the most important side reaction is the oligomerization of the half rings. Beside the desired dimers also trimers, tetramers, and other oligomers are formed, which can undergo further oligomerization reactions or may cyclize. These cyclic oligomers are still soluble and therefore they can be detected by GPC. In case of the template connected half rings, we assume that the oligomers formed through an intermolecular reaction cross-link, most likely form insoluble polymers, and are therefore not detected in the GPC analysis. The template has therefore two effects in the cyclization: (1) The terminal acetylenes are hold in proximity, thus, an intramolecular reaction is favored over an intermolecular reaction. (2) If an intermolecular coupling has occurred, the template leads to easily separable (insoluble) byproducts. However, the unexpected moderate yield in the template-directed synthesis suggests that the material may slowly decompose under the cyclization condition. Since other protocols (e.g., CuCl/CuCl$_2$ in pyridine) did not give reproducible results, we tested whether high-dilution conditions can be omitted. For this purpose, we performed the cyclization towards macrocycle **1c** not under pseudo high-dilution conditions but by stirring a solution of the complete starting material of **1c** at once in THF, piperidine, Pd(PPh$_3$)Cl$_2$ and CuI as catalysts and 1,4-benzoquinone as oxidant for 3 h at 60 °C and obtained **1c** in 56% yield (after purification, see Supporting Information File 1). This result additionally emphasizes the potential of template-mediated reactions, which not only can be more efficient in terms of reducing byproducts but also paves the way towards a fast coupling protocol.

Phase behavior
Thermal properties
By means of polarized optical microscopy (POM) and differential scanning calorimetry (DSC) we investigated the thermal properties of the macrocycles **1–4**. The transition temperatures are shown in Figure 3 and listed in Table 1.

Figure 3: (a) Melting points (T_m) and clearing points (T_{cl}) of macrocycles with different interior. [a]First heating. (b) DSC heat-flux curves of **1a–d** (10 K/min).
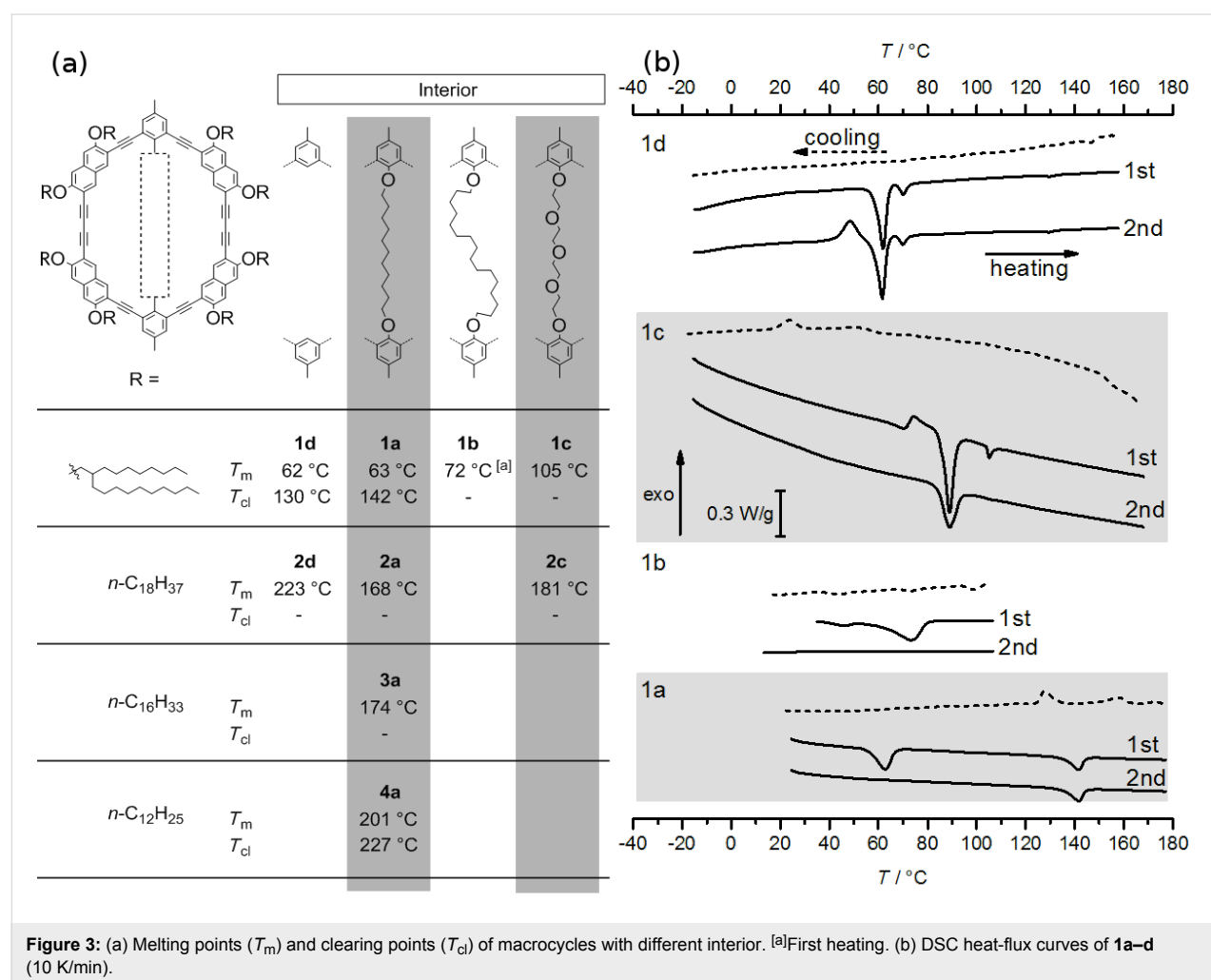
Table 1: Phase transitions and corresponding enthalpies of the discussed macrocycles.

Macrocycle (template)[a]	Transition temperatures [°C] (enthalpies [kJ/mol])[b]
1a (C11)	C 63 (20.4) Col_r 143 (10.5) I
1b (C16)	C 72 (33.8) I [c]
1c (4EG)	C_1 89 (45.8) I,C_2 105 (3.1) I [d]
1d (0)	C 62 (33.8) N_1 70 (4.3) N_2 130 (0.6) I [e]
2a (C11)	C_1 51 (53.0) C_2 168 (38.5) I
2c (4EG)	C_1 66 (84.2) C_2 130 (1.1) $C_3$181 (44.0) I
2d (0)	C_1 74 (128) C_2 223 (68.3) I
3a (C11)	C_1 51 (59) C_2 174 (40.9) I
4a (C11)	C 199 (40.8) LC 216 (0.4) I [f]

[a]0 = no intraannular substituent; C11 = undecyl diether ($-O(CH_2)_{11}O-$); C16 = hexadecyl diether ($-O(CH_2)_{16}O-$); 4EG = tetraethylene glycol ($-O(CH_2CH_2O)_4-$). [b]Upon heating. C, C_2, C_3 = crystalline phase, I = isotropic phase, LC = liquid crystalline phase, N_1, N_2 = discotic nematic phase, Col_r = rectangular columnar phase. [c]Only in the first scan. No crystallization upon cooling. [d]The sample melts isotropic at 89 °C, except for few crystallites, which melt at 105 °C. [e]In the second and following heating scans, right before the first transition a cold crystallization exotherm is observed (48 °C, 4.6 kJ/mol). [f]The observed Schlieren-texture strongly indicated the formation of a nematic phase (see the Supporting Information File 1).

Extraannular substitution

It is well known that the periphery of discotic molecules generally dominates their thermal behavior. Shortening the side chains usually increases the melting point, whereas longer side chains or branched alkyl groups have the opposite effect [47,52,53]. However, when the side groups become too long or bulky, the compound melts isotropically and does not exhibit a mesophase [47]. By comparing the macrocycles **1a**, **2a**, **3a**, and **4a**, all with the same intraannular alkyl template the melting points decrease with increasing length of the extraannular alkyl chains. The lowest transition temperature is observed for **1a**, with branched side chains (Figure 3a), as it is also observed for other discotics. However, only two of the studied compounds (**1a** and **4a**) are able to form liquid crystalline (lc) mesophases indicating for the other compounds an unfavorable ratio of the core to the periphery size [54].

Intraannular substitution

The lc phase stability of **1a** within a wide temperature range (63 °C to 142 °C) stimulated the investigation of the derivatives **1b–d** to elucidate the influence of the intraannular substitution on the phase behavior. In addition, we addressed the question whether an interior change could lead to liquid crystallinity in **2**.

From the DSC and POM investigations in combination with the chemical structure of the compounds the following observations can be summarized: Although **1d** has an empty lumen it has a similar melting point (62 °C) as **1a** (63 °C), whose cavity crosses an alkyl bridge. Prolonging the intraannular alkyl chain length raises this transition temperature towards 72 °C (**1b**). If a polar template (**1c**) is used instead, the melting point reaches

89–105 °C (there are most probably two polymorphs, which melt at different temperatures). For comparison, compounds **2a–d** melt at 168 °C (**2a**), 181 °C (**2c**), and 223 °C (**2d**), respectively (Figure 3, Table 1).

POM investigations indicate that **1a** and **1d** exhibit lc phases. Above the melting point, the sample of **1a** exhibits a fan shaped texture under the POM and shear tests indicate a wax-like viscosity of that phase (Figure 4a). The melt becomes isotropic when heated above 148 °C and the lc phase reappears upon cooling below 140 °C. **1d** forms in the temperature interval between 70 °C and 130 °C a birefringent lc phase with a characteristic Schlieren-texture (Figure 4b). Here, too, the lc phase reappears upon cooling from the isotropic melt (123 °C).

At lower temperatures, the mesophases of both, **1a** and **1d**, first solidify and slowly crystallize. The DSC results nicely confirm the POM observations. Corresponding endotherms for the melting and clearing points are visible in the thermograms of **1a** as well as **1d** (Figure 3b, Table 1). The sample of **1d** seems to melt at 62 °C (33 kJ/mol) into a nematic phase (N_1) followed by a transition into another nematic phase (N_2) at 70 °C (4.3 kJ/mol). The X-ray data of both phases are alike (see below). Upon cooling, no crystallization can be observed, either for **1a** or **1d**. However, for **1d** an exotherm followed by an endotherm is observed upon the second heating indicating crystallization and melting during the experiment. Clear hints on a stable mesophase could be obtained neither for **1b** nor for **1c**. From the DSC it seems that also **1c** exhibits an lc phase between 89 °C and 105 °C. However, from the POM and X-ray data we assume that **1c** forms at least two polymorphs which have different melting points. Unfortunately, their formation
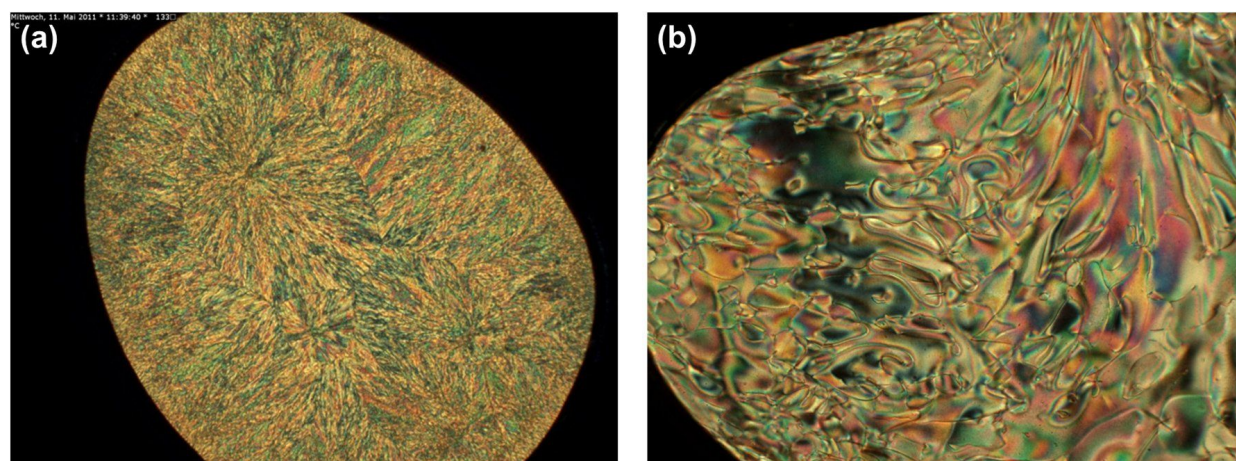
Figure 4: POM images of (a) **1a** (20×, 133 °C, upon cooling); (b) **1d** (20×, 84 °C, upon heating).

during the heating runs does not occur systematically but randomly.

These observations clearly show that also the intraannular substitution has a considerable influence on the thermal behavior of the macrocycles. The melting point increases in the order **1d** ≈ **1a** < **1b** < **1c**, showing the contribution of the intraannular template on the thermal behavior of the compounds. While the melting points of **1a** and **1d** are similar, the longer template in **1b** increases the melting point slightly and the additional interactions provided by the polar template in **1c** increase the melting point even further. However, the latter two compounds are not liquid crystalline. For **1b** can be assumed that the template is longer than the ring diameter and this leads to a loop in the molecule preventing the formation of an lc phase. For **1c**, the length of the template seems to be similar to the alkyl template in **1a**. However, the tendency of oligoethylene oxides to obtain a helical conformation [55] may fold the arylene–acetylene backbone into a boat conformation which is no longer a discotic mesogen. For the macrocycles **2a–d**, the melting points are rather high and clearly above the isotropization temperatures observed for **1a** and **1d**. The high melting point of **2d** might be explained by an interlocking of the molecules as a result of the empty interior of the rigid backbone [41]. A similar observation was also been made earlier on arylene–acetylene macrocycles. The fact that **1d** has a low melting point similar to **1a** although the interior is empty, is remarkable and prompted us to investigate **1a** and **1d** in more detail by X-ray diffraction to gain deeper insight into the structure of their liquid crystalline phases.

X-ray diffraction

A sample of **1d** was kept in a glass capillary (Ø 1 mm) in a temperature-controlled heating stage and partially aligned in a magnetic field, another one and that of **1a** were surface aligned at the sample – air interface on a glass plate on a temperature controlled heating stage, all on slow cooling (~0.1 K/min) from the isotropic liquid. 2D patterns were recorded by an area detector HIStar (Siemens/Bruker) using Ni-filtered Cu Kα radiation.

The patterns of **1d**, the compound without intraannular substitution, show in the isotropic liquid at 160 °C (Figure 5a) the usual outer diffuse scattering at about 4.6 Å characteristic for the average distance between the molecules along their short axes and between the side chains. In the small angle region there are two diffuse rings. These can be an indication of molecular aggregates which are already formed in the isotropic liquid [38]. The pattern slightly changes on cooling at the transition to the liquid crystalline phase and the sample becomes partially aligned in the magnetic field (Figure 5b and Supporting Information File 1 Figure S1 and Table S1). All reflections remain diffuse. Hence, it is a phase without long-range positional order
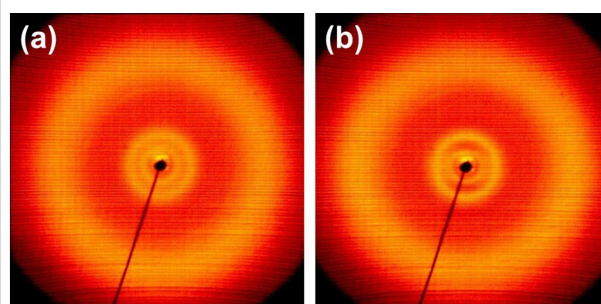
Figure 5: 2D X-ray patterns for **1d:** (a) isotropic liquid at 160 °C, (b) partially aligned liquid crystalline phase at 120 °C on cooling. The magnetic field is parallel to the meridian of the pattern.

and should be a kind of a nematic phase, in agreement with the optical textures. Obviously, similar clusters as in the isotropic phase are observed in the nematic phase. No changes of the X-ray pattern indicating a phase transition could be detected on heating above or on cooling below 70 °C (see Figure S1 in Supporting Information File 1) in contrast to those found for the nematic discotic (N_D)–nematic columnar (N_C) transition in liquid crystalline polymers [56] and for the N_D–nematic lateral (N_L) transition in liquid crystalline charge transfer complexes [57]. Neither magnetic nor surface alignment of the samples was sufficient to get evidence for or against a uniaxial nematic (N_u)–biaxial nematic (N_b) transition which has been extensively discussed in literature (see, e.g., [58]). The texture of the sample in the POM investigations did also not show significant changes like those observed for the N–N_x transition of liquid crystalline dimers and bent-core liquid crystals which has recently been identified as a nematic–twist bent nematic (N_{TB}) transition (see, e.g., [59,60]). Therefore the nature of the phase change indicated by the DSC measurements could not be clarified yet.

The X-ray pattern for the isotropic liquid of **1a** (Figure 6a) closely resembles that of **1d**, only the intensity ratio for the two inner rings differs. The changes at the phase transitions are more dramatic as in case of **1d** (Figure 6b). Indeed, the outer scattering also shows a ring-like part and one with four maxima, but the latter are found 45° above and below the equator and the inner scattering splits into Bragg reflections (Figure 6d) which can be indexed on a rectangular two-dimensional lattice (plane group *p2gg*, reflections *h0* only observed for *h* = 2*n* and 0*k* for *k* = 2*n*, cp. Figure 6c) with cell parameters *a* = 28.9 Å, *b* = 52.0 Å at 100 °C (Supporting Information File 1, Table S2) similar, for instance, to the 2D symmetry of the columnar lc phases of macrocycles reported in [40].

A plausible packing for the molecules is a stacking of the macrocycles in columns, in which the mean planes of the cycles have a 45° tilt angle with respect to the columnar axes. The columns in turn are arranged in the 2D lattice described above. Assuming one molecule in the cross section of a column with C_2 symmetry, the number of columns and hence of molecules in the cross section of the unit cell in this lattice is 2. For this packing model a reasonable density of 1.17 g/cm³ is calculated using an average stacking distance *h* = 4.6 Å / cos 45° = 6.5 Å of the macrocycles along the columnar axis (ρ_{calc} = n_{cell}*M/V_{cell}/A with a volume of an average 3D unit cell V_{cell} = *a* * *b* * *h* = 9768.2 Å³ and A = Avogadro constant). The assumed packing model also allows to understand the columnar phase stability. A MMFF calculation (Spartan '08) of a short column of tilted macrocycles shows a local minimum arrangement with a close contact between the intraannular alkyl chains
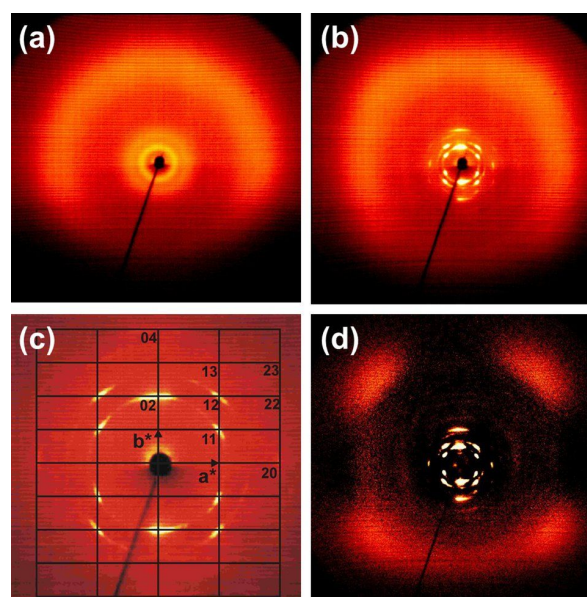
Figure 6: 2D X-ray patterns for **1a:** (a) isotropic liquid at 150 °C, (b) columnar mesophase at 100 °C, surface aligned on cooling, (c) small angle region at 100 °C with reciprocal axes and indices for the 2D lattice of the columnar phase, (d) scattering at 150 °C subtracted from that at 100 °C to enhance the effect of the anisotropic distribution of the diffuse scattering.

(Figure 7). It might be the additional packing effect of the intraannular alkyl chains which stabilizes the columnar phase. A similar effect (although with polar intraannular ester groups) has been observed previously [40]. However, in that particular case, the analogue non-filled macrocycle is not liquid crystalline. The packing model in Figure 7 also indicates that the longer intraannular alkyl bridge of **1b** prevents a close packing of the rings and leads in this case even to the absence of the lc phase.

Conclusion

In summary, shape-persistent macrocycles with intraannular bridges were synthesized by oxidative Glaser-coupling of the appropriate acetylenes. The bridges serve during the synthesis as a covalent template. Compounds with branched extraannular side chains exhibit in some cases liquid crystalline phases. Depending on the ring interior, either a nematic (empty interior) or a columnar phase (alkyl template) could be observed, as determined by differential scanning calorimetry, optical microscopy and X-ray scattering. It can be assumed that the additional van der Waals interaction between the stretched intraannular alkyl chains stabilize the packing of the rings on top of each other. When the alkyl bridge is longer than the ring interior or when an oligoether template crosses the ring, no lc behavior is observed. In both cases an induced non-planarity of the macrocycles is assumed.
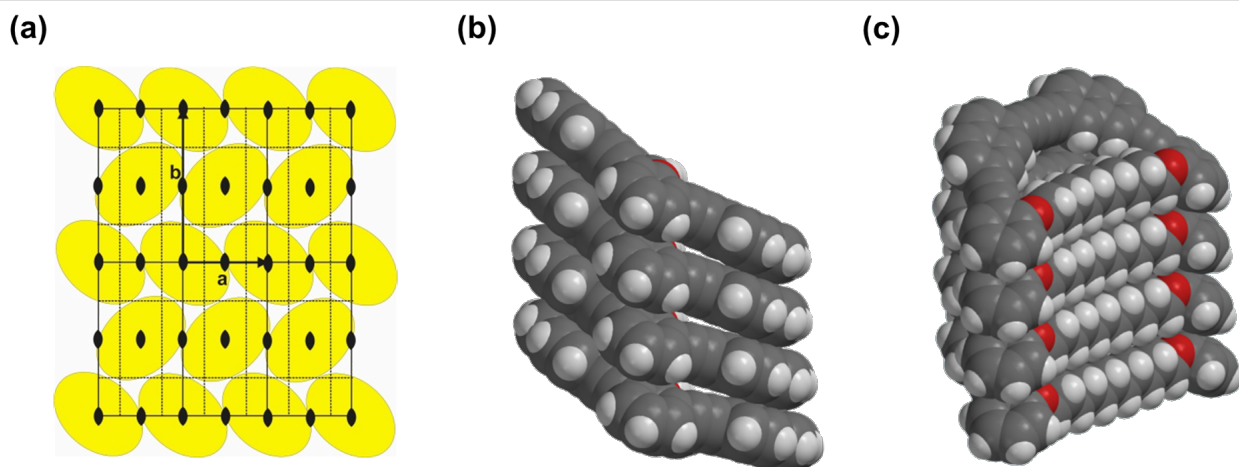
Figure 7: Model of the molecular packing in the columnar mesophase of **1a**: (a) 2D packing scheme for the columns in the liquid crystalline phase (plane group *p2gg*, arbitrary cross section of the columns to fit the symmetry); MMFF calculation (Spartan '08) of a tetramer of the macrocycles; (b) suggested stacking of the macrocycles within one column (side chains omitted for clarity); (c) visualization of the intraannular alkyl chain packing within the columns.

Supporting Information

Supporting Information File 1
Complete experimental details, including ^{1}H and ^{13}C NMR spectra.
[http://www.beilstein-journals.org/bjoc/content/supplementary/1860-5397-10-89-S1.pdf]

Acknowledgments

References

1. Iyoda, M.; Yamakawa, J.; Rahman, M. J. *Angew. Chem., Int. Ed.* **2011,** *50,* 10522–10553. doi:10.1002/anie.201006198

2. Avendaño, C.; Müller, E. A. *Soft Matter* **2011,** *7,* 1694–1701. doi:10.1039/c0sm00905a

3. Zhang, W.; Moore, J. S. *Angew. Chem., Int. Ed.* **2006,** *45,* 4416–4439. doi:10.1002/anie.200503988

4. Höger, S. *Chem.–Eur. J.* **2004,** *10,* 1320–1329. doi:10.1002/chem.200305496

5. Grave, C.; Schlüter, A. D. *Eur. J. Org. Chem.* **2002,** 3075–3098. doi:10.1002/1099-0690(200209)2002:18<3075::AID-EJOC3075>3.0.CO;2-3

6. Haley, M.; Pak, J.; Brand, S. Macrocyclic Oligo(phenylacetylenes) and Oligo(phenyldiacetylenes). In *Carbon Rich Compounds II: Macrocyclic Oligoacetylenes and Other Linearly Conjugated Systems;* de Meijere, A., Ed.; Springer: Berlin/Heidelberg, 1999; Vol. 201, pp 81–130.

7. Tahara, K.; Balandina, T.; Furukawa, S.; De Feyter, S.; Tobe, Y. *CrystEngComm* **2011,** *13,* 5551–5558. doi:10.1039/c1ce05336a

8. Chen, T.; Pan, G.-B.; Wettach, H.; Fritzsche, M.; Höger, S.; Wan, L.-J.; Yang, H.-B.; Northrop, B. H.; Stang, P. J. *J. Am. Chem. Soc.* **2010,** *132,* 1328–1333. doi:10.1021/ja907220f

9. Mena-Osteritz, E.; Bäuerle, P. *Adv. Mater.* **2006,** *18,* 447–451. doi:10.1002/adma.200501575

10. Pan, G.-B.; Cheng, X.-H.; Höger, S.; Freyland, W. *J. Am. Chem. Soc.* **2006,** *128,* 4218–4219. doi:10.1021/ja060469f

11. Vollmeyer, J.; Jester, S.-S.; Eberhagen, F.; Prangenberg, T.; Mader, W.; Höger, S. *Chem. Commun.* **2012,** *48,* 6547–6549. doi:10.1039/c2cc32804f

12. Wettach, H.; Höger, S.; Chaudhuri, D.; Lupton, J. M.; Liu, F.; Lupton, E. M.; Tretiak, S.; Wang, G.; Li, M.; De Feyter, S.; Fischer, S.; Förster, S. *J. Mater. Chem.* **2011,** *21,* 1404–1415. doi:10.1039/c0jm02150d

13. Cantin, K.; Rondeau-Gagné, S.; Néabo, J. R.; Daigle, M.; Morin, J.-F. *Org. Biomol. Chem.* **2011,** *9,* 4440–4443. doi:10.1039/c1ob05441d

14. Nakagaki, T.; Harano, A.; Fuchigami, Y.; Tanaka, E.; Kidoaki, S.; Okuda, T.; Iwanaga, T.; Goto, K.; Shinmyozu, T. *Angew. Chem., Int. Ed.* **2010,** *49,* 9676–9679. doi:10.1002/anie.201004992

15. Fritzsche, M.; Jester, S.-S.; Höger, S.; Klaus, C.; Dingenouts, N.; Linder, P.; Drechsler, M.; Rosenfeldt, S. *Macromolecules* **2010,** *43,* 8379–8388. doi:10.1021/ma1016242

16. Che, Y.; Yang, X.; Zhang, Z.; Zuo, J.; Moore, J. S.; Zang, L. *Chem. Commun.* **2010,** *46,* 4127–4129. doi:10.1039/c0cc00823k

17. Balakrishnan, K.; Datar, A.; Zhang, W.; Yang, X.; Naddo, T.; Huang, J.; Zuo, J.; Yen, M.; Moore, J. S.; Zang, L. *J. Am. Chem. Soc.* **2006,** *128,* 6576–6577. doi:10.1021/ja0618550

18. Rosselli, S.; Ramminger, A.-D.; Wagner, T.; Silier, B.; Wiegand, S.; Häußler, W.; Lieser, G.; Scheumann, V.; Höger, S. *Angew. Chem., Int. Ed.* **2001,** *40,* 3137–3141. doi:10.1002/1521-3773(20010903)40:17<3137::AID-ANIE3137>3.0.CO;2-#

19. Höger, S.; Bonrad, K.; Mourran, A.; Beginn, U.; Möller, M. *J. Am. Chem. Soc.* **2001,** *123,* 5651–5659. doi:10.1021/ja003990x

20. Moore, J. S. *Acc. Chem. Res.* **1997,** *30,* 402–413. doi:10.1021/ar950232g

21. Tobe, Y.; Utsumi, N.; Kawabata, K.; Naemura, K. *Tetrahedron Lett.* **1996,** *37,* 9325–9328. doi:10.1016/S0040-4039(97)82954-1

22. Zhang, J.; Moore, J. S. *J. Am. Chem. Soc.* **1992,** *114,* 9701–9702. doi:10.1021/ja00050a083

23. Jin, Y.; Zhang, A.; Huang, Y.; Zhang, W. *Chem. Commun.* **2010,** *46,* 8258–8260. doi:10.1039/c0cc02941f

24. Kim, J.-K.; Lee, E.; Lee, M. *Macromol. Rapid Commun.* **2010,** *31,* 980–985. doi:10.1002/marc.200900879

25. Seo, S. H.; Chang, J. Y.; Tew, G. N. *Angew. Chem., Int. Ed.* **2006,** *45,* 7526–7530. doi:10.1002/anie.200600688

26. Xu, Y.; Smith, M. D.; Geer, M. F.; Pellechia, P. J.; Brown, J. C.; Wibowo, A. C.; Shimizu, L. S. *J. Am. Chem. Soc.* **2010,** *132,* 5334–5335. doi:10.1021/ja9107066

27. Höger, S.; Enkelmann, V. *Angew. Chem., Int. Ed. Engl.* **1996,** *34,* 2713–2716. doi:10.1002/anie.199527131

28. Höger, S.; Morrison, D. L.; Enkelmann, V. *J. Am. Chem. Soc.* **2002,** *124,* 6734–6736. doi:10.1021/ja017628+

29. Bushby, R. J.; Kawata, K. *Liq. Cryst.* **2011,** *38,* 1415–1426. doi:10.1080/02678292.2011.603262

30. Bisoyi, H. K.; Kumar, S. *Chem. Soc. Rev.* **2010,** *39,* 264–285. doi:10.1039/b901792p

31. Shimura, H.; Yoshio, M.; Kato, T. *Org. Biomol. Chem.* **2009,** *7,* 3205–3207. doi:10.1039/b908669b

32. Seo, S. H.; Jones, T. V.; Seyler, H.; Peters, J. O.; Kim, T. H.; Chang, J. Y.; Tew, G. N. *J. Am. Chem. Soc.* **2006,** *128,* 9264–9265. doi:10.1021/ja060354b

33. Kumar, S. *Chem. Soc. Rev.* **2006,** *35,* 83–109. doi:10.1039/b506619k

34. Bushby, R. J.; Lozman, O. R. *Curr. Opin. Colloid Interface Sci.* **2002,** *7,* 343–354. doi:10.1016/S1359-0294(02)00085-7

35. Zhang, J.; Moore, J. S. *J. Am. Chem. Soc.* **1994,** *116,* 2655–2656. doi:10.1021/ja00085a070

36. Fritzsche, M.; Bohle, A.; Dudenko, D.; Baumeister, U.; Sebastiani, D.; Richardt, G.; Spiess, H. W.; Hansen, M. R.; Höger, S. *Angew. Chem., Int. Ed.* **2011,** *50,* 3030–3033. doi:10.1002/anie.201007437

37. Naddo, T.; Che, Y.; Zhang, W.; Balakrishnan, K.; Yang, X.; Yen, M.; Zhao, J.; Moore, J. S.; Zang, L. *J. Am. Chem. Soc.* **2007,** *129,* 6978–6979. doi:10.1021/ja070747q

38. Laschat, S.; Baro, A.; Steinke, N.; Giesselmann, F.; Hägele, C.; Scalia, G.; Judele, R.; Kapatsina, E.; Sauer, S.; Schreivogel, A.; Tosoni, M. *Angew. Chem., Int. Ed.* **2007,** *46,* 4832–4887. doi:10.1002/anie.200604203

39. Mindyuk, O. Y.; Stetzer, M. R.; Heiney, P. A.; Nelson, J. C.; Moore, J. S. *Adv. Mater.* **1998,** *10,* 1363–1366. doi:10.1002/(SICI)1521-4095(199811)10:16<1363::AID-ADMA1363>3.0.CO;2-V

40. Fischer, M.; Lieser, G.; Rapp, A.; Schnell, I.; Mamdouh, W.; De Feyter, S.; De Schryver, F. C.; Höger, S. *J. Am. Chem. Soc.* **2004,** *126,* 214–222. doi:10.1021/ja038484x

41. Höger, S.; Cheng, X. H.; Ramminger, A.-D.; Enkelmann, V.; Rapp, A.; Mondeshki, M.; Schnell, I. *Angew. Chem., Int. Ed.* **2005,** *44,* 2801–2805. doi:10.1002/anie.200462319

42. Höger, S.; Enkelmann, V.; Bonrad, K.; Tschierske, C. *Angew. Chem., Int. Ed.* **2000,** *39,* 2267–2270. doi:10.1002/1521-3773(20000703)39:13<2267::AID-ANIE2267>3.0.CO;2-7

43. Li, Q.; Huang, R.; Xiong, S.; Xie, X. *Liq. Cryst.* **2012,** *39,* 249–258. doi:10.1080/02678292.2011.636843

44. Höger, S.; Weber, J.; Leppert, A.; Enkelmann, V. *Beilstein J. Org. Chem.* **2008,** *4,* No. 1. doi:10.1186/1860-5397-4-1

45. Ziegler, A.; Mamdouh, W.; Ver Heyen, A.; Surin, M.; Uji-i, H.; Abdel-Mottaleb, M. M. S.; De Schryver, F. C.; De Feyter, S.; Lazzaroni, R.; Höger, S. *Chem. Mater.* **2005,** *17,* 5670–5683. doi:10.1021/cm051386l

46. Collings, P. J.; Hird, M. *Introduction to Liquid Crystals: Chemistry and Physics;* Taylor & Francis: London, 1997. doi:10.4324/9780203211199

47. Collard, D. M.; Lillya, C. P. *J. Am. Chem. Soc.* **1991,** *113,* 8577–8583. doi:10.1021/ja00023a001

48. Höger, S. *J. Polym. Sci., Part A: Polym. Chem.* **1999,** *37,* 2685–2698. doi:10.1002/(SICI)1099-0518(19990801)37:15<2685::AID-POLA1>3.0.CO;2-S

49. Rucareanu, S.; Schuwey, A.; Gossauer, A. *J. Am. Chem. Soc.* **2006,** *128,* 3396–3413. doi:10.1021/ja057117d

50. McCallien, D. W. J.; Sanders, J. K. M. *J. Am. Chem. Soc.* **1995,** *117,* 6611–6612. doi:10.1021/ja00129a033

51. Höger, S.; Meckenstock, A.-D. *Chem.–Eur. J.* **1999,** *5,* 1686–1691. doi:10.1002/(SICI)1521-3765(19990604)5:6<1686::AID-CHEM1686>3.0.CO;2-0

52. Pisula, W.; Feng, X.; Müllen, K. *Adv. Mater.* **2010,** *22,* 3634–3649. doi:10.1002/adma.201000585

53. Kumar, S. *Chemistry of Discotic Liquid Crystals: From Monomers to Polymers;* CRC Press: Boca Raton, 2010. doi:10.1201/b10457

54. Kohne, B.; Praefcke, K. *Chem.-Ztg.* **1985,** *109,* 121–127.

55. Gnanou, Y.; Fontanille, M. *Organic and Physical Chemistry of Polymers;* John Wiley & Sons: Hoboken, New Jersey, 2008; Vol. 1. doi:10.1002/9780470238127

56. Kouwer, P. H. J.; Jager, W. F.; Mijs, W. J.; Picken, S. J. *Macromolecules* **2000,** *33,* 4336–4342. doi:10.1021/ma991808a

57. Kouwer, P. H. J.; Jager, W. F.; Mijs, W. J.; Picken, S. J. *Macromolecules* **2001,** *34,* 7582–7584. doi:10.1021/ma011007j

58. Tschierske, C.; Photinos, D. J. *J. Mater. Chem.* **2010,** *20,* 4263–4294. doi:10.1039/b924810b

59. Cestari, M.; Diez-Berart, S.; Dunmur, D. A.; Ferrarini, A.; de la Fuente, M. R.; Jackson, D. J. B.; Lopez, D. O.; Luckhurst, G. R.; Perez-Jubindo, M. A.; Richardson, R. M.; Salud, J.; Timimi, B. A.; Zimmermann, H. *Phys. Rev. E* **2011,** *84,* 031704. doi:10.1103/PhysRevE.84.031704

60. Chen, D.; Nakata, M.; Shao, R.; Tuchband, M. R.; Shuai, M.; Baumeister, U.; Weissflog, W.; Walba, D. M.; Glaser, M. A.; MacLennan, J. E.; Clark, N. A. *Phys. Rev. E* **2014,** *89,* 022506. doi:10.1103/PhysRevE.89.022506

Substitution effect and effect of axle's flexibility at (pseudo-)rotaxanes

Friedrich Malberg, Jan Gerit Brandenburg, Werner Reckien, Oldamur Hollóczki, Stefan Grimme[*] and Barbara Kirchner[*]

Abstract

This study investigates the effect of substitution with different functional groups and of molecular flexibility by changing within the axle from a single C–C bond to a double C=C bond. Therefore, we present static quantum chemical calculations at the dispersion-corrected density functional level (DFT-D3) for several Leigh-type rotaxanes. The calculated crystal structure is in close agreement with the experimental X-ray data. Compared to a stiffer axle, a more flexible one results in a stronger binding by 1–3 kcal/mol. Alterations of the binding energy in the range of 5 kcal/mol could be achieved by substitution with different functional groups. The hydrogen bond geometry between the isophtalic unit and the carbonyl oxygen atoms of the axle exhibited distances in the range of 2.1 to 2.4 Å for six contact points, which shows that not solely but to a large amount the circumstances in the investigated rotaxanes are governed by hydrogen bonding. Moreover, the complex with the more flexible axle is usually more unsymmetrical than the one with the stiff axle. The opposite is observed for the experimentally investigated axle with the four phenyl stoppers. Furthermore, we considered an implicit continuum solvation model and found that the complex binding is weakened by approximately 10 kcal/mol, and hydrogen bonds are slightly shortened (by up to 0.2 Å).

Introduction

Rotaxanes are prototypes for molecular machines and molecular switches [1-3]. They are mechanically interlocked molecules consisting of a macrocycle, called "wheel", threaded on a linear chain, termed "axle", see Figure 1 for examples. Typically, the axle has at least one recognition site – often hydrogen bond donors or acceptors [4,5] – for the wheel, because most rotaxanes are obtained from template synthesis [6,7]. Bulky stopper groups at the ends of the axle prevent the wheels from dethreading. Rotaxanes without their stopper groups are often referred to as pseudorotaxanes. It is implicitly assumed that

these stopper functionalities have no further influence on the electronic structure of the axle, hence neither on the axle–wheel interaction.

Applications of rotaxanes are many-fold, for example there is an interest in understanding the motions carried out by both entities with respect to each other. This can lead to molecular machines via pirouetting [8], or molecular shuttles [9,10] via shifting the axle back and forth within the wheel. The Stoddart group synthesized the first rotaxane-based molecular shuttle in 1991 [11]. It consisted of a tetracationic wheel, which was able to move back and forth between two identical hydroquinol stations. These symmetrically surrounded a polyether axle, which was terminated at the ends by large triisopropylsilyl stoppers [11]. Other rotaxane systems were also studied. For instance, Leigh and coworkers synthesized several rotaxane shuttles in the last years [12]. Many of these rotaxanes are based on a benzylic amide macrocycle with isophtalamide units building up twofold hydrogen bonds to an acceptor axle. The Schalley group often used a similar hydrogen bond motif for the design of molecular shuttles with the Vögtle–Hunter tetralactam macrocycle next to several other combinations [13-15]. Fernandes et al. recently published a further interesting application of rotaxanes [16,17]. The axle consisted of a peptide, which can be released from the wheel by the according reaction, thus allowing the rotaxane to function as a high-precision delivery system. The authors introduced a system, which – in contrast to the first generation of these kinds of rotaxanes – showed water solubility and contained appropriate locations for substitutions in order to improve its properties [16].

Theoretical investigations on rotaxanes accompanied or even preceded experimental work frequently, thus showing that theory offers many viable tools for the understanding and the development of rotaxanes. Zerbetto et al. showed that the shuttling motion can be separated from the other degrees of freedom, and that the effective coordinate of the motion can be described as a double-minimum potential [18]. The co-conformer stability for rotaxane based molecular shuttles was investigated by means of molecular modeling [19]. The Peyerimhoff group has carried out an in depth study of the rotaxane formation [20]. A later study investigated the shuttling motion of the wheel as a one-dimensional translation, together with the influence of the Kohn–Sham frontier orbitals of wheel and axle upon conductivity and electron tunneling along the rotaxane [21]. A quantum chemical shuttling motion study of rotaxane-based molecular switching devices has revealed how the modification of the redox states of both entities results in changes of the computational energy profile [22]. The formation of α-cyclodextrin-based [3]pseudorotaxanes in the gas phase was studied by means of density functional

calculations [23]. Molecular mechanics calculations were used for a free energy calculation of an α-cyclodextrin rotaxane system and for the investigation of low-barrier molecular rotary motors with rotaxane architecture [24]. The co-conformational selectivity of two dibenzo-24-crown-8 macrocycles to ammonia binding sites in a [3]rotaxane [25], and the hydrogen bonding strength in polymeric urethane rotaxanes in a mean-field model [26] were investigated by semiempirical methods.

In our groups, we investigated the main binding motif for rotaxane systems of the Vögtle [27-30], Schalley- [29-31], and Leigh-type [27]. We performed an energetic and vibrational analysis for the twofold hydrogen bonds in order to understand the binding pattern [28]. A close relationship between the strength of the hydrogen bond and the charge of the acceptor oxygen was detected [32]. Substitution with electron-withdrawing groups weakens the twofold hydrogen bond, whereas substitution with electron-donating groups led to an increase of interaction energy. In the vibrational spectra, the red shift for both the C=O stretching mode and the N–H stretching mode was correlated to the binding energies of the hydrogen bonds [27]. Compared with single hydrogen bonds, the twofold hydrogen bonds showed shorter red shifts for the N–H stretch modes but larger red shifts for the C=O stretch mode [27]. Different density functionals, including one functional with an empirical correction for dispersion interaction, for the treatment of such rotaxane complexes were studied. We compared these density functional theory (DFT) results with Møller–Plesset second-order perturbation theory (MP2) calculations [29]. The contribution of the London dispersion interaction to the total interaction energy in the gas phase is of the same magnitude as the hydrogen bonding interaction (about −14 kcal/mol).

The molecular functionality of rotaxanes is solely based on the interplay of different non-covalent interactions between the axle and the wheel. Therefore, the understanding of these (mostly) attractive forces is crucial for the development of the field. Also, by understanding how one can modify or even tune the axle–wheel interplay, rotaxanes for different purposes can be designed enhancing the applicability of such materials. This study aims to understand rotaxanes with respect to its non-covalent interactions on the molecular level and to contribute to a more rational design of new molecular machines. Therefore, we investigated the energetics by substitution the rotaxanes with different functional groups and by changing the degree of molecular flexibility.

Computational methodologies

The structures of all compounds were fully optimized without any symmetry constraints. Density functional theory (DFT)

with the gradient-corrected meta-functional TPSS combined with the resolution of identity technique (RI) and the def2-TZVP basis set were applied [33,34] together with the dispersion correction D3 [35,36]. This level of theory is abbreviated as TPSS-D3/def2-TZVP. All molecular calculations were performed by using the TURBOMOLE 6.4 program package [33]. The convergence criterion for the geometry optimization was set to 10^{-4} atomic units for the norm of the Cartesian gradient. The SCF-convergence was set to 10^{-6} atomic units.

The adiabatic complex interaction energies ΔE^{int} were calculated according to the supramolecular approach by subtracting the energies of the relaxed monomers $E_{\text{guest}}^{\text{relax}}$, $E_{\text{wheel}}^{\text{relax}}$ from the total complex energy E^{tot} [37,38].

$$\Delta E^{\text{int}} = E^{\text{tot}} - E_{\text{wheel}}^{\text{relax}} - E_{\text{guest}}^{\text{relax}} \qquad (1)$$

Interaction energies were counterpoise-corrected by the procedure introduced by Boys and Bernardi. The basis set superposition error (BSSE) does not exceed 3 kcal/mol (about 5% of ΔE^{int}) for any of the complexes calculated. In order to confirm the nature of the stationary point obtained, we performed an analytical frequency analysis with the aoforce module [39-41] resulting in only positive values for the minima. As a first approximation to solvation, we applied the conductor-like screening model (COSMO) [42]. This a continuum solvation model, where the solute molecule forms a cavity within the dielectric continuum of permittivity ε that represents the solvent, and which neglects the cavitation and the solute–solvent dispersion term. For ε we chose 4.806 which is the value of chloroform. The distance of solvents to van der Waals radii of the atom (standard values were chosen here) was set to 1.3 Å. The Hammett parameters are taken from [43].

Computational details for periodic calculation

The periodic calculations were carried out with the Vienna ab-initio simulation package VASP 5.3 [44,45]. We utilized the GGA functional PBE [46] in combination with a projector-augmented plane wave basis set (PAW) [47,48] with energy cutoff of 1000 eV. The Brillouin zone was sampled with a Γ-centered $2 \times 1 \times 1$ k-mesh. The crystal was fully optimized (including cell parameters) until all forces were below 0.005 eV/Å. The PBE functional was corrected for missing non-local correlation interactions through the atom-pairwise London dispersion correction D3 in the Becke–Johnson damping scheme [35,36]. A single (isolated) dimer was optimized with the same technical setup in a large unit cell with minimum intermolecular atom-atom distance of 16 Å. This method combination provides reliable results for both the gas phase and

the solid state as shown in a number of publications by us [49-51] and other groups [45,52].

Structures under study

The hereby considered pseuodorotaxanes (Figure 1) consist of an amide axle inside the cavity of a macrocycle, which contains two isophtalamide units. One kind of the investigated axles is a fumaramide derivative with a C=C double bond and two connected amide groups (labeled as Leigh-type-DB, **DB** throughout the article) [2,53], and the other kind is a succinic amide derivative with a C–C single bond, and two connected amide groups (labeled as Leigh-type-SB, **SB** throughout the article) [2,53]. Due to the aforementioned structure of the wheel and the axle, and since the wheel-O=C···NH-axle type interplay is prohibited by the substitution of the corresponding hydrogen atoms by either a methyl group (Figure 1 top) or a benzyl group (Figure 1 bottom), only four hydrogen bonds can be formed between the subunits through wheel–NH···O=C-axle interactions. At the two different axles with single and double bond, the phenyl groups of the axle will be substituted symmetrically in order to investigate the substitution effect. Moreover, the influence of the flexibility of the axle, see Figure 1 upper part, will be investigated. The rotaxanes with di-phenyl groups are analyzed in order to allow comparison to experimental data.

Results and Discussion
Crystal structure

The fully optimized crystal structure agrees very well with the experimental X-ray structure, see Table 1. The unit cell volume (Vol) is smaller than the experimental value by only 1.7%. Typical thermal cell expansions (from calculated 0 K to measured 100 K) are 2–3%. A recent study showed that PBE-D3 (with a large basis set) overestimates molecular sizes by approximately 1% [54]. Therefore, the calculated cell volume is in a reasonable agreement with the experimental value when thermal expansion effects are considered in the comparison. The optimization is performed without symmetry constraints, and the correct space group (monoclinic) is reproduced, i.e., all cell angles differ by less than 0.3° from the X-ray structure.

Because the molecular structure is rather flexible, we observe interesting crystal packing effects. We compared the highlighted intramolecular distances and angles from experiment and theory in Figure 2. As a result, we exemplified the influence of non-covalent interactions. The distances R_1, R_2, and R_3 are significantly smaller in the crystal compared to the gas phase structure. The torsion angles φ_1 and φ_2 describe the relative tilting between the flexible phenyl rings, which differs by more than 10° between crystal and gas phase. All these geometrical data are very well reproduced by the PBE-D3/1000 eV calculations, see third column in Table 1. However, the gas
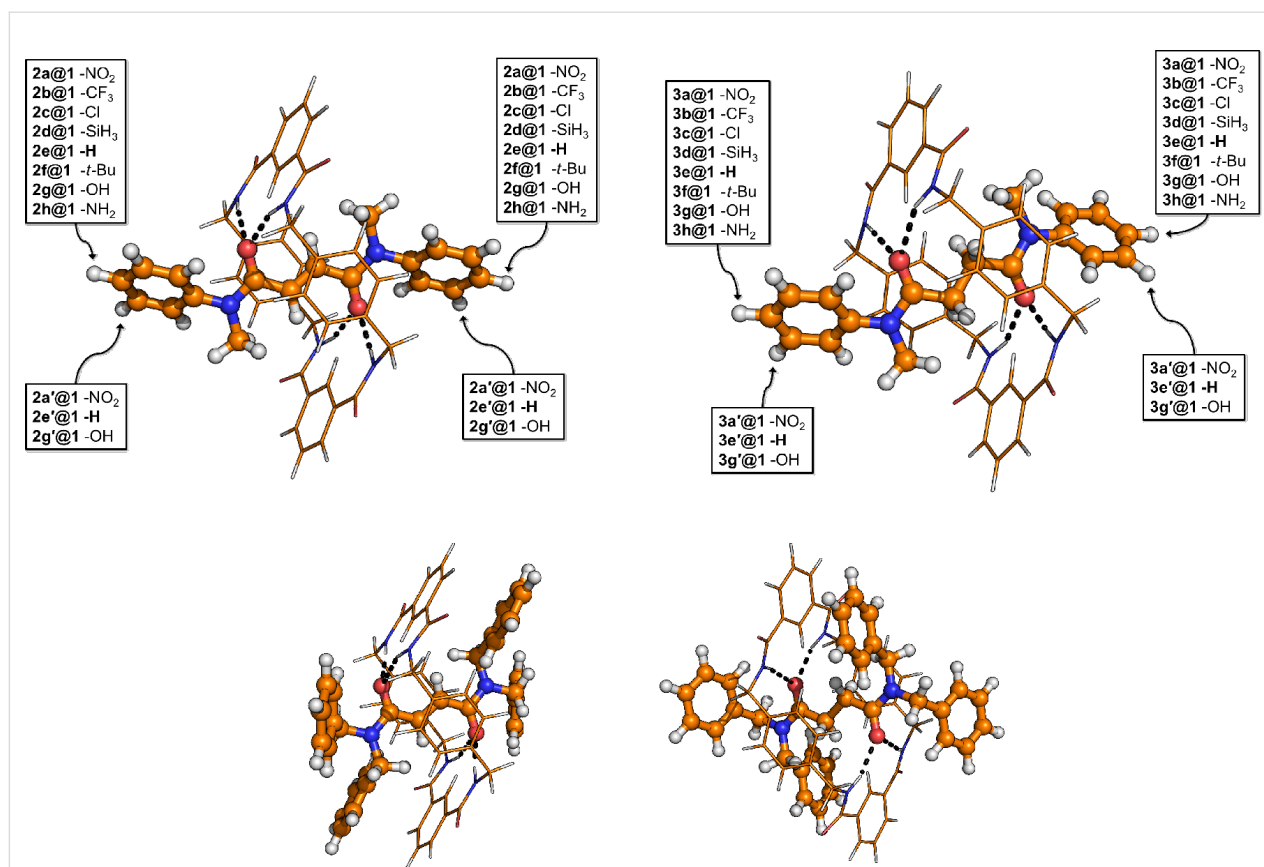
Figure 1: Chemical structure of the investigated systems. Left: Double bond within the axle; Right: Single bond within the axle. Red marks oxygen atoms, blue nitrogen atoms, orange carbon atom and hydrogen atoms are given in white. The labeling according to the substitution is given in bold letters. Structures below will be denoted **4@1** (left) and **5@1** (right).

Table 1: Comparison of the X-ray structure of the rotaxane with the computed crystal and gas phase geometries. The structures are optimized at the PBE-D3/1000 eV level (TPSS-D3 with the def2-TZVP basis). The first block shows the cell parameters describing the intermolecular packing, whereas the second block highlights some intramolecular distances and angles (compare with Figure 2). Distances in parentheses denote the corresponding length to the heavy (non-hydrogen) atom.

| | Reference | Crystal | Gas phase | |
	X-ray	PBE-D3	PBE-D3	TPSS-D3
a /Å	9.79	9.69	—	—
b /Å	16.16	16.16	—	—
c /Å	16.87	16.78	—	—
β /°	105.0	105.3	—	—
Vol /Å^3	2579	2535	—	—
R_1 /Å	2.01(2.98)	1.97(2.97)	2.11(3.10)	2.11(3.10)
R_2 /Å	2.24(3.16)	2.11(3.11)	2.30(3.28)	2.35(3.31)
R_3 /Å	2.31(3.13)	2.19(3.09)	2.25(3.28)	2.28(3.30)
R_4 /Å	8.24	8.19	9.25	9.11
φ_1 /°	−1.7	−1.2	−4.0	−2.2
φ_2 /°	5.16	4.4	−9.7	−7.0

phase calculations (5th and 6th column in Table 1) show that one has to be careful when comparing calculated gas phase structures with measured crystal geometries.
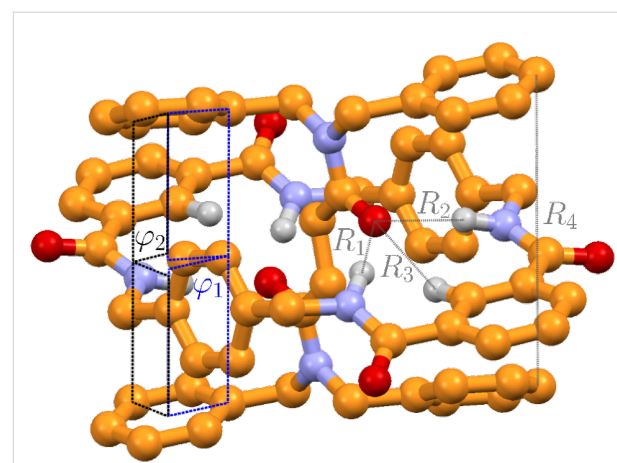
Figure 2: Molecular geometry of one rotaxane optimized in periodic boundaries at the PBE-D3/1000 eV level. Hydrogen atoms are omitted for clarity. Some intramolecular distances and angles are highlighted.

The calculated lattice energy (for one rotaxane, excluding phonon contributions) of 77.7 kcal/mol is quite large but in a reasonable range for a molecule of this size. Recent benchmark studies showed that lattice energies on the PBE-D3/1000 eV level deviate by less than 9% from (thermal back-corrected) experimental sublimation energies [55]. The excellent agreement of the utilized theoretical method with the X-ray experiment justifies its application in the following sections. Mostly for technical reasons we have chosen PBE-D3 in the solid state calculations but TPSS-D3 in the molecular treatments. According to many benchmark calculations (see, e.g., [49,51,56]), both functionals perform very similar for non-covalent interaction (TPSS-D3 being even somewhat better for hydrogen bonding), which supports the above conclusion.

Substitution effect

The interaction energies in Table 2 show that the more flexible axle (**SB**) binds stronger to the wheel than the less flexible ethylene-containing axle (**DB**) for all pseudorotaxanes studied. The difference between the substituted **DB** and **SB** amounts to 1–3 kcal/mol. Substituents with −M/−I effect bind more weakly than those with +M/+I effect, which fits neatly to the fact that the axle in this investigated system accepts the hydrogen bond and therefore prefers electrons to be shifted towards the functional group. Interestingly, the substitution effects seem to be almost additive, i.e., for both the **SB** and the **DB** structure changes in the energy range of 5 kcal/mol can be obtained with the appropriate functional group, compare for example **2a@1** to **2h@1** and **3a@1** to **3h@1**.

A qualitative insight of the varying binding situation can be gained from the electrostatic potential shown for six rotaxanes in Figure 3. The electron withdrawing groups reduce the hydrogen bond accepting character of the oxygen atoms (see reduced red color and increase in blue color of **2a@1** in Figure 3 compared to **2e@1**), the π-electron donating groups, on the other hand, increase the hydrogen bond accepting character (see more pronounced red areas and less pronounced blue color of **2f@1** in Figure 3 compared to **2e@1**).

In order to understand the origin of the different binding energies, we consider the most direct interaction between axle and wheel, namely the hydrogen bond accepted by the axle and donated from the wheel, as possible influence. Since the wheel and the axle are symmetric, and there are two recognition sites between axle and wheel, the latter sites strongly resemble each other in geometrical parameters. Thus, we only consider one binding site (isophtalic unit) with its hydrogen bonds. Note, that the hydrogen bond in the **DB** systems are more symmetrical than in **SB** systems. As the choice of the binding site is sort of arbitrary, we always choose the one with the shortest N–H···O distance. The full data can be found in the Supporting Information File 1.

The hydrogen bonds listed in Table 3 fall in the range of 2.1 to 2.4 Å, and their angles range from 150 to 180 degrees. The hydrogen bonds are only roughly correlated to the strength of the interaction between axle and wheel, i.e., the variations within different substitutions are too small to discuss them within the error of the method. However, a general shortening of the hydrogen bonds with increasing energies is visible, compare **2a@1**, **2e@1** and **2h@1**. Moreover, there are more symmetrical hydrogen bonding situations in the middle of the listed data in Table 3 (e.g., **2e@1**). Furthermore, there is a

Table 2: Interaction energies E_{int} for the different pseudorotaxane systems, labeling see Figure 1. The first two columns list the substituents succeeded by their effects (mesomeric or inductive). The last line gives the values for the di-phenyl structures. In the last column, the Hammett-parameters are given.

			E_{int} kcal/mol		E_{int} kcal/mol	σ
−I, −M	*p*-NO$_2$	**2a@1**	−41.2	**3a@1**	−43.1	0.78
−I	*p*-CF$_3$	**2b@1**	−42.4	**3b@1**	−44.9	0.54
−I,(+M)	*p*-Cl	**2c@1**	−43.0	**3c@1**	−45.4	0.23
+I,(−M)	*p*-SiH$_3$	**2d@1**	−44.1	**3d@1**	−45.9	0.10
—	*p*-H	**2e@1**	−44.7	**3e@1**	−46.5	0.00
+I	*p*-*t*-Bu	**2f@1**	−44.9	**3f@1**	−47.6	−0.20
−I, +M	*p*-OH	**2g@1**	−45.7	**3g@1**	−46.8	−0.37
−I, +M	*p*-NH$_2$	**2h@1**	−46.5	**3h@1**	−48.4	−0.66
−I, −M	*m*-NO$_2$	**2a'@1**	−43.7	**3a'@1**	−45.5	0.71
−I, +M	*m*-OH	**2g'@1**	−45.1	**3g'@1**	−47.5	0.12
	p-2Ph	**4@1**	−56.1	**5@1**	−58.7	—
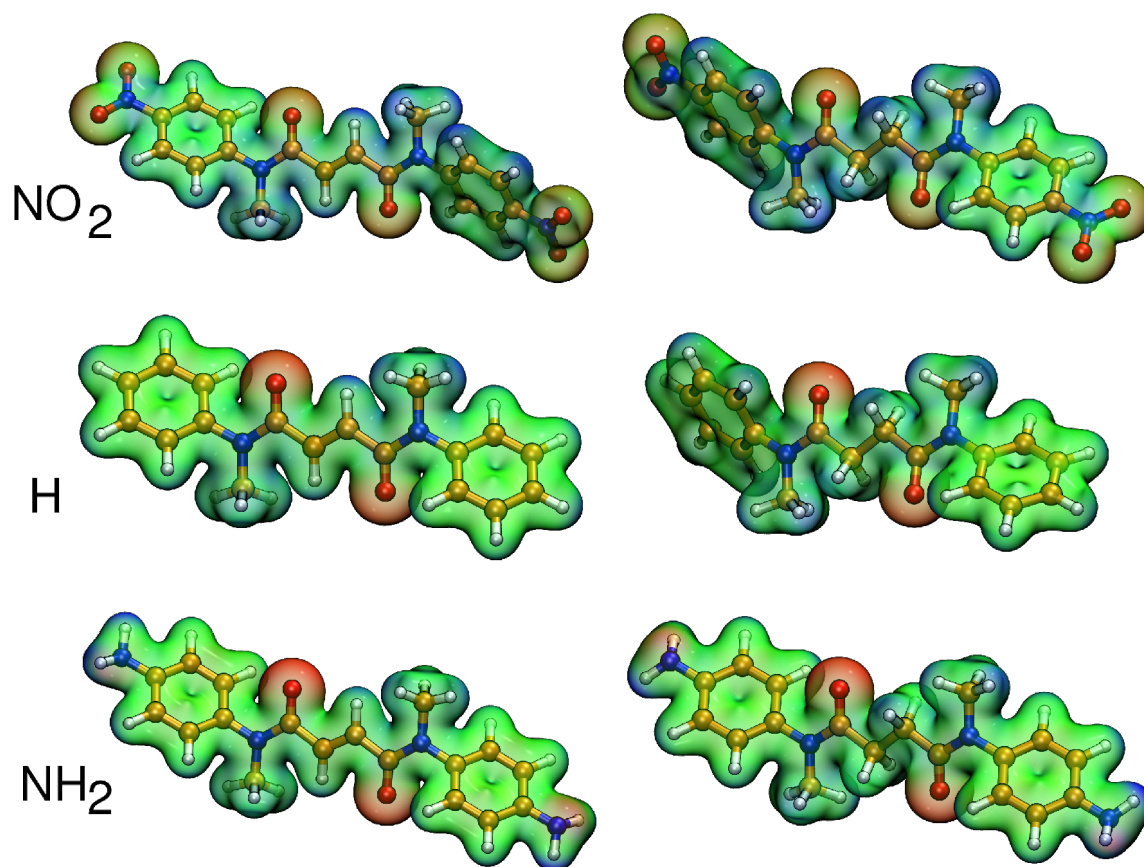
Figure 3: Electrostatic potential for the complexes **2a@1** (top left), **2e@1** (middle left), **2h@1** (lower left) and **3a@1** (top right), **3e@1** (middle right), **3h@1** (lower right).

Table 3: Hydrogen bond distances in Å for the different pseudorotaxane systems, for labeling see Figure 2. The second and third last lines show the substitution at the meta-position.

		R_1	R_2	R_3		R_1	R_2	R_3
p-NO$_2$	**2a@1**	2.24	2.40	2.29	**3a@1**	2.18	2.42	2.26
p-CF$_3$	**2b@1**	2.21	2.38	2.27	**3b@1**	2.16	2.43	2.24
p-Cl	**2c@1**	2.23	2.29	2.26	**3c@1**	2.15	2.35	2.22
p-SiH$_3$	**2d@1**	2.17	2.35	2.22	**3d@1**	2.15	2.34	2.21
p-H	**2e@1**	2.21	2.22	2.20	**3e@1**	2.14	2.33	2.20
p-*t*-Bu	**2f@1**	2.21	2.27	2.24	**3f@1**	2.11	2.39	2.20
p-OH	**2g@1**	2.08	2.18	2.34	**3g@1**	2.14	2.30	2.19
p-NH$_2$	**2h@1**	2.15	2.22	2.17	**3h@1**	2.11	2.34	2.18
m-NO$_2$	**2a'@1**	2.23	2.44	2.32	**3a'@1**	2.14	2.63	2.31
m-OH	**2g'@1**	2.26	2.22	2.22	**3g'@1**	2.13	2.38	2.22
p-2Ph	**4@1**	2.04	2.50	2.27	**5@1**	2.11	2.35	2.28

significant difference (0.1–0.2 Å) between **SB** and **DB**. Considering these two(three)-fold hydrogen bonds, **SB** is less symmetric indicated by the shorter short N–H···O bond and the longer long N–H···O bond compared to **DB**. The di-phenyl rotaxanes exhibit the opposite trend, the shortest and longest hydrogen bond is given in **4@1**. The given energy trend is

maintained, the longest N–H⋯O bond in **4@1** is much longer (2.5 Å) than other long N–H⋯O bonds. This also shows the importance of such stopper groups for the interactions within the rotaxanes, as they have notable electronic influence. Thus, their role is not necessarily restricted to the mere mechanical prevention of a dethreading of the axle, which was also witnessed for diketopiperazine-based amide rotaxanes [57].

In Table 2, also the Hammett σ parameters are given. These substituent parameters [43] are the difference of the pK_a values of substituted and non-substituted benzoic acids, they can be correlated with the interaction energies resulting in good correlation coefficients of 0.9880 (**DB**) and 0.9596 (**SB**) if only the para-positions are considered, see Figure 4. This fitted linear regression curve are as follows:

$$\textbf{DB}: \; y = 3.7075 \text{ kcal/mol} \cdot \sigma - 44.255 \text{ kcal/mol} \quad (2)$$

$$\textbf{SB}: \; y = 3.3739 \text{ kcal/mol} \cdot \sigma - 46.25 \text{ kcal/mol} \quad (3)$$

Equation 2 and Equation 3 can be used to estimate the contributions of different substituents given the σ-values are provided.
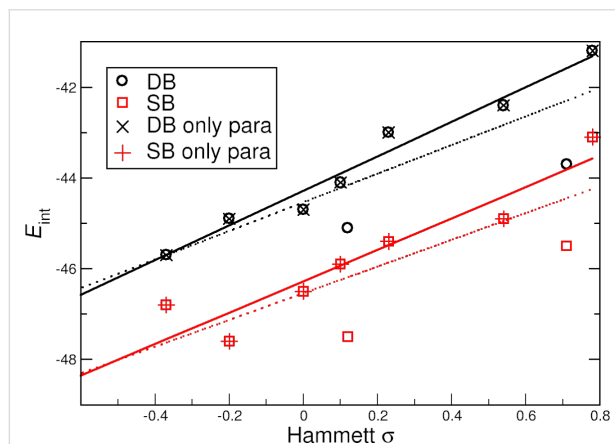
Figure 4: Interaction energies plotted against the Hammett σ parameters. The values are given in Table 1. Black curves: **DB** and red curves: **SB**. The solid lines are fits to all energies of the para-substitution only, the dotted lines are linear regressions to all interaction energies.

Solvent effects

As expected, the presence of the solvent decreases the binding energy by 11–14 kcal/mol, see Table 4. Even though the trends in the difference between single and double bond binding energy is constantly 1–4 kcal/mol. By comparison of the total energies of the complex, separated wheel, and axle, this can be assigned to the stabilization of the complex and wheel by approximately 20 kcal/mol, whereas the axle is only stabilized by 10 kcal/mol.

Table 4: Interaction energies E_{int} for the different pseudorotaxane systems applying a solvent model, labeling see Figure 1. The first two columns list the substituents succeeded by their effects (mesomeric or inductive) as in Table 2.

			E_{int} kcal/mol		E_{int} kcal/mol
−I, −M	*p*-NO$_2$	**2a@1**	−29.6	**3a@1**	−31.0
—	*p*-H	**2e@1**	−32.4	**3e@1**	−33.8
−I, +M	*p*-NH$_2$	**2h@1**	−33.7	**3h@1**	−35.1
	p-2Ph	**4@1**	−42.1	**5@1**	−45.6

In the following, we focus on the hydrogen bonded systems and repeat the previously described distances (Table 3) for the corresponding solvated systems in Table 5. Again the distances roughly follow the trend that with increasing binding energy the distances are shorter.

The hydrogen bonding situation in the complexes with single bond is still less symmetrical, but the shorter N-H⋯O bond for the solvated is not shorter than in the **DB** complexes. Typically, the distances in the solvated complexes are shorter up to 0.16 Å compared to the unsolvated systems. Considering the reduced binding energies, this is unusual. Comparing different intra- and intermolecular bonds, it appears that this arrangement of shorter and thus stronger hydrogen bonds stems from a more bowed axle with respect to the wheel.

Conclusion

We investigated several rotaxanes by static quantum chemical calculations in order to gain insight into the interplay of

Table 5: Hydrogen bond geometry in Å for the different pseudorotaxane systems with solvent model, labeling see Figure 2. The second and third last lines show the substitution at the meta-position.

		R_1	R_2	R_3		R_1	R_2	R_3
p-NO$_2$	**2a@1**	2.19	2.41	2.30	**3a@1**	2.12	2.47	2.27
p-H	**2e@1**	2.11	2.16	2.16	**3e@1**	2.12	2.28	2.19
p-NH$_2$	**2h@1**	2.08	2.14	2.13	**3h@1**	2.09	2.18	2.14
p-2Ph	**4@1**	2.02	2.43	2.20	**5@1**	2.07	2.27	2.23

different non-covalent interactions. Therefore, we studied the substitution of the rotaxanes with different functional groups and the degree of molecular flexibility by changing within the axle from a single C–C bond to a double C=C bond. In order to assess the methodology used, we calculated the crystal structure and found a very good agreement with the experiment. For instance, deviations of the unit cell volume were less than 2%. However, care has to be taken when comparing results calculated in the gas phase with those obtained in the condensed phase due to non-local crystal packing effects.

The computed DFT-D3 formation energies of the non-covalently bound rotaxanes in the gas phase range from about −41 to −58 kcal/mol which is typical for supramolecular complexes of this size [50]. For the investigated modified axles, we found that – as expected – a more flexible axle binds stronger than the stiffer axle. Exchanging a double with a single bond leads to an increase of absolute value in binding energy of 1–3 kcal/mol. Alterations of the binding energy in the range of 5 kcal/mol could be achieved for substitution with different functional groups. Thus, it is possible to modulate the rotaxane binding by changing different chemical parts in the region of 1–5 kcal/mol, which should show an influence of the inter-related motion as well. We also investigated the hydrogen bond geometry between the isophtalic unit and the carbonyl oxygen atoms of the axle and found distances in the range of 2.1 to 2.4 Å for 6 contact points. This shows that to a large amount the interactions in the investigated rotaxanes are governed by hydrogen bonding. On the one hand, the single bound complex usually is less symmetric in exhibiting one short and one long N-H⋯O bond than the double bond containing complex. On the other hand, the opposite is observed for the experimentally investigated axle with the four phenyl stoppers. One might assume that the terminal groups play a minor role in the interplay within the rotaxane and serve only to prevent the axle mechanically from dethreading. However, we clearly demonstrated the importance of such rotaxanes parts as the stopper groups also for intramolecular interactions of the rotaxanes.

Considering an implicit solvent model (COSMO), the complex binding is weakened by approximately 10 kcal/mol. This is due to the fact that the individual parts of the rotaxane are differently stabilized in the solvent. Thus, the axle is less stabilized than the wheel and the complex. Interestingly, we observed slightly shortened (for up to 0.2 Å) hydrogen bonds for all investigated systems. This is supported by a more tilted axle in the solvent.

In future, we plan to explicitly study the different motions within such complex systems. The main focus is on the influence of simple chemical differences such as substitution or dealkylation.

Acknowledgements

Supporting Information

Supporting Information File 1
Geometry and structure data.
[http://www.beilstein-journals.org/bjoc/content/
supplementary/1860-5397-10-131-S1.pdf]

References

1. Schalley, C. A., Ed. *Analytical Methods in Supramolecular Chemistry,* 2nd ed.; Wiley-VCH: Weinheim, Germany, 2012.
2. Rijs, A. M.; Crews, B. O.; de Vries, M. S.; Hannam, J. S.; Leigh, D. A.; Fanti, M.; Zerbetto, F.; Buma, W. J. *Angew. Chem., Int. Ed.* **2008,** *47,* 3174–3179. doi:10.1002/anie.200705627
3. Christen, H. F.; Vögtle, F., Eds. *Organische Chemie;* Band III; Otto Salle Verlag: Frankfurt am Main, 1994.
4. Jäger, R.; Vögtle, F. *Angew. Chem., Int. Ed. Engl.* **1997,** *36,* 930–944. doi:10.1002/anie.199709301
5. Leigh, D. A.; Murphy, A.; Smart, J. P.; Slawin, A. M. Z. *Angew. Chem., Int. Ed. Engl.* **1997,** *36,* 728–732. doi:10.1002/anie.199707281
6. Schalley, C. A.; Weilandt, T.; Brüggemann, J.; Vögtle, F. *Top. Curr. Chem.* **2004,** *248,* 141–200. doi:10.1007/b99913
7. Kay, E. R.; Leigh, D. A.; Zerbetto, F. *Angew. Chem., Int. Ed.* **2006,** *46,* 72–191. doi:10.1002/anie.200504313
8. Hancock, L. M.; Beer, P. D. *Chem. Commun.* **2011,** *47,* 6012–6014. doi:10.1039/c1cc11224d
9. Panman, M. R.; Bodis, P.; Shaw, D. J.; Bakker, B. H.; Newton, A. C.; Kay, E. R.; Leigh, D. A.; Buma, W. J.; Brouwer, A. M.; Woutersen, S. *Phys. Chem. Chem. Phys.* **2012,** *14,* 1865–1875. doi:10.1039/c1cp22146a
10. Barrell, M. J.; Leigh, D. A.; Lusby, P. J.; Slawin, A. M. Z. *Angew. Chem., Int. Ed.* **2008,** *47,* 8036–8039. doi:10.1002/anie.200802745
11. Anelli, P. L.; Spencer, N.; Stoddart, J. F. *J. Am. Chem. Soc.* **1991,** *113,* 5131–5133. doi:10.1021/ja00013a096
12. Baggerman, J.; Haraszkiewicz, N.; Wiering, P. G.; Fioravanti, G.; Marcaccio, M.; Paolucci, F.; Kay, E. R.; Leigh, D. A.; Brouwer, A. M. *Chem.–Eur. J.* **2013,** *19,* 5566–5577. doi:10.1002/chem.201204016
13. Ghosh, P.; Federwisch, G.; Kogej, M.; Schalley, C. A.; Haase, D.; Saak, W.; Lützen, A.; Gschwind, R. M. *Org. Biomol. Chem.* **2005,** *3,* 2691–2700. doi:10.1039/b506756a

14. Jiang, W.; Nowosinski, K.; Löw, N. L.; Dzyuba, E.; Klautzsch, F.; Schäfer, A.; Huuskonen, J.; Rissanen, K.; Schalley, C. *J. Am. Chem. Soc.* **2012,** *134,* 1860–1868. doi:10.1021/ja2107096

15. Talotta, C.; Gaeta, C.; Qi, Z.; Schalley, C. A.; Neri, P. *Angew. Chem., Int. Ed.* **2013,** *52,* 7437–7441. doi:10.1002/anie.201301570

16. Fernandes, A.; Viterisi, A.; Aucagne, V.; Leigh, D. A.; Papot, S. *Chem. Commun.* **2012,** *48,* 2083–2085. doi:10.1039/c2cc17458h

17. Lewandowski, B.; De Bo, G.; Ward, J. W.; Papmeyer, M.; Kuschel, S.; Aldegunde, M. J.; Gramlich, P. M. E.; Heckmann, D.; Goldup, S. M.; D'Souza, D. M.; Fernandes, A. E.; Leigh, D. A. *Science* **2013,** *339,* 189–193. doi:10.1126/science.1229753

18. Leigh, D. A.; Troisi, A.; Zerbetto, F. *Angew. Chem., Int. Ed.* **2000,** *39,* 350–353. doi:10.1002/(SICI)1521-3773(20000117)39:2<350::AID-ANIE350>3.0. CO;2-D

19. Altieri, A.; Bottari, G.; Dehez, F.; Leigh, D. A.; Wong, J. K. Y.; Zerbetto, F. *Angew. Chem., Int. Ed.* **2003,** *42,* 2296–2300. doi:10.1002/anie.200250745

20. Schalley, C. A.; Reckien, W.; Peyerimhoff, S.; Baytekin, B.; Vögtle, F. *Chem.–Eur. J.* **2004,** *10,* 4777–4789. doi:10.1002/chem.200400365

21. Deng, W.-Q.; Muller, R. P.; Goddard, W. A., III. *J. Am. Chem. Soc.* **2004,** *126,* 13562–13563. doi:10.1021/ja036498x

22. Hirva, P.; Haukka, M.; Pakkanen, T. A. *J. Mol. Model.* **2008,** *14,* 879–886. doi:10.1007/s00894-008-0331-y

23. Yu, Y.; Cai, W.; Chipot, C.; Sun, T.; Shao, X. *J. Phys. Chem. B* **2008,** *112,* 5268–5271. doi:10.1021/jp711413a

24. Ben Shir, I.; Sasmal, S.; Mejuch, T.; Sinha, M. K.; Kapon, M.; Keinan, E. *J. Org. Chem.* **2008,** *73,* 8772–8779. doi:10.1021/jo801350b

25. Zheng, X.; Sohlberg, K. *J. Phys. Chem. A* **2006,** *110,* 11862–11869. doi:10.1021/jp056665a

26. Marand, E.; Hu, Q.; Gibson, H.; Veytsman, B. *Macromolecules* **1996,** *29,* 2555–2562. doi:10.1021/ma950569y

27. Kirchner, B.; Spickermann, C.; Reckien, W.; Schalley, C. A. *J. Am. Chem. Soc.* **2010,** *132,* 484–494. doi:10.1021/ja902628n

28. Reckien, W.; Kirchner, B.; Peyerimhoff, S. D. *J. Phys. Chem. A* **2006,** *110,* 12963–12970. doi:10.1021/jp065327m

29. Reckien, W.; Spickermann, C.; Eggers, M.; Kirchner, B. *Chem. Phys.* **2008,** *343,* 186–199. doi:10.1016/j.chemphys.2007.09.027

30. Spickermann, C.; Felder, T.; Schalley, C. A.; Kirchner, B. *Chem.–Eur. J.* **2008,** *14,* 1216–1227. doi:10.1002/chem.200700479

31. Kaufmann, L.; Dzyuba, E. V.; Malberg, F.; Löw, N. L.; Groschke, M.; Brusilowskij, B.; Huuskonen, J.; Rissanen, K.; Kirchner, B.; Schalley, C. A. *Org. Biomol. Chem.* **2012,** *10,* 5954–5964. doi:10.1039/C2OB25196E

32. Reckien, W.; Peyerimhoff, S. D. *J. Phys. Chem. A* **2003,** *107,* 9634–9640. doi:10.1021/jp030219a

33. Ahlrichs, R.; Bär, M.; Häser, M.; Horn, H.; Kölmel, C. *Chem. Phys. Lett.* **1989,** *162,* 165–169. doi:10.1016/0009-2614(89)85118-8

34. Becke, A. D. *Phys. Rev. A* **1988,** *38,* 3098–3100. doi:10.1103/PhysRevA.38.3098

35. Grimme, S.; Antony, J.; Ehrlich, S.; Krieg, H. *J. Chem. Phys.* **2010,** *132,* 154104. doi:10.1063/1.3382344

36. Grimme, S.; Ehrlich, S.; Goerigk, L. *J. Comput. Chem.* **2011,** *32,* 1456–1465. doi:10.1002/jcc.21759

37. Koßmann, S.; Thar, J.; Kirchner, B.; Hunt, P. A.; Welton, T. *J. Chem. Phys.* **2006,** *124,* 174506. doi:10.1063/1.2191493

38. Kirchner, B.; Reiher, M. *J. Am. Chem. Soc.* **2002,** *124,* 6206–6215. doi:10.1021/ja017703g

39. Deglmann, P.; Furche, F.; Ahlrichs, R. *Chem. Phys. Lett.* **2002,** *362,* 511–518. doi:10.1016/S0009-2614(02)01084-9

40. Deglmann, P.; Furche, F. *J. Chem. Phys.* **2002,** *117,* 9535–9538. doi:10.1063/1.1523393

41. Deglmann, P.; May, K.; Furche, F.; Ahlrichs, R. *Chem. Phys. Lett.* **2004,** *384,* 103–107. doi:10.1016/j.cplett.2003.11.080

42. Klamt, A.; Schüürmann, G. *J. Chem. Soc., Perkin Trans. 2* **1993,** 799–805. doi:10.1039/p29930000799

43. Hansch, C.; Leo, A.; Taft, R. W. *Chem. Rev.* **1991,** *91,* 165–195. doi:10.1021/cr00002a004

44. Kresse, G.; Furthmüller, J. *Comput. Mater. Sci.* **1996,** *6,* 15–50. doi:10.1016/0927-0256(96)00008-0

45. Bučko, T.; Hafner, J.; Lebègue, S.; Angyán, J. G. *J. Phys. Chem. A* **2010,** *114,* 11814–11824. doi:10.1021/jp106469x

46. Perdew, J. P.; Burke, K.; Ernzerhof, M. *Phys. Rev. Lett.* **1996,** *77,* 3865–3868. doi:10.1103/PhysRevLett.77.3865

47. Blöchl, P. E. *Phys. Rev. B* **1994,** *50,* 17953–17979. doi:10.1103/PhysRevB.50.17953

48. Kresse, G.; Joubert, D. *Phys. Rev. B* **1999,** *59,* 1758–1775. doi:10.1103/PhysRevB.59.1758

49. Goerigk, L.; Grimme, S. *Phys. Chem. Chem. Phys.* **2011,** *13,* 6670–6688. doi:10.1039/c0cp02984j

50. Grimme, S. *Chem.–Eur. J.* **2012,** *18,* 9955–9964. doi:10.1002/chem.201200497

51. Brandenburg, J. G.; Grimme, S. *Theor. Chem. Acc.* **2013,** *132,* 1399. doi:10.1007/s00214-013-1399-8

52. Burns, L. A.; Vázquez-Mayagoitia, A.; Sumpter, B. G.; Sherrill, C. D. *J. Chem. Phys.* **2011,** *134,* 084107. doi:10.1063/1.3545971

53. Kay, E. R.; Leigh, D. A. *Top. Curr. Chem.* **2005,** *262,* 133–177. doi:10.1007/128_011

54. Grimme, S.; Steinmetz, M. *Phys. Chem. Chem. Phys.* **2013,** *15,* 16031–16042. doi:10.1039/c3cp52293h

55. Brandenburg, J. G.; Grimme, S. *Top. Curr. Chem.* **2014,** *345,* 1–23. doi:10.1007/128_2013_488

56. Moellmann, J.; Grimme, S. *Organometallics* **2013,** *32,* 3784–3787. doi:10.1021/om400386x

57. Dzyuba, E. V.; Kaufmann, L.; Löw, N. L.; Meyer, A. K.; Winkler, H. D. F.; Rissanen, K.; Schalley, C. A. *Org. Lett.* **2011,** *13,* 4838–4841. doi:10.1021/ol201915j

Triazol-substituted titanocenes by strain-driven 1,3-dipolar cycloadditions

Andreas Gansäuer[*1], Andreas Okkel[1], Lukas Schwach[1], Laura Wagner[2], Anja Selig[2] and Aram Prokop[3]

Abstract

An operationally simple, convenient, and mild strategy for the synthesis of triazole-substituted titanocenes via strain-driven 1,3-dipolar cycloadditions between azide-functionalized titanocenes and cyclooctyne has been developed. It features the first synthesis of titanocenes containing azide groups. These compounds constitute 'second-generation' functionalized titanocene building blocks for further synthetic elaboration. Our synthesis is modular and large numbers of the complexes can in principle be prepared in short periods of time. Some of the triazole-substituted titanocenes display high cyctotoxic activity against BJAB cells. Comparison of the most active complexes allows the identification of structural features essential for biological activity.

Introduction

Group 4 metallocenes and derivatives of Cp_2TiCl_2, in particular, continue to be in the focus of contemporary research as a promising class of cytotoxic compounds [1-10], as efficient reagents and catalysts [11-16], as organometallic gelators [17-20], and in their own right [21,22]. In order to further investigate and improve these properties it is mandatory to access as yet unexplored functional titanocenes. This is most easily achieved with modular, efficient, and general strategies for the synthesis of these complexes. Classical approaches with metala-

tion at the end of the sequence usually do not meet these requirements. This is because introduction of functional groups is difficult due to the nucleophilicity of the cyclopentadienyl anions before metalation and the electrophilicity of titanium after metalation [21,22].

We have devised a conceptually different approach addressing these issues. It relies on the use of carboxylate-containing titanocene building blocks [23-25]. From these compounds the

corresponding acid chlorides can be prepared by addition of SOCl$_2$. The acid chloride group is more electrophilic than the [TiCl$_2$] fragment and therefore many titanocenes containing ligands with pending amide, ester, and ketone groups can be prepared with classical organic acylation reactions (Friedel–Crafts reaction, esterification, amide synthesis, Scheme 1). Some of these complexes have been used as organometallic gelators [19,20], as a novel class of cytostatic compounds [26], and catalysts for unusual radical cyclizations [27-31]. The ketone and amide substituted catalysts are cationic due to the intramolecular coordination of the carbonyl group [30,31]. This feature is essential for the cytostatic and catalytic activity. Moreover, in the amide complexes hydrogen bonding of the N–H bond to chloride or [ZnCl$_4$]$^{2-}$ is a crucial structural feature [31]. The gelation ability of the neutral ester-substituted titanocenes critically depends on the steric demand of the substituents on the cyclopentadienyl ligands. The carboxylates are valuable complexes for mediating highly chemoselective Barbier type allylations [32,33].

These findings demonstrate that the properties of our functional titanocenes critically depend on both the direct environment of the Ti center and the periphery of the complex. Therefore, it is desirable to develop novel entries to titanocenes with even higher structural and functional diversity to improve the observed functions. An especially attractive approach is the use of already functionalized building blocks as starting materials in diversity oriented synthesis that increases the molecular complexity. Any synthetic methodology used in this context must take into account the sensitivity of the titanocene towards nucleophiles.

We decided to address these issues by employing cationic amide-substituted titanocenes as building blocks and strain-driven 1,3-dipolar cycloadditions [34-40] as synthetic methodology for the preparation of such 'second-generation' functional titanocenes. This line of action seemed especially appealing for two reasons. First, the cationic amide titanocenes have already displayed interesting activity and therefore serve as our lead structures. Second, the strain-driven 1,3-dipolar cycloadditions have evolved as extremely mild reactions for the functionalization of complex molecules. Since no metal complexes are required to catalyze the 1,3-dipolar cycloaddition [41-43], the reaction can be even used for the functionalization of biomolecules in living systems and has therefore been called bioorthogonal [34,35].

To the best of our knowledge, no examples of the Ti-containing substrates for our strategy, i.e., azide-functionalized titanocenes, have been reported in the literature. One aspect of our study is to establish if such complexes are stable and readily available in high yield. It should be noted that only a single example of a Cu-catalyzed 1,3-dipolar cycloaddition with an alkyne-functionalized titanocene has been described [44]. Therefore, the properties of triazol-substituted titanocenes, the products of the 1,3-dipolar cycloaddition, are also largely unexplored.

Results and Discussion
Synthesis of the titanocenes
Preparation of the starting materials
We started our investigation with the preparation of azide-substituted cationic titanocenes. To this end, the titanocene carboxylates **1**–**3** shown in Figure 1 were employed as
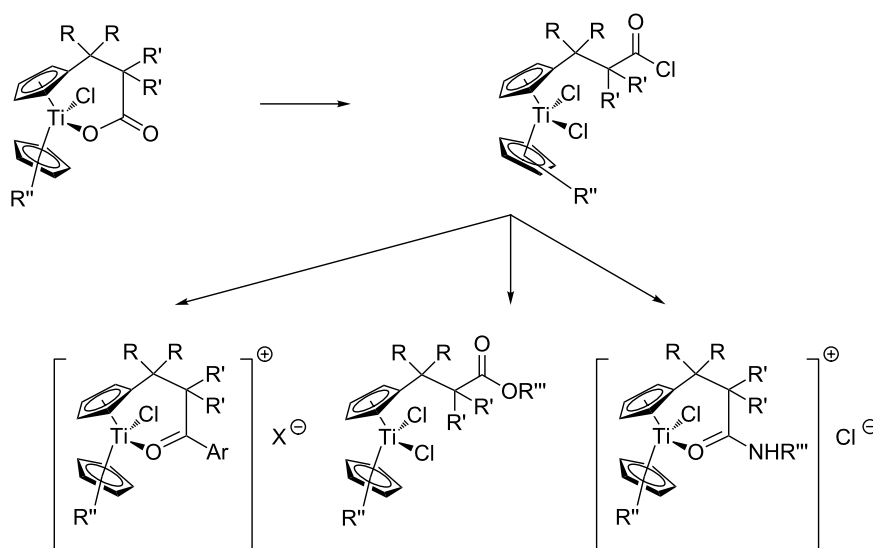
Scheme 1: Modular titanocene synthesis via acylation reactions [24].

substrates because their substitution pattern should allow a first simple assessment of structure–activity relationships.
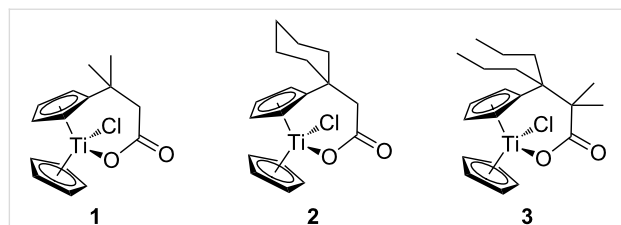
Figure 1: Carboxylates employed as titanocene starting materials for azide-substituted complexes.

The compounds **A**–**D** shown in Figure 2 were used as amino-substituted azides. They are readily obtained from the corresponding diazides through a Staudinger reaction (see Supporting Information File 1 for details) [45,46]. As for the carboxylates the different tether lengths and substitution patterns of the arene allow to study the effect of substitution on the activity of the complexes. The ether tether in **B** serves as a model for PEG.

The titanocene carboxylates **1**–**3** were transformed into the corresponding acid chlorides and then reacted with amino azides **A**–**D** in the presence of NaH without purification of the acid chlorides. Typical results are summarized in Table 1.
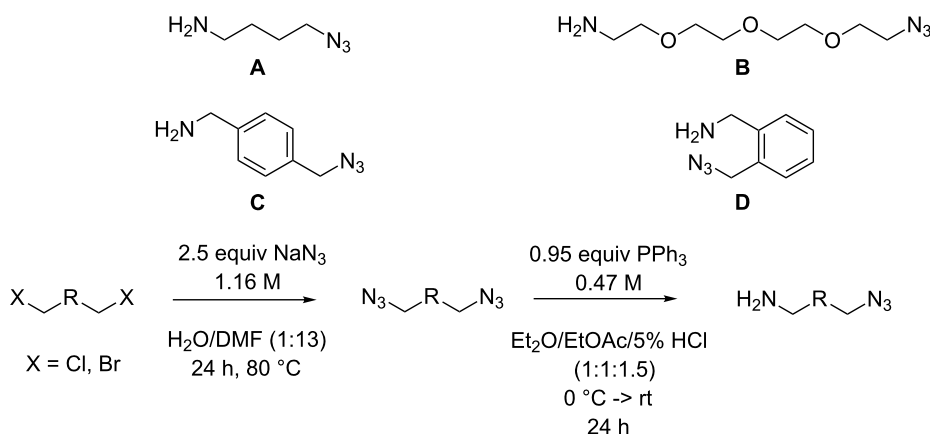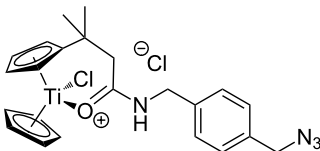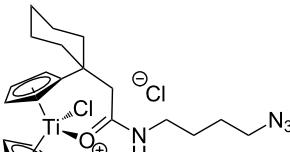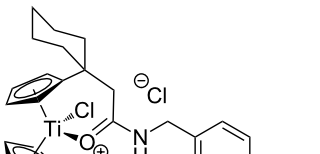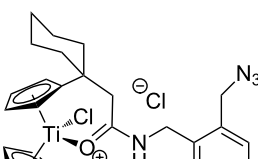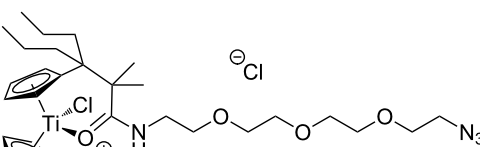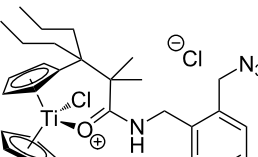
Figure 2: Azides employed in this study and conditions for their synthesis.

Table 1: Synthesis of cationic titanocenes containing azides (yield over two steps, see Supporting Information File 1 for details).

substrates	product	yield/[%]
1, A	**4**	78
1, B	**5**	51

Table 1: Synthesis of cationic titanocenes containing azides (yield over two steps, see Supporting Information File 1 for details). (continued)

1, **C**	**6**	89
2, **A**	**7**	89
2, **C**	**8**	63
2, **D**	**9**	71
3, **B**	**10**	51
3, **D**	**11**	31

Gratifyingly, the acylation reactions proceed without problems and the azide-functionalized titanocenes can generally be obtained in good yields after 16 h. The somewhat lower yields obtained with carboxylate **3** are probably due to an increased bulkiness of the ligand's substituents. It should be noted that polyether groups can be readily incorporated into cationic titanocenes. This suggests that the cationic titanocenes can be readily immobilized by covalent binding to PEG.

In general, our results clearly demonstrate that the azide group is compatible with cationic titanocenes. Moreover, it is obvious that large libraries of such titanocenes can be accessed from our carboxylates in short periods of time.

Strain-driven 1,3-dipolar cycloadditions

With the new titanocene building blocks in hand we turned our attention to their further functionalization through the strain-driven 1,3-dipolar cycloaddition with cyclooctyne. The original conditions of Wittig [36], the reaction of cyclooctyne with phenyl azide, and the numerous applications pioneered by Bertozzi suggest that the reaction proceeds under mild conditions [34,35,37-40]. Therefore, we simply mixed the titanocenes

and cyclooctyne in CH$_2$Cl$_2$ at room temperature. The concentration of the substrates was intentionally kept low (0.1 M) to avoid a too intense evolution of heat. Typical examples of the reaction are summarized in Table 2.
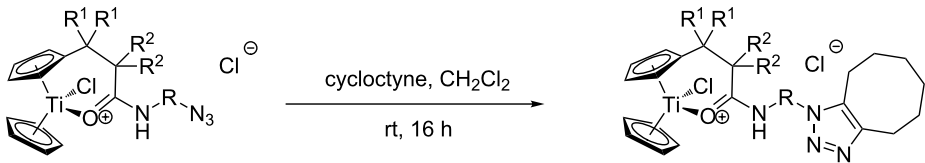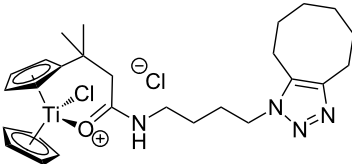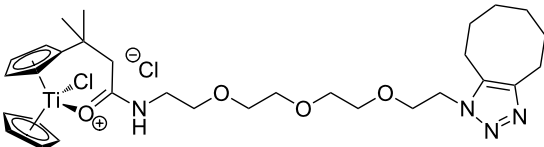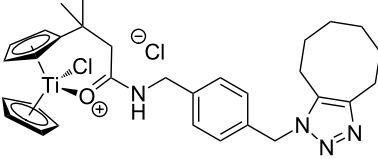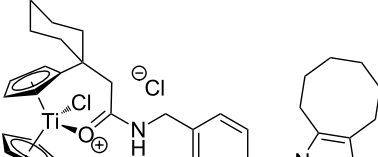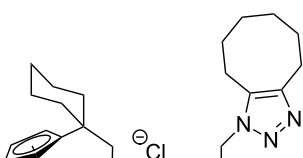
The results demonstrate that the strain-driven 1,3-dipolar cycloaddition is a convenient and very mild route to triazole-functionalized cationic titanocenes. The yields between 75% and 92% are satisfying. It should be noted that the polyether-substituted complexes **13** and **17** are obtained in high yield. This opens further interesting perspectives for the immobilization of titanocene complexes.

Cytotoxicity studies

One of the pertinent features of titanocenes is their cytotoxicity [1-5]. Therefore, we investigated this particular property of our

Table 2: Strain-driven 1,3-dipolar cycloadditions between cyclooctyne and azide-functionalized titanocenes in CH$_2$Cl$_2$ (0.1 M).

titanocene	product	yield/[%]
4	**12**	80
5	**13**	88
6	**14**	78
8	**15**	79
9	**16**	79

Table 2: Strain-driven 1,3-dipolar cycloadditions between cyclooctyne and azide-functionalized titanocenes in CH_2Cl_2 (0.1 M). (continued)

10	**17**	92
11	**18**	75
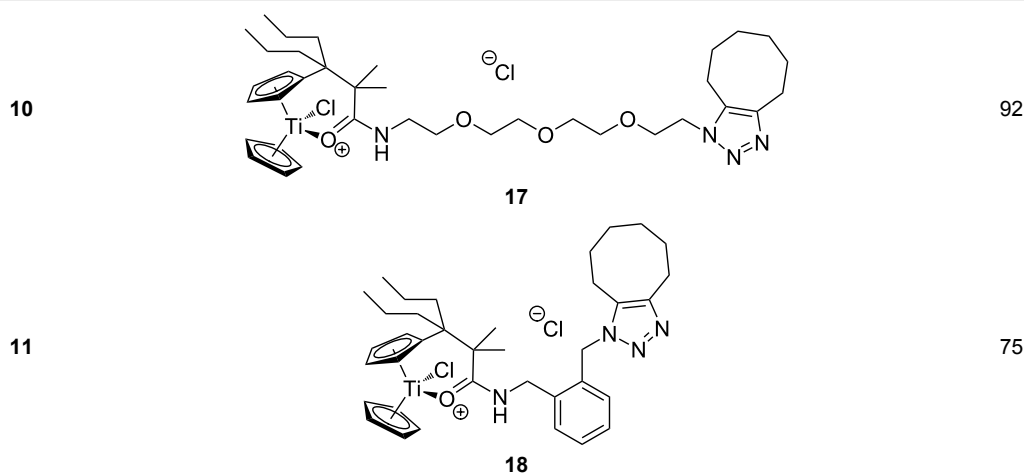
novel complexes. To guarantee comparability with a previous study [26] we discuss our results of the lymphoma cell line BJAB. Cell surface transmembrane receptor CD95, through which apoptosis can be induced, is expressed by BJAB cells. Cell death can be induced in these cells both by the extrinsic and the intrinsic apoptosis-signalling pathway [47-49]. Therefore, BJAB cells are well-suited for studying the induction of apoptosis by our cationic titanocenes [50-53]. It is logical to study apoptosis induction, expressed as AC_{50} values, instead of nonspecific cytotoxicity, which is usually reported as LC_{50} values, because cytotoxic drugs operate by specific induction of apoptosis. So we determined the AC_{50} values of our

titanocenes, i.e., the concentrations causing specific apoptosis in 50% of lymphoma cells, counting all cells with membrane damage.

The azide-substituted complexes showed no significant apoptosis induction ($AC_{50} > 100$ μM). Introduction of the triazole ring through 1,3-dipolar cycloaddition markedly changes the activity of our titanocenes as a function of the substitution pattern. The most active complexes are highlighted in Figure 3.

Gratifyingly, **18**, together with a ketone-substituted titanocene, displays the highest activity against the BJAB cell line of our

15
35 μM

16
25 μM

18
12.5 μM
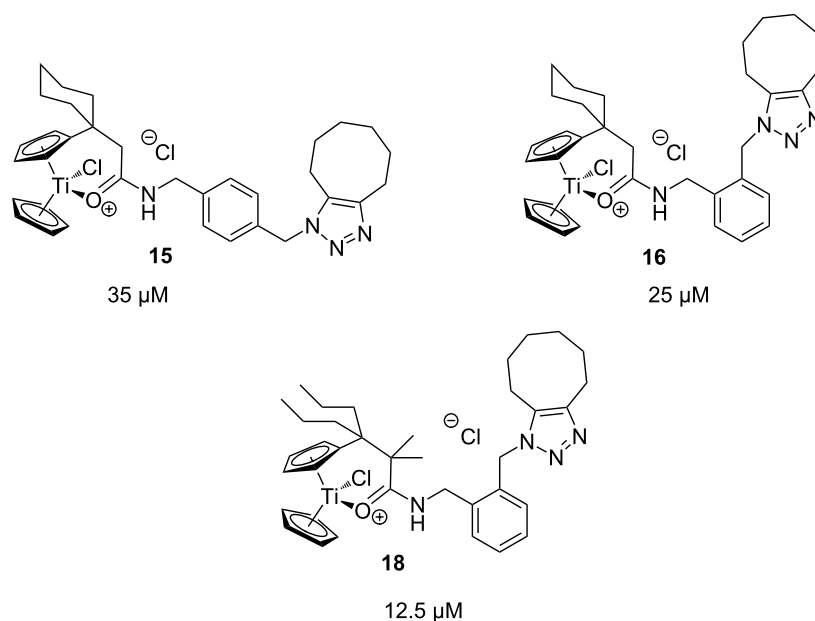
Figure 3: Most active titanocenes of this study and their AC_{50} values.

cationic carbonyl-substituted titanocenes. Comparison of the three most active complexes also allows the identification of structural features essential for cytotoxic activity. First, a bulky substitution of the cyclopentadienyl ligand is favorable. Second, positioning of the triazol in close proximity – ortho-substitution in **16** leads to a lower AC_{50} value than para-substitution in **15** – of the metal center enhances the biological activity.

Conclusion

In summary, we have devised an operationally simple, convenient, and mild strategy for the synthesis of triazole substituted titanocenes via strain-driven 1,3-dipolar cycloadditions between azide-functionalized titanocenes and cyclooctyne. It features the first synthesis of titanocenes containing azide groups. These compounds constitute functionalized 'second-generation' titanocene building blocks for further synthetic elaboration. Our synthesis is modular and large numbers of the complexes can in principle be prepared in short periods of time. Some of the triazole-substituted titanocenes display high cyctotoxic activity against BJAB cells. Comparison of the most active complexes allows the identification of structural features essential for biological activity.

Future studies will concentrate on the preparation of neutral and of enantiomerically pure triazole-substituted titanocenes, also via metal catalyzed cycloadditions, for further increasing the biological activity of the complexes and for applications in enantioselective [54,55] cyclizations [56-58].

Supporting Information

Supporting Information File 1

Experimental procedures and compound characterization, cytotoxicity studies.

[http://www.beilstein-journals.org/bjoc/content/
supplementary/1860-5397-10-169-S1.pdf]

Acknowledgements

References

1. Buettner, K. M.; Valentine, A. M. *Chem. Rev.* **2012,** *112,* 1863–1881. doi:10.1021/cr1002886

2. Hartinger, C. G.; Metzler-Nolte, N.; Dyson, P. J. *Organometallics* **2012,** *31,* 5677–5685. doi:10.1021/om300373t

3. Tshuva, E. Y.; Ashenhurst, J. A. *Eur. J. Inorg. Chem.* **2009,** 2203–2218. doi:10.1002/ejic.200900198

4. Strohfeldt, K.; Tacke, M. *Chem. Soc. Rev.* **2008,** *37,* 1174–1187. doi:10.1039/b707310k

5. Köpf-Maier, P.; Köpf, H. *Chem. Rev.* **1987,** *87,* 1137–1152. doi:10.1021/cr00081a012

6. Sirignano, E.; Saturnino, C.; Botta, A.; Sinicropi, M. S.; Caruso, A.; Pisano, A.; Lappano, R.; Maggiolini, M.; Longo, P. *Bioorg. Med. Chem. Lett.* **2013,** *23,* 3458–3462. doi:10.1016/j.bmcl.2013.03.059

7. Schur, J.; Manna, C. M.; Deally, A.; Köster, R. W.; Tacke, M.; Tshuva, E. Y.; Ott, I. *Chem. Commun.* **2013,** *49,* 4785–4787. doi:10.1039/c3cc38604j

8. Kater, L.; Claffey, J.; Hogan, M.; Jesse, P.; Kater, B.; Strauss, S.; Tacke, M.; Prokop, A. *Toxicol. in Vitro* **2012,** *26,* 119–124. doi:10.1016/j.tiv.2011.09.010

9. González-Pantoja, J. F.; Stern, M.; Jarzecki, A. A.; Royo, E.; Robles-Escajeda, E.; Varela-Ramírez, A.; Aguilera, R. J.; Contel, M. *Inorg. Chem.* **2011,** *50,* 11099–11110. doi:10.1021/ic201647h

10. Gao, L. M.; Vera, J. L.; Matt, J.; Meléndez, E. *J. Biol. Inorg. Chem.* **2010,** *15,* 851–859. doi:10.1007/s00775-010-0649-7

11. Carter, M. B.; Schiøtt, B.; Gutiérrez, A.; Buchwald, S. L. *J. Am. Chem. Soc.* **1994,** *116,* 11667–11670. doi:10.1021/ja00105a006

12. Pohlki, F.; Doye, S. *Angew. Chem., Int. Ed.* **2001,** *40,* 2305–2308. doi:10.1002/1521-3773(20010618)40:12<2305::AID-ANIE2305>3.0.CO;2-7

13. Cuerva, J. M.; Justicia, J.; Oller-López, J. L.; Oltra, J. E. *Top. Curr. Chem.* **2006,** *264,* 63–91. doi:10.1007/128_025

14. Gansäuer, A.; Justicia, J.; Fan, C.-A.; Worgull, D.; Piestert, F. *Top. Curr. Chem.* **2007,** *279,* 25–52. doi:10.1007/128_2007_130

15. Gansäuer, A.; Fleckhaus, A.; Lafont, M. A.; Okkel, A.; Kotsis, K.; Anoop, A.; Neese, F. *J. Am. Chem. Soc.* **2009,** *131,* 16989–16999. doi:10.1021/ja907817y

16. Streuff, J.; Feurer, M.; Bichovski, P.; Frey, G.; Gellrich, U. *Angew. Chem., Int. Ed.* **2012,** *51,* 8661–8664. doi:10.1002/anie.201204469

17. Dastidar, P. *Chem. Soc. Rev.* **2008,** *37,* 2699–2715. doi:10.1039/b807346e

18. Piepenbrok, M.-O. M.; Lloyd, G. O.; Clarke, N.; Steed, J. W. *Chem. Rev.* **2010,** *110,* 1960–2004. doi:10.1021/cr9003067

19. Klawonn, T.; Gansäuer, A.; Winkler, I.; Lauterbach, T.; Franke, D.; Nolte, R. J. M.; Feiters, M. C.; Börner, H.; Hentschel, J.; Dötz, K. H. *Chem. Commun.* **2007,** 1894–1895. doi:10.1039/b701565h

20. Gansäuer, A.; Winkler, I.; Klawonn, T.; Nolte, R. J. M.; Feiters, M. C.; Börner, H. G.; Hentschel, J.; Dötz, K. H. *Organometallics* **2009,** *28,* 1377–1382. doi:10.1021/om801022c

21. Halterman, R. L. *Chem. Rev.* **1992,** *92,* 965–994. doi:10.1021/cr00013a011

22. Qian, Y.; Huang, J.; Bala, M. D.; Lian, B.; Zhang, H.; Zhang, H. *Chem. Rev.* **2003,** *103,* 2633–2690. doi:10.1021/cr020002x

23. Gansäuer, A.; Franke, D.; Lauterbach, T.; Nieger, M. *J. Am. Chem. Soc.* **2005,** *127,* 11622–11623. doi:10.1021/ja054185r

24. Gansäuer, A.; Winkler, I.; Worgull, D.; Franke, D.; Lauterbach, T.; Okkel, A.; Nieger, M. *Organometallics* **2008,** *27,* 5699–5707. doi:10.1021/om800700c

25. Gansäuer, A.; Okkel, A.; Worgull, D.; Schnakenburg, G. *Organometallics* **2010,** *29,* 3227–3230. doi:10.1021/om100245r

26. Gansäuer, A.; Winkler, I.; Worgull, D.; Lauterbach, T.; Franke, D.; Selig, A.; Wagner, L.; Prokop, A. *Chem.–Eur. J.* **2008,** *14,* 4160–4163. doi:10.1002/chem.200800407

27. Gansäuer, A.; Lauterbach, T.; Geich-Gimbel, D. *Chem.–Eur. J.* **2004,** *10,* 4983–4990. doi:10.1002/chem.200400685

28. Friedrich, J.; Dolg, M.; Gansäuer, A.; Geich-Gimbel, D.; Lauterbach, T. *J. Am. Chem. Soc.* **2005,** *127,* 7071–7077. doi:10.1021/ja050268w

29. Friedrich, J.; Walczak, K.; Dolg, M.; Piestert, F.; Lauterbach, T.; Worgull, D.; Gansäuer, A. *J. Am. Chem. Soc.* **2008,** *130,* 1788–1796. doi:10.1021/ja077596b

30. Gansäuer, A.; Worgull, D.; Knebel, K.; Huth, I.; Schnakenburg, G. *Angew. Chem., Int. Ed.* **2009,** *48,* 8882–8885. doi:10.1002/anie.200904428

31. Gansäuer, A.; Knebel, K.; Kube, C.; van Gastel, M.; Cangönül, A.; Daasbjerg, K.; Hangele, T.; Hülsen, M.; Dolg, M.; Friedrich, J. *Chem.–Eur. J.* **2012,** *18,* 2591–2599. doi:10.1002/chem.201102959

32. Jiménez, T.; Morcillo, S. P.; Martín-Lasanta, A.; Collado-Sanz, D.; Cárdenas, D. J.; Gansäuer, A.; Justicia, J.; Cuerva, J. M. *Chem.–Eur. J.* **2012,** *18,* 12825–12833. doi:10.1002/chem.201201534

33. Morcillo, S. P.; Martinez-Peragón, Á.; Jakoby, V.; Mota, A. J.; Kube, C.; Justicia, J.; Cuerva, J. M.; Gansäuer, A. *Chem. Commun.* **2014,** *50,* 2211–2213. doi:10.1039/c3cc49230c

34. Sletten, E. M.; Bertozzi, C. R. *Angew. Chem., Int. Ed.* **2009,** *48,* 6974–6998. doi:10.1002/anie.200900942

35. Jewett, J. C.; Bertozzi, C. R. *Chem. Soc. Rev.* **2010,** *39,* 1272–1279. doi:10.1039/b901970g

36. Wittig, G.; Krebs, A. *Chem. Ber.* **1961,** *94,* 3260–3275. doi:10.1002/cber.19610941213

37. Agard, N. J.; Prescher, J. A.; Bertozzi, C. R. *J. Am. Chem. Soc.* **2004,** *126,* 15046–15047. doi:10.1021/ja044996f

38. Gordon, C. G.; Mackey, J. L.; Jewett, J. C.; Sletten, E. M.; Houk, K. N.; Bertozzi, C. R. *J. Am. Chem. Soc.* **2012,** *134,* 9199–9208. doi:10.1021/ja3000936

39. Hudak, J. E.; Barfield, R. M.; de Hart, G. W.; Grob, P.; Nogales, E.; Bertozzi, C. R.; Rabuka, D. *Angew. Chem., Int. Ed.* **2012,** *51,* 4161–4165. doi:10.1002/anie.201108130

40. de Almeida, G.; Sletten, E. M.; Nakamura, H.; Palaniappan, K. K.; Bertozzi, C. R. *Angew. Chem., Int. Ed.* **2012,** *51,* 2443–2447. doi:10.1002/anie.201106325

41. Tornøe, C. W.; Christensen, C.; Meldal, M. *J. Org. Chem.* **2002,** *67,* 3057–3064. doi:10.1021/jo011148j

42. Rostovtsev, V. V.; Green, L. G.; Fokin, V. V.; Sharpless, K. B. *Angew. Chem., Int. Ed.* **2002,** *41,* 2596–2599. doi:10.1002/1521-3773(20020715)41:14<2596::AID-ANIE2596>3.0.CO;2-4

43. Zhang, L.; Chen, X.; Xue, P.; Sun, H. H. Y.; Williams, I. D.; Sharpless, K. B.; Fokin, V. V.; Jia, G. *J. Am. Chem. Soc.* **2005,** *127,* 15998–15999. doi:10.1021/ja054114s

44. Zagerman, J.; Deally, A.; Metzler-Nolte, N.; Müller-Bunz, H.; Wallis, D.; Tacke, M. *Polyhedron* **2011,** *30,* 2387–2390. doi:10.1016/j.poly.2011.05.036

45. Golobov, Y. M.; Kasukhin, L. F. *Tetrahedron* **1992,** *48,* 1353–1406. doi:10.1016/S0040-4020(01)92229-X

46. Köhn, M.; Breinbauer, R. *Angew. Chem., Int. Ed.* **2004,** *43,* 3106–3116. doi:10.1002/anie.200401744

47. Bantel, H.; Engels, I. H.; Völter, W.; Schulze-Osthoff, K.; Wesselborg, S. *Cancer Res.* **1999,** *59,* 2083–2090.

48. Klener, P., Jr.; Anděra, L.; Klener, P.; Nečas, E.; Živný, J. *Folia Biol. (Prague, Czech Repub.)* **2006,** *52,* 34–44.

49. Meiler, J.; Schuler, M. *Curr. Drug Targets* **2006,** *7,* 1361–1369. doi:10.2174/138945006778559175

50. Wieder, T.; Prokop, A.; Bagci, B.; Essmann, F.; Bernicke, D.; Schulze-Osthoff, K.; Dörken, B.; Schmalz, H.-G.; Daniel, P. T.; Henze, G. *Leukemia* **2001,** *15,* 1735–1742. doi:10.1038/sj.leu.2402284

51. Diller, R. A.; Riepl, H. M.; Rose, O.; Frias, C.; Henze, G.; Prokop, A. *Planta Med.* **2007,** *73,* 755–761. doi:10.1055/s-2007-981545

52. Prokop, A.; Wrasidlo, W.; Lode, H.; Herold, R.; Lang, F.; Henze, G.; Dörken, B.; Wieder, T.; Daniel, P. T. *Oncogene* **2003,** *22,* 9107–9120. doi:10.1038/sj.onc.1207196

53. Rudner, J.; Lepple-Wienhues, A.; Budach, W.; Berschauer, J.; Friedrich, B.; Wesselborg, S.; Schulze-Osthoff, K.; Belka, C. *J. Cell Sci.* **2001,** *114,* 4161–4172.

54. Gansäuer, A.; Fan, C.-A.; Keller, F.; Karbaum, P. *Chem.–Eur. J.* **2007,** *13,* 8084–8090. doi:10.1002/chem.200701021

55. Gansäuer, A.; Shi, L.; Otte, M. *J. Am. Chem. Soc.* **2010,** *132,* 11858–11859. doi:10.1021/ja105023y

56. Gansäuer, A.; Pierobon, M. *Synlett* **2000,** 1357–1359. doi:10.1055/s-2000-7133

57. Gansäuer, A.; Pierobon, M.; Bluhm, H. *Synthesis* **2001,** 2500–2520. doi:10.1055/s-2001-18713

58. Barrero, A. F.; Quilez del Moral, J. F.; Sánchez, E. M.; Arteaga, J. F. *Eur. J. Org. Chem.* **2006,** 1627–1641. doi:10.1002/ejoc.200500849

Theoretical study of the adsorption of benzene on coinage metals

Werner Reckien, Melanie Eggers and Thomas Bredow[*]

Abstract

The adsorption of benzene on the M(111), M(100) and M(110) surfaces of the coinage metals copper (M = Cu), silver (M = Ag) and gold (M = Au) is studied on the basis of density functional theory (DFT) calculations with an empirical dispersion correction (D3). Variants of the Perdew–Burke–Ernzerhof functionals (PBE, RPBE and RevPBE) in combination with different versions of the dispersion correction (D3 and D3(BJ)) are compared. PBE-D3, PBE-D3(BJ) and RPBE-D3 give similar results which exhibit a good agreement with experimental data. RevPBE-D3 and RevPBE-D3(BJ) tend to overestimate adsorption energies. The inclusion of three-center terms (PBE-D3(ABC)) leads to a slightly better agreement with the experiment in most cases. Vertical adsorbate–substrate distances are calculated and compared to previous theoretical results. The observed trends for the surfaces and metals are consistent with the calculated adsorption energies.

Introduction

The adsorption of organic molecules on metals is of great interest since the formation of thin films and self-assembled monolayers opens the way toward a functionalization of surfaces [1-8]. The adsorbed molecules often contain an aromatic framework that can be substituted with functional groups. The bonding between the surface and the adsorbate is an interplay between electrostatic interaction, including charge transfer (CT) to the surface, and covalent contributions [9-11]. In addition, it was found that dispersion interaction plays a crucial role for the adsorption of large aromatic compounds on metal surfaces [9-11]. This holds in particular for the adsorption on the coinage metals copper, silver and gold. Therefore, a theoretical treatment of this process requires methods that provide an accurate description of these weak interactions. Density functional theory (DFT) is established as a standard method for quantum-chemical solid-state calculations [12]. However, DFT has the well known shortcoming that it fails to describe dispersion effects. Consequently, standard DFT

methods are not suitable for the calculation of the adsorption of aromatic compounds. In the last years much effort has been directed to the development of DFT methods that eliminate this shortage [13-24]. One of them is a damped empirical correction called DFT-D3 which was proposed by Grimme et al. for molecular systems [13]. The D3-dispersion correction to the DFT energy is calculated by summation over pair potentials. Non-additive effects of dispersion interaction can be treated on the basis of three-body terms D3(ABC) [13]. The most recent DFT-D3(BJ) method [16] differs from the original DFT-D3 essentially only in the damping function for short range interaction. Due to the computational efficiency of the D3 correction schemes it is possible to perform DFT-D3 calculations with nearly the same computational effort as standard DFT calculations. Only the calculation of three-body terms can become expensive for large systems, and is therefore usually carried out only for the final energy estimation. For molecular systems one can obtain with DFT-D3 results that are close to coupled cluster singles doubles with perturbative triples (CCSD(T)) results at the cost of GGA-DFT calculations. In recent years the DFT-D3 method has been extended to periodic systems [25]. In a few cases [26,27] it is observed that the metal C_6 dispersion coefficients for bulk systems can be largely reduced compared to the values of free atoms. Indeed this does not apply to the coinage metals Cu, Ag, and Au. The C_6 parameters for these metals are already converged [28]. In addition, it is known that metal substrates show significant dispersion screening effects that can modify the polarizabilities and C_6 coefficients of adsorbed molecules [29,30]. In principle these effects should be included in the coordination number dependent C_6 coefficients of the D3 correction. We checked this by calculating the C_3 coefficients for the benzene adsorption on the Au(111) surface.

Previous theoretical studies of the adsorption of organic compounds on silver and gold surfaces resulted in a good agreement with experimental results [9-11,26]. However, a systematic comparison of the different DFT-D3 approaches is still missing. One aim of this work is the comparison of different DFT-D3 methods for the description of the adsorption of aromatic compounds on this surfaces. We therefore present a theoretical study of the adsorption of benzene on the M(111), M(100) and M(110) surfaces of the coinage metals copper, silver and gold. The benzene molecule was selected because it is a building block of many organic compounds that are used for surface functionalization. As mentioned above the binding between the metal and the adsorbate is often dominated by dispersion interaction to the aromatic framework. Therefore the study of the bonding between benzene and the metal surfaces is of great interest. In addition, although the adsorption of benzene on some of these surfaces has been subject of previous theoretical studies [29-39], this is the first work in which the adsorp-

tion on the most important coinage metal surfaces is systematically studied with the same method. Different from our previous study on benzene/Ag(111) [25], we apply a variety of DFT methods and dispersion corrections, and investigate all low-index surfaces.

Computational methodologies

We used the plane-wave code VASP [40-42] in combination with the projector-augmented wave method to account for the core electrons [43] for all calculations. We applied our recent implementation [25] of Grimme's dispersion correction (DFT-D3) [13,16]. The dispersion corrected DFT-D3 energy $E_{\text{DFT-D}}$ is calculated by adding an empirical correction energy E_{disp} to the DFT energy E_{DFT}, see Equation 1.

$$E_{\text{DFT-D}} = E_{\text{DFT}} + E_{\text{disp}} \qquad (1)$$

In this work we used the gradient-corrected PBE [44], RPBE [45], and RevPBE [46] functionals in combination with the original D3 [13] as well as with the newer D3(BJ) dispersion correction [16]. These methods were chosen since they represent a selection of standard GGA functionals, which are available in most of the software for quantum chemical solid state studies. The computational effort of hybrid functionals is too large for these systems and cheaper methods like DFTB-D3 [47] lack suitable parameters, e.g., for gold. We also checked the impact of the three-body terms (D3(ABC)). These three-center terms D3(ABC) were introduced in the D3 correction scheme since the long-range part of the interaction between three ground-state atoms is not exactly equal to the pairwise interaction energies [13]. From third-order perturbation theory one gets the Axilrod–Teller–Muto dispersion term for the consideration of the non-additivity of dispersion interaction. D3(ABC) is calculated according to Equation 2

$$\text{D3(ABC)} = \sum_{\text{ABC}} f_{\text{damp}} \frac{C_9^{\text{ABC}} \left(3\cos(\theta_a)\cos(\theta_b)\cos(\theta_c) + 1 \right)}{r_{\text{AB}} r_{\text{BC}} r_{\text{CA}}} \qquad (2)$$

The C_9^{ABC} coefficients are the geometric mean of the C_6-coefficients, θ_a, θ_b and θ_c are the angles of the triangle, which is formed by the three atoms, and f_{damp} is the damping function. The Axilrod–Teller–Muto dispersion terms can be neglected for molecular systems [13]. However, recent studies indicate that their impact is larger for periodic systems that are more densely packed.

We performed calculations with the PBE-D3, PBE-D3(BJ), PBE-D3(ABC), RPBE-D3, RevPBE-D3, and RevPBE-D3(BJ) approaches. We used a cutoff energy of 400 eV for the plane-wave valence basis and a 3 × 3 × 1 *k*-point mesh for reciprocal-

space integration. Preliminary convergence studies showed that these values are an optimal compromise between accuracy and computational efficiency. The calculated structure parameters and adsorption energies changed by several mÅ and kJ/mol, respectively, when larger cutoff energies 600 eV and 900 eV were used. However, the reported trends did not change.

The systems investigated are formed by the clean, unreconstructed M(100), M(111), or M(110) surfaces as substrate and one benzene molecule as adsorbate. We chose a

$$\begin{pmatrix} 4 & 0 \\ 0 & 4 \end{pmatrix}$$

supercell with four atomic layers for the adsorption on the M(100) and M(111) surfaces and a

$$\begin{pmatrix} 2 & -3 \\ 2 & 3 \end{pmatrix}$$

supercell with seven atomic layers for the adsorption on the M(110) surfaces. For each surface we performed calculations for different adsorption sites and orientations of the benzene molecule.

Geometry optimizations were performed with the PBE-D3 method, which was already used for the study of PTCDA on the Ag(111), Ag(100) and Ag(110) surfaces [9]. For these calculations we chose an energy convergence criterion of 10^{-6} eV for the SCF energy, and of $5 \cdot 10^{-3}$ eV/Å for the ionic relaxation (forces are converged if smaller than $5 \cdot 10^{-3}$ eV/Å). The first three atomic layers of M(100) and M(111) and the first five atomic layers of M(110) were relaxed while the atoms of the lowermost layers were kept at their bulk-like positions. We give two different values for the adsorption distance. d_1 is the vertical distance between the adsorbate and the topmost layer of the surface. The adsorption of benzene effects a slight relaxation of the surface. Therefore we calculate d_1 with respect to the mean value of the *z*-coordinates. d_2 is the distance between the adsorbate and the hypothetical topmost surface layer for an unrelaxed surface. The latter is given since this enables a comparison to data which have been derived from normal incidence X-ray standing waves (NIX-SW) spectroscopy. This may be useful for a comparison with future experimental results, similar to our previous studies [9-11]. Both distances are determined by calculating the difference between the averaged *z*-coordinate of the carbon atoms and the surface atoms.

Potential curves are obtained on the basis of single-point calculations with the PBE-D3, PBE-D3(BJ), PBE-D3(ABC), RPBE-D3, RevPBE-D3(BJ) and RPBE-D3 approaches. We

stepwise altered the distance between the benzene molecule and the unrelaxed surface from 2.5 Å to 5.0 Å. Since d_1 and d_2 do not differ for the potential curve we give only one adsorption distance *d*. Adsorption energies E_{ads} are calculated according to the supramolecular approach: $E_{ads} = E(\text{system}) - E(\text{surface}) - E(\text{adsorbate})$. A Bader analysis [48,49] was performed in order to study the net charge transfer between the surfaces and the adsorbed molecule.

Results and Discussion

First we identified the most stable adsorption sites on the basis of PBE-D3 optimizations by placing the benzene molecule on different adsorption sites and calculating the adsorption energies. The following discussion is limited to the most stable adsorption sites for each surface. Other adsorption sites are higher in energy by 2 to 15 kJ/mol. This points to a relatively high mobility of benzene on the surfaces assuming that the corresponding activation barriers are of similar magnitude. We did not calculate the transition states because this was not the scope of the present study. We also checked that the orientation of the flat lying molecules with respect to the underlying surfaces has no significant influence to the adsorption energies and geometries: A stepwise rotation of the molecule around the *z*-axis changes E_{ads} by less than 1 kJ/mol in each case.

The results of the optimizations are summarized in Table 1. It was found that all metals have the same preferred adsorption sites for the M(111) and M(100) surfaces, the threefold hollow site for M(111) and the fourfold hollow site for M(100), see Figure 1. As a general trend we observe that structures with shorter C–metal distances are more stable than the others. For the M(110) surface it was found that Cu prefers benzene adsorption on a fourfold hollow position, whereas Ag and Au prefer a bridge position, see Figure 1. The notation of the adsorption places refers to the center of the benzene molecule.

The binding between benzene and copper is the largest of all investigated surfaces. E_{ads} is calculated to $E_{ads} = -117$ kJ/mol for Cu(110), $E_{ads} = -114$ kJ/mol for Cu(100) and $E_{ads} = -97$ kJ/mol for Cu(111). For gold the adsorption energies are $E_{ads} = -85$ kJ/mol for the Au(110), $E_{ads} = -87$ kJ/mol for the Au(100), and $E_{ads} = -85$ for the Au(111) surface. The lowest adsorption energies are calculated for the silver surfaces, $E_{ads} = -76$ kJ/mol for Ag(110), $E_{ads} = -75$ kJ/mol for Ag(100) and $E_{ads} = -72$ kJ/mol for Ag(111). It is worth to mention that the adsorption energies on a given metal are almost independent from the surface type. The sole exception is the Cu(110) surface the adsorption energy of which is about -20 kJ/mol smaller than E_{ads} on Cu(100) and Cu(110). For all other systems we find that the adsorption energies on the selected surface planes are within the range of 3 kJ/mol. The results are summarized in Figure 2.

Table 1: Adsorption energies E_{ads} in kJ/mol and adsorption distances d_1 and d_2 in Å obtained with the PBE-D3 functional. d_1 is calculated with respect to the topmost layer of the surface, d_2 (estimated with respect to the unrelaxed surface) is for the sake of comparison to NIX-SW experiments.

surface	E_{ads}			d_1			d_2		
	Cu	Ag	Au	Cu	Ag	Au	Cu	Ag	Au
(111)	−97	−72	−85	2.86	3.17	3.10	2.87	3.19	3.18
(100)	−114	−75	−87	2.45	3.00	2.93	2.47	3.04	3.01
(110)	−117	−76	−85	2.35	2.78	2.84	2.33	2.80	2.84
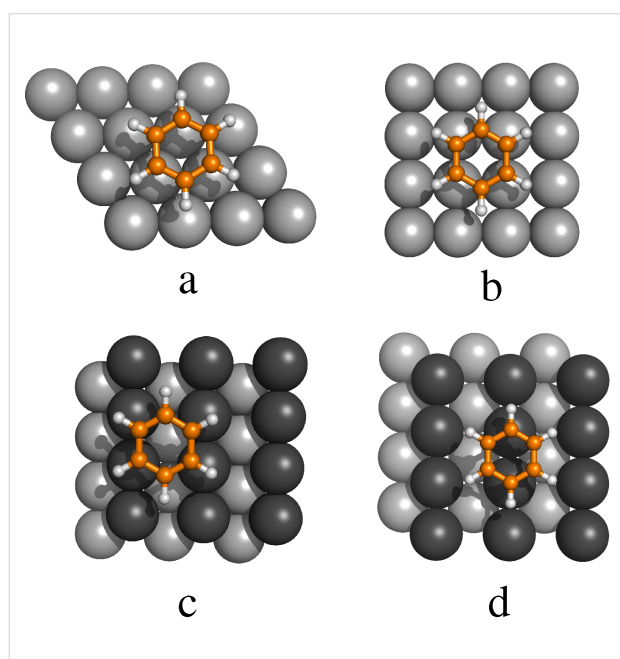
Figure 1: Preferred adsorption sites for benzene: threefold hollow for M(111) (a), fourfold hollow for M(100) (b), fourfold hollow for Cu(110) (c), and bridge for M(110) (d).
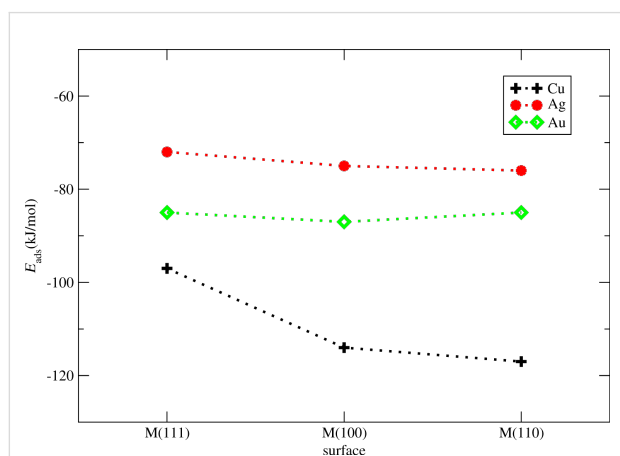
Figure 2: Benzene on Cu, Ag, and Au surfaces. Calculated adsorption energies in kJ/mol for M(111), M(100), and M(110), M = Cu, Ag, Au.

In contrast we observe larger variations for the adsorption distances d_1 and d_2. We limit the discussion to the d_1 values. The d_2 values are only given in order to enable a comparison to future NIX-SW studies. We observe that d_1 is smallest for the (110) surfaces and largest for the (111) surfaces. By comparison of the metals we observe, that the adsorption distances are shortest for the copper surfaces and longest for the silver surfaces. The adsorption distances are $d_1 = 2.86$ Å for Cu(111), $d_1 = 2.45$ Å for Cu(100), $d_1 = 2.35$ Å for Cu(110), $d_1 = 3.17$ Å for Ag(111), $d_1 = 3.00$ Å for Ag(100), $d_1 = 2.78$ Å for Ag(110), $d_1 = 3.10$ Å for Au(111), $d_1 = 2.93$ Å for Au(100) and $d_1 = 2.84$ Å for Au(110). This trend is consistent with the calculated adsorption energies, which are smallest for silver and largest for copper. Unfortunately, to the best of our knowledge no experimentally determined distances are available for these systems. However, previous experimental and theoretical studies of PTCDA on the Ag(111), Ag(100) and Ag(110) surfaces [9,10] indicate that the PBE-D3 and PBE-D3(BJ) approaches give accurate adsorption distances.

A closer look at the optimized structures reveals that the benzene molecule and the underlying surfaces are only slightly affected by adsorption. Therefore, the following comparison of different DFT-D approaches has been performed on the basis of potential curves with fixed structures of benzene and surface. The results of these calculations are summarized in Table 2. The potential curves for the silver surfaces are shown in Figure 3. The potential curves for the copper and gold surfaces are included in Supporting Information File 1.

In all cases the vertical distances obtained with the potential curves for PBE-D3 are in good agreement with the results of the full geometry optimization. This confirms the validity of the simplified approach.

It was found, that PBE-D3 and PBE-D3(BJ) give similar results for all surfaces. The PBE-D3(BJ) adsorption energies tend to be about 4 kJ/mol larger in absolute value than the PBE-D3 energies. This behavior is to be expected: Both methods essentially only differ in the empirical damping function for short-range

Table 2: Results for the adsorption of benzene obtained from potential curves. E_{ads} is given in kJ/mol, d is given in Å.

	Cu(111)		Cu(100)		Cu(110)	
	E_{ads}	d	E_{ads}	d	E_{ads}	d
PBE-D3	−96	2.88	−110	2.58	−111	2.46
PBE-D3(BJ)	−93	2.85	−108	2.58	−113	2.44
RPBE-D3	−100	2.81	−108	2.60	−104	2.54
RevPBE-D3	−127	2.73	−139	2.52	−126	2.50
RevPBE-(BJ)	−143	2.71	−154	2.56	−150	2.44
PBE-D3(ABC)	−76	2.95	−99	2.61	−93	2.49
exp.	−69	—		—	−99	—

	Ag(111)		Ag(100)		Ag(110)	
	E_{ads}	d	E_{ads}	d	E_{ads}	d
PBE-D3	−71	3.20	−75	3.05	−74	2.82
PBE-D3(BJ)	−76	3.08	−82	2.91	−81	2.76
RPBE-D3	−72	3.12	−73	3.06	−69	2.91
RevPBE-D3	−91	3.07	−88	3.04	−81	2.84
RevPBE-(BJ)	−111	2.96	−112	2.85	−105	2.74
PBE-D3(ABC)	−59	3.24	−64	3.09	−63	2.84
exp.	−67	—		—		—

	Au(111)		Au(100)		Au(110)	
	E_{ads}	d	E_{ads}	d	E_{ads}	d
PBE-D3	−83	3.16	−87	3.04	−92	2.72
PBE-D3(BJ)	−84	3.08	−89	2.94	−95	2.69
RPBE-D3	−84	3.10	−85	3.03	−84	2.81
RevPBE-D3	−105	3.07	−103	3.01	−101	2.73
RevPBE-(BJ)	−121	2.98	−123	2.87	−123	2.69
PBE-D3(ABC)	−70	3.19	−74	3.06	−79	2.73
exp.	−73	—		—		—

interaction. The RPBE-D3 curves are quite similar to the PBE-D3 curves. Some deviations are found only for the M(110) surfaces. The difference is less than 8 kJ/mol for all systems. RevPBE and RevPBE-D3(BJ) show larger deviations from the PBE-D3 results. The RevPBE-D3(BJ) adsorption energies are in the range of −31 to −47 kJ/mol, E_{ads}(RevPBE-D3) is 7 to 31 kJ/mol more negative than E_{ads}(PBE-D3). Both approaches overestimate the interaction between benzene and the metal surfaces, in particular RevPBE-D3(BJ). In the second to last line of Table 2 we give the results of PBE-D3(ABC) calculations. The three-body correction to dispersion is repulsive in this case. This is in line with a previous study of the influence of the three-body terms to periodic systems. The PBE-D3(ABC) adsorption energies are 11 to 20 kJ/mol less negative than the PBE-D3 energies. As expected it was found that none of the pure DFT functionals is able to give a correct description of the adsorption. Most potential curves (not shown) are repulsive over the entire distance range. Only the potential curves obtained with the PBE functional exhibit some very flat minima

in the range of −10 kJ/mol at larger distances. Accordingly the calculated adsorption energies can be almost solely ascribed to the dispersion correction. The contribution of E_{disp} to the adsorption energy is larger than 90% for all systems. This confirms that the surface–adsorbate interaction is dominated by dispersion interaction.

Nevertheless we also calculated the charge transfer between benzene and the metal surfaces on the basis of a Bader analysis in order to investigate electrostatic contributions to the interactions. For the Cu(111), Ag(111) and all gold surfaces we observe only a small charge transfer, between 0.02 a.u. (for Ag(111)) and 0.12 a.u. (for Au(100)) from benzene to the metal surface. For the other systems we calculate a small charge transfer from the surface to the benzene molecule in the range of 0.03 (for Ag(100)) to 0.07 a.u. (for Cu(110)). As expected this charge transfer is much smaller than the one between functionalized aromatic compounds and coinage metal surfaces [9,11]. The different direction of the charge transfer may be

Figure 3: Potential curves for the adsorption of benzene on the (a) Ag(111), (b) Ag(100), and (c) Ag(110) surfaces.
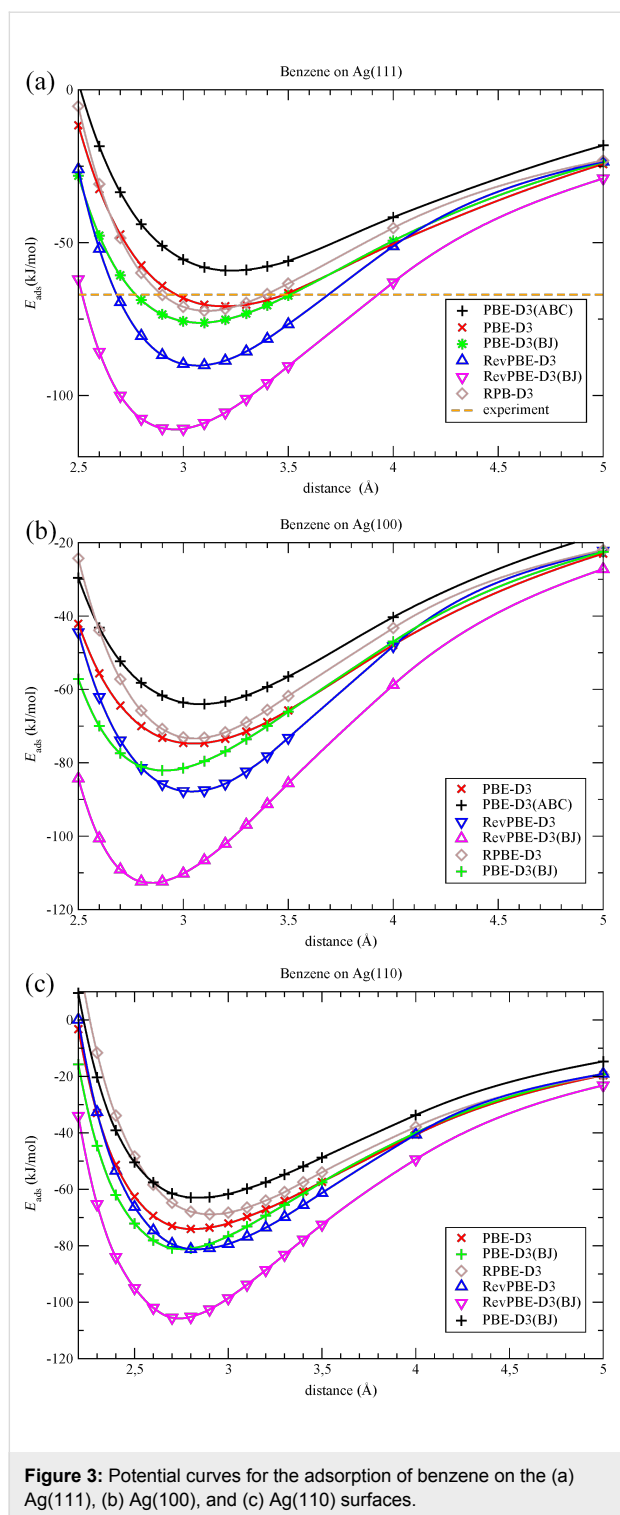
explained by the work function of the metal surfaces. Systems which exhibit a charge transfer to the metal have a larger work function as the systems, in which the charge transfer takes is directed to the adsorbate. The calculated work functions are 4.07 eV for Ag(100), 4.08 eV for Cu(110), 4.13 eV for Ag(110), 4.19 eV for Cu(100), 4.30 eV for Ag(111) 4.49 eV for

Cu(111), 4.77 eV for Au(110), 4.88 eV for Au(100) and 4.91 eV for Au(111).

In Table 3 we compare our calculated results obtained with PBE-D3 and PBE-D3(ABC) to available theoretical and experimental data. The theoretical values show a quite large fluctuation range. In a few cases the deviations can be explained by well known shortcomings of the used methods, which are discussed in literature. However, even the recently developed dispersion DFT methods (vdW-DF and PBE+vdW) exhibit fluctuations of up to 30 kJ/mol for adsorption energies and 0.4 Å for adsorption distances. In general, our results are in good agreement with those other theoretical works that include dispersion effects. Experimental adsorption energies are −69 kJ/mol for Cu(111), −67 kJ/mol for Ag(111), −73 kJ/mol for Au(111), and −99 kJ/mol for Cu(110) [50]. PBE-D3 and RPBE-D3 give the best agreement for the Ag(111) surface. These methods overestimate E_{ads} by 4 or rather 5 kJ/mol. The deviation of PBE-D3(BJ) (overestimation) and PBE-D3(ABC) (underestimation) are of the order of 10 kJ/mol. It appears that all standard DFT-D methods tend to overestimate E_{ads} on the Cu(111) and Au(111) surfaces by at least 10 (Au(111)) to 24 kJ/mol (Cu(111)). The deviations are substantially reduced to −3 kJ/mol for Au(111) and 7 kJ/mol for Cu(111) if the PBE-D3(ABC) method is used. For the Cu(110) surface RPBE-D3 shows the smallest deviation, −5 kJ/mol. PBE-D3 and PBE-D3(BJ) overestimate E_{ads} by 12 to 14 kJ/mol, whereas PBE-D3(ABC) leads to a slight underestimation of 6 kJ/mol. Contributions from the zero-point energy and thermal corrections that lower the adsorption energies are not considered in this work. If these are taken into account we conclude that PBE-D3, PBE-D3(BJ) and RPBE-D3 give a good agreement to experimental adsorption energies. For the M(111) surfaces we get a slightly better agreement if the three-center terms are considered. RevPBE-D3 and RevPBE-D3(BJ) differ by up to −58 kJ/mol (RevPBE-D3) and −74 kJ/mol from the experimental results. Therefore we conclude that RevPBE-D3 and RevPBE-D3(BJ) methods are not suited for the calculation of aromatic organic compounds on these metal surfaces. However, the application of the other DFT-D methods treated in this work can be recommended.

The differences in adsorption distances for the recommended methods are in the range from 0.03 to 0.18 Å. As expected, PBE-D3(ABC) gives the largest distances for all systems due to the repulsive nature of the three-center terms. However, the deviation from the PBE-D3 distance is less than 0.07 Å. Therefore it is possible to neglect these contributions in structure optimizations without significant loss of accuracy, which is advantageous since the calculation of the three-center terms is rather expensive for large systems.

Table 3: Comparison of adsorption energies E_{ads} in kJ/mol and adsorption distances d in Å with available theoretical and experimental data.

system	E_{ads}	d	method, source
Cu(111)	−79	2.83	optB86b, [37]
	−71	2.91	optB88, [37]
	−66	3.14	optPBE, [37]
	−51	3.46	revPBE, [37]
	−47	3.39	rPW86, [37]
	−34	3.6	MP2, [35]
	−3	—	PW91, [36]
	−98	3.04	PBE+vdW [29]
	−76	2.79	PBE+vdW^{surf} [29]
	−48	4.14	vdW-DF [29]
	−45	3.38	vdW-DF2 [29]
	−61	3.08	optPBE-vdW [29]
	−66	3.12	optB88-vdW [29]
	−69		opt-B86b-vdW [29]
	−96	2.88	PBE-D3, this work
	−76	2.95	PBE-D3(ABC), this work
	−69	—	experiment, [51,52]
Cu(110)	−109	2.003	VWN, [39]
	−39	—	GGA-DFT [38]
	−111	2.46	PBE-D3, this work
	−93	2.49	PBE-D3(ABC), this work
	−99	—	experiment, [51]
Ag(111)	−72	—	PBE+vdW^{surf}, [31]
	−70	—	optB88-vdW, [31]
	−73	3.02	optB86b, [37]
	−70	3.08	optB88, [37]
	−69	3.23	optPBE, [37]
	−53	3.51	revPBE, [37]
	−50	3.40	rPW86, [37]
	−32	3.7	MP2, [35]
	−5	—	PW91, [36]
	−80	3.14	PBE+vdW [29]
	−70	2.96	PBE+vdW^{surf} [29]
	−50	3.95	vdW-DF [29]
	−45	3.40	vdW-DF2 [29]
	−65	3.29	optPBE-vdW [29]
	−69	3.12	optB88-vdW [29]
	−73	3.10	opt-B86b-vdW [29]
	−71	3.20	PBE-D3, this work
	−59	3.24	PBE-D3(ABC), this work
	−67	—	experiment, [52,53]
Au(111)	−83	3.03	optB86b, [37]
	−79	3.08	optB88, [37]
	−69	3.21	optPBE, [37]

Table 3: Comparison of adsorption energies E_{ads} in kJ/mol and adsorption distances d in Å with available theoretical and experimental data. (continued)

	−54	3.44	revPBE, [37]
	−53	3.31	rPW86, [37]
	−71	3.05	PBE+vdW^{surf}, [31]
	−76	3.23	optB88-vdW, [31]
	−57	3.44	vdW-DF, [31]
	−54	3.29	vdW-DF2, [31]
	−41	3.7	RPBE-vdW, [32]
	−30	3.8	MP2, [35]
	−8	—	PW91, [36]
	−77	3.21	PBE+vdW [29]
	−70	3.05	PBE+vdW^{surf} [29]
	−57	3.44	vdW-DF [29]
	−54	3.29	vdW-DF2 [29]
	−72	3.22	optPBE-vdW [29]
	−76	3.23	optB88-vdW [29]
	−81	3.12	opt-B86b-vdW [29]
	−83	3.16	PBE-D3, this work
	−70	3.19	PBE-D3(ABC), this work
	−73	—	experiment, [52,54]
Au(100)	−185	2.376	VWN, [34]
	−87	3.04	PBE-D3, this work
	−74	3.06	PBE-D3(ABC), this work

In Table 4 we give the C_3 coefficients for the benzene adsorption on the Au(111) surface. The data are compared to the C_3 coefficient for the PBE+vdW^{surf} functional, which is constructed to reproduce the exact values [29]. The C_3 coefficients are fitted from the pure dispersion interaction term at large distances according to the method described in [29].

It was found that PBE-D3, PBE-D3(BJ) RPBE-D3, RevPBE-D3 and RevPBE-D3(BJ) overestimate (by 30%) the C_3 coefficients compared to PBE+vdW^{surf} whereas PBE-D3(ABC)

Table 4: C_3 coefficients in eV·Å^3 for benzene on the Au(111) surface.

method	C_3	
PBE-D3	12.23 ± 0.24	
PBE-D3(BJ)	12.23 ± 0.24	
RPBE-D3	11.95 ± 0.22	
RevPBE-D3	12.48 ± 0.27	
RevPBE-D3(BJ)	13.42 ± 0.49	
PBE-D3(ABC)	3.89 ± 0.39	
PBE+vdW^{surf}	9.16 ± 0.08	[29]

underestimates them (by 50%). It has to be mentioned, however, that the values of the C_3 coefficients strongly depend on the functional. For example, in [29] values between 4 and 9 eV·Å^3 have been reported. Accordingly, we think that our deviations are within a reliable range.

Conclusion

The adsorption of benzene on the M(111), M(100) and M(110) surface of the coinage metals copper, silver and gold is studied with different DFT-D3 methods. RevPBE-D3 and RevPBE-D3(BJ) overestimate the surface–adsorbate interaction, PBE-D3, PBE-D3(BJ) and RPBE-D3 give similar results for adsorption energies with better agreement to experimental data. The calculated adsorption energies decrease in the ordering Cu > Au > Ag and M(110) > M(100) > M(111). The latter trend can be explained with the increasing coordination number of the surface metal atoms. The higher reactivity of gold compared to silver is attributed to the larger polarizability of the gold atoms. The adsorption distances are almost the same on these two surfaces due to the similar van der Waals radii of 172 pm for Ag [55] and 166 pm for Au [55]. Hence, the larger C_6 coefficients of 317.2 a.u. for the gold atoms [56] (compared to 268.6 a.u. for the silver atoms [56]) result in a larger dispersion interaction between the surface and the substrate. Copper has the smallest polarizability of the three metals. The C_6 coefficients for the surface atoms is 175.0 a.u. within the D3-correction [56]. However, the benzene molecules come closer to the copper surfaces due to the smaller van der Waals radius of 140 pm [55]. From there the dispersion interaction to the copper surface is largest although Cu has the smallest C_6 coefficients. PBE-D3, PBE-D3(BJ) and RPBE-D3 tend to slightly overestimate the adsorption energies in comparison to experiment, in particular for the Cu(111) surface. This effect is reduced when the three-body correction to dispersion is considered. The PBE-D3(ABC) adsorption energies are smaller in absolute value by 10 to 20 kJ/mol compared to the standard PBE-D3 values. This leads in most cases to a slightly better agreement with the available experimental results. As a result of this work we recommend DFT-D methods like PBE-D3, PBE-D3(BJ) or RPBE-D3 for the theoretical study of the adsorption of aromatic compounds on metal surfaces. Due to the high computational cost of the evaluation of three-center terms, we suggest to perform geometry optimizations with PBE-D3 followed by single-point calculations with PBE-D3(ABC) for adsorption energies. Surprisingly, we realize that the RevPBE-D3 and RevPBE-D3(BJ) methods, which yield a more realistic description of the adsorption of small molecules on ionic surfaces [26], seem to be not suitable for the present systems. Since the pure RevPBE potential curves are repulsive one can ascribe the observed overestimation of the adsorption energies solely to the dispersion correction.

We give adsorption distances with respect to the topmost layer of the relaxed surface, and with respect to the hypothetical topmost surface layer for an unrelaxed surface. The latter allows for a comparison to data from NIX-SW spectroscopy. It was found, that vertical distances are smallest for the M(110) surfaces and largest for the M(111) surfaces, in accordance with the trends of the adsorption energies. The distances on the copper surfaces are in the range from 2.35 to 2.86 Å, the distances on the silver surfaces in the range from 2.78 to 3.17 Å, and the distances on the gold surfaces are in the range from 2.84 to 3.18 Å. It will be interesting to compare these data with future experimental data.

Supporting Information

Supporting information features potential curves for the adsorption on the Cu(111), Cu(100), Cu(110), Au(111), Au(100), and Au(110) surfaces.

Supporting Information File 1
Potential curves for adsorption of benzene on copper and gold surfaces.
[http://www.beilstein-journals.org/bjoc/content/supplementary/1860-5397-10-185-S1.pdf]

Acknowledgements

References
1. Hausschild, A.; Karki, K.; Cowie, B. C. C.; Rohlfing, M.; Tautz, F. S.; Sokolowski, M. *Phys. Rev. Lett.* **2005,** *94,* 036106. doi:10.1103/PhysRevLett.94.036106
2. Ji, W.; Lu, Z. Y.; Gao, H. J. *Phys. Rev. B* **2008,** *77,* 113406. doi:10.1103/PhysRevB.77.113406
3. Kilian, L.; Hausschild, A.; Temirov, R.; Soubatch, S.; Schöll, A.; Bendounan, A.; Reinert, F.; Lee, T. L.; Tautz, F. S.; Sokolowski, M.; Umbach, E. *Phys. Rev. Lett.* **2008,** *100,* 136103. doi:10.1103/PhysRevLett.100.136103
4. Romaner, L.; Nabok, D.; Puschnig, P.; Zojer, E.; Ambrosch-Draxl, C. *New J. Phys.* **2009,** *11,* 053010. doi:10.1088/1367-2630/11/5/053010
5. Tours, J. M.; Jones, L.; Pearson, D. L.; Lamba, J. J. S.; Burgin, T. B.; Whitesides, G. M.; Allara, D. A.; Parikh, A. N.; Atre, S. V. *J. Am. Chem. Soc.* **1995,** *117,* 9529. doi:10.1021/ja00142a021
6. Witte, G.; Wöll, C. *J. Mater. Res.* **2004,** *19,* 1889. doi:10.1557/JMR.2004.0251
7. Barlow, S. M.; Raval, R. *Surf. Sci. Rep.* **2003,** *50,* 201. doi:10.1016/S0167-5729(03)00015-3
8. Umbach, T. R.; Fernandez-Torrente, I.; Ladenthin, J. N.; Pascual, J. I.; Franke, K. J. *J. Phys.: Condens. Matter* **2012,** *24,* 354003. doi:10.1088/0953-8984/24/35/354003

9. Bauer, O.; Mercurio, G.; Willenbockel, M.; Reckien, W.; Schmitz, C.; Fiedler, B.; Soubatch, S.; Bredow, T.; Tautz, F.; Sokolowski, M. *Phys. Rev. B* **2012,** *86,* 235431. doi:10.1103/PhysRevB.86.235431

10. Mercurio, G.; Bauer, O.; Willenbockel, M.; Fairley, N.; Reckien, W.; Schmitz, C.; Fiedler, B.; Soubatch, S.; Bredow, T.; Sokolowski, M.; Tautz, F. *Phys. Rev. B* **2013,** *87,* 045421. doi:10.1103/PhysRevB.87.045421

11. Fiedler, B.; Reckien, W.; Bredow, T.; Beck, J.; Sokolowski, M. *J. Phys. Chem. C* **2014,** *118,* 3035–3048. doi:10.1021/jp407579z

12. Dronskowski, R. *Computational Chemistry of Solid State Materials: A Guide for Materials Scientists, Chemists, Physicists and others;* Wiley-VCH: Weinheim, 2005. doi:10.1002/9783527612277

13. Grimme, S.; Antony, J.; Ehrlich, S.; Krieg, H. *J. Chem. Phys.* **2010,** *132,* 154104. doi:10.1063/1.3382344

14. Grimme, S. *J. Comput. Chem.* **2004,** *25,* 1463–1473. doi:10.1002/jcc.20078

15. Grimme, S. *J. Comput. Chem.* **2006,** *27,* 1787–1799. doi:10.1002/jcc.20495

16. Grimme, S.; Ehrlich, S.; Goerigk, L. *J. Comput. Chem.* **2011,** *32,* 1456–1465. doi:10.1002/jcc.21759

17. Klimes, J.; Bowler, D. R.; Michaelides, A. *J. Phys.: Condens. Matter* **2010,** *22,* 022201. doi:10.1088/0953-8984/22/2/022201

18. Ruiz, V. G.; Liu, W.; Zojer, E.; Scheffler, M.; Tkatchenko, A. *Phys. Rev. Lett.* **2012,** *108,* 146103. doi:10.1103/PhysRevLett.108.146103

19. Dion, M.; Rydberg, H.; Schröder, E.; Langreth, D. C.; Lundqvist, B. I. *Phys. Rev. Lett.* **2004,** *92,* 246401. doi:10.1103/PhysRevLett.92.246401

20. Zhao, Y.; Schultz, N. E.; Truhlar, D. G. *J. Chem. Theory Comput.* **2006,** *2,* 364–382. doi:10.1021/ct0502763

21. Thonhauser, T.; Cooper, V. R.; Li, S.; Puzder, A.; Hyldgaard, P.; Langreth, D. C. *Phys. Rev. B* **2007,** *76,* 125112. doi:10.1103/PhysRevB.76.125112

22. Vydrov, O. A.; Voorhis, T. V. *J. Chem. Phys.* **2010,** *133,* 244103. doi:10.1063/1.3521275

23. Harl, J.; Kresse, G. *Phys. Rev. B* **2008,** *77,* 045136. doi:10.1103/PhysRevB.77.045136

24. Rohlfing, M.; Bredow, T. *Phys. Rev. Lett.* **2008,** *101,* 266106. doi:10.1103/PhysRevLett.101.266106

25. Reckien, W.; Janetzko, F.; Peintinger, M.; Bredow, T. *J. Comput. Chem.* **2012,** *33,* 2023–2031. doi:10.1002/jcc.23037

26. Ehrlich, S.; Moellmann, J.; Reckien, W.; Bredow, T.; Grimme, S. *ChemPhysChem* **2011,** *12,* 3414–3420. doi:10.1002/cphc.201100521

27. Moellmann, J.; Ehrlich, S.; Tonner, R.; Grimme, S. *J. Phys.: Condens. Matter* **2012,** *24,* 424206. doi:10.1088/0953-8984/24/42/424206

28. S. Grimme, private communication.

29. Carrasco, J.; Liu, W.; Michaelides, A.; Tkatchenko, A. *J. Chem. Phys.* **2014,** *140,* 084704. doi:10.1063/1.4866175

30. Liu, W.; Ruiz, V. G.; Zhang, G.; Santra, B.; Ren, X.; Scheffler, M.; Tkatchenko, A. *New J. Phys.* **2013,** *15,* 053046. doi:10.1103/PhysRevB.86.245405

31. Liu, W.; Carrasco, J.; Santra, B.; Michaelides, A.; Scheffler, M.; Tkatchenko, A. *Phys. Rev. B* **2012,** *86,* 245405. doi:10.1103/PhysRevB.86.245405

32. Wellendorff, J.; Kelkkanen, A.; Mortensen, J. J.; Lundqvist, B. I.; Bligaard, T. *Top. Catal.* **2010,** *53,* 378–383. doi:10.1007/s11244-010-9443-6

33. Jenkins, S. J. *Proc. R. Soc. London, Ser. A* **2009,** *465,* 2949–2976. doi:10.1098/rspa.2009.0119

34. Chen, W.; Cao, M.-J.; Liu, S.-H.; Lu, C.-H.; Xu, Y.; Li, J.-Q. *Chem. Phys. Lett.* **2006,** *417,* 414–418. doi:10.1016/j.cplett.2005.09.141

35. Caputo, R.; Prascher, B. P.; Staemmler, V.; Bagus, P. S.; Wöll, C. *J. Phys. Chem. A* **2007,** *111,* 12778–12784. doi:10.1021/jp076339q

36. Bilic, A.; Jeffrey, A. B.; Hush, N. S.; Hoft, R. C.; Ford, M. J. *J. Chem. Theory Comput.* **2006,** *2,* 1093–1105. doi:10.1021/ct050237r

37. Yildirim, H.; Greber, T.; Kara, A. *J. Phys. Chem. C* **2013,** *117,* 20572–20583. doi:10.1021/jp404487z

38. Atodiresei, N.; Caciuc, V.; Blügel, S.; Hölscher, H. *Phys. Rev. B* **2008,** *77,* 153408. doi:10.1103/PhysRevB.77.153408

39. Rogers, B. L.; Shapter, J. G.; Ford, M. J. *Surf. Sci.* **2004,** *548,* 29–40. doi:10.1016/j.susc.2003.11.026

40. Kresse, G.; Hafner, J. *Phys. Rev. B* **1993,** *47,* 558–561. doi:10.1103/PhysRevB.47.558

41. Kresse, G.; Hafner, J. *Phys. Rev. B* **1994,** *49,* 14251–14269. doi:10.1103/PhysRevB.49.14251

42. Kresse, G.; Furtmüller, J. *Phys. Rev. B* **1996,** *54,* 11169–11186. doi:10.1103/PhysRevB.54.11169

43. Kresse, G.; Joubert, D. *Phys. Rev. B* **1999,** *59,* 1758–1775. doi:10.1103/PhysRevB.59.1758

44. Perdew, J. P.; Burke, K.; Ernzerhof, M. *Phys. Rev. Lett.* **1996,** *77,* 3865–3868. doi:10.1103/PhysRevLett.77.3865

45. Hammer, B.; Hansen, L. B.; Norskov, J. K. *Phys. Rev. B* **1999,** *59,* 7413–7421. doi:10.1103/PhysRevB.59.7413

46. Zhang, Y.; Yang, W. *Phys. Rev. Lett.* **1998,** *80,* 890. doi:10.1103/PhysRevLett.80.890

47. Rezac, J.; Hobza, P. *J. Chem. Theory Comput.* **2012,** *8,* 141. doi:10.1021/ct200751e

48. Bader, R. F. W. *Atoms in Molecules. A Quantum Theory;* Oxford Science Publications/Clarendon Press: London, 1990.

49. Henkelman, G.; Arnaldsson, A.; Jonsson, H. *Comput. Mater. Sci.* **2006,** *36,* 354. doi:10.1016/j.commatsci.2005.04.010

50. Lomas, J. R.; Baddeley, C. J.; Tikhov, M. S.; Lambert, R. M. *Langmuir* **1995,** *11,* 3048. doi:10.1021/la00008a033

51. Xi, M.; Yang, M.; Jo, S.; Bent, B.; Stevens, P. *J. Chem. Phys.* **1995,** *101,* 9122. doi:10.1063/1.468041

52. Campbell, C. T.; Sellars, J. R. V. *J. Am. Chem. Soc.* **2012,** *134,* 18109. doi:10.1021/ja3080117

53. Zhou, X. L.; Castro, M. E.; White, J. M. *Surf. Sci.* **1990,** *238,* 215. doi:10.1016/0039-6028(90)90079-N

54. Syomin, D.; Kim, J.; Koel, B. E.; Ellison, G. B. *J. Phys. Chem. B* **2001,** *105,* 8387. doi:10.1021/jp012069e

55. Bondi, A. *J. Phys. Chem.* **1964,** *68,* 441. doi:10.1021/j100785a001

56. Homepage of the D3-correction. http://www.thch.uni-bonn.de/tc/dftd3 (accessed Feb 27, 2014).

Macrocyclic bis(ureas) as ligands for anion complexation

Claudia Kretschmer, Gertrud Dittmann and Johannes Beck[*]

Abstract

Two macrocyclic bis(ureas) **1** and **2**, both based on diphenylurea, have been synthesized. Compound **1** represents the smaller ring with two ethynylene groups as linkers and **2** the larger ring with two butadiynylene groups. On thermal treatment to 130 °C molecule **1** splits up into two dihydroindoloquinolinone (**3**) molecules. Both compounds **1** and **2** form adducts with polar molecules such as dimethyl sulfoxide (DMSO) and dimethylformamide (DMF) and act as complexing agents towards a series of anions (Cl^-, Br^-, I^-, NO_3^-, HSO_4^-). The crystal structures of **3**, **2**·2DMSO, **2**·2DMF, and of the complex $NEt_4[Br·2]$ have been determined. Quantitative investigations of the complexation equilibria were performed via ^1H NMR titrations. While **1** is a rather weak complexing agent, the large ring of **2** binds anions with association constants up to log K = 7.93 for chloride ions.

Introduction

Supramolecular chemistry – the "chemistry beyond the molecule" – is an area of modern chemistry, which has grown exponentially in the last decades [1,2]. Among the many concepts of supramolecular interactions, anion coordination chemistry has always been an intensively explored field, which still offers substantial progress [3-5].

The urea group has proven to be an excellent anion receptor. The ability to form two directional hydrogen bonds through the highly polarized N−H groups towards different kinds of anions allows for building particular molecular arrangements. Incorporation of two or three urea groups into one molecular

entity enables the formation of complex building units. Tripodal tris(ureas) were synthesized, which contain tetrahedral oxoanions like phosphate or sulfate [6,7] and ligands with three concatenated urea functions were shown to form 2:2 complexes with phosphate anions [8]. Anion complexation is also possible with a rigid planar ligand, as was shown by indole-based macrocycles [9]. This ligand system represents a stiff ring of two bis(indole) units connected via two ethynylene groups as linkers. As proven by a crystal structure determination, a chloride ion fits into the cavity bound via four N−H···Cl bonds and strong complexation was observed with several other anions. In the ^1H NMR spectra a significant dependence of the chemical

shift of the N−H proton with the kind of bound anion was observed and the association constants as high as log K = 6.2 for Cl⁻ were determined.

We achieved the synthesis of a macrocyclic planar bis(triazene), in which two diphenyltriazene units were linked by two ethynylene groups. On deprotonation, a dianionic planar bis(triazenide) ligand is formed, which takes up several different transition metal ions, preferredly in the divalent state [10]. Linking two diphenylurea groups by one ethynylene or butadiynylene group gives a stiff arrangement but leaves one degree of freedom in the system, since rotation around the linking group is possible. This approach was realized by Steed and coworkers, who showed that on adding chloride ions planarization occurs and a rather high binding constant of log K = 2.55 for the complexation of Cl⁻ was determined [11]. Introducing a second bridging unit would give a ring containing two diphenylurea units connected via two stiff linking units. Since the urea unit N−C(O)−N and the triazenide unit N−N=N are isosteric, we complemented our bis(triazene) ligand system by cyclic bis(ureas). This opens the possibility for complexation of cations and anions with two isosteric ligands, just under exchange of the active groups within the respective ring system. Here we describe our results concerning macrocyclic bis(ureas) with a rather rigid molecular entity.

Results and Discussion

The synthesis of the two macrocyclic diphenylureas **1** and **2** proceeds straightforward from the respective 2,2'-diamino derivatives of diphenylethyne (tolane) and diphenylbuta-1,3-diyne with carbonyldiimidazole (Scheme 1).

In both cases, the cyclization products were selectively formed in good yields. The quest for the molecular conformation is challenging for both molecules. Since the bis(triazenide) congeners of **1** and **2** are planar, one can presume an analogous

molecular shape for the bis(ureas). All attempts to obtain single crystals of **1** for a structure determination failed. Crystallization from solution gave only microcrystalline material. When we tried to obtain crystals via vacuum sublimation, a complete vaporisation at temperatures above 130 °C and deposition of colourless crystals were observed. A crystal structure analysis of the deposited crystals, however, revealed that a fragmentation and rearrangement reaction had occurred. Under the applied conditions **1** is completely converted to dihydroindoloquinolinone **3** (Scheme 2).

Scheme 2: Formation of dihydroindoloquinolinone **3** from **1** by vacuum sublimation.
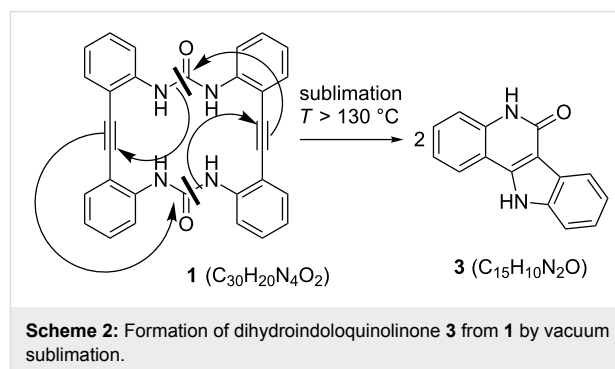
In accordance with the effortlessness of the conversion reaction, the mass spectrum of **1** is dominated by the [M/2]⁺ signal. The indoloquinolinone **3** forms essentially planar molecules (see Supporting Information File 1, Figure S8). Indoloquinolinones can be synthesized by multistep procedures from suitable precursors [12-14]. Using thermolysis for the synthesis of indoloquinolines has already been reported. Cyclization of aminophenyl substituted tolane isocyanates lead to indoloquinolinones. The crystal structure of the *N*-methylated congener of **3** has been determined [15].

Thermal treatment of **2** does not lead to fragmentation or sublimation of volatile material as observed for **1**. Macrocycle **2** is
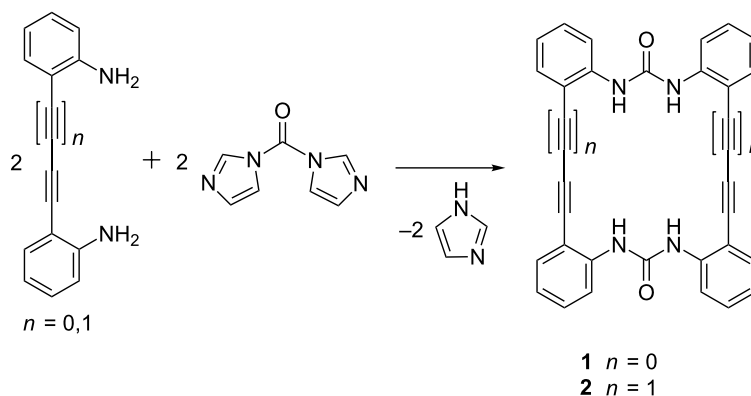
Scheme 1: Synthesis of the macrocyclic bis(ureas) **1** and **2**.

soluble in dimethylformamide (DMF) or dimethyl sulfoxide (DMSO) and can be crystallized from solution as light-yellow crystals (see Supporting Information File 1, Figure S4). These crystals incorporate associated solvent molecules, which are difficult to remove and lead to discrepancies in the elemental analyses towards the calculated compositions even after excessive pumping at elevated temperatures. A bluish coloration of the yellow material is already observed after prolonged keeping under vacuum at ambient temperature. Thermal treatment in vacuo at temperatures above 200 °C leaves a dark blue material (see Supporting Information File 1, Figure S2). Dissolving the blue material in DMF or DMSO leads to an almost complete dissolution and a yellow solution, leaving behind only a small portion of dark insoluble material. The nature of the yellow-to-blue transformation is presently unclear. Partial cyclization reactions in the solid material or formation of polymers via radical mechanisms seem probable.

When crystallized from DMF or DMSO, **2** forms stable 1:2 adducts with these solvent molecules. Crystals were examined by X-ray single crystal diffraction [16]. Both compounds, **2**·2DMF and **2**·2DMSO, are not crystallographically isotypic but the molecular entities are completely analogous and may be discussed jointly. In both cases the macrocyclic ring is mainly flattened and two molecules of DMF or DMSO are coordinated above and below the ring plane (Figure 1). A plane through all atoms except the C and O atoms of the urea groups is rather well fulfilled with the largest deviation found for C13 with 0.3 Å. The urea groups themselves are planar but tilted by 28° against the main plane of the outer ring. This is caused by the N−H···O bonds to the O atom of the DMF molecule with H···O separations of 2.00(1) and 2.07(2) Å. The somewhat lower basicity of DMSO is manifested in longer N−H···O bonds of 2.09(1) and 2.18(2) Å in the **2**·2DMSO adduct.

Since immediate experimental data for the structure of the unsolvated macrocyclic bis(ureas) were not obtainable, we used molecular mechanics calculations as implemented in the SPARTAN program suite [17] to calculate the respective structures. In both cases, the molecules are obtained as far from planarity (see Supporting Information File 1, Figure S6 and Figure S7). Actually, a strong tilting is expected for both **1** and **2**. According to these calculations, the small ring of **1** forces the two urea groups into a head-to-tail arrangement with short intramolecular hydrogen bridges. An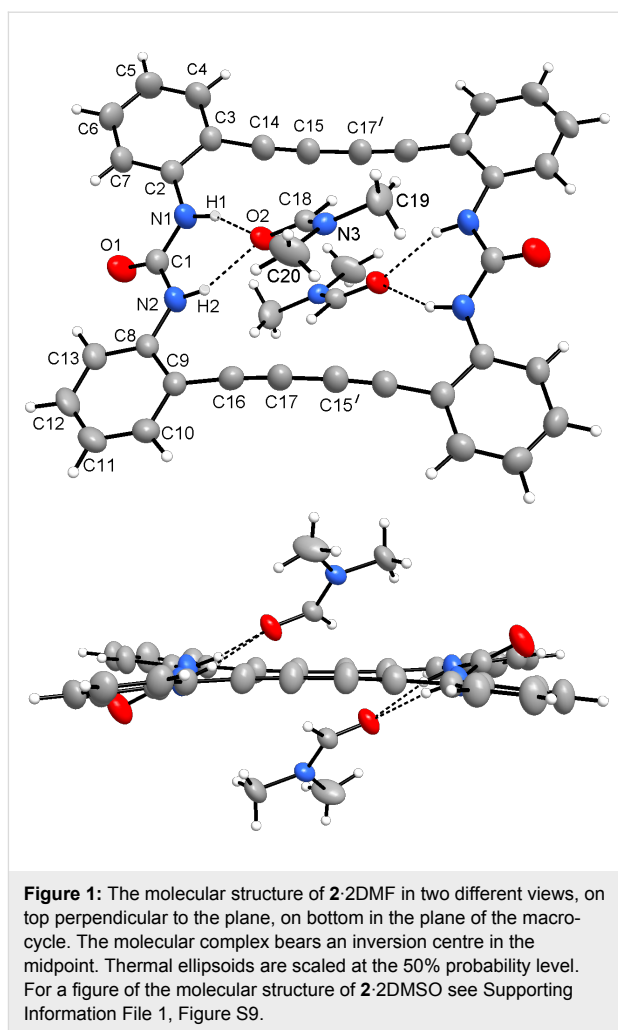 even stronger tilting of the molecule is expected for **2**. Here, the distances are too large for any intramolecular N−H···O bridging bonds.

As a strong anion complexing agent **2** binds halide anions even in DMSO as solvent, despite DMSO itself is bound to the urea functional groups (Figure 1). If an excess of NEt₄Br is added to

Figure 1: The molecular structure of **2**·2DMF in two different views, on top perpendicular to the plane, on bottom in the plane of the macrocycle. The molecular complex bears an inversion centre in the midpoint. Thermal ellipsoids are scaled at the 50% probability level. For a figure of the molecular structure of **2**·2DMSO see Supporting Information File 1, Figure S9.

a solution of **2** in DMSO, on slow evaporation yellow crystals of NEt₄[Br·**2**] are separated. The crystal structure consists of ion pairs, tetraethylammonium cations and bromide anions, which are located in the cavity of the macrocycle (Figure 2). The ligand is strongly tilted. The four N−H···Br bonds, however, show uniform lengths (H1−Br, 2.72; H2−Br, 2.74; H3−Br, 2.75; H4−Br, 2.71 Å; N−H···O angles 149–169°). The representation with space filling radii shows that the halide anion fits well into the bis(urea) ring. The ammonium ions are located in the saddle shaped cavity formed by the twisted bis(urea).

The binding properties of **1** and **2** towards anions were studied by ¹H NMR spectroscopy. As **2** was sufficiently soluble, tetrahydrofuran (THF) turned out as a suitable solvent for the spectroscopic investigations. On addition of tetrabutylammonium salts with different anions significant changes in the spectra emerge. The N−H proton resonances are shifted downfield with increasing effect in the order of $I^- < HSO_4^- < NO_3^- < Br^- < Cl^-$. With the large complex anion PF_6^-, however, no effect was detected, indicating that no interaction occurred. The

Figure 2: Molecular structure of the anionic complex in NEt₄[Br·**2**]. Two different representations are given, on top with thermal ellipsoids scaled at the 50% probability level, on bottom in a space filling representation showing the strong twist of the macrocyclic bis(urea) ligand.

Figure 3: ¹H NMR spectra of **2** in THF-d_8 after addition of several different tetrabutylammonium salts. The N−H proton resonances show a distinct dependence on the kind of the present anion.

For **1**, which is in pure form soluble only in DMF or DMSO, it was possible to record spectra in acetone-d_6, since the solubility was highly increased by the addition of ammonium salts and subsequent complex formation. The effects on the N−H proton resonances are weaker compared with **2** (see Supporting Information File 1, Figure S11).

Since no signals of the free host and of the anionic complexes are simultaneously present, the exchange rate between the anion and the host molecules is fast compared to the NMR timescale. However, the broadening of the signals by adding anion amounts around 0.5 equivalents may be interpreted as a coalescence phenomenon caused by an exchange between loaded and unloaded host. After the amount of the anion reaches a molar ratio of 1:1, the N−H proton resonance of **2** shows no further increase in the shift, indicating that a 1:1 complex has been formed (Figure 4). To ensure the composition of the host–guest complexes Job plots were used. The function molar fraction vs the product of molar fraction multiplied by the shift change Δδ allows for the determination of the molar fractions of host and guest. From the maximum of the extrapolated curve the molar fraction of the complex is obtained (see Supporting Information File 1). For I⁻, NO₃⁻, and Br⁻ maxima at 0.50, 0.54, and

phenyl proton resonances are also affected by the effect. The protons at positions A, B, C (see Figure 3) are shifted slightly upfield, while the phenyl protons in position D *ortho* to the urea substituents are shifted downfield for the weaker complexes with HSO₄⁻ and NO₃⁻ but upfield for the stronger complexes formed with Br⁻ and Cl⁻. The effect on the phenyl protons amounts to maximally 0.3 ppm and is much weaker than the effect on the urea protons where shifts up to 1.7 ppm are observed. The relatively strong influence on the resonances of the ortho positioned protons may arise from the interaction with the carbonyl oxygen atom of the urea groups. This interaction is sensitive on the conformation of the flexible macrocyclic ring system. Comparing the crystal structures of **2**·2DMSO/DMF with [Br·**2**]⁻ shows a slight decrease of the mean O···H(ortho) distance from 2.32 to 2.25 Å.

Figure 4: ^{1}H NMR spectra of **2** in THF-d_8 after addition of increasing molar equivalents of tetrabutylammonium nitrate. The N−H proton resonance shows a distinct downfield shift depending on the concentration of the anion. The small invariant DMF signal originates from the solvent of recrystallization used to purify the sample for the NMR experiments.

0.55 were found, which leads to the ratio of one host molecule and one guest molecule. For Cl⁻, the anion with the strongest shift effect, a maximum at 0.68 is present, indicating a complex of two bis(urea) molecules and one chloride ion. For the smaller macrocyclus **1** the Job plots do not show a distinct plateau after addition of one equivalent of anion. Here, doubtless an interaction is present but apparently not a distinct host–guest complex formation.

The binding constants were determined with the help of the program WinEQNMR2 [18]. Table 1 contains the obtained constants. The association constants of **2** with nitrate, bromide and iodide were obtained by fitting the titration curves and the subsequent calculation to a 1:1 binding mode. This binding mode was already confirmed by the Job plots for all anions except Cl⁻. Because the Job plot for the complex formation between **2** and nitrate shows the maximum of the curve not exactly at a molar ratio of 0.5 additional investigations via ESI

mass spectrometry studies of NEt₄[NO₃·**2**] were undertaken. Signals at m/z = 515.2 and 578.2 clearly indicate the masses of the neat macrocycle **2** and the complex [NO₃·**2**]. Signals originating from higher masses at 640.13 (**2** with two molecules nitrate) or 1094.31 (two molecules of **2** with one molecule nitrate) could not be detected. So the 1:1 binding mode seems the most plausible ratio. After evaluating the Job plots of the complex of **2** and chloride, a 2:1 binding mode for the calculation of the association constants was used. Reliable association constants for the smaller macrocycle **1** could only be obtained in the case of chloride.

A short look at the binding constants reflects the amount of the chemical shifts in the ^{1}H NMR spectra. Bromide is bound strongly to **2** in the 1:1 binding mode. Nitrate is bound weaker than bromide but still stronger than iodide, and chloride in the 2:1 binding mode shows a high association constant of log K = 7.93. The binding constants for the known ring opened

Table 1: Binding constants of the macrocyclic bis(ureas) **1** and **2** towards different anions. All anions were used as tetrabutylammonium salts. Compound **2** was dissolved in THF-d_8 and **1** in DMSO-d_6. All NMR spectra were taken at room temperature (298 K).

Anion	Receptor **2**		Receptor **1**	
	K	log K	K	log K
I⁻	1775 ± 97 M⁻¹	3.25		
NO₃⁻	43.556 ± 430 M⁻¹	4.64		
Br⁻	5.1·10⁶ ± 5100 M⁻¹	6.71		
Cl⁻	8.57·10⁷ ± 9.21·10⁴ M⁻²	7.93	202 M⁻¹	2.31

congener of **2** are significantly lower (log K (Cl$^-$) = 2.55 and log K (Br$^-$) = 1.56) [11] underlining the vast influence of the macrocyclic effect.

Conclusion

Two macrocyclic bis(ureas) have been synthesized and examined for their anion complexation properties. The larger ring with two butadiynylene groups as spacers turned out as a suitable receptor for small anions with high binding constants. The molecule is flexible. In the complex with a bromide ion embedded in the ring cavity, the cyclic ligand is strongly tilted. The smaller cycle with ethynylene groups as linkers is a much weaker anion complexing agent.

Experimental

The procedures for the syntheses of **1**, **2**, and **3** and the spectroscopic characterizations are described in detail in Supporting Information File 1.

Supporting Information

Supporting Information File 1

Detailed experimental procedures, details of the crystal structure determinations and spectroscopic data for **1**, **2**, and **3**.

[http://www.beilstein-journals.org/bjoc/content/supplementary/1860-5397-10-193-S1.pdf]

Supporting Information File 2

X-ray crystallographic data for **2**·2DMF, **2**·2DMSO, NEt$_4$[Br·**2**], **3**, CCDC 993209, CCDC 993210, CCDC 993207, CCDC 993208.

[http://www.beilstein-journals.org/bjoc/content/supplementary/1860-5397-10-193-S2.cif]

Acknowledgements

References

1. Atwood, J. L.; Davies, J. E. D.; MacNicol, D. D.; Vögtle, F.; Lehn, J.-M. *Comprehensive Supramolecular Chemistry;* Pergamon, Elsevier Science Ltd.: Oxford, 1996; Vol. 1–11.
2. Steed, J. W.; Atwood, J. L. *Supramolecular Chemistry,* 2nd ed.; John Wiley & Sons: Chichester, 2009. doi:10.1002/9780470740880
3. Beer, P. D.; Gale, P. A. *Angew. Chem., Int. Ed.* **2001,** *40,* 486–516. doi:10.1002/1521-3773(20010202)40:3<486::AID-ANIE486>3.0.CO;2-P
4. Gale, P. A.; Gunnlaugson, T., Eds. Thematic issue on Supramolecular Chemistry of Anionic Species. *Chem. Soc. Rev.* **2010,** *39,* 3581–4008.
5. Gale, P. A. *Chem. Commun.* **2011,** *47,* 82–86. doi:10.1039/c0cc00656d
6. Custelcean, R.; Remy, P.; Bonnesen, P. V.; Jiang, D.; Moyer, B. A. *Angew. Chem., Int. Ed.* **2008,** *47,* 1866–1870. doi:10.1002/anie.200704937
7. Wu, B.; Liang, J.; Yang, J.; Jia, C.; Yang, X.-J.; Zhang, H.; Tang, N.; Janiak, C. *Chem. Commun.* **2008,** 1762–1764. doi:10.1039/b719019k
8. Zhang, Y.; Zhang, R.; Zhao, Y.; Ji, L.; Jia, C.; Wu, B. *New J. Chem.* **2013,** *37,* 2266–2270. doi:10.1039/c3nj00401e
9. Chang, K.-J.; Moon, D.; Lah, M. S.; Jeong, K.-S. *Angew. Chem., Int. Ed.* **2005,** *117,* 8140–8143. doi:10.1002/ange.200503121
10. Beck, J.; Hörner, M.; Dittmann, G. *Eur. J. Inorg. Chem.* **2009,** 4314–4319. doi:10.1002/ejic.200900470
11. Swinburne, A. N.; Paterson, M. J.; Beeby, A.; Steed, J. W. *Chem.–Eur. J.* **2010,** *16,* 2714–2718. doi:10.1002/chem.200903293
12. Stadlbauer, W.; Kappe, T. *Monatsh. Chem.* **1984,** *115,* 467–475. doi:10.1007/BF00810008
13. Mulwad, V. V.; Lohar, M. V. *Indian J. Chem., Sect. B* **2003,** *42,* 1937–1942.
14. Zhang, X.; Zhang-Negrerie, D.; Deng, J.; Du, Y.; Zhao, K. *J. Org. Chem.* **2013,** *78,* 12750–12759. doi:10.1021/jo4023292
15. Li, H.; Yang, H.; Petersen, J. L.; Wang, K. K. *J. Org. Chem.* **2004,** *69,* 4500–4508. doi:10.1021/jo049716t
16. Sheldrick, G. M. *Acta Crystallogr., Sect. A* **2008,** *64,* 112–122. doi:10.1107/S0108767307043930
    The crystal structure solutions and refinements were performed using the Shelx programs (Shelxs93 and Shelxl93): G. M. Sheldrick, Shelx-Programs for Crystal Structure Solution and Refinement. All details concerning the crystal structure determinations may be found in the Supporting Information File 1.
17. *Spartan 10,* Program for Calculation of Molecular Properties; Wavefunction Inc.: Irvine, CA, USA.
18. Hynes, M. J. *J. Chem. Soc., Dalton Trans.* **1993,** 311–312. doi:10.1039/dt9930000311

A new charge-tagged proline-based organocatalyst for mechanistic studies using electrospray mass spectrometry

J. Alexander Willms, Rita Beel, Martin L. Schmidt, Christian Mundt
and Marianne Engeser[*]

Abstract

A new 4-hydroxy-L-proline derivative with a charged 1-ethylpyridinium-4-phenoxy substituent has been synthesized with the aim of facilitating mechanistic studies of proline-catalyzed reactions by ESI mass spectrometry. The charged residue ensures a strongly enhanced ESI response compared to neutral unmodified proline. The connection by a rigid linker fixes the position of the charge tag far away from the catalytic center in order to avoid unwanted interactions. The use of a charged catalyst leads to significantly enhanced ESI signal abundances for every catalyst-derived species which are the ones of highest interest present in a reacting solution. The new charged proline catalyst has been tested in the direct asymmetric inverse aldol reaction between aldehydes and diethyl ketomalonate. Two intermediates in accordance with the List–Houk mechanism for enamine catalysis have been detected and characterized by gas-phase fragmentation. In addition, their temporal evolution has been followed using a microreactor continuous-flow technique.

Introduction

Electrospray ionization (ESI) mass spectrometry [1] has not only developed into a standard characterization method for an extremely broad variety of substances [2], but has also been recognized as a valuable tool for studying reaction mechanisms by transferring species of a reacting solution directly into the gas phase of a mass spectrometer [3-7]. The technique allows glimpses into the reacting solution as a function of time [8] and beyond that a characterization of transient intermediates by tandem mass spectrometry. ESI mass-spectrometric mechanistic studies have been reported for a broad range of reaction types ranging from transition metal-catalyzed polymerization [6,9] and coupling reactions [8,10-17] to purely organic Diels–Alder reactions [18,19] to cite only a few representative examples.

However, the detection of transient reactive species is often hindered by their very low concentration. A reacting solution of a catalytic transformation typically contains quite a number of different species. Side products, off-cycle resting states, reagent degradation products and impurities of various origins may be present in much higher concentration than the interesting reactive intermediates. Thus, ESI spectra of reacting solutions can be frustratingly complicated and the transient species of interest might be superposed with a large number of more intense background signals [20]. In quantification using ESI, the detection limit has been lowered significantly by selected ion monitoring in MS/MS mode [2]. Similarly, transient reactive species have been successfully extracted from the chemical noise by collision-induced dissociation (CID) MS/MS [20]. However, it is not possible to identify unknown or unexpected species by this strategy.

As a major drawback of ESI mass spectrometry in general, the signal intensity does not directly parallel the concentration, but the so called ESI response, i.e., the ionization probability during the ESI process [2,21]. Hence it happens that the reaction intermediates of interest are concealed by easily ionizable other compounds present in the reacting solution. A convenient approach to solve this problem is the use of covalently attached charge tags [6,8,9,12,22,23]. Charge-tagging the catalyst selectively enhances the signal abundances of all catalyst-derived species in a reacting solution and thus facilitates the identification of low-concentrated transient catalytic species. As a complementary approach, charge-tagged substrates have been used to easily identify ("fish for") efficient catalysts [6,9].

Since the year 2000, enantioselective catalysis based on small organic metal-free molecules has become an enormously growing research topic [24-30]. A large variety of organocatalyzed reactions with high efficiency and selectivity are nowadays known so that organocatalysis complements current catalytic fields such as organometallic or enzymatic catalysis as an independent subdomain [24-30]. Parallel to the enormous growth of organocatalytic applications in synthesis, mechanistic studies on organocatalytic reactions [31-38] using ESI mass spectrometry [20,39-49] have been reported. The pioneering studies of List and Barbas [50] revealed that the amino acid L-proline is an effective catalyst for a great variety of organic reactions, such as the direct asymmetric aldol reaction, one of the most important C–C bond-forming reactions in organic synthesis [51]. The currently accepted mechanism suggests a central enamine intermediate which forms a Zimmerman–Traxler-like transition state with the acceptor substrate [36,37]. The activity and enantioselectivity achieved by proline in many cases is thought to be due to a templating effect of the OH group directing the aldehyde in a preferred position

via hydrogen bonding [24,25]. It is still controversial whether oxazolidinone formation plays a pivotal role in the catalytic cycle or just serves as an rate limiting parasitic off-cycle equilibrium [31,33,35,52].

Thus, we aimed to synthesize a charge-tagged L-proline-based organocatalyst for mechanistic studies by ESIMS. Few proline derivatives carrying a covalently fixed charge have been reported by now [43,53]. They consist of an imidazolium salt attached to hydroxyproline via an ester group at the end of a flexible alkyl spacer. Interestingly, such charge tags can cause an enhancement of the catalytic performance through electrosteric activation [53], but backfolding can also alter and disturb the catalytic process and induce the formation of side products [43]. In order to fix the charge far away from the catalytic center and thus leave the original catalytic activity of L-proline preferably undisturbed, we chose a stiff 1-ethylpyridinium unit as charge-carrier separated from the catalytic center by a rigid phenyl linker (Figure 1).
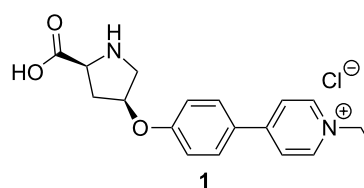
Figure 1: The new charge-tagged proline-derived catalyst **1**.

We then tested the applicability of **1** for ESIMS mechanistic studies on the first "inverse" crossed aldol reaction (Scheme 1) published in 2002 by Jørgensen and coworkers [54] in which the aldehyde acts as the donor in contrast to the "normal" crossed aldol mechanism. It represents an interesting version of a typical proline-catalyzed reaction for which, to the best of our knowledge, mechanistic studies have not been reported so far.
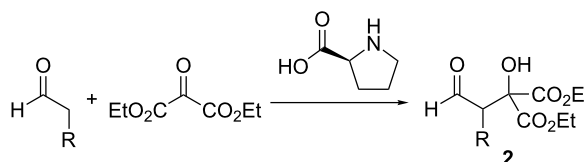
Scheme 1: Inverse aldol reaction with aldehyde donors according to Jørgensen [54]. We studied the reaction for R = Ph (labelled **a** throughout this manuscript) and for R = Et (**b**).

Results and Discussion
Synthesis
Formation of the charge-carrying unit was accomplished starting from commercially available 4-bromophenol using a

strategy reported by Diemer et al. [55]. Protection of the hydroxy group to yield **3** [56] was followed by Suzuki cross-coupling with commercial pyridine-4-boronic acid leading to **4**. Subsequent deprotection led to 4-(pyridine-4-yl)phenol (**5**) (Scheme 2) [55].

The preparation of the charge-tagged catalyst **1** starting from doubly-protected hydroxyproline **6** [57] is depicted in Scheme 3. To introduce a suitable leaving group for the following step of the synthesis, compound **6** was mesylated to give the derivative **7** [58] for which crystals suitable for X-ray analysis have been obtained (Figure 2). An S$_N$2 reaction with **5** [55] led to **8**. We abandoned our initial shorter synthetic route based on a Mitsunobu reaction leading from **6** directly to **8** due to severe purification difficulties. Compound **8** could be charge-tagged to **9** using ethyl bromide. Finally, the free catalyst **1** was obtained by acidic deprotection [59].
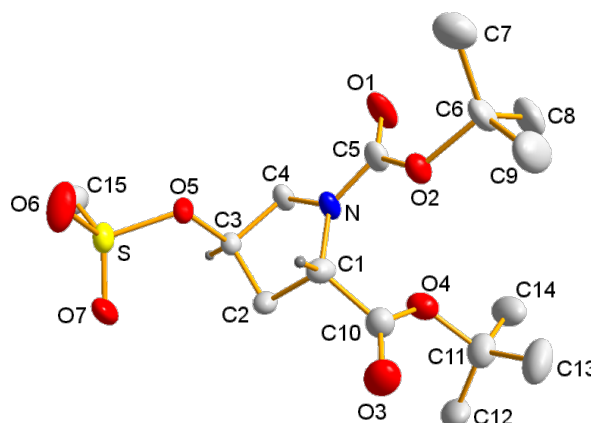
Figure 2: Molecular structure of **7** in the solid state.
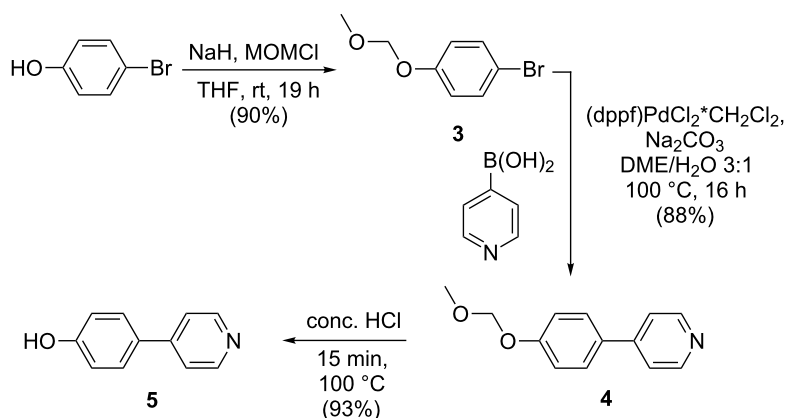
Scheme 2: Synthesis of 4-(pyridin-4-yl)phenol (**5**).
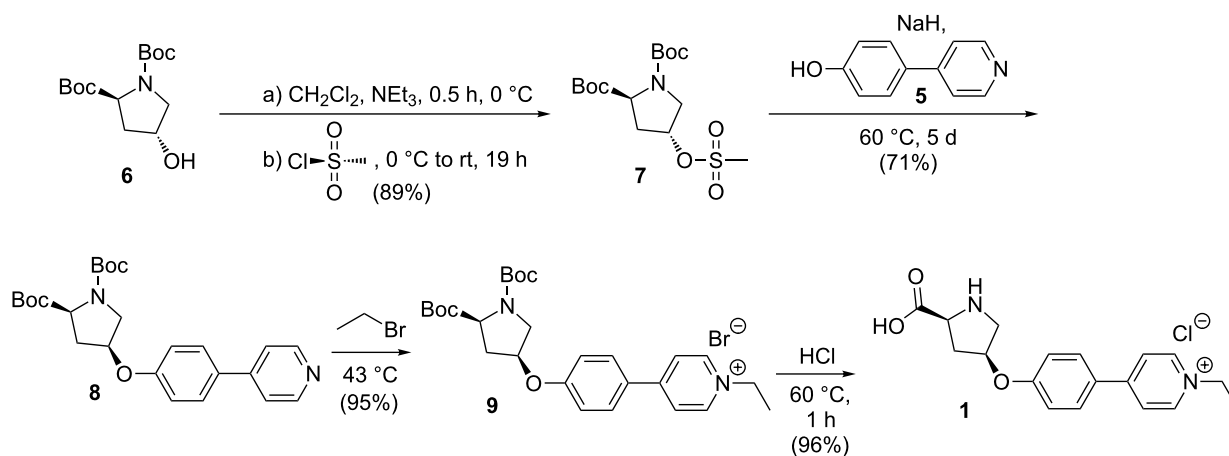
Scheme 3: Synthesis of the charge-tagged proline catalyst **1**.

Mechanism of the Jørgensen inversed aldol reaction

According to the mechanistic model for enamine catalysis from List and Houk [36-38], the aldol reaction from Jørgensen should proceed via the catalytic cycle shown in Scheme 4. We began our experiments with a test whether the charge tag does not disturb the catalysis. Indeed, **1** can achieve the formation of aldol products **2a** and **2b**, respectively, under the reaction conditions given in the literature [54]. Performed in simultaneous parallel reaction batches, **1** provides just about the same yields as unmodified proline and byproducts were not observed. Further, it is important to note that the substrates do not show any reaction when no catalyst, be it charge-tagged or not, is present in the solution.

The easiest way of ESI reaction monitoring – mixing the reagents and measuring ESI spectra after various time intervals – is restricted to reaction times longer than approximately one minute and therefore not appropriate for fast conversions like aldol reactions. We thus decided to use a more complicated experimental setup of two mixing tees connected on-line to the mass spectrometer (Figure 3) to detect individual intermediates of both reactions by ESIMS. These so-called continuous-flow experiments [5,20] allow the sampling of reaction times down to seconds. Solutions of the reagents are mixed in the first microreactor and diluted to concentrations suitable for ESIMS in the second microreactor. The reaction time between the mixing event and the electrospray is determined by the flow rates and capillary lengths. Mass spectra of a solution of diethyl
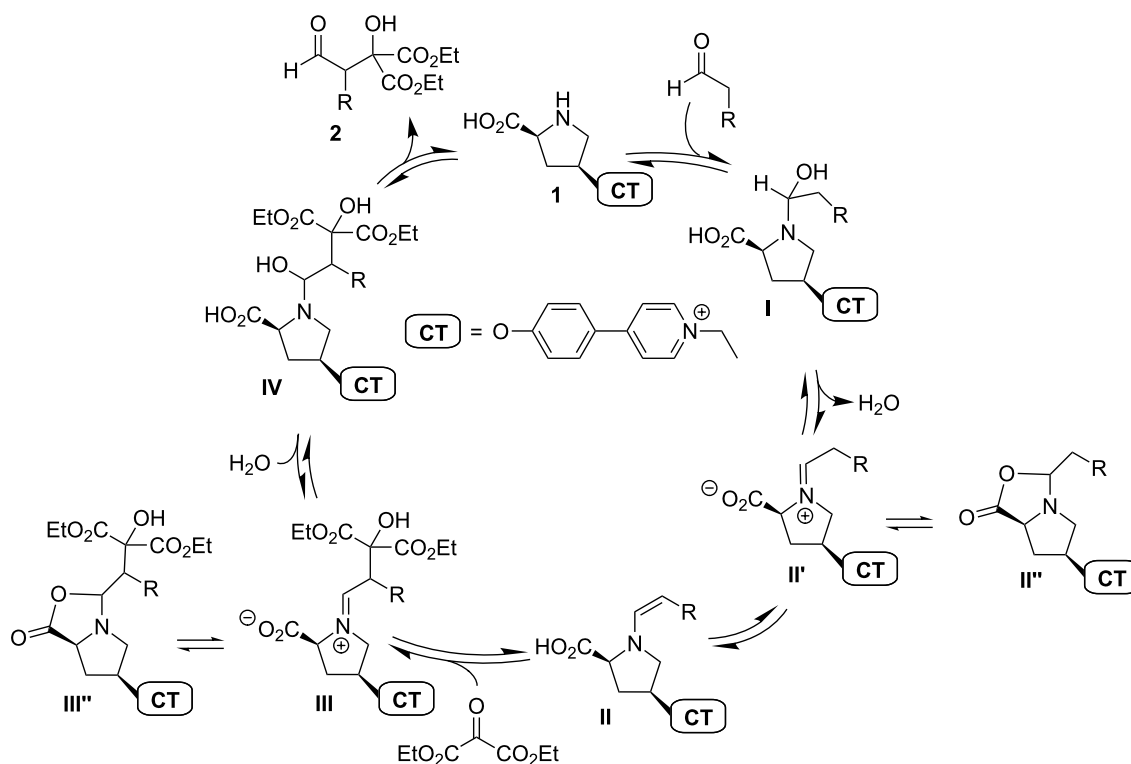
Scheme 4: Proposed catalytic cycle [36-38] for the aldol reaction with aldehyde donors [54]; CT = charge tag, **a**: R = Ph, **b**: R = Et.
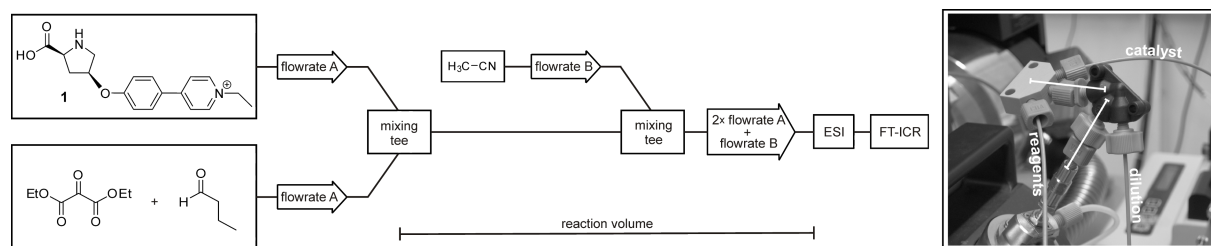
Figure 3: Experimental setup for continuous-flow ESIMS experiments using two mixing tee microreactors directly coupled to the ESI needle.

ketomalonate, butyraldehyde and unmodified L-proline or **1**, respectively, are depicted in Figure 4.

The mass spectra shown in Figure 4 do not exhibit abundant signals for the reactants, even though these are present in the solution in excess to all other species, a fact that is due to the poor ESI response of ketoesters and even more so of aldehydes. In the case of the proline-catalyzed solution (Figure 4a), the catalyst is not visible either, because of an instrumental discrimination of low masses unfortunately unavoidable with our instrument. Instead, two expected intermediates of the catalytic cycle indeed are observed in reasonable abundances (Figure 4a): The signal at *m/z* 170.12 corresponds to [**IIb**untagged + H]+ and the one at *m/z* 344.17 is assigned to [**IIIb**untagged + H]+. In contrast, signals for the remaining two intermediates **Ib**untagged and **IVb**untagged have not been found, which probably is due to their very low concentration in the reaction equilibria as well as to their facile fragmentation during ESI. Note that the group of Metzger has successfully achieved the detec-

tion of a similar intermediate for the aldol reaction beween acetone and selected benzaldehydes using rather unusual and presumably extremely soft ESI conditions, and their results indeed confirm its facile fragmentation [20].

Interestingly, the signal at *m/z* 290.12 can be assigned to a further transient species of the reaction – it corresponds to a protonated adduct of proline with diethyl ketomalonate. This adduct might simply be a non-covalently bound aggregate, i.e., a typical ESI phenomenon [2], but with regard to the rather low concentrations used here and the observation of the analogous species in the proton-free charge-tagged case (see below), we prefer its assignment to a hemiaminal species formed in analogy to intermediate **I** by interaction of the proline nitrogen with the keto group of the ketomalonate (structure depicted in Figure 4a). In this special case, elimination of water is not possible due to the lack of adjacent hydrogen atoms. Its formation thus represents an off-cycle equilibrium dead-end in the course of the intended inverse aldol reaction.
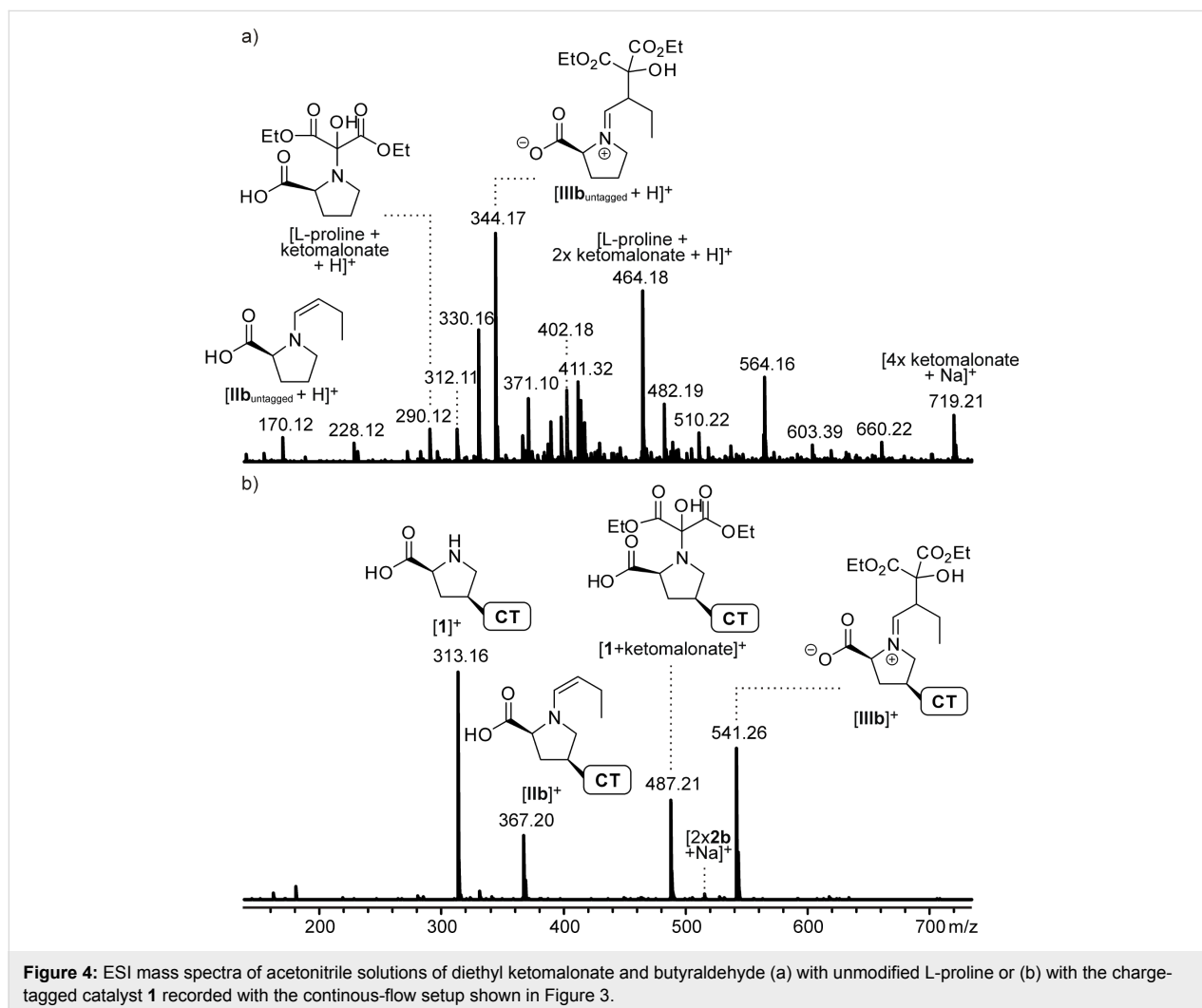
Figure 4: ESI mass spectra of acetonitrile solutions of diethyl ketomalonate and butyraldehyde (a) with unmodified L-proline or (b) with the charge-tagged catalyst **1** recorded with the continous-flow setup shown in Figure 3.

In light of the relatively high abundances observed for the reaction intermediates catalyzed by uncharged L-proline, the implementation of a charge tag might have been considered unnecessary. However, the effect of using the charge-tagged catalyst **1** is impressive (Figure 4b). The obvious reduction of spectral complexity and chemical noise due to the strongly enhanced ESI response of **1** and all its derivatives underlines the great benefits of the charge-tagging strategy. In addition to the catalyst **1** at *m/z* 313.16, the three transient species discussed above are found almost exclusively and in very high abundances, i.e., the enamine [**IIb**]$^+$ at *m/z* 367.20, the iminium [**IIIb**]$^+$ at *m/z* 541.26 and the side product [**1** + ketomalonate]$^+$ at *m/z* 487.21. Please note that the abundance of the latter varies significantly between different reaction runs, in contrast to the signals of the other intermediates whose appearances are highly reproducible. Very similar findings are observed when phenylacetaldehyde instead of butyraldehyde is used. In particular, intermediates [**IIa**]$^+$ and [**IIIa**]$^+$ have been detected in high abundances.

Again, we unfortunately have not been successful in finding suitable electrospray conditions to detect the fragile intermediates [**Ia**]$^+$/[**Ib**]$^+$ and [**IVa**]$^+$/[**IVb**]$^+$. More importantly, however, additional species that are not present in the unlabeled reference system have not been observed. There are no indications for an interference of the charge tag with the catalysis, in contrast to the findings with the flexible imidazolium-labeled proline derivatives reported previously [43].

The mere detection of ions at *m/z* 415.20 (R = Ph) and 367.20 (R = Et), respectively, is not a proof for the presence of reactive enamines [**IIa**]$^+$/[**IIb**]$^+$ since the isomeric zwitterionic iminiums [**II'a**]$^+$/[**II'b**]$^+$ and oxazolidinones [**II''a**]$^+$/[**II''b**]$^+$ (Scheme 4) have the same elemental composition. Using one of the most important mass spectrometric means for structure elucidation, collision-induced dissociation (CID) experiments have been perfomed. The results for R = Et are shown in Figure 5.
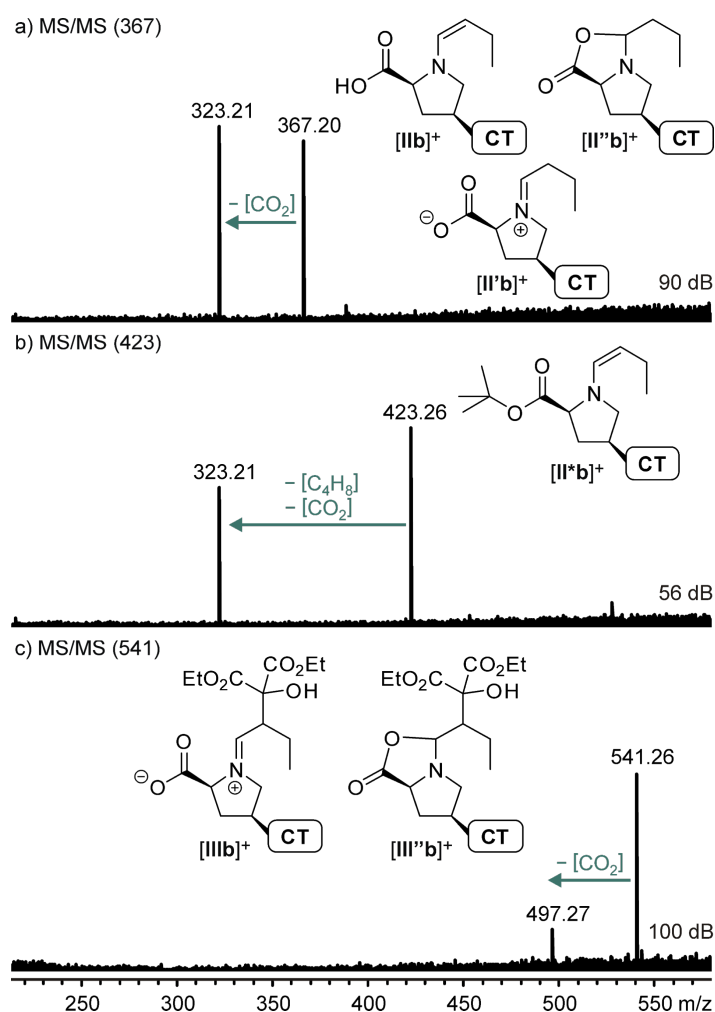
Figure 5: ESI(+) CID MS/MS spectra of mass-selected intermediates a) [**IIb**]$^+$, b) the butyl ester derivative [**II*b**]$^+$, c) [**IIIb**]$^+$.

All four mass-selected ions $[IIa]^+/[IIb]^+$ and $[IIIa]^+/[IIIb]^+$ show a very strong propensity to expel CO_2 which even happens during the ESI process via in-source fragmentation when slightly harsher ionization conditions are used. This fragmentation is in perfect accordance with the zwitterionic iminium structures **II'** and **III** and can also be rationalized for the oxazolidinone alternative **II''**, whereas it requires an additional hydrogen shift from the enamine structure **II**. On the other hand, the comparison with the fragmentation of the structurally related ion $[II*b]^+$ (Figure 5b) is instructive. It doubtlessly possesses an enamine structure since it can neither form a zwitterionic iminium ion nor undergo lactonization to oxazolidinone **II''b** because of its *tert*-butyl blocked carboxylic acid function. The fragmentation of $[II*b]^+$ exclusively consists of a loss of $[C_5,H_8,O_2]$ which should correspond to a concerted or very fast stepwise elimination of isobutene and CO_2 leading to the same product ion at *m/z* 323.21 as the expulsion of CO_2 from *m/z* 367.20. Interpreting the isobutene loss as a closed-shell McLafferty-type rearrangement leads to the postulation of a (very short-lived undetected) intermediate enamine $[IIb]^+$ which then obviously is able to undergo a facile CO_2 elimination. Thus, the fragmentation spectra unfortunately do not allow a clear discrimination of the three possible structures **II**, **II'**, and **II''**.

Marquez and Metzger mass-selected a signal corresponding to the protonated enamine from acetone and untagged L-proline and observed the elimination of CH_2O_2 (formic acid) instead of CO_2 as main fragmentation component during CID [20]. The protonation during the ESI process presumably occurs at the nitrogen atom which enables a direct 1,2-elimination of formic acid. In our case, the respective charge-tagged species are detected in their original form without additional proton which explains the differing fragmentation route.

To monitor the temporal evolution of intermediates during the aldol reaction with the continous-flow setup, series of ESI spectra at different reaction time stages have been recorded by varying the flow rate of the analyte solutions or by changing the length of the capillary connecting both mixing tees. A resulting graph of the normalized relative intensities vs calculated reaction time is provided in Figure 6.

The graph displays a rise of the concentration of **IIb** during the first seconds of the reaction accompanied by a decrease of **1**. Subsequently, an increase of **IIIb** occurs indicating that **IIIb** is formed out of **IIb** which is consistent with the mechanism in Scheme 4. The gradual increase of the final aldol product **2b** is visible as well; an enlargement of a factor of 100 has been used in the presentation of Figure 6 due to its much lower ESI response. Overall, these experiments reflect a very reasonable
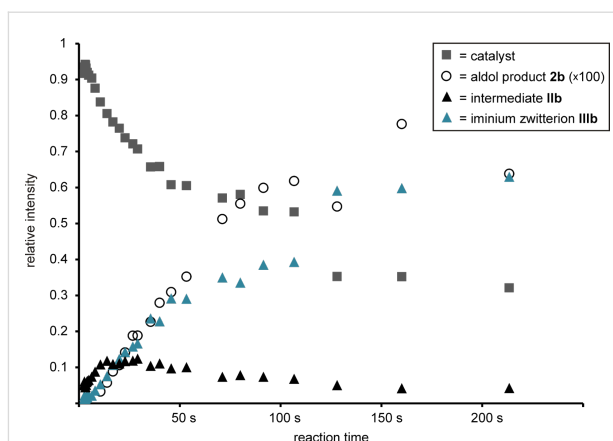
Figure 6: Normalized relative intensities in ESI spectra recorded for the inverse aldol reaction of butyraldehyde, diethyl ketomalonate and charge-tagged catalyst **1** at different time stages using the continous-flow setup with two microreactors shown in Figure 3.

qualitative picture of the reaction behaviour and show that the use of catalyst **1** is suitable for the examination of L-proline-catalyzed reactions via ESIMS. However, we refrain from a quantitative kinetic modeling of the data to extract rate constants [8] because we encountered certain limitations of the method. Most importantly, we could not obtain an exact reproducibility of reaction times, probably because of quasi-unavoidable variations in the actual (dead) volumes of the setup inter alia due to varying minor capillary blockings. Moreover, we face a slight increase of signal abundances with measuring time (not reaction time) because analytes gradually accumulate in the system the longer their solutions are passed through. The extent of this effect depends on the height of the flow rate which necessarily has to be changed when observing a reaction process with the continuous-flow method. Nevertheless, we would like to emphasize that the quality of the experiments surely suffices to depict the "chronological trend" of the reaction process.

Conclusion

We present the synthesis of the charge-tagged L-proline derived catalyst **1** in which a rigid phenylpyridine linker fixes the charge tag far away from the catalytically active center in order to avoid unwanted interactions. In a comparative continous-flow electrospray mass spectrometric study, the new charged catalyst **1** and neutral L-proline have been used to investigate the proline-catalyzed inverse crossed aldol reaction of aldehydes with diethyl ketomalonate. Two key intermediates of the List–Houk mechanism for enamine catalysis in addition to a transient off-cycle species could be observed experimentally. The use of **1** further allows facile access to a qualitative picture of the temporal evolution of catalyst-containing intermediates. We plan to use the new proline catalyst with a non-interfering charge-label presented here as a tool to study the templating

role of the hydroxy group in L-proline-catalyzed reactions in the gas-phase in the near future.

Experimental
Synthesis

Reactions under inert gas atmosphere were performed under argon using standard Schlenk techniques and oven-dried glassware prior to use. Thin-layer chromatography was performed on aluminum TLC plates silica gel 60F$_{254}$ from Merck. Detection was carried out under UV light (254 and 366 nm). Products were purified by column chromatography on silica gel 60 (40–63 µm) from Merck. The ^{1}H and ^{13}C NMR spectra were recorded on a Bruker Avance 300 spectrometer, at 300.1 and 75.5 MHz, or a Bruker AM 400, at 400.1 MHz and 100.6 MHz, at 293 K, respectively. The ^{1}H NMR chemical shifts are reported on the δ scale (ppm) relative to residual non-deuterated solvent as the internal standard. The ^{13}C NMR chemical shifts are reported on the δ scale (ppm) relative to deuterated solvent as the internal standard. Signals were assigned on the basis of ^{1}H, ^{13}C, HMQC, and HMBC NMR experiments. Most solvents were dried, distilled, and stored under argon according to standard procedures. 4-Bromophenol, 4-pyridinylboronic acid, *trans*-*N*-(*tert*-butoxycarbonyl)-4-hydroxy-L-proline, L-proline, diethyl ketomalonate, phenylacetaldehyde and butyraldehyde were used as received from commercial sources.

4-Bromophenol methoxymethyl ether (3) [56]: 4-Bromophenol (3.00 g, 17.2 mmol) was dried under reduced pressure and dissolved in dry THF (160 mL) under inert gas atmosphere. NaH (1.32 g, 52.0 mmol) was added and the mixture was stirred at rt for 0.5 h. Methoxymethyl chloride (2.08 mL, 26.0 mmol) was added dropwise and the resulting suspension was stirred for 19 h. The reaction was quenched by the addition of a MeOH/H$_2$O mixture (1:1, 150 mL) and the aqueous phase was extracted with CH$_2$Cl$_2$ (4 × 50 mL). The combined organic extracts were dried with MgSO$_4$ and the solvents were removed in vacuo. The crude product was purified by column chromatography on silica gel using cyclohexane/ethyl acetate (10:1) as eluent (R_f 0.61). Compound **3** was obtained as colorless oil (3.38 g, 90%). The spectroscopic data confirm the reported ones [56].

4-[4-(Methoxymethoxy)phenyl]pyridine (4) [55]: 4-Bromophenol methoxymethyl ether (**3**, 1.5 g, 6.9 mmol), 4-pyridinyl-boronic acid (1.02 g, 7.5 mmol), [1,1'-bis(diphenyl-phosphino)ferrocene]palladium(II) dichloride dichloromethane complex (0.22 g, 0.28 mmol) and Na$_2$CO$_3$ (8.78 g, 82.4 mmol) were suspended in a H$_2$O/1,2-dimethoxyethane mixture (1:3, 75 mL), heated to 100 °C und stirred for 16 h. The resulting mixture was filtered and the filtrate was mixed with H$_2$O (75 mL) and CH$_2$Cl$_2$ (75 mL) for phase separation. The

aqueous phase was extracted with CH$_2$Cl$_2$ (2 × 75 mL), the combined organic extracts were dried with MgSO$_4$ and the solvents were removed in vacuo. The crude product was purified by column chromatography on silica gel using ethyl acetate with 5% triethylamine as eluent (R_f 0.50). Compound **4** was obtained as white solid (1.31 g, 88%). The spectroscopic data confirm the reported ones [55].

4-(Pyridine-4'-yl)phenol (5) [55] and **(2*S*,4*R*)-*tert*-butyl *N*-*tert*-butyloxycarbonyl-4-hydroxyprolinate (6)** [57] were prepared according to literature protocols.

(2*S*,4*R*)-*tert*-Butyl *N*-*tert*-butoxycarbonyl-4-oxymethanesulfonyloxyprolinate (7) was prepared according to a known procedure [58] which was slightly modified: (2*S*,4*R*)-*tert*-butyl *N*-*tert*-butyloxycarbonyl-4-hydroxyprolinate (**6**, 3.14 g, 10.9 mmol) was dissolved in CH$_2$Cl$_2$ (55 mL) and cooled to 0 °C. Triethylamine (3.01 mL, 21.5 mmol) was added and the mixture was stirred for 0.5 h. Methanesulfonyl chloride (1.33 mL, 17.1 mmol) was added dropwise over 10 min and the resulting solution was stirred overnight without further cooling. The reaction was quenched by the addition of a saturated solution of NaHCO$_3$ (70 mL) and the aqueous phase was extracted with CH$_2$Cl$_2$ (2 × 50 mL). The combined organic extracts were dried with MgSO$_4$ and the solvents were removed in vacuo. The crude product was purified by column chromatography on silica gel using cyclohexane/ethyl acetate (2:3) as eluent (R_f 0.61). Compound **7** was obtained as colorless solid (3.55 g, 89%). Crystals suitable for X-ray analysis have been obtained by slow diffusion of cyclohexane into a Et$_2$O solution of **7**. ^{1}H NMR (400 MHz, CD$_3$OD) δ 5.26 (s, 1H, CH$_2$C*H*CH$_2$), 4.30–4.23 (m, 1H, CH$_2$C*H*N), 3.83–3.76 (m, 1H, NC*H*$_2$CH), 3.70–3.63 (m, 1H, NC*H*$_2$CH), 3.14 (s, 3H, S-C*H*$_3$), 2.67–2.56 (m, 1H, CHC*H*$_2$CH), 2.28–2.19 (m, 1H, CHC*H*$_2$CH), 1.50–1.44 (m, 18H, C(C*H*$_3$)$_3$) ppm; ^{1}H NMR (400 MHz, CD$_3$OD, 333 K) δ 5.26 (s, 1H, CH$_2$C*H*CH$_2$), 4.30–4.26 (m, 1H, CH$_2$C*H*N), 3.83–3.74 (m, 1H, NC*H*$_2$CH), 3.72–3.63 (m, 1H, NC*H*$_2$CH), 3.12 (s, 3H, S-C*H*$_3$), 2.67–2.54 (m, 1H, CHC*H*$_2$CH), 2.30–2.20 (m, 1H, CHC*H*$_2$CH), 1.48 (s, 9H, C(C*H*$_3$)$_3$), 1.46 (s, 9H, C(C*H*$_3$)$_3$) ppm; ^{13}C NMR (100 MHz, CD$_3$OD) δ 173.0/172.9 (*C*=O), 155.6 (*C*=O), 83.1 (*C*(CH$_3$)$_3$), 82.1/81.9 (*C*(CH$_3$)$_3$), 80.6/79.9 (CH$_2$*C*HCH$_2$), 59.5/59.4 (CH$_2$*C*HN), 54.1/53.7 (N*C*H$_2$CH), 38.3 (S-*C*H$_3$), 37.3 (CH*C*H$_2$CH), 28.6 (C(*C*H$_3$)$_3$), 28.3/28.2 (C(*C*H$_3$)$_3$) ppm; ^{13}C NMR (125 MHz, CD$_3$OD, 333 K) δ 172.9 (*C*=O), 155.6 (*C*=O), 83.1 (*C*(CH$_3$)$_3$), 82.1 (*C*(CH$_3$)$_3$), 80.5/79.8 (CH$_2$*C*HCH$_2$), 59.5 (CH$_2$*C*HN), 53.9/53.5 (N*C*H$_2$CH), 38.5 (S-*C*H$_3$), 38.3/37.3 (CH*C*H$_2$CH), 28.7 (C(*C*H$_3$)$_3$), 28.3 (C(*C*H$_3$)$_3$) ppm; HRESIMS (*m/z*): [M + Na]$^+$ calcd for C$_{15}$H$_{27}$NNaO$_7$S, 388.1406; found, 388.1398. The NMR data are consistent with the reported ones measured in CDCl$_3$ [58,60].

(2*S*,4*S*)-*tert*-Butyl *N*-*tert*-butoxycarbonyl-4-(4-(pyridine-4-yl)phenoxy)prolinate (8): 4-(Pyridine-4'-yl)phenol (**5**, 0.63 g, 3.7 mmol) and NaH (0.14 g, 5.5 mmol) were dissolved in dry DMSO (100 mL) under inert gas atmosphere. The suspension was heated to 60 °C and stirred for 1.5 h. (2*S*,4*R*)-*tert*-Butyl *N*-*tert*-butoxycarbonyl-4-methanesulfonyloxyprolinate (**7**, 1.33 g, 3.7 mmol) was added and the mixture was stirred for 5 d at 60 °C. The reaction progress was controlled by thin-layer chromatography. The reaction was quenched by the addition of H_2O (100 mL) and the aqueous phase was extracted with CH_2Cl_2 (2 × 80 mL) and with Et_2O (2 × 80 mL). The combined organic extracts were dried with Na_2SO_4 and the solvents were removed in vacuo. Remaining DMSO was removed by distillation. The crude product was purified by column chromatography on silica gel using cyclohexane/ethyl acetate (1:3) with 5% triethylamine as eluent (R_f 0.50). Compound **8** was obtained as colorless solid (1.14 g, 71%). ^{1}H NMR (300 MHz, CD$_3$OD) δ 8.55–8.45 (m, 2H, $H_{o\text{-py}}$), 7.72 (d, ^3J = 8.8 Hz, 2H, $H_{m\text{-ph}}$), 7.67 (d, ^3J = 6.1 Hz, 2H, $H_{m\text{-py}}$), 7.06/7.00 (d, ^3J = 8.8 Hz, 2H, $H_{o\text{-ph}}$), 5.06 (s, 1H, CH$_2$C*H*CH$_2$), 4.41–4.26 (m, 1H, CH$_2$C*H*N), 3.86–3.72 (m, 1H, NC*H*$_2$CH), 3.72–3.57 (m, 1H, NC*H*$_2$CH), 2.67–2.49 (m, 1H, CHC*H*$_2$CH), 2.47–2.37 (m, 1H, CHC*H*$_2$CH), 1.51–1.40 (m, 18H, C(C*H*$_3$)$_3$) ppm; ^{13}C NMR (75 MHz, CD$_3$OD) δ 172.5/172.5 (*C*=O), 159.7/159.5 (*C*=O), 156.0 (C_{ph}−O), 150.4 ($C_{o\text{-py}}$−H), 150.1 ($C_{p\text{-py}}$−C), 131.7/131.4 ($C_{p\text{-ph}}$−C), 129.6/129.4 ($C_{m\text{-ph}}$−H), 122.5 ($C_{m\text{-py}}$−H), 117.3/117.2/117.2 ($C_{o\text{-ph}}$−H), 82.9/82.7/82.6 (*C*(CH$_3$)$_3$), 81.9/81.6 (*C*(CH$_3$)$_3$), 77.2/76.2 (CH$_2$*C*HCH$_2$), 60.1/59.8 (CH$_2$*C*HN), 53.6/53.2 (N*C*H$_2$CH), 37.1/36.4 (CH*C*H$_2$CH), 28.7/28.6 (C(*C*H$_3$)$_3$), 28.4 (C(*C*H$_3$)$_3$) ppm; HRESIMS (*m/z*): [M + H]$^+$ calcd for $C_{25}H_{33}N_2O_5$, 441.2389; found, 441.2390.

4-(4-((3*S*,5*S*)-1,5-Bis(*tert*-butoxycarbonyl)pyrrolidine-3-yloxy)phenyl)-1-ethylpyridinium bromide (9): (2*S*,4*S*)-*tert*-Butyl *N*-*tert*-butoxycarbonyl-4-(4-(pyridine-4-yl)phenoxy)prolinate (**8**, 0.22 g, 0.5 mmol) was dissolved in bromoethane (13.0 mL, 174.2 mmol), heated to 43 °C and stirred for 5 d. Bromoethane was removed in vacuo. Compound **9** was obtained as yellowish-brown solid (0.26 g, 95%). ^{1}H NMR (400 MHz, CD$_3$OD) δ 8.89 (d, ^3J = 6.8 Hz, 2H, $H_{o\text{-py}}$), 8.35 (d, ^3J = 6.8 Hz, 2H, $H_{m\text{-py}}$), 8.08/7.99 (m, 2H, $H_{m\text{-ph}}$), 7.18/7.11 (d, ^3J = 8.9 Hz, 2H, $H_{o\text{-ph}}$), 5.19–5.13 (m, 1H, CH$_2$C*H*CH$_2$), 4.63 (q, ^3J = 7.4 Hz, 2H, C*H*$_2$CH$_3$), 4.43–4.36 (m, 1H, CH$_2$C*H*N), 3.89–3.73 (m, 1H, NC*H*$_2$CH), 3.71–3.58 (m, 1H, NC*H*$_2$CH), 2.71–2.55 (m, 1H, CHC*H*$_2$CH), 2.47–2.40 (m, 1H, CHC*H*$_2$CH), 1.67 (t, ^3J = 7.4 Hz, 3H, CH$_2$C*H*$_3$), 1.52-1.42 (m, 18H, C(C*H*$_3$)$_3$) ppm; ^{13}C NMR (100 MHz, CD$_3$OD) δ 172.5/172.4 (*C*=O), 162.0 (C_{ph}−O), 157.0 ($C_{p\text{-py}}$−C), 155.9 (*C*=O), 145.2 ($C_{o\text{-py}}$−H), 131.2/131.1 ($C_{m\text{-ph}}$−H), 127.5 ($C_{p\text{-ph}}$−C), 125.0 ($C_{m\text{-py}}$−H), 117.8/117.7 ($C_{o\text{-ph}}$−H), 82.7/82.6 (*C*(CH$_3$)$_3$), 81.6 (*C*(CH$_3$)$_3$), 77.6/76.6 (CH$_2$*C*HCH$_2$), 60.0/59.8 (CH$_2$*C*HN), 57.2

(*C*H$_2$CH$_3$), 53.6/53.2 (N*C*H$_2$CH), 37.1/36.3 (CH*C*H$_2$CH), 28.7/28.6 (C(*C*H$_3$)$_3$), 28.3 (C(*C*H$_3$)$_3$), 16.7 (CH$_2$*C*H$_3$) ppm; HRESIMS (*m/z*): [M]$^+$ calcd for $C_{27}H_{37}N_2O_5$, 469.2697; found, 469.2692.

4-(4-((3*S*,5*S*)-5-Carboxypyrrolidin-3-yloxy)phenyl)-1-ethyl-pyridinium bromide (1) was prepared analogous to a known procedure [59] and obtained as beige-brown solid (96%). ^{1}H NMR (400 MHz, CD$_3$OD) δ 8.92 (d, ^3J = 6.4 Hz, 2H, $H_{o\text{-py}}$), 8.37 (d, ^3J = 6.4 Hz, 2H, $H_{m\text{-py}}$), 8.06 (d, ^3J = 8.6 Hz, 2H, $H_{m\text{-ph}}$), 7.27/7.20 (d, ^3J = 8.6 Hz, 2H, $H_{o\text{-ph}}$), 5.42 (s, 1H, CH$_2$C*H*CH$_2$), 4.73–4.58 (m, 3H, C*H*$_2$CH$_3$ and CH$_2$C*H*N), 3.82–3.62 (m, 2H, NC*H*$_2$CH), 2.85–2.73 (m, 1H, CHC*H*$_2$CH), 2.71–2.63 (m, 1H, CHC*H*$_2$CH), 1.67 (t, ^3J = 7.3 Hz, 3H, CH$_2$C*H*$_3$) ppm; ^{13}C NMR (100 MHz, CD$_3$OD) δ 171.0 (*C*=O), 160.9 (C_{ph}−O), 156.9 ($C_{p\text{-py}}$−C), 145.4 ($C_{o\text{-py}}$−H), 131.0 ($C_{m\text{-ph}}$-H), 128.5 ($C_{p\text{-ph}}$-C), 125.2 ($C_{m\text{-py}}$−H), 118.0 ($C_{o\text{-ph}}$−H), 77.3/76.7 (CH$_2$*C*HCH$_2$), 59.8 (CH$_2$*C*HN), 57.4 (*C*H$_2$CH$_3$), 52.7 (N*C*H$_2$CH), 35.7 (CH*C*H$_2$CH), 16.7 (CH$_2$*C*H$_3$) ppm; HRESIMS (*m/z*): [M]$^+$ calcd for $C_{18}H_{21}N_2O_3$, 313.1547; found, 313.1563.

Diethyl 2-hydroxy-2-(2-oxo-1-phenylethyl)malonate (2a) was prepared according to the reported procedure [54] and obtained as orange oil. The synthesis was carried out twice, once using L-proline (82%), once using **1** as catalyst (79%).

Diethyl 2-hydroxy-2-(1-oxobutan-2-yl)malonate (2b) was prepared according to the reported procedure [54] and obtained as orange oil (using L-proline: 83%, using **1**: 80%).

Crystal structure determination: X-ray crystallographic analysis of **7** was performed on a Nonius KappaCCD diffractometer using graphite monochromated Mo Kα radiation (λ = 0.71073 Å). Intensities were measured by fine-slicing φ- and ω-scans and corrected for background, polarization and Lorentz effects. A semi-empirical absorption correction was applied for the data sets following Blessing's method [61]. The structure was solved by direct methods and refined anisotropically by the least squares procedure implemented in the ShelX program system [62]. The hydrogen atoms were included isotropically using the riding model on the carbon atoms. Selected data: Crystal dimensions 0.36 × 0.20 × 0.11 mm^3, $C_{15}H_{27}NO_7S$, *M* = 365.4424, orthorhombic, space group $P2_12_12_1$, *a* = 7.44860(10), *b* = 8.94580(10), *c* = 28.7024(4) Å, α = 90°, β = 90°, γ = 90°, *V* = 1912.55(4) Å^3, *Z* = 4, ρ = 1.269 g cm^{-3}, μ = 0.203 mm^{-1}, F(000) = 748, 18641 reflections (2θ$_{max}$ = 27.99°) measured (4566 unique, R_{int} = 0.0606, completeness = 99.4%), *R* (*I* > 2σ(*I*)) = 0.0708, *wR*$_2$ (all data) = 0.2054. GOF = 1.052 for 224 parameters and 14 restraints, largest diff. peak and hole 1.557/−0.438 e Å^3. CCDC-1016532

contains the supplementary data for this structure. These data can be obtained free of charge from http://www.ccdc.cam.ac.uk/data_request/cif.

Mass spectrometry

ESI mass spectra were recorded on a Bruker APEX IV Fourier-transform ion cyclotron resonance (FT–ICR) mass spectrometer with a 7.05 T magnet and an Apollo electrospray (ESI) ion source equipped with an off-axis 70° spray needle. Analyte solutions were fed into high pressure PEEK mixing tees from Alltech and then introduced into the ion source with a single- and a dual syringe pump from Cole Parmer and KD Scientific, respectively, at flow rates of 50 µL/h to 16 mL/h. The continuous-flow experiments were performed with a setup of two mixing tees. The first one was used for mixing a solution of both butyraldehyde and diethyl ketomalonate (each 2 mmol/L) with a solution of the catalyst (1 mmol/L) and the second mixing tee served for sufficient dilution. Different reaction times were achieved by changing either the length of the capillary connecting both tees or by varying the flow rate. The theoretical reaction time between **1** and the reactants has been calculated from the experimental flow rates considering the volumes of both mixing tees and the connecting capillaries and under the assumption that the dilution in the second mixing tee decreases the reaction rate in the fashion of a bimolecular elementary reaction. For longer reaction times (>200 s), the results can be compared with the ones from simple ESI measurements recorded at various times after offline mixing of the reaction partners. The results from both techniques match reasonably well, even though the reaction times calculated for the continous-flow setup seem to be slightly underestimated.

Ionization parameters were adjusted as follows: capillary voltage: −2.380 to −3.800 V; end plate voltage −2300 to 3320 V; capexit voltage: 50 to 100 V; skimmer voltages: 7 to 17 V; temperature of drying gas: 50 to 80 °C. Nitrogen was used as nebulizing (1.38 to 4.14 bar) and drying gas (1.38 to 3.10 bar). The ions were accumulated in the instruments hexapole for 0.3 to 0.9 s, introduced into the FT–ICR cell which was operated at pressures below 10^{-10} mbar, and detected by a standard excitation and detection sequence. Collision-induced fragmentation was performed by on-resonance excitation with argon gas pulsed into the ICR cell followed by a pumping delay of 3–5 s. For each measurement, 8 to 64 scans were averaged. All signal assignments are based on exact mass determinations.

Acknowledgements

References

1. Fenn, J. B. *Angew. Chem., Int. Ed.* **2003,** *42,* 3871–3894. doi:10.1002/anie.200300605
2. Cole, B., Ed. *Electrospray Ionization Mass Spectrometry;* Wiley: New York, 1997.
3. Schröder, D. *Acc. Chem. Res.* **2012,** *45,* 1521–1532. doi:10.1021/ar3000426
4. Eberlin, M. N. *Eur. J. Mass Spectrom.* **2007,** *13,* 19–28. doi:10.1255/ejms.837
5. Santos, L. S.; Knaack, L.; Metzger, J. O. *Int. J. Mass Spectrom.* **2005,** *246,* 84–104. doi:10.1016/j.ijms.2005.08.016
6. Chen, P. *Angew. Chem.* **2003,** *115,* 2938–2954. doi:10.1002/ange.200200560
7. Plattner, D. A. *Top. Curr. Chem.* **2003,** *225,* 153–203. doi:10.1007/3-540-36113-8_5
8. Vikse, K. L.; Ahmadi, Z.; Manning, C. C.; Harrington, D. A.; McIndoe, J. S. *Angew. Chem.* **2011,** *123,* 8454–8456. doi:10.1002/ange.201102630
9. Adlhart, C.; Chen, P. *Helv. Chim. Acta* **2000,** *83,* 2192–2196. doi:10.1002/1522-2675(20000906)83:9<2192::AID-HLCA2192>3.0.CO;2-G
10. Oliveira, F. F. D.; dos Santos, M. R.; Lalli, P. M.; Schmidt, E. M.; Bakuzis, P.; Lapis, A. A. M.; Monteiro, A. L.; Eberlin, M. N.; Neto, B. A. D. *J. Org. Chem.* **2011,** *76,* 10140–10147. doi:10.1021/jo201990n
11. Vikse, K. L.; Henderson, M. A.; Oliver, A. G.; McIndoe, J. S. *Chem. Commun.* **2010,** *46,* 7412–7414. doi:10.1039/c0cc02773a
12. Schade, M. A.; Fleckenstein, J. E.; Knochel, P.; Koszinowski, K. *J. Org. Chem.* **2010,** *75,* 6848–6857. doi:10.1021/jo101337a
13. Thiery, E.; Chevrin, C.; Le Bras, J.; Harakat, D.; Muzart, J. *J. Org. Chem.* **2007,** *72,* 1859–1862. doi:10.1021/jo062491x
14. Santos, L. S.; Rosso, G. B.; Pilli, R. A.; Eberlin, M. N. *J. Org. Chem.* **2007,** *72,* 5809–5812. doi:10.1021/jo062512n
15. Enquist, P.-A.; Nilsson, P.; Sjöberg, P.; Larhed, M. *J. Org. Chem.* **2006,** *71,* 8779–8786. doi:10.1021/jo061437d
16. Sabino, A. A.; Machado, A. H. L.; Correia, C. R. D.; Eberlin, M. N. *Angew. Chem.* **2004,** *116,* 2568–2572. doi:10.1002/ange.200353076
17. Aliprantis, A. O.; Canary, J. W. *J. Am. Chem. Soc.* **1994,** *116,* 6985–6986. doi:10.1021/ja00094a083
18. Teichert, A.; Pfaltz, A. *Angew. Chem.* **2008,** *120,* 3408–3410. doi:10.1002/ange.200705082
19. Fürmeier, S.; Metzger, J. O. *J. Am. Chem. Soc.* **2004,** *126,* 14485–14492. doi:10.1021/ja046157z
20. Marquez, C. A.; Metzger, J. O. *Chem. Commun.* **2006,** 1539–1541. doi:10.1039/b518288c
21. Cech, N. B.; Enke, C. G. *Mass Spectrom. Rev.* **2001,** *20,* 362–387. doi:10.1002/mas.10008
22. Chisholm, D. M.; McIndoe, J. S. *Dalton Trans.* **2008,** 3933–3945. doi:10.1039/b800371h
23. Smith, R. L.; Kenttämaa, H. I. *J. Am. Chem. Soc.* **1995,** *117,* 1393–1396. doi:10.1021/ja00109a025
24. Berkessel, A.; Gröger, H., Eds. *Asymmetric Organocatalysis;* Wiley-VCH: Weinheim, 2005. doi:10.1002/3527604677
25. Dalko, P., Ed. *Enantioselective Organocatalysis;* Wiley-VCH: Weinheim, 2007. doi:10.1002/9783527610945

26. MacMillan, D. W. C. *Nature* **2008,** *455,* 304–308. doi:10.1038/nature07367
27. Melchiorre, P.; Marigo, M.; Carlone, A.; Bartoli, G. *Angew. Chem.* **2008,** *120,* 6232–6265. doi:10.1002/ange.200705523
28. Mukherjee, S.; Yang, J. W.; Hoffmann, S.; List, B. *Chem. Rev.* **2007,** *107,* 5471–5569. doi:10.1021/cr0684016
29. Dalko, P. I.; Moisan, L. *Angew. Chem.* **2004,** *116,* 5248–5286. doi:10.1002/ange.200400650
30. Notz, W.; Tanaka, F.; Barbas, C. F., III. *Acc. Chem. Res.* **2004,** *37,* 580–591. doi:10.1021/ar0300468
31. Schmid, M. B.; Zeitler, K.; Gschwind, R. M. *Angew. Chem.* **2010,** *122,* 5117–5123. doi:10.1002/ange.200906629
    Angew. Chem., Int. Ed. **2010,** *49,* 4997–5003. doi:10.1002/anie.200906629
32. Dinér, P.; Kjærsgaard, A.; Lie, M. A.; Jørgensen, K. A. *Chem. – Eur. J.* **2007,** *14,* 122–127. doi:10.1002/chem.200701244
33. Zotova, N.; Franzke, A.; Armstrong, A.; Blackmond, D. G. *J. Am. Chem. Soc.* **2007,** *129,* 15100–15101. doi:10.1021/ja0738881
34. Mathew, S. P.; Klussmann, M.; Iwamura, H.; Wells, D. H., Jr.; Armstrong, A.; Blackmond, D. G. *Chem. Commun.* **2006,** 4291–4293. doi:10.1039/b609926b
35. Iwamura, H.; Wells, D. H., Jr.; Mathew, S. P.; Klussmann, M.; Armstrong, A.; Blackmond, D. G. *J. Am. Chem. Soc.* **2004,** *126,* 16312–16313. doi:10.1021/ja0444177
36. Allemann, C.; Gordillo, R.; Clemente, F. R.; Cheong, P. H.-Y.; Houk, K. N. *Acc. Chem. Res.* **2004,** *37,* 558–569. doi:10.1021/ar0300524
37. List, B.; Hoang, L.; Martin, H. J. *Proc. Natl. Acad. Sci. U. S. A.* **2004,** *101,* 5839–5842. doi:10.1073/pnas.0307979101
38. Hoang, L.; Bahmanyar, S.; Houk, K. N.; List, B. *J. Am. Chem. Soc.* **2003,** *125,* 16–17. doi:10.1021/ja028634o
39. Bächle, F.; Duschmalé, J.; Ebner, C.; Pfaltz, A.; Wennemers, H. *Angew. Chem.* **2013,** *125,* 12851–12855. doi:10.1002/ange.201305338
40. Regiani, T.; Santos, V. G.; Godoi, M. N.; Vaz, B. G.; Eberlin, M. N.; Coelho, F. *Chem. Commun.* **2011,** *47,* 6593–6595. doi:10.1039/c1cc10678c
41. Beel, R.; Kobialka, S.; Schmidt, M. L.; Engeser, M. *Chem. Commun.* **2011,** *47,* 3293–3295. doi:10.1039/c0cc05347c
42. Alachraf, M. W.; Handayani, P. P.; Hüttl, M. R. M.; Grondal, C.; Enders, D.; Schrader, W. *Org. Biomol. Chem.* **2011,** *9,* 1047–1053. doi:10.1039/c003433a
43. Maltsev, O. V.; Chizhov, A. O.; Zlotin, S. G. *Chem. – Eur. J.* **2011,** *17,* 6109–6117. doi:10.1002/chem.201100388
44. Amarante, G. W.; Benassi, M.; Milagre, H. M. S.; Braga, A. A. C.; Maseras, F.; Eberlin, M. N.; Coelho, F. *Chem. – Eur. J.* **2009,** *15,* 12460–12469. doi:10.1002/chem.200900966
45. Schrader, W.; Handayani, P. P.; Zhou, J.; List, B. *Angew. Chem.* **2009,** *121,* 1491–1494. doi:10.1002/ange.200804353
46. Schrader, W.; Handayani, P. P.; Burstein, C.; Glorius, F. *Chem. Commun.* **2007,** 716–718. doi:10.1039/b613862d
47. Milagre, C. D. F.; Milagre, H. M. S.; Santos, L. S.; Lopes, M. L. A.; Moran, P. J. S.; Eberlin, M. N.; Rodrigues, J. A. R. *J. Mass Spectrom.* **2007,** *42,* 1287–1293. doi:10.1002/jms.1173
48. Marquez, C. A.; Fabbretti, F.; Metzger, J. O. *Angew. Chem.* **2007,** *119,* 7040–7042. doi:10.1002/ange.200700266
49. Santos, L. S.; Pavam, C. H.; Almeida, W. P.; Coelho, F.; Eberlin, M. N. *Angew. Chem.* **2004,** *116,* 4430–4433. doi:10.1002/ange.200460059
50. List, B.; Lerner, R. A.; Barbas, C. F., III. *J. Am. Chem. Soc.* **2000,** *122,* 2395–2396. doi:10.1021/ja994280y
51. Machajewski, T. D.; Wong, C.-H. *Angew. Chem.* **2000,** *112,* 1406–1430. doi:10.1002/(SICI)1521-3757(20000417)112:8<1406::AID-ANGE1406>3.0.CO;2-R
    Angew. Chem., Int. Ed. **2000,** *39,* 1352–1375. doi:10.1002/(SICI)1521-3773(20000417)39:8<1352::AID-ANIE1352>3.0.CO;2-J
52. Seebach, D.; Beck, A. K.; Badine, D. M.; Limbach, M.; Eschenmoser, A.; Treasurywala, A. M.; Hobi, R.; Prikoszovich, W.; Linder, B. *Helv. Chim. Acta* **2007,** *90,* 425–471. doi:10.1002/hlca.200790050
53. Bottoni, A.; Lombardo, M.; Miscione, G. P.; Montroni, E.; Quintavalla, A.; Trombini, C. *ChemCatChem* **2013,** *5,* 2913–2924. doi:10.1002/cctc.201300399
54. Bøgevig, A.; Kumaragurubaran, N.; Jørgensen, K. A. *Chem. Commun.* **2002,** 620–621. doi:10.1039/b200681b
55. Diemer, V.; Chaumeil, H.; Defoin, A.; Fort, A.; Boeglin, A.; Carré, C. *Eur. J. Org. Chem.* **2006,** 2727–2738. doi:10.1002/ejoc.200600030
56. Gu, W.; She, X.; Pan, X.; Yang, T.-K. *Tetrahedron: Asymmetry* **1998,** *9,* 1377–1380. doi:10.1016/S0957-4166(98)00118-9
57. Chabaud, P.; Pèpe, G.; Courcambeck, J.; Camplo, M. *Tetrahedron* **2005,** *61,* 3725–3731. doi:10.1016/j.tet.2005.02.006
58. Tanaka, K.; Sawanishi, H. *Tetrahedron: Asymmetry* **1998,** *9,* 71–77. doi:10.1016/S0957-4166(97)00594-6
59. Cotton, R.; Johnstone, A. N.; North, M. *Tetrahedron Lett.* **1994,** *35,* 8859–8862. doi:10.1016/S0040-4039(00)78517-0
60. Pícha, J.; Vanek, V.; Buděšínský, M.; Mládková, J.; Garrow, T. A.; Jiráček, J. *Eur. J. Med. Chem.* **2013,** *65,* 256–275. doi:10.1016/j.ejmech.2013.04.039
61. Blessing, R. H. *Acta Crystallogr., Sect. A* **1995,** *51,* 33–38. doi:10.1107/S0108767394005726
62. Sheldrick, G. M. SHELXS97 and SHELXL97, University of Göttingen, Germany, 1997.

BEILSTEIN JOURNAL OF ORGANIC CHEMISTRY

Lateral ordering of PTCDA on the clean and the oxygen pre-covered Cu(100) surface investigated by scanning tunneling microscopy and low energy electron diffraction

Stefan Gärtner[1,2], Benjamin Fiedler[1], Oliver Bauer[1], Antonela Marele[3]
and Moritz M. Sokolowski[*1]

Full Research Paper

Address:
[1]Institut für Physikalische und Theoretische Chemie der Universität Bonn, Wegelerstrasse 12, 53115 Bonn, Germany, [2]Present address: Light Technology Institute, Karlsruhe Institute of Technology (KIT), Engesserstr.13, 76131 Karlsruhe, Germany and [3]Departamento de Física de la Materia Condensada, Universidad Autónoma de Madrid, 28049, Madrid, Spain

Email:
Moritz M. Sokolowski[*] - sokolowski@pc.uni-bonn.de

* Corresponding author

Abstract

We have investigated the adsorption of perylene-3,4,9,10-tetracarboxylic acid dianhydride (PTCDA) on the clean and on the oxygen pre-covered Cu(100) surface [referred to as $(\sqrt{2} \times 2\sqrt{2})R45° - 2O/Cu(100)$] by scanning tunneling microscopy (STM) and low energy electron diffraction (LEED). Our results confirm the $(4\sqrt{2} \times 5\sqrt{2})R45°$ superstructure of PTCDA/Cu(100) reported by A. Schmidt et al. [*J. Phys. Chem.* **1995**, *99*, 11770–11779]. However, contrary to Schmidt et al., we have no indication for a dissociation of the PTCDA upon adsorption, and we propose a detailed structure model with two intact PTCDA molecules within the unit cell. Domains of high lateral order are obtained, if the deposition is performed at 400 K. For deposition at room temperature, a significant density of nucleation defects is found pointing to a strong interaction of PTCDA with Cu(100). Quite differently, after preadsorption of oxygen and formation of the $(\sqrt{2} \times 2\sqrt{2})R45° - 2O/Cu(100)$ superstructure on Cu(100), PTCDA forms an incommensurate monolayer with a structure that corresponds well to that of PTCDA bulk lattice planes.

Introduction

Interfaces between organic semiconductors and metals have gained large interest because they are present in many applications, e.g., organic field-effect transistors [1] or organic light-emitting diodes [2]. In order to obtain a fundamental understanding of the interactions at these interfaces, the adsorption of perylene-3,4,9,10-tetracarboxylic acid dianhydride (PTCDA) on single crystal surfaces of noble metals has been studied intensively as a model system [3]. On the coinage metal surfaces, the interaction strength of PTCDA increases from physisorption to stronger chemisorption from Au over Ag to Cu. On the (111)

surfaces, this is reflected by the decreasing adsorption heights [4-6] and the increasing charge transfer from the metal into the former lowest unoccupied molecular orbital (LUMO) of the PTCDA molecule [7].

For the more open and hence, with respect to the Cu(111) surface, more reactive Cu(100) surface two experimental investigations have been reported [8,9]. Interestingly, they both proposed a dissociative adsorption of PTCDA [8,9] which appears plausible in view of the surface reactivity of Cu(100). However, the two experiments came to slightly different conclusions concerning the dissociation: Schmidt et al. interpret their X-ray photoelectron spectroscopy (XPS) and thermal programed desorption (TPD) data by a loss of the two anhydride O atoms of PTCDA upon adsorption [8]. Andreasson et al. supposed, on the basis of ultraviolet photoelectron spectroscopy (UPS) data, a molecular species after adsorption on Cu(100) which has lost all O atoms, i.e., both the four carboxylic and the two anhydride O atoms [9]. In addition, the two publications reported different superstructures of PTCDA on Cu(100). Schmidt et al. found a $(4\sqrt{2} \times 5\sqrt{2})R45°$ superstructure [8], whereas Andreasson et al. reported a (4.5×4.5) structure [9]. The smaller unit cell of the latter fits to the proposed loss of all O atoms. Both structures were suggested on the basis of low energy electron diffraction (LEED) measurements. Scanning tunneling microscopy (STM) data has not been reported yet.

Therefore, the aim of our combined LEED and STM investigation was twofold: on the one hand to clarify the superstructure of PTCDA on Cu(100), and on the other hand to gain new information about the possible dissociation of PTCDA upon adsorption on Cu(100). In addition, we adsorbed PTCDA on a Cu(100) surface that was passivated by preadsorbing oxygen in order to test the impact of the change in the interfacial interaction on the lateral ordering.

Experimental

The experiments were carried out under ultrahigh vacuum (UHV) conditions. The UHV apparatus consisted of two chambers operated at a base pressure of about 2×10^{-10} mbar. The first chamber was used for the preparation of the sample. The cleaning procedure for the Cu(100) crystal consisted of several cycles of sputtering with Ar^+ ions at an energy of 1000 eV and at a sample temperature of 620 K for 30 min and subsequent annealing at 770 K for 60 min. PTCDA was purchased from Sigma-Aldrich and purified by gradient sublimation. The deposition was performed at sample temperatures of 300–450 K, using a rate of 0.2 monolayers min^{-1}. The coverages (θ) were determined from the evaluation of STM images, and in the following one monolayer (1 ML) refers to a coverage equiva-

lent to that of the ordered first layer. The preparation chamber was also equipped with a microchannel plate low energy electron diffraction apparatus (MCP-LEED) from OCI Vacuum Microengineering. The LEED measurements were done at sample temperatures of 280–400 K using beam currents of 1–20 nA. The distortions of the LEED images due to the planar microchannel plate were corrected by a home-written software [10].

The second chamber contained a beetle-type variable temperature STM (VT STM) from RHK technology. All STM images were recorded in constant current mode with a self-cut Pt/Ir tip at room temperature (rt). The given bias voltage U_{bias} refers to the sample. After recording the images were treated with histogram alignment (which optimizes the images by inducing an offset for every scan line) and moderate smoothing. For accurate length determination, the STM scanner was calibrated from images of the bare Cu(100) surface. The lengths of the adsorbate unit cell vectors (a_0 and b_0) were determined from STM images as follows. In order to minimize errors from thermal drift only those images were used where the fast and more robust scan direction was parallel to the direction of the considered unit cell vector within ±5°. The angle γ_0 between the unit cell vectors $\mathbf{a_0}$ and $\mathbf{b_0}$ was derived from the relative rotation of the fast scan direction that was needed to align it with one or the other unit cell vector. The reported values and errors of the unit cell parameters were computed by statistical averaging of the measured values. The respective errors are the standard deviations plus errors related to uncertainty of the calibration factors of the STM scanner. Other systematic errors are difficult to quantify and are therefore not specified.

To prepare the oxygen covered Cu(100) surface we used a procedure similar to the one reported in [11]. The clean crystal was exposed to an oxygen pressure of 1×10^{-6} mbar for 8 min at a temperature of 470 K. Thereafter an annealing step at 700 K for 10 min was performed. Deposition of PTCDA on this oxygen modified Cu(100) surface was carried out at a sample temperature of 300 K with a similar rate as above.

Results
PTCDA/Cu(100)
Ordering for deposition at 400 K

The structure described in the following section was observed after deposition of about 0.5 ML PTCDA at an elevated sample temperature of 400 K. The dependence of the structure on the sample temperature during deposition and the coverage will be described later.

As illustrated by the STM image in Figure 1(a), PTCDA forms islands of an ordered structure on Cu(100). The island edges are
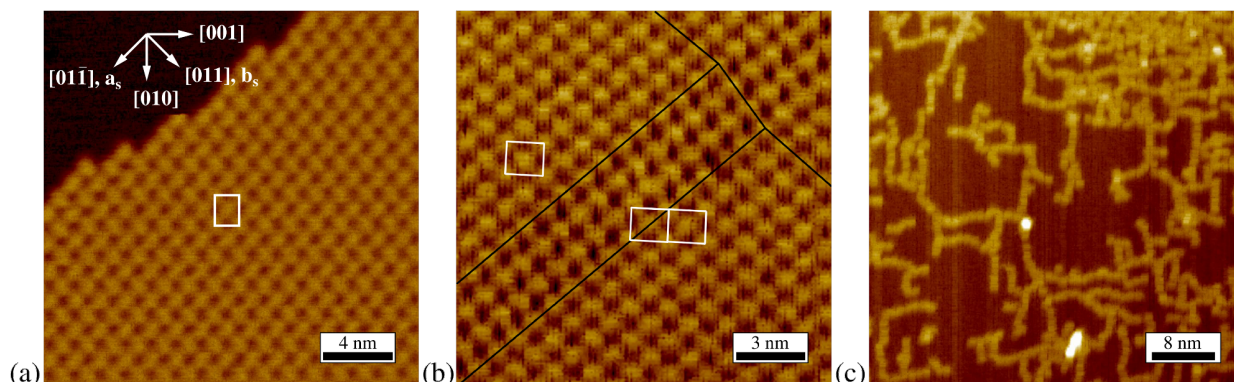
Figure 1: Different STM images of PTCDA on Cu(100). (a) Ordered structure observed after deposition at a sample temperature of 400 K. The upper left corner shows the bare Cu(100) surface. The unit cell of the structure is indicated (U_{bias} = −1.2 V, I_T = 68 pA, 21.6 × 21.6 nm^2, θ ≈ 0.5 ML). (b) Misfit area between two translational domains. The black lines are guide lines for the eye. The unit cells are indicated (U_{bias} = −0.8 V, I_T = 63 pA, 16.3 × 16.3 nm^2). (c) PTCDA agglomerates after annealing at 550 K for 5 min (U_{bias} = −1.9 V, I_T = 91 pA, 47.5 × 47.5 nm^2).

often parallel to the diagonal of the unit cell, as visible in the upper left part of Figure 1(a). The structure can be described by a rectangular unit cell, marked in white in Figure 1(a), which contains two differently oriented PTCDA molecules (see also Figure 3(a), below). All parameters measured from STM images of this superstructure are given in the second column of Table 1. Within the error bars we find that the unit cell vectors of the adsorbate structure a_0 and b_0 are parallel to the [001] and the [010] direction of Cu(100), respectively. This is deduced from the angle $φ_0$ between a_0 and the substrate vector a_s and the angle $γ_0$ between a_0 and b_0 (see also Figure 3(b), below). Due to the different lengths of a_0 and b_0, two rotational domains of the PTCDA structure on Cu(100) are possible. For comparison the unit cell parameters of the commensurate $(4\sqrt{2} × 5\sqrt{2})R45°$ superstructure reported by Schmidt et al. [8] are given in the first column of Table 1. They agree very well with those determined by us from STM data.

The right part of Figure 2(a) shows the LEED pattern of the PTCDA/Cu(100) including the first order spots of the substrate. A simulation of the LEED pattern is shown on the left. The substrate spots are drawn in black; the two domains of the $(4\sqrt{2} × 5\sqrt{2})R45°$ superstructure are drawn in red and blue. The simulated LEED pattern explains well the experimental LEED pattern. We note that in this LEED pattern and in those observed at higher electron energies, superstructure spots of high order are well visible. This indicates a commensurate superstructure, because in this case multiple scattering from the substrate can contribute to the superstructure spots, thus increasing the intensities of the LEED spots at higher orders. For a commensurate structure, a PTCDA induced buckling of the Cu(100) surface is very conceivable. This can also contribute to the intensities of the superstructure LEED spots. We note that a significant surface buckling was recently derived from density functional theory calculations for PTCDA on

Table 1: Overview on the unit cell parameters of structures of PTCDA on Cu(100) (column two) and on the $(\sqrt{2} × 2\sqrt{2})R45° − 2O/Cu(100)$ surface (column three). For PTCDA/Cu(100) the parameters calculated for the commensurate $(4\sqrt{2} × 5\sqrt{2})R45°$ structure derived by Schmidt et al. [8] are compared to those we derived from our STM data. $γ_0$ denotes the angle between the unit cell vectors a_0 and b_0, the lengths are a_0 and b_0, respectively. $φ_0$ denotes the angle between a_0 and the vector a_s of the unit cell of the Cu(100) surface along the $[01\bar{1}]$ direction (see Figure 4(d)). The last row of the table gives the superstructure matrices M_0 with respect to the substrate vectors of Cu(100).

	PTCDA/Cu(100)		PTCDA/O/Cu(100)
	$(4\sqrt{2} × 5\sqrt{2})R45°$ [8]	Own STM results	STM results
a_0 [Å]	14.46	14.5 ± 0.3	12.2 ± 0.3
b_0 [Å]	18.08	18.0 ± 0.4	19.3 ± 0.4
$γ_0$ [°]	90	89.9 ± 0.8	89.3 ± 1.2
$φ_0$ [°]	45	45.2 ± 0.8	38.8 ± 0.8
M_0	$\begin{pmatrix} 4 & 4 \\ -5 & 5 \end{pmatrix}$	$\begin{pmatrix} 4.00 \pm 0.14 & 4.02 \pm 0.14 \\ -4.98 \pm 0.18 & 4.96 \pm 0.18 \end{pmatrix}$	$\begin{pmatrix} -3.72 \pm 0.14 & 3.00 \pm 0.13 \\ 4.80 \pm 0.23 & 5.82 \pm 0.23 \end{pmatrix}$

Figure 2: (a) LEED pattern of PTCDA on Cu(100) observed after deposition at a sample temperature of 400 K (62.5 eV, θ ≈ 0.5 ML). Left hand side: Corresponding calculated LEED pattern. The reciprocal unit cells of the Cu(100) surface (black) and of the two symmetry equivalent domains of the commensurate $(4\sqrt{2} \times 5\sqrt{2})R45°$ superstructure (blue and red) are indicated. (b) LEED pattern of PTCDA on $(\sqrt{2} \times 2\sqrt{2})R45° - 2O$/Cu(100) (16.6 eV, θ ≈ 0.5 ML). Left hand side: Corresponding calculated LEED pattern. The reciprocal unit cells of the $(\sqrt{2} \times 2\sqrt{2})R45° - 2O$/Cu(100) (blue and red) and the four symmetry equivalent domains of the incommensurate superstructure of PTCDA according to the matrix $\mathbf{M}_0$ (see third column of Table 1) are indicated. Note that the unit cells of the $(\sqrt{2} \times 2\sqrt{2})R45° - 2O$/Cu(100) surface do not fit completely into the depicted area of the reciprocal space.

Ag(111), Ag(100) and Ag(110) [12]. Therefore it seems reasonable to assume a PTCDA induced buckling on Cu(100), too.

From LEED patterns at lower electron energies we further find that the (1,0) and (3,0) spots are not visible. This indicates a systematic extinction for the (*n*,0) and (0,*n*) spots with *n* = odd

which is due to a *p2gg* symmetry of the structure (i.e., the presence of two perpendicular glide planes). It was already noted by Schmidt et al. [8] and related to a *p2gg* symmetry of the PTCDA layer. As we will describe below, application of this symmetry to the entire adsorption complex (including the Cu(100) substrate) restricts the possible adsorption sites of PTCDA.

The commensurate matrix $\mathbf{M}_0$ of the $(4\sqrt{2} \times 5\sqrt{2})R45°$ superstructure corresponds to the observed LEED pattern, and within the error bars, $\mathbf{M}_0$ is identical with the matrix we calculated from the STM measurements (see Table 1). Therefore our data obtained for deposition of PTCDA on Cu(100) at an elevated sample temperature of 400 K confirm the structure proposed by Schmidt et al. [8]. We did not observe the structure proposed by Andreasson et al. [9].

Kinetic hindrance for deposition at 300 K

Depending on the sample temperature during the deposition the fraction of $(4\sqrt{2} \times 5\sqrt{2})R45°$ ordered regions on the covered surface varies. For lower deposition temperatures (300–350 K) we find only small domains of typically less than 50 Å in diameter which are separated by misfit areas between them. In these misfit areas, the structure slightly deviates from the $(4\sqrt{2} \times 5\sqrt{2})R45°$ superstructure. Figure 1(b) shows such a misfit area between two translational domains of the superstructure. We use the term misfit area instead of the usually used term domain boundaries in order to emphasize that these areas have a certain width and span several unit cells. The structure of the misfit areas exhibits some flexibility and varies depending on the relative positions of the $(4\sqrt{2} \times 5\sqrt{2})R45°$ domains which are connected. Apparently, at lower deposition temperatures the surface mobility of the PTCDA molecules is too small to allow the structural adaptation of different translational or rotational domains which have resulted from incoherent nucleation. This causes a significant fraction of the surface to be covered by misfit areas.

In the same way as the edges of islands, the borders between ordered domains and misfit areas are also often orientated parallel to the diagonal of the adsorbate unit cell. Due to the misfit areas LEED patterns of samples prepared at low temperatures show only broad and weak spots. From STM images we find that for a deposition temperature of 300 K only about 65% of the covered surface is ordered in the $(4\sqrt{2} \times 5\sqrt{2})R45°$ superstructure, whereas this fraction increases to 90% for a deposition temperature of 400 K. In each case, the rest of the surface is covered by misfit areas. In addition to the decreasing fraction of the misfit areas, the average domain size increases for higher deposition temperatures. Whilst for a deposition temperature of 300 K, the average domain size is only about 50 nm², deposi-

tion at 400 K leads to an average size of about 150 nm². LEED images show that post annealing at 450 K for 10 min of a sample prepared at a temperature of 300 K transforms the misfit areas into ordered domains of the $(4\sqrt{2} \times 5\sqrt{2})R45°$ superstructure. Before the post annealing, closely adjacent LEED spots could not be distinguished due to their broadness, whereas this was well possible afterwards. The resulting LEED pattern is identical to the one of a sample prepared at 400 K. However, further annealing at 550 K for 5 min leads to a complete destruction of the ordered superstructure. In the LEED pattern the adsorbate spots have vanished then, and STM images show only chain-like disordered structures, as illustrated in Figure 1(c), which will be discussed further below in the Discussion section.

In contrast to the temperature, a variation of the coverage has no strong influence on the quality of the superstructure. Finally, our LEED and STM data (not shown) confirm that even the second layer of PTCDA orders according to the $(4\sqrt{2} \times 5\sqrt{2})R45°$ superstructure, as it was already proposed by Schmidt et al. [8].

The adsorption site

We now turn to a more detailed analysis of the packing within the unit cell. Figure 3(a) shows a close up view of the $(4\sqrt{2} \times 5\sqrt{2})R45°$ superstructure of PTCDA on Cu(100). The influence of the thermal drift has been corrected by determination of the unit cell in the uncorrected image and setting its parameters to the commensurate ones. In order to determine the orientation of the two molecules within the unit cell the outer contours of the molecules given by the van der Waals spheres [13] were superimposed and fitted to the STM image. With an estimated uncertainty of about ±3° the long molecular axes are oriented 45° with respect to the unit cell vectors. Therefore the two PTCDA molecules within each cell are positioned perpendicular to each other in an L-shape arrangement and their long molecular axes are parallel to the [011] and the [01$\bar{1}$] directions of Cu(100), respectively.

As visible in Figure 3(a), the STM contrast of the two molecules within the unit cell is identical and independent on the orientation of the molecule. This observation was also made for STM images taken at other bias voltages than 1.3 V (used for Figure 3(a)), namely of −1.2 V, −0.55 V, and 0.86 V. Hence we propose that both molecules exhibit identical adsorption sites. This conclusion is based on the observation of a significantly different STM contrast for structures where two PTCDA molecules are on different adsorption sites in the unit cell, e.g., for PTCDA on Ag(111) [14]. The difference in the STM contrast is a consequence of the different electronic coupling of the molecules to the substrate on the two different sites. We note

Figure 3: (a) High resolution STM image of the $(4\sqrt{2} \times 5\sqrt{2})R45°$ structure of PTCDA on Cu(100). Here the influence of the thermal drift has been corrected (U_{bias} = 1.3 V, I_T = 67 pA, 6.3 × 5.5 nm²). 3 × 3 unit cells and the van der Waals radii [13] of the PTCDA molecules are indicated (black lines). (b) Hardsphere model for the $(4\sqrt{2} \times 5\sqrt{2})R45°$ structure of PTCDA on Cu(100). Carbon atoms: dark grey, oxygen atoms: red, and hydrogen atoms: white, copper atoms light grey. Further details see text.

however that the observation of the STM contrast is not a firm argument for identical adsorption sites and may require validation by other methods.

Under the condition that one PTCDA molecule is positioned at the edge and one at the center of the unit cell, as it is derived from the STM images, two identical adsorption sites are only possible, if the centers of the two molecules are positioned on bridge sites of the Cu(100) surface (see Figure 3(b)). Since the (100) surface exhibits two different bridge sites, rotated by 90° to each other, two possibilities exist for positioning the adsorbate structure on Cu(100).

For both possibilities the whole adsorbate/substrate complex exhibits all symmetry elements which are required for the *p2gg* symmetry of the $(4\sqrt{2} \times 5\sqrt{2})R45°$ superstructure derived from LEED, and in both cases the application of all symmetry elements of the substrate leads to two rotational domains, in agreement with the experimental findings. We cannot exclude one of the two possibilities on the basis of our data so far. However we propose that the structure imaged in Figure 3(b), is favorable because in this structure the carbon atoms of the anhydride groups (C_{func}) come on on-top positions, which would be not the case for the alternative structure. A side-to-side illustration of both possibilities is given in Supporting Information File 1. We note that due to the different lattice constant of Cu compared to Ag, an arrangement of all carboxylic O atoms close to on-top sites, as it is found for PTCDA on Ag(100) [12] is not possible. Hence, the positioning of the C_{func} atoms on top-positions may act as an alternative surface bonding motive here. In the model proposed by Schmidt et al. [8], the PTCDA molecules exhibit two different adsorption sites: The center of one molecule is positioned on a four-fold hollow site, whereas the other one is positioned on an on-top site. This model would hence contradict our observation of an identical STM contrast for both molecules in the unit cell. In addition, the adsorbate/substrate complex of the model proposed by Schmidt et al. has a reduced symmetry compared to the adsorbate layer alone and we expect that the extinctions in the LEED pattern due the *p2gg* symmetry would be lifted, similar to the situation seen for PTCDA/Ag(111) [14].

PTCDA in the oxygen pre-covered Cu(100) surface

The adsorption of atomic oxygen on Cu(100) induces a missing row reconstruction where every fourth $\langle 001 \rangle$ row of copper atoms is missing, leading to a $(\sqrt{2} \times 2\sqrt{2})R45° - 2O/Cu(100)$ superstructure [15]. This reconstruction is illustrated in Figure 4(d) (below). The structural details have been taken from [15]. The corresponding unit cell, containing two oxygen atoms, is indicated in lower right corner of Figure 4(d). We note that the structural description has been discussed in the literature for some time concluding in this missing row reconstruction (see references in [15]). Our LEED and STM measurements confirm that the preparation procedure described above leads to the formation of this $(\sqrt{2} \times 2\sqrt{2})R45° - 2O/Cu(100)$ superstructure with two rotational domains.

PTCDA forms large, nearly defect-free domains on the $(\sqrt{2} \times 2\sqrt{2})R45° - 2O/Cu(100)$ surface, already at a deposition temperature of 300 K. Figure 4(a) shows an STM image of a terrace with a nominal coverage of 1 ML of PTCDA. The terrace is limited by a descending and an ascending step. Interestingly, the ordered PTCDA structure is only present in the region adjacent to the descending step (see lower left corner of
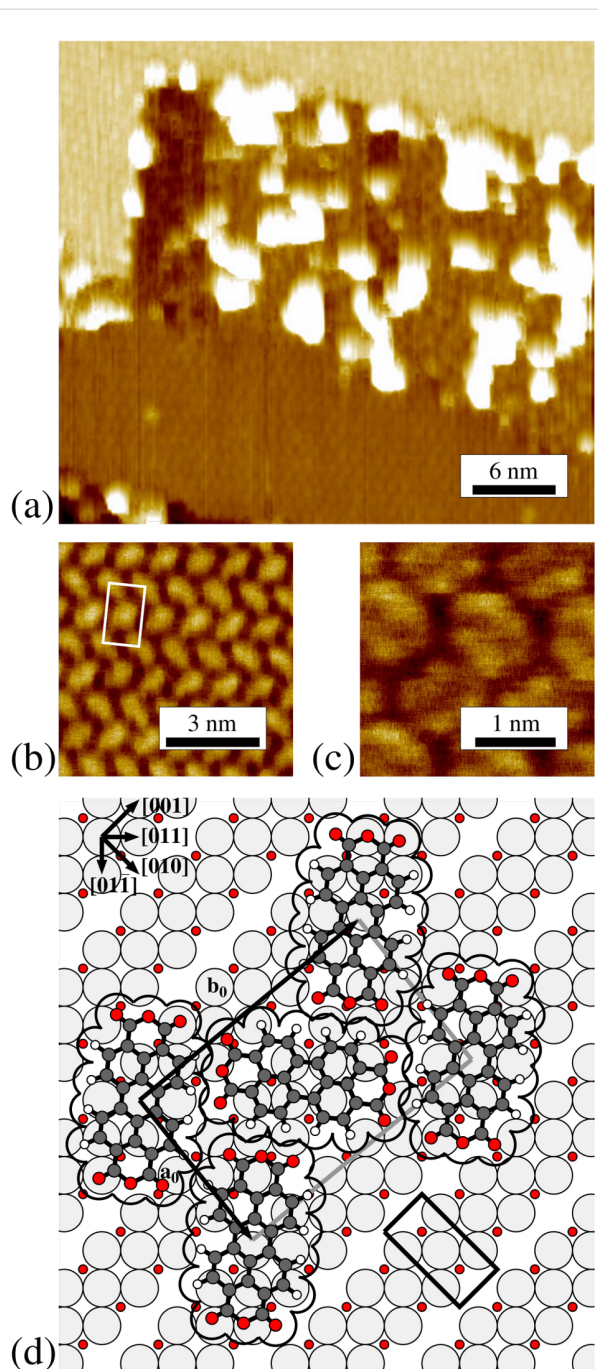
Figure 4: Different STM images of PTCDA on the $(\sqrt{2} \times 2\sqrt{2})R45° - 2O/Cu(100)$ surface. (a) STM image of a terrace, which is fully covered by PTCDA. The terrace is limited by an ascending and a descending step in the upper and lower parts of the image, respectively ($U_{bias} = -3.0$ V, $I_T = 49$ pA, 38.8 × 35.0 nm^2). (b) Image of the ordered incommensurate structure of PTCDA on this surface ($U_{bias} = -1.6$ V, $I_T = 59$ pA, 8.0 × 8.0 nm^2). (c) High resolution image of the ordered structure showing submolecular resolution ($U_{bias} = 1.2$ V, $I_T = 84$ pA, 3.1 × 3.1 nm^2). (d) Hardsphere model for the incommensurate structure of PTCDA on $(\sqrt{2} \times 2\sqrt{2})R45° - 2O/Cu(100)$. The unit cell of the 2O/Cu(100) surface is drawn in the right lower corner. In order to reduce the complexity only the topmost layer of one domain of the $(\sqrt{2} \times 2\sqrt{2})R45° - 2O$ superstructure is drawn. The same color code as in Figure 3 applies.

Figure 4(a)). Further away from the step, a disordered structure with bright protrusions appears, extending to the ascending step. This type of disordered structure at the lower step edge sites is also present at low coverages. We propose that it may be possible that individual Cu atoms get pulled out of the step edges here and interact more strongly with the PTCDA molecules closer to the steps, leading to the formation of these clusters. Presumably the effect is promoted by the presence of the oxygen induced reconstruction and hence only present on the O pre-covered Cu(100) surface, and not on the bare Cu(100) surface.

The step edges of the PTCDA covered surface are facetted and the straight sections run parallel to the [001] and [010] directions. The steps are hence orientated parallel or perpendicular to the missing rows of the $(\sqrt{2} \times 2\sqrt{2})R45° - 2O/Cu(100)$ surface, as already observed for the uncovered 2O/Cu(100) surface. We take this as an indication that the $(\sqrt{2} \times 2\sqrt{2})R45° - 2O/Cu(100)$ superstructure remains unchanged underneath the PTCDA adsorbate layer. This is also confirmed by LEED patterns of PTCDA on 2O/Cu(100) which show the reconstruction spots, although with damped intensities. Because of the small size of the domains of the 2O/Cu(100) reconstruction of less than 50 nm^2 (in agreement with [16]) the PTCDA superstructure overgrows the domain boundaries of the 2O/Cu(100) surface.

A close up of the ordered PTCDA structure is shown in Figure 4(b). The unit cell (marked in white) contains two PTCDA molecules with different orientations. In contrast to the superstructure of PTCDA on bare Cu(100), the longer vector **b$_0$** of the unit cell forms an angle of about 6° with respect to the [001] direction of (100) surface and also the dimensions of the unit cell vectors differ with respect to those of PTCDA on bare Cu(100). We note that contrary to the situation on bare Cu(100) we get a more pronounced submolecular contrast of the PTCDA for similar tunneling parameters (see Figure 4(c) in comparison with Figure 3(a)) which we interpret as an indication for the electronic decoupling from the substrate. The structural parameters derived by STM are given in Table 1. The corresponding superstructure is incommensurate with respect to the bare Cu(100) as well as to the 2O/Cu(100) surface. This indicates a weak interaction of the PTCDA with the surface. The diffraction pattern of the PTCDA superstructure is simulated in the left part of Figure 2(b) and compared with the observed LEED pattern, which is displayed in the right part. The direction of the substrate vectors are indicated by black lines. The unit cells of the two rotational domains of the underlying $(\sqrt{2} \times 2\sqrt{2})R45° - 2O$ reconstruction are indicated in red and blue. The remaining spots are all explained well by four symmetry equivalent domains of the PTCDA superstructure, consisting two mirror domains of the PTCDA structure on both of the two rotational

domains of the 2O/Cu(100) surface. The respective unit cells are indicated in Figure 2(b). Notably, the (1,0) and the (0,1) LEED spots of the PTCDA layer cannot be detected. We explain this extinction with the *p2gg* symmetry of the PTCDA layer. Due to its incommensurability with the 2O/Cu(100) substrate, the scattering of the substrate does not contribute to the LEED spots of the PTCDA layer and hence does not have an effect on the extinction of the (1,0) and (0,1) spots. This is different from the situation discussed above for the commensurate structures of PTCDA on Cu(100) or Ag(111), where the substrate can lift the extinction rule.

As noted, the four symmetry equivalent domains of PTCDA consist of two pairs of mirror domains. A structure model of one domain is shown in Figure 4(d). (We note that we have chosen the domain, which fulfills the requirements of naming superstructures defined by Barlow and Raval [17].) A symmetry equivalent domain is obtained by a mirror operation with respect to the [001] direction or the [010] direction, respectively. The second pair of domains is then obtained by a 90° rotation of the underlying $(\sqrt{2} \times 2\sqrt{2})R45° - 2O$ superstructure, yielding its symmetry equivalent rotational domain. However, we propose that all four symmetry equivalent PTCDA domains exist on both rotational domains of the $(\sqrt{2} \times 2\sqrt{2})R45° - 2O/Cu(100)$ structure, because the PTCDA superstructure overgrows the respective domain boundaries (see above).

Discussion
Structural considerations

It is interesting to compare the lateral ordering within the commensurate $(4\sqrt{2} \times 5\sqrt{2})R45°$ superstructure of PTCDA on Cu(100) with that within the commensurate $(4\sqrt{2} \times 4\sqrt{2})R45°$ superstructure of PTCDA on Ag(100) [18]. Both structures contain two PTCDA molecules per unit cell, in perpendicular orientation to each other, motivated by the electrostatic interaction between the partially negatively charged anhydride groups and the positively charged perylene cores. On Cu(100) the area per molecule corresponds to 131.2 Å^2. This value is very comparable to that for PTCDA on Ag(100) (132.9 Å^2). Both values are about 10% larger than the area per molecule in the lattice planes of PTCDA bulk crystals of the α or β-modification (120 Å^2) [19]. Interestingly the unit cell on Cu(100) is rectangular, while it is quadratic on Ag(100). We propose that this is mainly a consequence of the smaller lattice constant of Cu with respect to Ag in combination with a strong chemisorptive interaction of PTCDA with the substrate, leading to a preferred azimuthal orientation of the long molecular axes along the [011] and the [01$\bar{1}$] directions.

The bonding of the PTCDA molecule to the Cu(100) substrate is of course most important for the structure formation. It causes

the preferential orientation of the molecular axes along the [011] and the [01$\bar{1}$] directions, i.e., the close packed rows of the substrate, because the resulting high symmetry of the adsorbate complex presumably optimizes the molecule/substrate interactions. On Cu(100), the two hypothetic commensurate structures with a quadratic unit cell, which yield this orientation of the molecules along the [011] and the [01$\bar{1}$] directions, are either too large (($5\sqrt{2} \times 5\sqrt{2}$)$R45°$ /163.8 Å^2 per molecule) or too small (($4\sqrt{2} \times 4\sqrt{2}$)$R45°$ /105.1 Å^2 per molecule). Other quadratic commensurate superstructures on Cu(100) with a similar size to that of PTCDA/Ag(100) are rotated with respect to the former. Such a structure is, e.g., $\mathbf{M}_0 = \begin{pmatrix} 5 & 4 \\ -4 & 5 \end{pmatrix}$ with 134.5 Å^2 per molecule and $\varphi_0 = 38.7°$. However, under the assumption that the favorable orientation of the long molecular axes along the [011] and the [01$\bar{1}$] directions was maintained in this structure, the spaces between the anhydride groups would be too small, which is unfavorable due to the negative partial charges on these groups. We note that we actually found this superstructure as a minor phase at the beginning of our experiments due to a (presumably partially positively charged) contamination, e.g., carbon, which stabilized the closeness of the anhydride groups. Due to an increasing cleanliness of the sample during the following experiments this structure disappeared. In conclusion, on Cu(100), a rectangular unit cell is preferred because this cell yields orientations of the long molecular axes along the [011] and the [01$\bar{1}$] directions and simultaneously optimizes the intermolecular interaction of the negatively charged anhydride groups with the positively charged perylene cores.

Bonding and dissociation

We suppose that UPS will reveal a chemisorptive bonding of PTCDA on Cu(100) with filling of the former LUMO, similar to the situation that was found on Ag(100) [20]. We note that the UPS measurements from Andreasson et al. of PTCDA on Cu(100) can also be interpreted in this way [9], although these results have to be taken with some caution, because of the different structure they found. The ordering of the second layer of PTCDA on Cu(100) with the same commensurate structure as the monolayer further points to a strong interaction with the Cu substrate. This is in contrast to the formation of an incommensurate second layer of PTCDA on Ag(100) [18]. The formation of kinetically stabilized misfit areas at a deposition temperature of 300 K on Cu(100) is also indicative for the strong interfacial interaction on Cu(100). On Ag(100), PTCDA forms highly ordered domains already at this temperature [18]. Therefore the corrugation of the bonding potential for PTCDA/Cu(100) seems to be significantly larger compared to PTCDA/Ag(100), which leads to a lower diffusion constant and hence the need of higher preparation temperatures for highly ordered layers.

However, the question whether the chemisorption is dissociative or not still needs to be answered. So far, all our structural findings stand against dissociative adsorption: (a) In STM images, like Figure 3(a), the van der Waals-radii of the PTCDA molecules fit well to the measured electron density, although a loss of only the bridging oxygen atoms could certainly not be recognized. (b) The derived structure can be well understood from arguments based on intact PTCDA molecules, in particular the area per molecule agrees well with the expected one. (c) The structural order in the layer improves upon moderate heating to 400 K. If dissociation took place during the deposition, we would expect that heating would activate the formation of irreversible intermolecular and/or molecule substrate bonds which would counteract the formation of a long range ordered structure.

Data reported in the literature does not give a firm proof of a dissociative adsorption of PTCDA on Cu(100). The XPS measurements by Schmidt et al. were carried out with PTCDA on a polycrystalline copper foil [8]. Therefore the result that the ratio C:O is about 6:1 instead of 4:1 for a low coverage (indicating the presence of only four instead of six oxygen atoms per PTCDA molecule) cannot be easily transferred to the single crystal Cu(100) surface. Schmidt et al. support their conclusion also by TPD experiments of PTCDA on Cu(100) [8], in which they did not observe a peak of the fragment $m/z = 124$ for a coverage of 1 ML. This observation could be due to PTCDA dissociation during the adsorption process, but it is also conceivable that the dissociation occurs at elevated temperatures during the TPD experiment itself. This scenario is known from other chemisorptive systems, like PTCDA/Ag(111), [21]. Our STM data support such a scenario also for PTCDA on Cu(100). Figure 1(c) shows the chain like structure observed after annealing the ($4\sqrt{2} \times 5\sqrt{2}$)$R45°$ superstructure for 5 min at 550 K. Some chains are isolated and some chains are packed closer together, probably with remaining PTCDA molecules in between them (see upper right corner of Figure 1(c)). Since there are apparently also chains with threefold connection points, a simple polymeric reaction, which took place at the reactive anhydride groups of the PTCDA molecules can be excluded. However, it is hence feasible that at this elevated temperatures the PTCDA molecules have undergone different kinds of chemical reactions. Therefore no intact desorption can be expected, in agreement with the TPD experiments of Schmidt et al. [8]. A non-dissociative adsorption on Cu(100) is further corroborated by STM images of PTCDA on the even more open, and hence more reactive, Cu(110) surface, where no dissociation after adsorption at rt and post annealing at 450 K was found [22]. In conclusion we state that in spite of the strong interaction between PTCDA and Cu(100) there are no indications for a dissociation during adsorption.

Surface passivation

The situation changes drastically for the adsorption of PTCDA on the oxygen induced reconstruction of the Cu(100) surface. The structure is incommensurate and has a unit cell of a size of 12.2×19.3 Å^2, which is hence very similar to that of the respective lattice plane in bulk PTCDA crystals of the β-modification. The area per molecule is 117.7 Å^2 which has to be compared with 120.6 Å^2 for the β-modification. This indicates a dominant character of the intermolecular interactions in this system. All these observations reveal that for this system the adsorbate/adsorbate interactions have more influence on the structure formation than the adsorbate/substrate interactions, which contrasts with the findings for PTCDA on bare Cu(100), where the latter interactions are dominant.

Thus the $(\sqrt{2} \times 2\sqrt{2})R45° - 2O$ superstructure passivates the reactive Cu(100) surface effectively. A similar phenomena is known for the adsorption of PTCDA on the reactive Ni(111) surface. In that case the interaction on the free surface is so strong that the molecules do not diffuse over the surface and hence do not form an ordered structure [23], whereas on $p(2 \times 2) - O/ /Ni(111)$ a well ordered herringbone structure was observed [24]. The passivation with an oxygen layer therefore leads to an increase of the diffusion constant. On Cu(100) an elevated surface temperature of 400 K is needed to obtain a highly ordered structure, whereas this is possible for PTCDA on $(\sqrt{2} \times 2\sqrt{2})R45° - 2O/Cu(100)$ already at rt.

Conclusion

From STM and LEED data we confirm the commensurate $(4\sqrt{2} \times 5\sqrt{2})R45°$ superstructure of PTCDA on Cu(100) proposed by Schmidt et al. [8]. A structure model where both molecules in the unit cell are on identical sites has been derived. On the basis of our structural data, there are no indications for dissociation during the adsorption. However, kinetic barriers hinder the lateral ordering at 300 K, leading to significant misfit areas between the ordered domains. These can be avoided if the preparation is performed at 400 K. STM images show that at 550 K the PTCDA molecules undergo a chemical reaction, which prohibits intact desorption. On the oxygen passivated $(\sqrt{2} \times 2\sqrt{2})R45° - 2O/Cu(100)$ surface, the interfacial interaction is strongly reduced, leading to an ordered PTCDA layer with an incommensurate structure.

Supporting Information

Supporting Information File 1

Two possible adsorption sites of PTCDA on Cu(100). [http://www.beilstein-journals.org/bjoc/content/supplementary/1860-5397-10-213-S1.pdf]

References

1. Horowitz, G. *Adv. Mater.* **1998,** *10,* 365–377. doi:10.1002/(SICI)1521-4095(199803)10:5<365::AID-ADMA365>3.0.CO;2-U
2. Kulkarni, A. P.; Tonzola, C. J.; Babel, A.; Jenekhe, S. A. *Chem. Mater.* **2004,** *16,* 4556–4573. doi:10.1021/cm049473l
3. Tautz, F. S. *Prog. Surf. Sci.* **2007,** *82,* 479–520. doi:10.1016/j.progsurf.2007.09.001
4. Hauschild, A.; Temirov, R.; Soubatch, S.; Bauer, O.; Schöll, A.; Cowie, B. C. C.; Lee, T.-L.; Tautz, F. S.; Sokolowski, M. *Phys. Rev. B* **2010,** *81,* 125432. doi:10.1103/PhysRevB.81.125432
5. Henze, S. K. M.; Bauer, O.; Lee, T. L.; Sokolowski, M.; Tautz, F. S. *Surf. Sci.* **2007,** *601,* 1566–1573. doi:10.1016/j.susc.2007.01.020
6. Gerlach, A.; Sellner, S.; Schreiber, F.; Koch, N.; Zegenhagen, J. *Phys. Rev. B* **2007,** *75,* 045401. doi:10.1103/PhysRevB.75.045401
7. Duhm, S.; Gerlach, A.; Salzmann, I.; Bröker, B.; Johnson, R. L.; Schreiber, F.; Koch, N. *Org. Electron.* **2008,** *9,* 111–118. doi:10.1016/j.orgel.2007.10.004
8. Schmidt, A.; Schuerlein, T. J.; Collins, G. E.; Armstrong, N. R. *J. Phys. Chem.* **1995,** *99,* 11770–11779. doi:10.1021/j100030a023
9. Andreasson, M.; Tengelin-Nilsson, M.; Ilver, L.; Kanski, J. *Synth. Met.* **2008,** *158,* 45–49. doi:10.1016/j.synthmet.2007.12.001
10. Ikonomov, J. *MCPdeskew;* Rheinische Friedrich-Wilhelms-Universität Bonn, 2010.
11. Jensen, F.; Besenbacher, F.; Laegsgaard, E.; Stensgaard, I. *Phys. Rev. B* **1990,** *42,* 9206–9209. doi:10.1103/PhysRevB.42.9206
12. Bauer, O.; Mercurio, G.; Willenbockel, M.; Reckien, W.; Schmitz, C. H.; Fiedler, B.; Soubatch, S.; Bredow, T.; Tautz, F. S.; Sokolowski, M. *Phys. Rev. B* **2012,** *86,* 235431. doi:10.1103/PhysRevB.86.235431
13. Bondi, A. *J. Phys. Chem.* **1964,** *68,* 441–451. doi:10.1021/j100785a001
14. Glöckler, K.; Seidel, C.; Soukopp, A.; Sokolowski, M.; Umbach, E.; Böhringer, M.; Berndt, R.; Schneider, W. D. *Surf. Sci.* **1998,** *405,* 1–20. doi:10.1016/S0039-6028(97)00888-1
15. Kittel, M.; Polcik, M.; Terborg, R.; Hoeft, J. T.; Baumgärtel, P.; Bradshaw, A. M.; Toomes, R. L.; Kang, J. H.; Woodruff, D. P.; Pascal, M.; Lamont, C. L. A.; Rotenberg, E. *Surf. Sci.* **2001,** *470,* 311–324. doi:10.1016/S0039-6028(00)00873-6
16. Wöll, C.; Wilson, R. J.; Chiang, S.; Zeng, H. C.; Mitchell, K. A. R. *Phys. Rev. B* **1990,** *42,* 11926–11929. doi:10.1103/PhysRevB.42.11926
17. Barlow, S. M.; Raval, R. *Surf. Sci. Rep.* **2003,** *50,* 201–341. doi:10.1016/S0167-5729(03)00015-3
18. Ikonomov, J.; Bauer, O.; Sokolowski, M. *Surf. Sci.* **2008,** *602,* 2061–2068. doi:10.1016/j.susc.2008.04.009
19. Möbus, M.; Karl, N.; Kobayashi, T. *J. Cryst. Growth* **1992,** *116,* 495–504. doi:10.1016/0022-0248(92)90658-6
20. Marks, M. Ph.D. Thesis, Philipps-Universität, Marburg, 2012. http://archiv.ub.uni-marburg.de/ubfind/Record/urn:nbn:de:hebis:04-z2013-0535
21. Zou, Y.; Kilian, L.; Schöll, A.; Schmidt, T.; Fink, R.; Umbach, E. *Surf. Sci.* **2006,** *600,* 1240–1251. doi:10.1016/j.susc.2005.12.050

22. Stöhr, M.; Gabriel, M.; Möller, R. *Surf. Sci.* **2002,** *507–510,* 330–334. doi:10.1016/S0039-6028(02)01266-9
23. Taborski, J.; Väterlein, P.; Dietz, H.; Zimmermann, U.; Umbach, E. *J. Electron Spectrosc. Relat. Phenom.* **1995,** *75,* 129–147. doi:10.1016/0368-2048(95)02397-6
24. Tiba, M. V.; Kurnosikov, O.; Flipse, C. F. J.; Koopmans, B.; Swagten, H. J. M.; Kohlhepp, J. T.; de Jonge, W. J. M. *Surf. Sci.* **2002,** *498,* 161–167. doi:10.1016/S0039-6028(01)01682-X

Molecular ordering at electrified interfaces: Template and potential effects

Thanh Hai Phan[*1,2,3] and Klaus Wandelt[1,4]

Full Research Paper

`Open Access`

Address:
[1]Institute of Physical and Theoretical Chemistry, University of Bonn, Wegelerstr. 12, 53115 Bonn, Germany, [2]Laboratory of Photochemistry and Spectroscopy, Department of Chemistry, Catholic University of Leuven, Celestijnenlaan 200F, B-3001, Hevelee, Belgium, [3]Physics Department, Quynhon University, 170 An Duong Vuong; Quynhon, Vietnam and [4]Institute of Experimental Physics, University of Wroclaw, MaxaBorna 9, 50-204, Wroclaw, Poland

Email:
Thanh Hai Phan[*] - phan@thch.uni-bonn.de

* Corresponding author

Abstract

A combination of cyclic voltammetry and in situ scanning tunneling microscopy was employed to examine the adsorption and phase transition of 1,1'-dibenzyl-4,4'-bipyridinium molecules (abbreviated as DBV^{2+}) on a chloride-modified Cu(111) electrode surface. The cyclic voltammogram (CV) of the Cu(111) electrode exposed to a mixture of 10 mM HCl and 0.1 mM $DBVCl_2$ shows three distinguishable pairs of current waves P1/P'1, P2/P'2, and P3/P'3 which are assigned to two reversible electron transfer steps, representing the reduction of the dicationic DBV^{2+} to the corresponding radical monocationic $DBV^{+\bullet}$ (P1/P'1) and then to the uncharged DBV^0 (P3/P'3) species, respectively, as well as the chloride desorption/readsorption processes (P2/P'2). At positive potentials (i.e., above P1) the DBV^{2+} molecules spontaneously adsorb and form a highly ordered phase on the $c(p \times \sqrt{3})$-precovered Cl/Cu(111) electrode surface. A key element of this DBV^{2+} adlayer is an assembly of two individual DBV^{2+} species which, lined up, forms a so-called "herring-bone" structure. Upon lowering the electrode potential the first electron transfer step (at P1) causes a phase transition from the DBV^{2+}-related herring-bone phase to the so-called "alternating stripe" pattern built up by the $DBV^{+\bullet}$ species following a nucleation and growth mechanism. Comparison of both observed structures with those found earlier at different electrode potentials on a $c(2 \times 2)Cl$-precovered Cu(100) electrode surface enables a clear assessment of the relative importance of adsorbate–substrate and adsorbate–adsorbate interactions, i.e., template vs self-assembly effects, in the structure formation process of DBV cations on these modified Cu electrode surfaces.

Introduction

The precise control of the self-organization of molecular layers on either conducting or dielectric substrates is regarded as one of the key factors in the successful design, characterization and fabrication of nanoscale molecular devices [1-4]. A big challenge for surface scientists is, thus, to find suitable model systems which enable to investigate the driving forces of molecular self-organization on surfaces and to simulate the working principles of the derived molecular devices. This so-called "bottom-up" strategy, i.e., the formation of supramolecular structures from vapor deposited simpler building blocks has become an important research direction in ultra-high vacuum (UHV) based surface science in recent years. However, promising organic compounds may not remain intact volatile, and may thus not be deposited via the gas phase. In those cases, it may be a promising strategy to deposit these molecules from solution instead. Besides, this preparation route is probably also more economic than operating a vacuum evaporation system, in particular if the organic building blocks come in water-soluble form.

In principle, the self-organization process of molecular adsorbates is driven by the interplay between adsorbate–adsorbate and adsorbate–substrate interactions. While the former depend on the specific nature of the molecular building blocks, e.g., their shape, polarity, functional groups, etc., and may include all possible interactions from van der Waals forces to covalent bonds, the latter are described by the so-called "corrugation function", i.e., the two-dimensional (2D) potential energy landscape representing the minimum total energy for all possible adsorbate–substrate configurations and, thereby, the interaction strength between the substrate and an adsorbate molecule at any surface site. If, in equilibrium, the adsorbate–adsorbate interactions dominate over the adsorbate–substrate interactions the molecules will essentially "self-assemble" independent of the substrate surface. If, however, the adsorbate–substrate interactions are very strong compared to the intermolecular forces the substrate will influence the structure of the adsorbate layer, provided a sufficient surface mobility allows the adsorbed molecules to reach their equilibrium positions, i.e., minima in the corrugation function. In this case the substrate surface acts as a "template". Under UHV conditions the activation energy for structural equilibration is usually provided by heating the substrate. If however, the organic species are deposited in ionic form from aqueous solution, as done in the present work, the obtained structure will additionally be influenced by electrostatic forces acting between the molecules and the substrate as well as between the molecules themselves. In this respect electrochemical deposition has the additional advantage that these electrostatic interactions can be "tuned" by the electrochemical potential in two ways. On the one hand the mere charge density

at the electrode surface itself determines the electrostatic forces between adsorbed ions, not only the organic species but also possibly co-adsorbed other ions present in the solution, and the substrate. On the other hand, driven by the electrode potential the molecular ions may undergo redox-reactions, thereby changing their own charge state. Both cases are expected to influence the deposition and structure formation of the molecular layers.

In this paper we will present results on the self-organization of 1,1'-dibenzyl-4,4'-bipyridinium, in short dibenzyl-viologen (DBV), cations on a chloride precovered Cu(111) electrode surface. A comparison of these findings with those described earlier for the same molecules on a chloride-modified Cu(100) electrode [5-7], will then enable us to arrive at a generalized picture of the influence of template and potential effects on the structure formation of these molecular ions on both chloride modified copper single crystal surfaces of different symmetry.

The motivation for the choice of viologen molecules is twofold. On the one hand molecular viologen-based self-assemblies have attracted a great deal of attention in recent years due to their widespread applications in electronic devices [8,9], and light-harvesting operators [10]. On the other hand the electrochemistry of viologens in solution is well documented in the literature [11,12]. In dicationic form dibenzyl-viologen molecules (DBV^{2+}) are well-known to undergo two successive reversible electron transfer steps yielding first the corresponding monocation radical $DBV^{+\bullet}$ and then the uncharged viologen species DBV^0, respectively. The first investigations on the surface redox chemistry as well as the self-assembly of DBV-species on a chloride modified Cu(100) surface, were presented by Safarowsky et al. and Pham et al. [5-7]. In the present paper we will describe for the first time the structural properties of self-assembled DBV on a chloride terminated Cu(111) electrode surface. Their comparison with the previous results obtained on the chloride precovered Cu(100) surface will clearly demonstrate the relative importance of adsorbate–substrate and adsorbate–adsorbate interactions, i.e., template-effects vs self-assembly, at different electrode potentials.

Results
Electrochemical characterization

The electrochemical characterization of the Cu(111) surface in both pure 10 mM HCl and the viologen containing (10 mM HCl + 0.1 mM DBV^{2+}) solution was done using cyclic voltammetry. Representative steady-state CVs are shown in Figure 1. The potential window of the Cu(111) electrode in the pure supporting electrolyte (10 mM HCl) is limited by the oxidative copper dissolution reaction (CDR) at the anodic limit and the

reductive hydrogen evolution reaction (HER) at the cathodic limit. At intermediate potentials, two peaks are seen which are due to chloride desorption/adsorption at −360 mV and −80 mV, respectively. Compared to this CV in pure hydrochloric acid, drastic changes are found in the cyclic voltamogram of the Cu(111) electrode in contact with the electrolyte containing 0.1 mM DBV^{2+}.

Figure 1: Cyclic voltammograms of Cu(111) in pure 10 mM HCl (dashed grey curve) and in viologen molecules containing (10mM HCl + 0.1 mM DBV^{2+}) solution (solid black curve); dE/dt = 10 mV/s; E = electrode potenial. CDR = copper dissolution reaction, HER = hydrogen evolution reaction. Reproduced with the permission from [16].
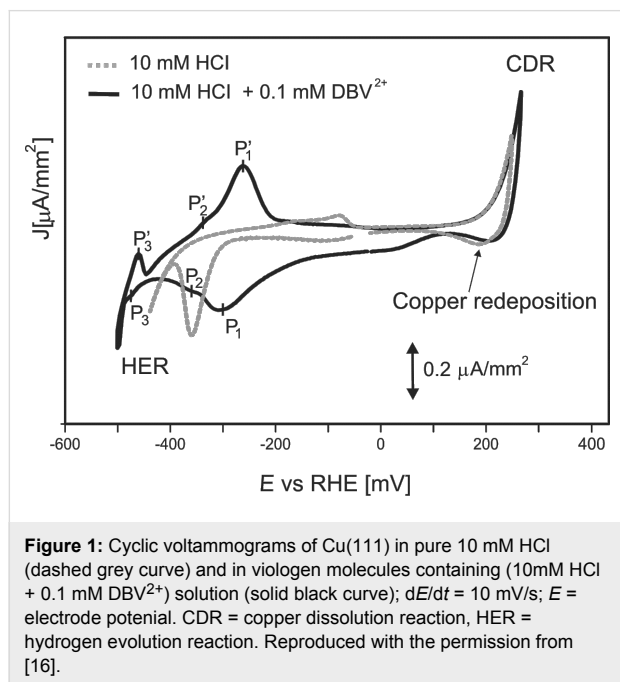
The first difference relates to a considerable shift of the HER towards lower potentials in the presence of the organic over-layer. This shift is most likely caused by viologen molecules blocking the most reactive surface sites for this reaction. The same effect was also reported by Pham et al. [6] and Safarowsky et al. [7] using a Cu(100) crystal as working electrode.

The second most obvious deviation concerns the appearance of three new pairs of peaks at potentials close to the HER. These additional current waves, namely P$_1$/P$_1$' and P$_2$/P$_2$' and P$_3$/P$_3$', are assigned to viologen-related redox-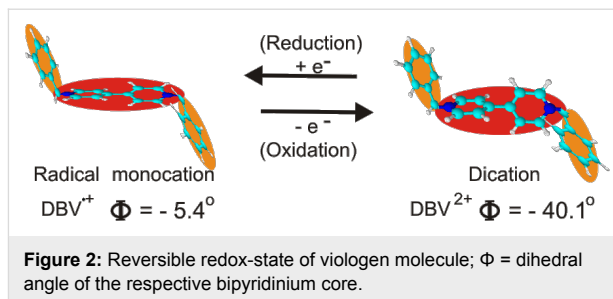processes (P$_1$/P$_1$' and P$_3$/P$_3$') [5-7,13-16], as well as to an order/disorder phase transition due to chloride desorption/adsorption [17]. As mentioned in the Introduction, the viologen dication (DBV^{2+}) is known to undergo two successive one-electron transfer steps in the electrochemical environment forming first the viologen monocation radical (DBV$^{+\bullet}$) (Figure 2) and then the uncharged molecule (DBV^0) (for details see [5,6,13-16], and the papers cited therein). While the dication and monocation radicals are soluble in aqueous solutions, the uncharged molecules can accumulate at the electrode surface due to their hydrophobic properties [4].

Figure 2: Reversible redox-state of viologen molecule; Φ = dihedral angle of the respective bipyridinium core.

The actual shape of the black cyclic voltammogram in Figure 1, in particular the relative intensities of the various peaks can be understood when considering the involvement of "solution species" and "surface limited" reactions, respectively. Starting at positive potentials, i.e., above P$_1$/P$_1$', the reduction/re-oxidation of both, the limited number of pre-adsorbed viologen dications (see XPS evidence below) and the continuously arriving viologen cations from solution, can be described by

$$DBV^{2+} + e^- \rightleftharpoons DBV^{+\bullet}$$
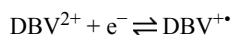
While DBV$^{+\bullet}$ species leaving the surface are known to form dimers in solution [5], DBV$^{+\bullet}$ species staying on the surface may also form polymeric chains (see below):

$$2\,DBV^{+\bullet} \rightleftharpoons [DBV_2]^{2+} \text{ (solution)}$$

$$n\,DBV^{+\bullet} \rightleftharpoons [DBV_n]^{n+} \text{ (surface)}$$

The reduction of the surface-confined species may even occur at an electrode potential different form that for the reduction of "solution species".

The further reduction of the monocation radicals to the fully uncharged viologen molecule DBV^0 (peak P$_3$ in Figure 1)

$$n\,DBV^{+\bullet} + n\,e^- \rightleftharpoons n\,DBV^0$$
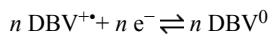
occurs already within the regime of massive hydrogen evolution. Since under these conditions reliable in situ STM measurements are not possible, the influence of this second reduction step on the structure of the deposit is not considered further here.

In the following sections we will now present and discuss in situ STM images as obtained for the electrode surface in different potential regimes. We start at potentials where the molecules retain their dicationic character (DBV^{2+}) in the adsorbed state, and then continue with results taken at potentials where the adsorbed molecules have undergone the first one-electron reduction step (at P$_1$ in Figure 1) and exist in their

monocation radical form DBV$^{+\bullet}$. These images clearly show the decisive influence of the respective charge state of the molecular species on the structure of the adsorbed DBV layer.

Structural characterizations

As documented in the literature [18-22] a well-ordered c(p × √3) layer of adsorbed chloride anions is formed on the Cu(111) surface (Figure 3) in the supporting HCl electrolyte, which, starting from a hexagonal c(√3 × √3)R30° structure at negative potentials exhibits the phenomenon of reversible electrocompression into a uniaxially incommensurate c(p × √3) structure with rectangular unit cell at positive potentials. This c(p × √3)Cl structure remains stable in the potential range between the copper dissolution reaction and about −300 mV (see Figure 1). In contrast to the larger halides, e.g., bromide and iodide, the chloride anions retain to a large extent their negative charge upon adsorption [23,24]. Hence, this regular array of anions can be regarded, similar to the c(2 × 2)Cl layer on Cu(100) (see below), as a suitable template for the adsorption of positively charged organic molecules.

Figure 3: Chloride-modified Cu(111) surface : a) STM image 70 nm × 70 nm, bias voltage U_b +220 mV, tunneling current I_t = 0.2 nA, E = 50 mV; b) STM image of the c(p × √3)Cl structure: 14.4 nm × 14.4 nm, 5.58 nm × 5.58 nm, I_t = 2.0 nA, U_b = 75 mV, E = 0.0 mV; c) Hard-sphere model of the chloride-modified Cu(111) surface.
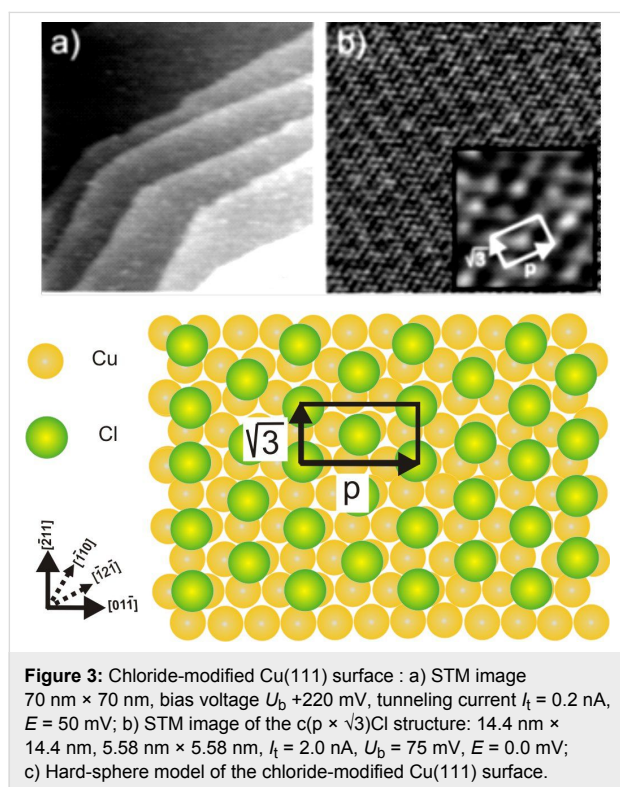
Exposing the c(p × √3)Cl terminated Cu(111) surface to the electrolyte containing DBV^{2+} ions at potentials between −50 mV and +50 mV vs RHE, i.e., in the potential regime above the first reduction peak P1 in Figure 1, results in the instantaneous formation of a highly ordered DBV^{2+} film. Figure 4 shows representative STM images describing the

surface morphology and molecular structure of the DBV^{2+} adlayer. First, the straight step-edges in Figure 4a running by each other at a typical angle of 120° still remain, providing a first indication of the persistence of the c(p × √3)Cl layer underneath the organic molecules (see also Figure 6). This indicates that the DBV^{2+} adlayer has no significant impact on the substrate-surface morphology, which is governed by the chemisorptive Cu–Cl bond. Two distinguishable domains rotated by an angle of 120° with respect to each other, denoted as I/I' and II/II' on the two different terraces shown, are observed in Figure 4a. A close inspection of the molecular arrangement makes it clear that the DBV^{2+} molecular rows within the domains are oriented parallel to step directions, the latter being aligned along the close-packed anion rows within the c(p × √3) chloride structure underneath [17,25]. As a result, the DBV^{2+} molecular rows are oriented parallel to the commensurate direction of the chloride lattice. Alternatively, they are aligned parallel to the ⟨$\overline{2}$11⟩ directions of the Cu(111) substrate (see Figure 3).

On the molecular level the rows consist of units of two bright oval dots assigned to the bipyridinium cores of individual DBV^{2+} molecules (Figure 2) that meet each other by an angle of 120 ± 2°. Using a line profile measurement along the white line in Figure 4c gives a length of about 0.72 ± 0.01 nm for one of the units (Figure 4d). This value is in complete agreement with the N–N distance of 0.71 nm within the DBV^{2+} molecules [5,12]. Based on this agreement in size, the given angle of 120°, and in particular, the consideration of electrostatic interactions between the bipyridinium core and the benzyl groups (for more details see the discussion below) we propose the molecular arrangement as shown in Figure 4c.

The structural correlation between the DBV^{2+} adlayer and the underlying chloride lattice could also be obtained by carefully varying the tunneling conditions [5,7,26]. Under "soft tunneling conditions", i.e., with high bias voltage and low tunneling current, the characteristic features of the DBV^{2+} adlayer are observed (Figure 5a). Conversely, the chloride lattice underneath becomes visible when "drastic tunneling conditions" are applied, i.e., low bias voltage and high tunneling current. In this circumstance, the tunneling tip serves as a molecular brush to locally remove the DBV^{2+} overlayer, leaving the c(p × √3)-Cl lattice behind (Figure 5b). By comparing panels 5a and 5b, it becomes evident that the individual bipyridinium cores of the DBV^{2+} molecules are aligned parallel to the underlying close-packed chloride rows, i.e., parallel to the ⟨$\overline{2}$11⟩ directions of the Cu(111) substrate, indicating the orienting effect of the lattice of the specifically adsorbed chloride anions on the structure of the adsorbed DBV^{2+} overlayer. This hints to a template effect rather than a mere self-assembly of the molecular dications on
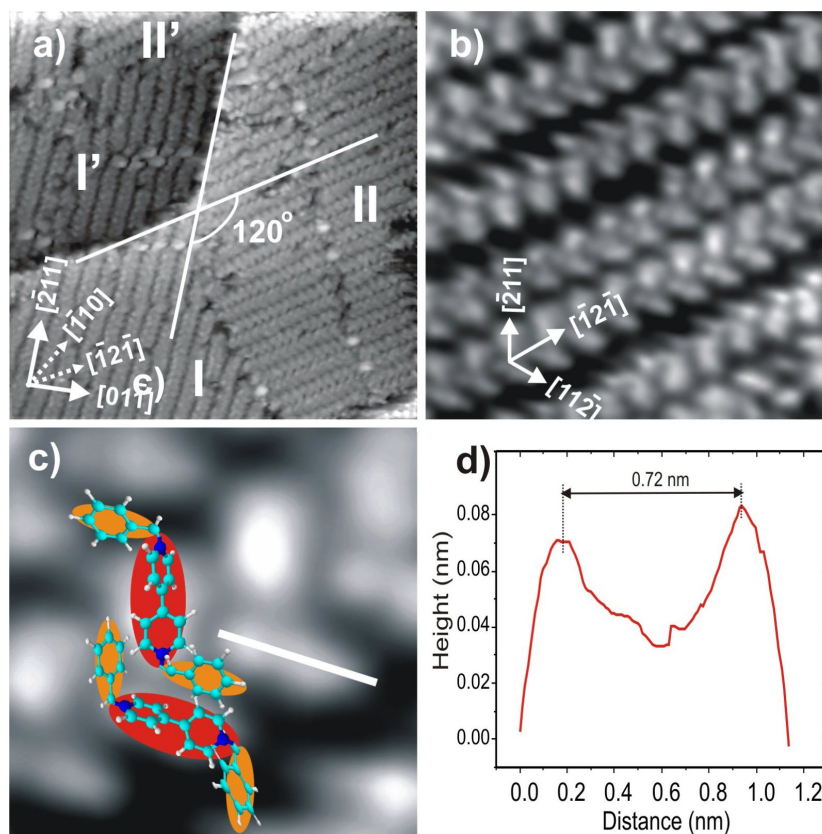
Figure 4: Typical STM images of the surface morphology and high-resolution images of the DBV^{2+} related herring-bone phase on Cl/Cu(111):
a) Surface morphology of the surface with a characteristic substrate step angle of 120° and two existing rotational domains (I/II; I'/II') of the DBV^{2+} herring-bone phase: 46.67 nm × 46.67 nm, U_b = 141 mV, I_t = 0.3 nA, E = −180 mV; b,c) Medium-scale (20.73 nm × 20.73 nm) and high-resolution (2.8 nm × 2.8 nm) STM image of the herring-bone phase, the latter showing two individual DBV^{2+} molecules in each structural element: U_b = 386 mV, I_t = 0.1 nA, E = +10 mV; d) Line profile recorded along the white line in Figure 4c indicating the length of the dipyridinium group of about 0.72 nm in perfect agreement with the N–N distance within the DBV^{2+} molecule. Figure 4a is reproduced with permission from [16].
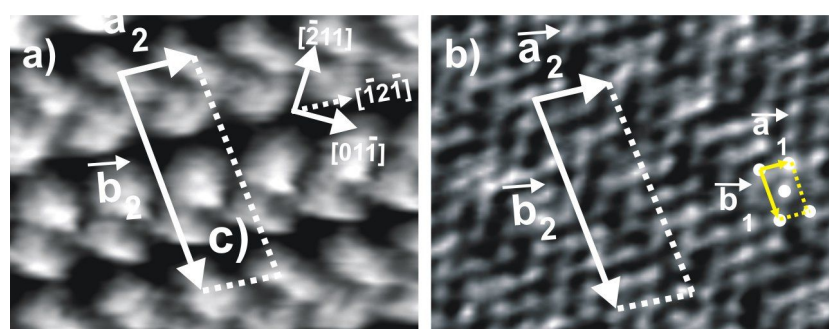
Figure 5: Structural correlation between the ordered DBV^{2+} herring-bone phase and the anionic chloride lattice underneath: a) 6.5 nm × 4.1 nm, U_b = 220 mV, I_t = 0.1 nA, E = −10 mV; b) 6.5 nm × 4.1 nm, U_b = 30 mV, I_t = 5.0 nA, E = −10 mV. $(\vec{a}_1; \vec{b}_1)$ and $(\vec{a}_2; \vec{b}_2)$ are the unit vectors of the chloride lattice and the herring-bone phase, respectively.

the Cl/Cu(111) surface. Again, based on a superposition of panels 5a and 5b, a precise determination of the DBV^{2+} unit cell with respect to the c(p × √3)-Cl phase underneath, the latter serving as an internal calibration lattice, is possible. As a result, the unit cell containing four DBV^{2+} molecules can be described

by a rectangular (2 × 2p) mesh with respect to the c(p × √3)-Cl lattice (Figure 5a). The lattice constants are estimated to $|\vec{a}_2|$ = 0.83 nm and $|\vec{b}_2|$ = 3.32 nm, respectively, enclosing an angle of 88 ± 2°. Alternatively, the unit-cell of the DBV^{2+} adlayer can be directly related to the copper substrate (1 × 1) mesh

assuming a (4p × 2√3) coincidence mesh. The surface coverage per domain was also calculated as Θ = 0.25 ML with respect to the underlying chloride lattice, or 14.49·10^{13} molecules/cm^2. A more detailed discussion of the molecular arrangement within the herringbone rows is postponed until section Discussion where we will also make a comparison with the corresponding system DBV on Cl/Cu(100).

The DBV-dication based herring-bone structure remains stable in the potential range more positive than −240 mV vs RHE, but it decays below this potential, giving rise to a surface phase transition. Namely, the herring-bone phase disintegrates gradually when the electrode potential approaches peak P$_1$ (cathodic potential sweep) in the solid black CV in Figure 1, where the viologen dication species (DBV^{2+}) are reduced to the corresponding monocation radicals (DBV$^{+•}$). Figure 6 shows this decay of the herring-bone structure and the simultaneous growth of the new stripe phase (Figure 6b and c) within the

potential regime from E = −240 mV to E = −285 mV, in which the 120° step edge serves as a positional marker. The phase-transition process starts preferentially at point defects and domain boundaries (as marked by the white arrows in Figure 6b) because this requires a relatively low activation energy. Finally, the new stripe pattern is completed right after the potential reaches the value of E = −285 mV (Figure 6d). The observation of two rotational domains I and II (and I' on the lower terrace, respectively) rotated by 120° elucidates the influence of the underlying substrate on the adsorption not only of the viologen dication (see above) but also of the monocation radical species. In fact, taking the symmetry of the substrate into account, three rotational domains in total should coexist on the Cu(111) surface. Additionally, the characteristic angle of 120° between substrate steps remains unaffected by this phase-transition process and rules out chloride desorption at these potentials. This rather hints to the molecular reduction as being the origin of the phase transition.
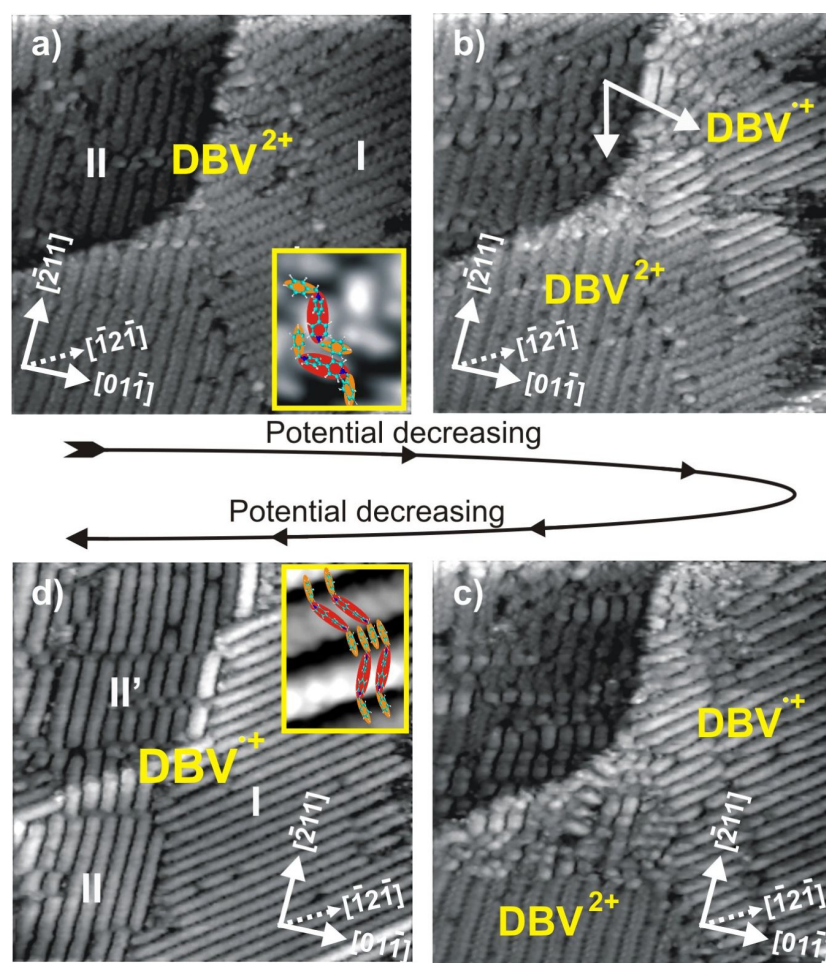
Figure 6: A series of STM images recorded with the same tunneling parameters (46.67 nm × 46.67 nm, U_b = 386 mV, I_t = 0.1 nA) showing the structural phase transition from the herring-bone phase to an alternating stacked stripe phase. Disintegration of the herring-bone phase and growth of the stripes starts preferentially at defect sites and step edges: a) E = −220 mV; b) E = −260 mV; c) E = −270 mV; d) E = −285 mV.

The first electron transfer-induced phase transition from the DBV^{2+} herring-bone phase to the stripe phase of the DBV$^{+\bullet}$ monocation radicals is a quasi-reversible process. The DBV^{2+} related herring-bone phase is gradually restored when the working potential is swept back towards the positive potential regime. A series of STM images recorded on the same surface area but at increasing electrode potentials, showing a phase transition from the stripe pattern back to the herring-bone phase, is shown in Figure 7. The stripe phase, as observed in Figure 7a (see inset), gradually desintegrates resulting in the reappearance of the herring-bone phase (Figure 7b), which finally completely replaces the stripe phase, as seen in Figure 7c (see inset). Similar to the transformation from the DBV^{2+} herring-bone phase to the DBV$^{+\bullet}$ stripe pattern, step-edges and defect points act as starting points for this phase-transition process. Comparing panels 7a and 7c, it becomes evident that the molecular row directions in the DBV^{2+} herring-bone phase are the same as in the DBV$^{+\bullet}$ stripe pattern, i.e., aligned parallel to substrate step edges. This observation again affirms the dominant role of interactions between the molecular adlayer and the underlying chloride lattice for the lateral ordering.

Recalling the stripe phase of the DBV$^{+\bullet}$ molecules, Figure 8 presents typical meso- and molecular-scale STM images of this phase formed on the chloride-terminated Cu(111) electrode surface. As mentioned above and shown in Figure 8a the stripes are aligned parallel to the directions of step edges; these directions coincide with the close-packed chloride rows underneath, and, hence, the $\langle\bar{2}11\rangle$ directions of the Cu(111) substrate (see [14] and papers cited therein). The higher resolution STM image in Figure 8b reveals further details of the internal structure of the rows, i.e., the molecular orientation and packing

arrangement. The elongated and parallel discs within the rows are assigned to individual DBV$^{+\bullet}$ monocation radicals. Within one row all molecules have the same orientation, whereas the orientation of the monocation radicals in adjacent rows is alternating, in that the molecules in neighboring rows are rotated by 120° with respect to each other (redish discs in Figure 8b) leading to a zig-zag appearance. Hitherto this stripe pattern will therefore be termed "alternating stripe" pattern, in contrast to the findings on Cl/Cu(100) (see below). As a consequence not only the directions of the rows are aligned to a symmetry direction of the substrate surface, but also the bipyridinium cores are oriented in the direction of close-packed chloride rows underneath. Moreover, an even closer look reveals i) that within one row all molecules are imaged with the same intensity, suggesting equivalent adsorption sites, while ii) every second row of the "alternating stripe" structure appears slightly brighter in the STM image. Considering the uniaxial incommensuracy of the chloride structure underneath in the direction perpendicular to the rows (see Figure 3), the most likely explanation for the latter phenomenon is that molecules in adjacent rows are situated on non-equivalent chloride rows underneath. The intermolecular distances within one and the same row as well as between adjacent stripes are measured as $d_{as}= 0.43 \pm 0.01$ nm and $s_{as}= 1.3 \pm 0.1$ nm, respectively [16].

Applying different tunneling conditions, as mentioned above, the structural correlation between the DBV$^{+\bullet}$ adlayer and the underlying chloride lattice can again be made visible (not shown here). On the basis of a superposition of both lattices, the derived unit cell containing two DBV$^{+\bullet}$ molecules can be expressed by a (1×4) coincidence mesh with respect to the c(p $\times \sqrt{3}$)Cl lattice with the lattice constants of $|\vec{a}_2| =$
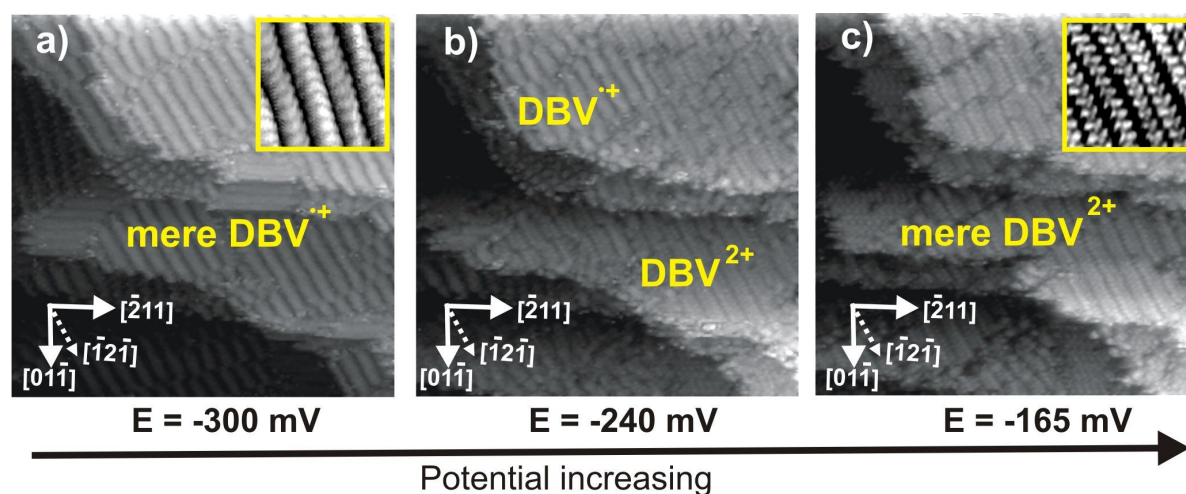
Figure 7: Series of STM images showing the desintegration of the stripe pattern and restoration of the corresponding herring-bone phase upon sweeping back toward positive potentials, 46.67 nm × 46.67 nm, $I_t = 0.1$ nA; a) $U_b = 240$ mV, $E = -300$ mV; b) $U_b = 200$ mV, $E = -240$ mV; b) $U_b = 233$ mV, $E = -165$ mV.
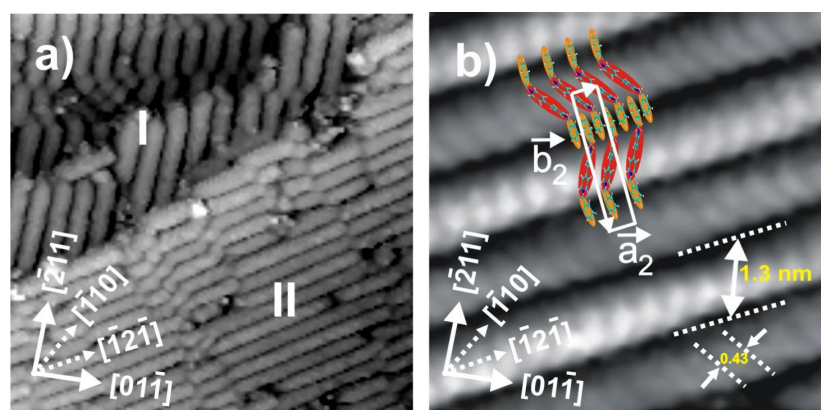
Figure 8: a) Typical STM image showing two rotational domains of the DBV[+•] alternating stripe pattern (see text): 35.49 nm × 35.49 nm, U_b = 386 mV, I_t = 0.1 nA, E_w = −280 mV; b) Molecularly resolved STM image of the DBV[+•] alternating stripe pattern, 5.06 nm × 5.06 nm, U_b = 298 mV, I_t = 0.1 nA, E_w = −286 mV. Reproduced with permission from [16].

0.43 ± 0.01 nm and $\left|\vec{b_2}\right|$ = 3.32 ± 0.1 nm, respectively. From this a DBV[+•] surface coverage per domain is calculated as Θ = 0.25 ML with respect to the c(p × √3)Cl layer serving as the template, or $14.30 \cdot 10^{13}$ molecules/cm^2.

Discussion

The principles of structure formation of the adsorbed DBV species become particularly clear when comparing the findings for the ordered phases of DBV on Cl/Cu(111) with those obtained on Cl/Cu(100). To this end we summarize here very briefly the previously published results for the DBV adsorption on Cl/Cu(100) in 10 mM HCl solution [5-7]. First of all the chloride anions are known to form a well-ordered c(2 × 2) structure on the Cu(100) surface (see Figure 11) between −300 mV (near the HER) and the onset of the CDR around

+150 mV vs RHE. As illustrated in Figure 9 a highly ordered layer of DBV^{2+} is observed at +50 mV on the chloride covered Cu(100) electrode in contact with the 0.1 mM DBVCl$_2$ containing 10 mM HCl electrolyte, forming a so-called "cavitand"-structure consisting of small squares with a hole in the center. Figure 9a shows two mirror domains of this phase denoted as I and II enclosing an angle of 32° between them. Of course, due to the four-fold symmetry of the Cu(100) surface there exist also mirror domains I' and II' rotated by 90° resulting in four possible domains in total.

A close inspection of the domain boundary in Figure 9a reveals that occasionally the small squares are incomplete (white arrow in Figure 9a) suggesting that the cavitands are actually formed from subunits. This is verified by the two high-resolution zoom-
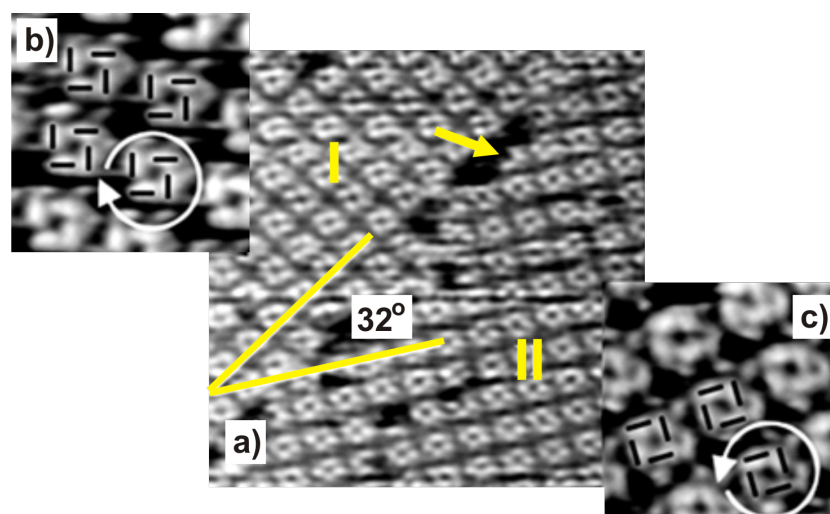
Figure 9: STM images of the DBV^{2+} cavitand phase on c(2 × 2)Cl/Cu(100); a) 29.2 nm × 29.2 nm, b) and c) 7.5 nm × 7.5 nm, I_t = 0.35 nA, U_b = 120 mV. Reproduced with permission from [7]. Copyright 2004 American Chemical Society.

ins in Figure 9b and c. Each cavitand consists of four individual DBV^{2+} species building a square-shaped motif with a cavity in the center. Since the four building blocks may be arranged in two different ways as illustrated in the two zoom-ins these cavitands occur in two circularly chiral enantiomers [5-7]. However, since neither the Cl/Cu(100) surface nor the DBV^{2+} species (Figure 2) are chiral in nature the DBV^{2+} covered Cl/Cu(100) surface as a whole is a racemate of enantiomeric domains like I and II in Figure 9a. The dicationic character of the DBV^{2+} building blocks of this cavitand structure was verified by ex situ XPS measurements using synchrotron radiation, namely by a dominant N(1s) signal at 402.1 eV [27]. Sweeping the electrode potential to a value below −200 mV vs RHE causes the disintegration of the cavitand structure and the formation of a stripe pattern (Figure 10) similar to the one shown in Figure 7a (inset) except that here the orientation of the individual molecular species in adjacent stripes is the same and not alternating. This new phase is a consequence of the reduction of the adsorbed DBV^{2+} dications (i.e., the building blocks of the cavitand structure) to monocation radicals $DBV^{+\bullet}$ [5,6], which form the polymeric stripes. The distance between adjacent stripes is $s_s = 1.8$ nm and the intermolecular distance within the $DBV^{+\bullet}$ stripes is $d_s = 3.6$ Å. A correlation of the molecular structure of the st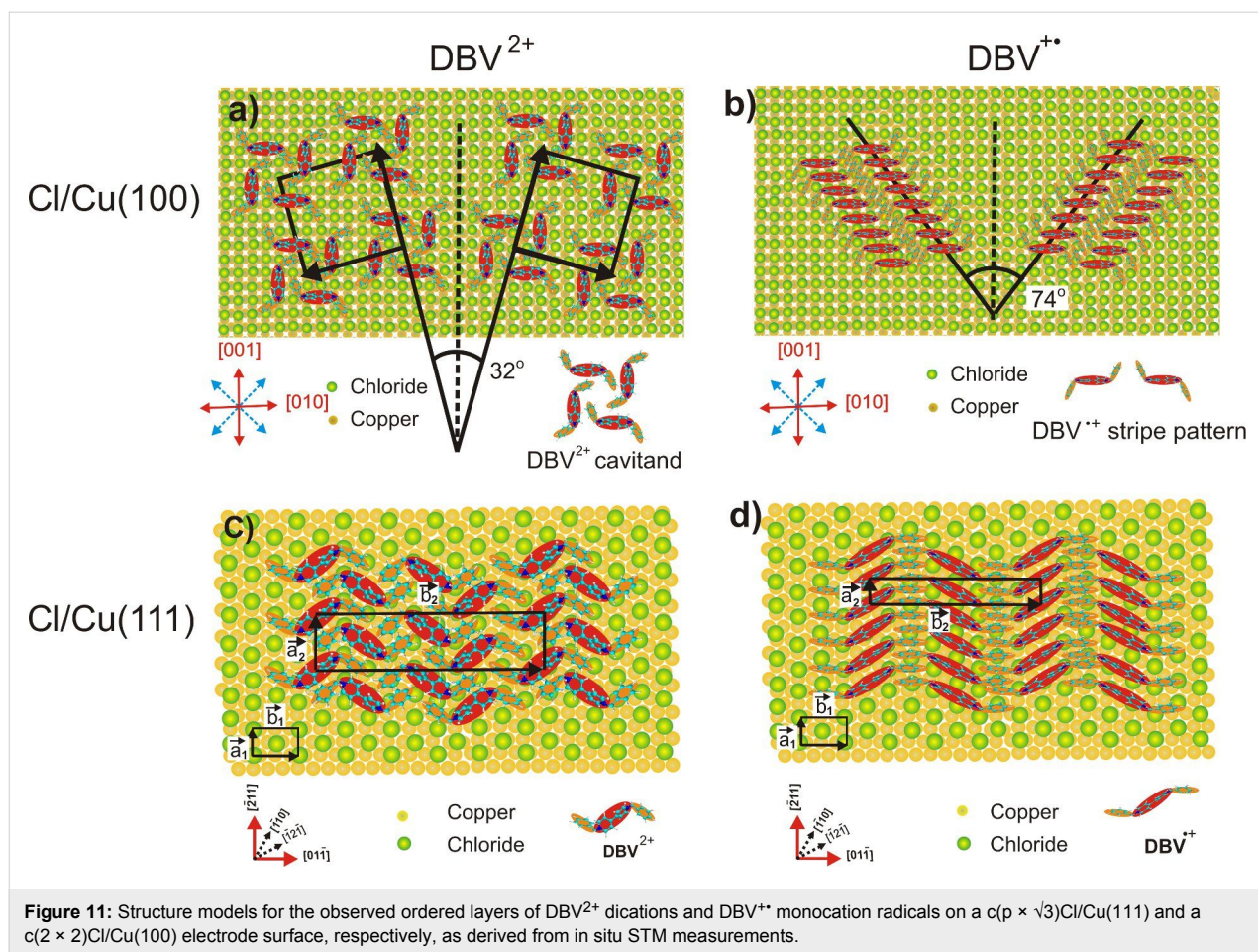ripes with that of the Cl-lattice underneath as deduced from STM images taken at different tunneling conditions as described above (Figure 10b,c) proves that the bipyridinium cores of the $DBV^{+\bullet}$ species are again oriented parallel to the close-packed chloride rows underneath. Unlike on Cl/Cu(111), however, not only have molecules in adjacent rows the same orientation but all molecular stripes on the Cl/Cu(100) appear also with the same brightness (Figure 10b).

All observations made for the adsorption of DBV on the chloride precovered Cu(111) and Cu(100) electrode surfaces for both the dicationic DBV^{2+} and the monocation radical $DBV^{+\bullet}$ species, respectively, are summarized in the structural models of Figure 11a–d.

First of all in both the DBV^{2+} dication and the $DBV^{+\bullet}$ monocation radical species the positive charge resides on the N-containing bipyridinium core as revealed by the N(1s) photoemission spectra [27], while the two benzyl groups, decoupled from the delocalized π-system of the bipyridinium core by the two CH_2 groups, are relatively more negatively charged. As a consequence the preferred adsorbate–adsorbate interactions are electrostatic attractions between the positive bipyridinium cores and the benzyl groups. In addition π–π-interactions between all π-systems of adjacent molecules will play a role with the stipulation that the benzyl groups take up a trans-conformation [6] as shown in Figure 2 and Figure 8b and in the structural models in Figure 11. In particular, the π–π interactions between neighboring monocation radicals are important which, by spin-pairing, are known to lead to the formation of dimers in solution [5]. The adsorbate–substrate interactions are obviously dominated by electrostatic interactions between the doubly (DBV^{2+}) or singly ($DBV^{+\bullet}$) charged bipyridinium cations and the negatively charged chloride layer underneath, with the additional remark that the anion density, and thus the negative charge density, on the chloride precovered Cu(111) surface is higher than on Cl/Cu(100). This manifests itself in the fact, that the respective coverages are consistently higher on the Cl/Cu(111) surface compared to Cl/Cu(100), namely $\Theta(DBV^{2+})$ = 0.075 and $\Theta(DBV^{+\bullet})$ = 0.20 on Cl/Cu(100) vs $\Theta(DBV^{2+})$ = 0.25 and $\Theta(DBV^{+\bullet})$ = 0.25 on Cl/Cu(111).
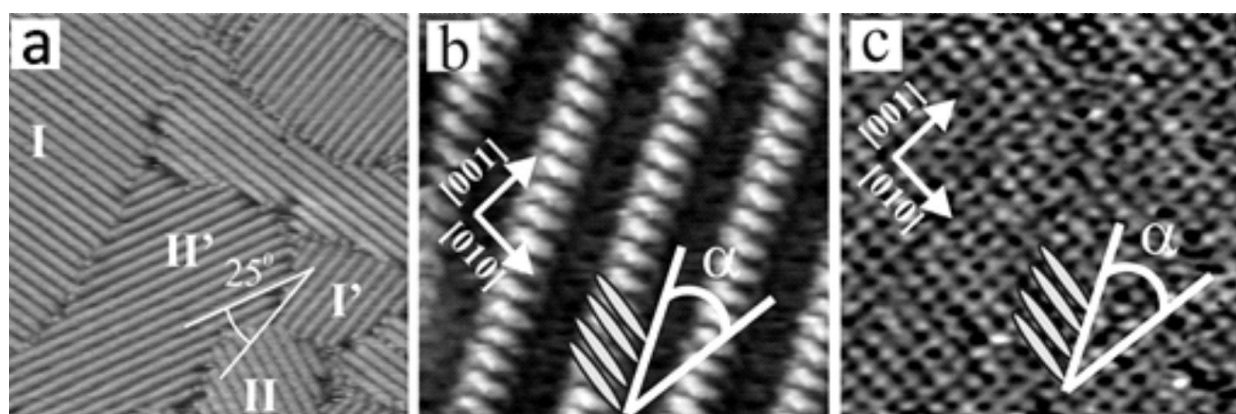
Figure 10: Typical STM image showing two rotational domains of the $DBV^{+\bullet}$ stripe pattern on Cl/Cu(100): a) 57.6 nm × 57.6 nm, U_b = 268 mV, I_t = 0.2 nA, E = −380 mV. Structural correlation between the stripe pattern and the underlying chloride lattice: 6.8 nm × 6.8 nm; b) U_b = 28 mV, I_t = 4 nA, E = −200 mV; c) U_b = 1 mV, I_t = 9 nA, E = −130 mV. Figure 10b and c are reproduced with permission from [5]. Copyright 2006 Royal Society of Chemistry.

Figure 11: Structure models for the observed ordered layers of DBV^{2+} dications and DBV$^{+\bullet}$ monocation radicals on a c(p × √3)Cl/Cu(111) and a c(2 × 2)Cl/Cu(100) electrode surface, respectively, as derived from in situ STM measurements.

Based on these possible interactions all structures of both the DBV^{2+} dications and the DBV$^{+\bullet}$ monocation radicals are consistently explainable (Figure 11). In all cases the positively charged bipyridinium cores are oriented parallel to the close-packed rows of the chloride anion lattice underneath in order to maximize the electrostatic attraction. This explains the parallel and 90° vs parallel and 120° orientation of both the individual DBV^{2+} or DBV$^{+\bullet}$ bipyridinium moieties as well as corresponding structural domains with respect to each other, on the Cl/Cu(100) and Cl/Cu(111) surface, respectively. Electrostatic repulsion between parallel oriented DBV^{2+} units leads to relatively large distances between them within the cavitand structure on Cu(100) and the "herring-bone" structure on Cu(111). Interestingly, these distances are multiples of the nearest-neighbor Cl–Cl distance, the shortest being 0.83 nm within the "herring-bone" structure on Cl/Cu(111). The directions of molecular rows of both the "alternating stripe" structure of DBV^{2+} dications and the stripe phase of DBV$^{+\bullet}$ monocation radicals on Cl/Cu(111) are also aligned with the directions of close-packed chloride ions underneath, resulting in three possible domains in total rotated by 120° with respect to each other. The existence of the mirror domains of the cavitand

structure ±16° off the direction of the two orthogonal directions of densely packed chloride rows on Cu(100) (Figure 11a), in turn, leads to four possible domains of the DBV^{2+} cavitand structure on Cl/Cu(100). Likewise, the molecular rows of the DBV$^{+\bullet}$ stripe phase on Cl/Cu(100) propagate 37° off the direction of closely packed chloride anions. This, together with the twofold symmetry of the Cu(100) substrate, results again in a total of four possible domains of this structure on Cl/Cu(100). Summarizing so far, the occurrence of the angles of 90° and 120° and the coincidence of the connecting line between the two N-atoms of a bipyridinium core with the direction of close-packed anion rows of c(p × √3)Cl/Cu(111) and c(2 × 2)Cl/Cu(100) reflects the influence of the symmetry of the respective substrate and the dominance of electrostatic adsorbate–substrate interactions.

Looking into the fine structure of the various phases, we find the largest distance as well as an orthogonal orientation between the DBV^{2+} as a consequence of the electrostatic repulsion between these dications in the cavitand phase on Cl/Cu(100). The benzyl groups inside the cavity may partly shield this repulsion between the DBV^{2+} units (Figure 11a). Within the DBV$^{+\bullet}$

stripes on Cl/Cu(100) the distance between the molecular units is only 0.36 nm due to a reduced electrostatic repulsion and an attractive π–π- and spin-pairing interaction between the parallel oriented monocation radicals (Figure 11b). Similar intermolecular distances have also been observed for π–π stacked phases of 2,2'-bipyridine on Au(111) [28] and Cu(111) [26]. Even though this distance is typical for π–π-interacting aromats [29], the measured distance of 0.36 nm agrees perfectly with the separation between parallel densely packed rows of chloride anions, again a manifestation of the strong electrostatic interaction with the substrate. The lateral displacement between adjacent DBV$^{+\bullet}$ bipyridinium cores within the rows, leading to the mirror domains off by ±37° from the ⟨110⟩ directions of the substrate, is probably due to steric hindrance between the trans-oriented benzyl groups of the DBV$^{+\bullet}$ units.

Also on the Cl/Cu(111) substrate the intermolecular distance of the parallel DBV^{2+} dications within the rows is large, and with 0.83 nm nearly twice the Cl–Cl distance along the commensurate direction of the c(p × √3)Cl layer between closely packed rows of the anion underlayer. This distance leaves enough space between two positively charged bipyridinium cores for a benzyl group of the neighboring row, thereby shielding the electrostatic repulsion between the former (Figure 11c). As a further consequence, the trans-conformation of the DBV^{2+} species matches the 120° orientation of adjacent bipyridinium cores within the "herring-bone" structure. The remaining benzyl groups may also π–π interact and are located within the dark lines between the "herring-bones". The model in Figure 11d summarizes the "alternating stripe" structure formed by the DBV$^{+\bullet}$ species on Cl/Cu(111). Both the individual monocation radicals as well as the stripe propagation direction are aligned in ⟨$\overline{2}$11⟩ directions, molecules in adjacent rows being rotated by 120°. The intermolecular distance of 0.43 nm within the rows, though still consistent with π–π interaction, equals precisely the Cl–Cl distance in the ⟨$\overline{2}$11⟩ direction of the substrate, again pointing to a dominance of adsorbate–substrate interactions.

Conclusion

The electrochemical behavior and a related structural transition of the 1,1'-dibenzyl-4,4'-bipyridinium molecule cations on a chloride-modified Cu(111) surface have been investigated by means of cyclic voltammetry and in situ scanning tunneling microscopy. Current waves in the cyclic voltammogram clearly indicate the potentials where reduction of the dications occurs first to the monocation radicals and then to the neutral molecules. At positive electrode potentials the dicationic DBV^{2+} molecules form a condensed and highly ordered "herring-bone" phase consisting of structural elements each formed by two individual DBV^{2+} molecules. In contrast, an "alternating stripe" pattern is observed for the molecules in their monocation

radical form (DBV$^{+\bullet}$) at negative potentials below the first reduction peak. In both cases, their structural motifs are predominantly governed by dominant electrostatic interactions between the adsorbate species, both in their dication and monocation radical form, and the negatively charged chloride lattice underneath. The phase transition from the DBV^{2+}-related "herring-bone" phase to the alterating stripe pattern based on the radical monocationic DBV$^{+\bullet}$ is observed as a reversible process occurring via nucleation and growth. Possible models for both the herring-bone phase and the alternating stripe pattern are proposed. Their detailed discussion also in the light of the corresponding findings for the same species on a c(2 × 2)Cl/Cu(100) electrode surface clearly points to a dominance of electrostatic adsorbate–substrate interactions, i.e., a strong template effect of both substrates on the self-organization of these organic surface films.

Experimental

In this work we have employed a combination of cyclic voltammetry (CV) and electrochemical scanning tunneling microscopy (EC-STM). The direct combination of in situ STM and CV in one and the same electrochemical cell permits a precise correlation of the obtained STM images with features in the corresponding CV data. The whole experimental setup is home-built and described in detail in [25]. The tunneling tips used in all experiments were electrochemically etched from 0.25 mm in diameter tungsten wire in 2 mM KOH solution, rinsed with high purity water, dried and subsequently insulated by passing them through a hot melt glue film (ethylen–vinylacetat copolymer).

The Cu(111) single crystal used was manufactured by MaTeck, Jülich, Germany. Prior to each series of STM measurements the copper sample was electropolished by immersing it into 50% orthophosphoric acid at an anodic potential of 2 V for about 20–40 s. This removes the native surface oxide film formed in air. In order to guarantee a reproducibly smooth surface even after several electropolishing procedures, a precision of the surface orientation of less than 0.5° off the (111) plane is required. Less well defined surfaces suffer a growing roughening with repeated cycles of electropolishing.

The chloride-modified Cu(111) surface, chosen here as substrate for the viologen films, was prepared and characterized by first carrying out CV and STM measurements several times in pure 10 mM HCl solution, i.e., the supporting electrolyte. This procedure also improves the quality of the Cu(111) surface due to the operation of the so-called "electrochemical annealing effect" [17,30]. For the adsorption of the molecular film on top of the chloride-terminated electrode surface, the pure supporting electrolyte was routinely substituted by a solution of 0.1 mM 1,1'-dibenzyl-4,4'-bipyridinium dichloride in 10 mM HCl

(10 mM HCl + 0.1 mM DBV^{2+}**)** at potentials between −50 mV and +50 mV vs RHE (reversible hydrogen electrode). In this paper all potentials of the Cu(111) electrode, i.e., the working electrode, are quoted with respect to a reversible hydrogen electrode, while a Pt wire is employed as counter electrode.

High purity water from a Milli-Q purification system (conductivity > 18 MΩ·cm, TOC < 4 ppb) and highest reagent grade chemicals were used for the preparation of all solutions. All electrolyte solutions were purged with oxygen-free argon gas for several hours before use.

Acknowledgements

References

1. Lehn, J.-M. *Supramolecular Chemistry;* Wiley-VCH: Weinheim, Germany, 1995.
2. Lehn, J.-M. *Angew. Chem., Int. Ed. Engl.* **1988,** *27,* 89–112. doi:10.1002/anie.198800891
3. Vögtle, F. *Supramolecular Chemistry: An Introduction;* Wiley and Sons: Chichester, UK, 1991.
4. Kaifer, A. E.; Gómez-Kaifer, M. *Supramolecular Electrochemistry;* Wiley-VCH: Weinheim, Germany, 1999. doi:10.1002/9783527613601
5. Pham, D.-T.; Gentz, K.; Zörlein, C.; Hai, N. T. M.; Tsay, S.-L.; Kirchner, B.; Kossmann, S.; Wandelt, K.; Broekmann, P. *New J. Chem.* **2006,** *30,* 1439–1451. doi:10.1039/b609421j
6. Pham, D.-T.; Tsay, S.-L.; Gentz, K.; Zörlein, C.; Kossmann, S.; Stay, J.-S.; Kirchner, B.; Wandelt, K.; Broekmann, P. *J. Phys. Chem. C* **2007,** *111,* 16428–16436. doi:10.1021/jp073469q
7. Safarowsky, C.; Wandelt, K.; Broekmann, P. *Langmuir* **2004,** *20,* 8261–8269. doi:10.1021/la048940a
8. Haiss, W.; van Zalinge, H.; Higgins, S. J.; Bethell, D.; Höbenreich, H.; Schiffrin, D. J.; Nichols, R. J. *J. Am. Chem. Soc.* **2003,** *125,* 15294–15295. doi:10.1021/ja038214e
9. Li, Z.; Han, B.; Meszaros, G.; Pobelov, I.; Wandlowski, T.; Blaszczyk, A.; Mayor, M. *Faraday Discuss.* **2006,** *131,* 121–143. doi:10.1039/b506623a
10. Imahori, H.; Norieda, H.; Yamada, H.; Nishimura, Y.; Yamazaki, I.; Sakata, Y.; Fukuzumi, S. *J. Am. Chem. Soc.* **2001,** *123,* 100–110. doi:10.1021/ja002154k
11. Bird, C. L.; Kuhn, A. T. *Chem. Soc. Rev.* **1981,** *10,* 49–82. doi:10.1039/cs9811000049
12. Monk, P. M. S. *The Viologens: physicochemical properties, synthesis and applications of the salts of 4,4'-bipyridines;* John Wiley and Sons Ltd.: Chichester, UK, 1998.
13. Tsay, S.-L.; Tsay, J.-S.; Fu, T.-Y.; Broekmann, P.; Sagara, T.; Wandelt, K. *Phys. Chem. Chem. Phys.* **2010,** *12,* 14950–14959. doi:10.1039/c0cp00865f
14. Röefzaad, M.; Jiang, M.; Zamlynny, V.; Wandelt, K. *J. Electroanal. Chem.* **2011,** *662,* 219–228. doi:10.1016/j.jelechem.2011.07.006
15. Kobayashi, K.; Fujisaki, F.; Yoshimine, T.; Nik, K. *Bull. Chem. Soc. Jpn.* **1986,** *59,* 3715–3722. doi:10.1246/bcsj.59.3715
16. Phan, T. H.; Wandelt, K. *Int. J. Mol. Sci.* **2013,** *14,* 4498–4524. doi:10.3390/ijms14034498
17. Broekmann, P.; Wilms, M.; Kruft, M.; Stuhlmann, C.; Wandelt, K. *J. Electroanal. Chem.* **1999,** *467,* 307–324. doi:10.1016/S0022-0728(99)00048-0
18. Stickney, J. L.; Ehlers, C. B. *J. Vac. Sci. Technol., A* **1989,** *7,* 1801–1805. doi:10.1116/1.576049
19. Kruft, M.; Wohlmann, B.; Stuhlmann, C.; Wandelt, K. *Surf. Sci.* **1997,** *377–379,* 601–604. doi:10.1016/S0039-6028(96)01461-6
20. Wilms, M.; Broekmann, P.; Kruft, M.; Stuhlmann, C.; Wandelt, K. *Appl. Phys. A* **1998,** *66* (Suppl. 1), S473–S475. doi:10.1007/s003390051185
21. Phan, T. H.; Wandelt, K. *Surf. Sci.* **2013,** *607,* 82–91. doi:10.1016/j.susc.2012.08.013
22. Phan, T. H. Ph.D. Thesis, Bonn University, Bonn, Germany, 2012.
23. Batina, N.; Kunitake, M.; Itaya, K. *J. Electroanal. Chem.* **1996,** *405,* 245–250. doi:10.1016/0022-0728(95)04480-9
24. Koper, M. T. M. *J. Electroanal. Chem.* **1998,** *450,* 189–201. doi:10.1016/S0022-0728(97)00648-7
25. Wilms, M.; Kruft, M.; Bermes, G.; Wandelt, K. *Rev. Sci. Instrum.* **1999,** *70,* 3641–3650. doi:10.1063/1.1149971
26. Safarowsky, C.; Rang, A.; Schalley, C. A.; Wandelt, K.; Broekmann, P. *Electrochim. Acta* **2005,** *50,* 4257–4268. doi:10.1016/j.electacta.2005.03.068
27. Breuer, S.; Pham, D. T.; Huemann, S.; Gentz, K.; Zoerlein, C.; Hunger, R.; Wandelt, K.; Broekmann, P. *New J. Phys.* **2008,** *10,* 125033. doi:10.1088/1367-2630/10/12/125033
28. Dretschkow, T.; Wandlowski, T. *Electrochim. Acta* **1999,** *45,* 731–740. doi:10.1016/S0013-4686(99)00252-2
29. Weck, M.; Dunn, A. R.; Matsumoto, K.; Coates, G. W.; Lobkovsky, E. B.; Grubbs, R. H. *Angew. Chem., Int. Ed.* **1999,** *38,* 2741–2745. doi:10.1002/(SICI)1521-3773(19990917)38:18<2741::AID-ANIE2741>3.0.CO;2-1
30. Giesen, M.; Beltramo, G.; Dieluweit, S.; Müller, J.; Ibach, H.; Schmickler, W. *Surf. Sci.* **2005,** *595,* 127–137. doi:10.1016/j.susc.2005.07.040

Self-assembled monolayers of shape-persistent macrocycles on graphite: interior design and conformational polymorphism

Joscha Vollmeyer, Friederike Eberhagen, Sigurd Höger and Stefan-S. Jester[*]

Abstract

Three shape-persistent naphthylene–phenylene–acetylene macrocycles of identical backbone structures and extraannular substitution patterns but different (empty, apolar, polar) nanopore fillings are self-assembled at the solid/liquid interface of highly oriented pyrolytic graphite and 1,2,4-trichlorobenzene. Submolecularly resolved images of the resulting two-dimensional (2D) crystalline monolayer patterns are obtained by in situ scanning tunneling microscopy. A concentration-dependent conformational polymorphism is found, and open and more dense packing motifs are observed. For all three compounds alike lattice parameters are found, therefore the intermolecular macrocycle distances are mainly determined by their size and symmetry. This is an excellent example that the graphite acts as a template for the macrocycle organization independent from their specific interior.

Introduction

One of the ultimate aims in supramolecular chemistry on solid surfaces is the formation of two-dimensional (2D) nanostructures that are capable of performing highly specific tasks as an effect of functional units that are implemented into the adlayer building blocks. An efficient functionality of such architectures will essentially rely on a precise control of the orientation and distribution of the molecules on the surface that is summarized in the field of 2D supramolecular engineering [1,2]. Shape-persistent arylene–alkynylene macrocycles are promising candidates as future mounts for functional units. These are separated

from each other and cannot interact intermolecularly if the rings are adsorbed in parallel to the substrate. The exterior of the macrocycles can be substituted with alkyl side chains (or their alkoxy analogs) that guarantee a sufficient compound solubility. The macrocycles can be co-assembled with other compounds at the surface [3,4], and they can also template the subsequent organization of guest molecules and thus a growth into the third dimension [5,6]. One of the most often used substrates for supramolecular surface patterning is highly oriented pyrolytic graphite (HOPG) which provides large atomically flat terraces

between step edges and a sufficient adsorbate mobility, required for the self-assembly process that leads to the 2D crystal formation.

For a more detailed understanding of the macrocycle–HOPG and macrocycle–macrocycle interactions, the following key aspects must be considered:

(i) how the extraannular alkyl side chains of the adsorbed macrocycles pack, and whether this can be compared to the packing of linear hydrocarbons on HOPG,

(ii) how the specific attachment of the extraannular alkyl chains at the macrocycle rims affects the packing, and

(iii) how the ring interior influences the packing of the macrocycles on HOPG.

First we address the structure of self-assembled alkyl chains on HOPG. Their methylene units adopt a staggered (anti) conformation and align along one of the three crystallographic main axis directions of the substrate. Their carbon backbones either orient (as most often observed) coplanar with the graphite surface (Figure 1a) and adopt equilibrium interchain distances, d_{eq}, of 0.43 nm [7-12], or they orient in an (also reported) stacked fashion (with the carbon backbones axially rotated by 90°; Figure 1b) and a d_{eq} of 0.35 nm [9-12].

Shape-persistent macrocycles on HOPG form non-covalent 2D assemblies held together by the van der Waals interaction between the alkyl side chains even without the presence of any

additional functional groups [13-15]. The templated alignment of the alkyl chains on the surface determines the commensurability or registry of the adsorbate vs substrate lattice vectors – even if extended rigid backbones act as cores of certain sizes and shapes [16] that provide anchor units for the alkyl chains. However, often the 2D superstructures are not predictable [17] or show a conformational polymorphism [18], also as an effect of varying compound concentrations in the supernatant solution [19,20]. A recent approach investigating macrocycles of triangular, quadratic, pentagonal, and hexagonal shapes that carry alkoxy side chains pointing away in normal direction from their sides has led to the concept of molecular polygons [4]. An example for the schematic design of an alkoxy side chain substituted molecular hexagon and its characteristic side-chain interdigitation concept are shown in Figure 2a and b, respectively. Two alkoxy side chains of each side interdigitate with two side chains of an adjacent macrocycle and form an ABAB interdigitation pattern along each HOPG main axis direction.

An increase of the concentration of the adsorbate molecules in the supernatant solution leads generally to denser but often significantly less specific or amorphous packing morphologies, as an uncharacteristic but variable number of the side chains are no longer adsorbed on the substrate, but point towards the solution phase [4]. The molecule–molecule interaction strength and the intermolecular distances originate from the length and the packing of the side chains that are adsorbed on the substrate. Reducing the symmetry of the hexagon, or reducing the numbers of side chains on some of the hexagon sides, should lead to an unequal van der Waals interaction strength along different directions, which would consequently allow also a

Figure 1: (a), (b) Two distinguishable packings of alkyl chains on cutouts of graphite are shown with the carbon backbones aligned (a) coplanar with the graphite surface [7-12], and (b) perpendicular to the graphite surface [9-12]. In both cases the chains align along one of the substrate main axis directions (i.e., d_1, d_2, or d_3) and adopt equilibrium distances of (a) d_{eq} = 0.43 nm or (b) d_{eq} = 0.35 nm [10].

Figure 2: (a)–(c) Schematic structure of a hexagonal shape-persistent macrocycle with extraannular alkoxy chains at its sides, the side chain interaction scheme, and the resulting pattern geometry. (a) Two (flexible, linear) alkoxy side chains of each hexagon side point along the normals of the latter. (b) Two side chains of neighboring hexagon sides interdigitate in an ABAB binding motif. Identical van der Waals binding occurs along all six directions determined by the three crystallographic main axes d_1, d_2, and d_3. (c) Hexagonal pattern of molecular hexagons where all alkoxy side chains are adsorbed on the substrate along the six HOPG main axis directions, d_1, d_2, and d_3, that are defined by the arrows in (a). Backbones are shown as bold black and grey lines, and the alkoxy side chains that after adsorption align along d_1, d_2, and d_3 are shown as solid lines, dash-dotted lines, and dash-double-dotted lines, respectively. The red lines indicate unit cell vectors a and b; the blue arrow indicates the backbone orientation, c.

prediction of the surface pattern at high concentrations. This should lead to a tailorable structure of both, the porous and dense polymorphs, or – in other words – an alteration between two discrete designable packings, here as an effect of the compound concentration in the supernatant solution phase. Note that contrary to "alterable" packings, the term "adaptable" has been previously applied to indicate (side chain substituted) units in shape-persistent macrocycles that change their orientation with respect to the overall backbone, e.g., as an effect of solvophobic effects by a rotation of the corresponding *p*-phenylenes [21].

In general, in order to achieve predictable 2D adsorbate geometries of shape-persistent macrocycles, as adjustable with atomic scale definition, it is essential that the unit cell parameters (and the packing architectures in general) do not change when the central unit is varied. The driving forces for their 2D self-assembly are most probably independent from the presence of additional functional groups pointing into the third dimension or located inside the cavity interior. To the best of our knowledge, only little effort has been spent so far on investigating the role of intraannular substituents on the 2D supramolecular surface patterns of macrocyclic compounds. Therefore, in addition to the concentration-driven conformational polymorphism that is yet attributed to a distinct extraannular substitution pattern as discussed above, we evaluate the role of the intraannular substitution on the 2D supramolecular self-assembly of macrocycles.

Compounds **1**–**3** (Figure 3) have the same macrocyclic rigid backbone and flexible octadecyloxy periphery and differ only in their intraannular substitution. While **1** has an empty interior, **2** contains an alkyl chain crossing the ring, and **3** a polar oligoether chain. The macrocycles are composed of four naphthylene units as upper and lower east and west corner building blocks, whereas the north and south corners are phenylene units.

Results and Discussion

All three compounds **1**–**3** form porous ("low concentration", Figure 4a–c) and dense ("high concentration", Figure 4d–f) adsorbate patterns, depend on the compound concentrations, as observed by scanning tunneling microscopy (STM).

Bright and dark parts in the STM images correspond to regions covered by aromatic backbones and alkoxy side chains, respectively [23], whereas the medium bright image color mostly represents regions covered by solvent molecules. For the porous patterns (polymorph A) of all three compounds, unit cells of $a_{n,A} = 4.6 \pm 0.2$ nm, $b_{n,A} = 4.7 \pm 0.2$ nm, $\gamma(a_{n,A}, b_{n,A}) = 57 \pm 2°$, $n = 1, 2, 3$, are indexed and are undistinguishable within the experimental resolution. The orientations of the backbones are defined by their north–south-axis directions $c_{n,A}$, $n = 1, 2, 3$, and all backbones are oriented with $\gamma(c_{n,A}, d_1) = 90 \pm 3°$ relative to the HOPG main axis direction d_1. In addition, the alignment of the unit cell vectors $b_{n,A}$, $n = 1, 2, 3$, with respect to d_1 is $\gamma(a_{1,A}, d_1) = 3 \pm 2°$, $\gamma(a_{2,A}, d_1) = 5 \pm 2°$, and $\gamma(a_{3,A}, d_1) = 3 \pm 2°$, and the values do not vary within the experimental error. In other words, the packing of all three compounds is independent on whether the cavity is empty (**1**), filled by an undecyl diether (**2**), or a tetraethylene glycol diether (**3**) strand. Rather, it

Figure 3: (a)–(c) Shape-persistent macrocycles with an empty cavity (**1**), an apolar interior (undecyl diether strand, **2**), and a polar interior (tetraethylene glycol strand, **3**). (a) Schematic structures. The bold lines represent the (identical) macrocycle backbones; the thin straight, dash-dotted, and dash-double-dotted lines indicate alkoxy side chains. (b) Chemical structures. (c) Molecular models. Backbone geometries of the shape-persistent macrocycles with different interiors were derived by force-field modelling (Spartan '08) restricted to 2D (including interaction with a graphene layer with fixed atom positions), and extraannular octadecyloxy side chains in staggered (anti) conformation were subsequently added (along d_1, d_2, and d_3 directions to adopt 60°/120° angles). The macrocycle sizes are indicated, and the cavity sizes d_{H-H} for **1** and d_{O-O} for **2** (with the 1,11-undecanediol interior) as well as for **3** (with the tetraethylene glycol interior) are given. Note that slightly varying macrocycle sizes are induced by the intraannular strands and vary by less than 2 Å. (b) and (c) are adapted with permission from [22]. Copyright 2012 The Royal Society of Chemistry.

is a result of the chemical structures of the backbones and extraannular side chains that is schematically represented in Figure 5a. Each naphthylene unit is 2,7-disubstituted to realize the 120° angle in the rigid macrocyclic backbone (Figure 3b), and carries additional octadecyloxy side chains at positions 3 and 6 of which one points along d_1 in the porous pattern (cf. Figure 5a). They form an ABAB packing motif (along d_1, cf. Figure 5b) and are (mostly) resolved by STM (Figure 4a–c). The other four alkoxy side chains of the four naphthylene corners point towards each of the four directions along d_2 and d_3 (cf. Figure 5a), with $\gamma(d_1,d_2) = \gamma(d_2,d_3) = 60°/120°$ as defined

by the HOPG substrate, and form AB alignment motifs (Figure 5c). Although the latter remain unresolvable by STM, the observed packing can only be explained by the alkoxy side chains oriented in this fashion [7-12].

If the compound concentrations (of **1–3** in TCB, respectively) are increased (from $2–3 \times 10^{-6}$ M to 10^{-5} M), denser packings are observed (polymorph B) as shown in Figure 4d–f. The indexed unit cells are for compound **1**: $a_{1,B} = 4.6 \pm 0.2$ nm, $b_{1,B} = 2.9 \pm 0.2$ nm, $\gamma(a_{1,B},b_{1,B}) = 66 \pm 2°$, for compound **2**: $a_{2,B} = 4.4 \pm 0.2$ nm, $b_{2,B} = 2.7 \pm 0.2$ nm, $\gamma(a_{2,B},b_{2,B}) = 71 \pm 2°$,
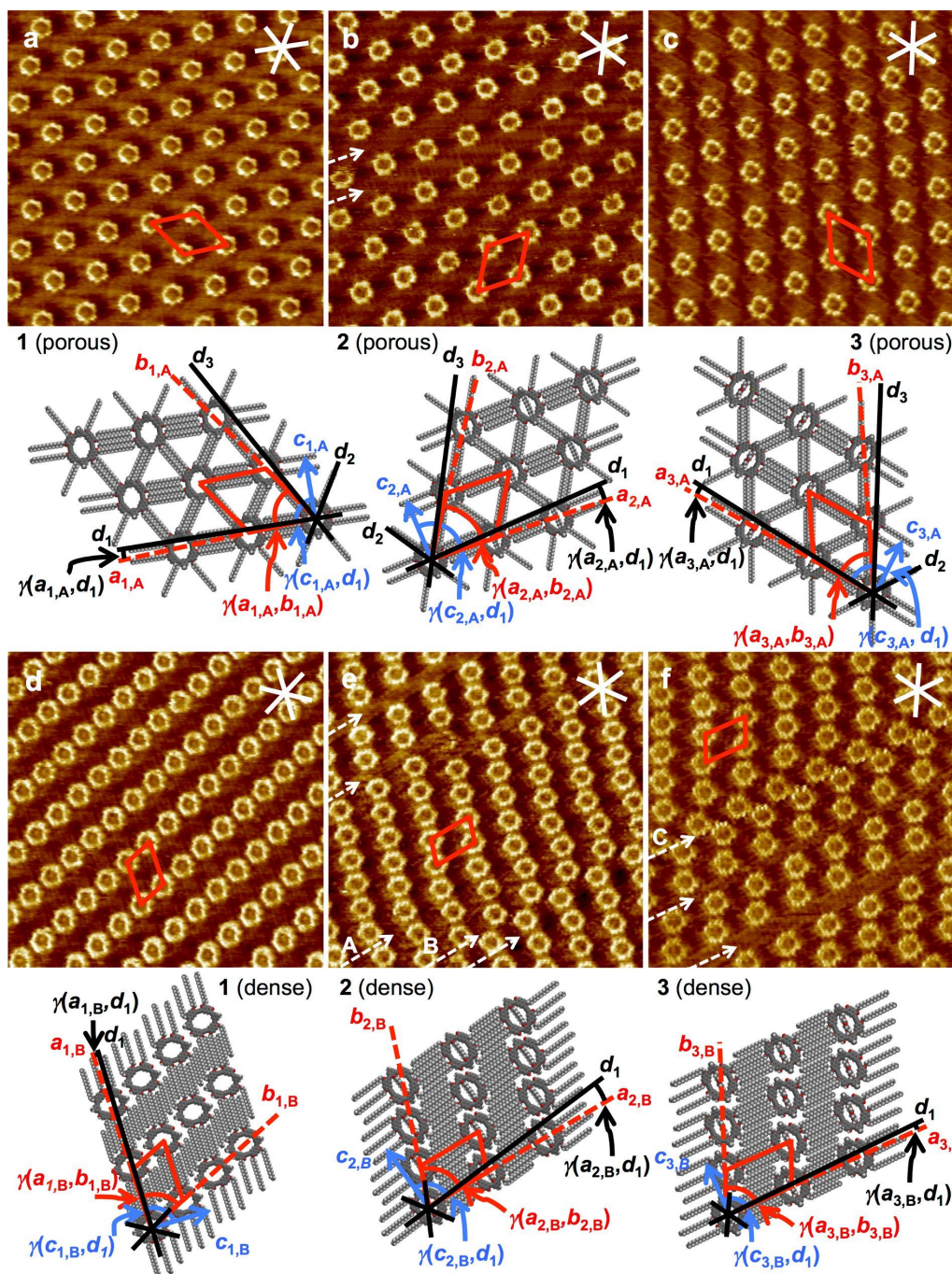
Figure 4: Scanning tunneling microscopy images and supramolecular models of (a)–(c) porous (= polymorph A) and (d)–(f) dense patterns (= polymorph B) of **1**–**3** at the TCB/HOPG interface. Image parameters, unit cells, and additional packing parameters are for the porous patterns: (a) **1**; c = 2 × 10^{-6} M, V_S = −1.0 V, I_t = 12 pA; $a_{1,A}$ = 4.6 ± 0.2 nm, $b_{1,A}$ = 4.7 ± 0.2 nm, γ($a_{1,A}$,$b_{1,A}$) = 57 ± 2°; γ($a_{1,A}$,d_1) = 3 ± 2°; γ($c_{1,A}$,d_1) = 90 ± 3°; (b) **2**; c = 2 × 10^{-6} M, V_S = −1.0 V, I_t = 7 pA; $a_{2,A}$ = 4.6 ± 0.2 nm, $b_{2,A}$ = 4.7 ± 0.2 nm, γ($a_{2,A}$,$b_{2,A}$) = 57 ± 2°; γ($a_{2,A}$,d_1) = 5 ± 2°; γ($c_{2,A}$,d_1) = 90 ± 3°; (c) **3**; c = 3 × 10^{-6} M, V_S = −1.2 V, I_t = 15 pA; $a_{3,A}$ = 4.6 ± 0.2 nm, $b_{3,A}$ = 4.7 ± 0.2 nm, γ($a_{3,A}$,$b_{3,A}$) = 57 ± 2°; γ($a_{3,A}$,d_1) = 3 ± 2°; γ($c_{3,A}$,d_1) = 90 ± 3°; and for the dense patterns: (d) **1**; c = 10^{-5} M, V_S = −1.2 V, I_t = 5 pA; $a_{1,B}$ = 4.6 ± 0.2 nm, $b_{1,B}$ = 2.9 ± 0.2 nm, γ($a_{1,B}$,$b_{1,B}$) = 66 ± 2°; γ($a_{1,B}$,d_1) = 1 ± 2°; γ($c_{1,B}$,d_1) = 90 ± 3°; (e) **2**; c = 10^{-5} M, V_S = −1.2 V, I_t = 30 pA; $a_{2,B}$ = 4.4 ± 0.2 nm, $b_{2,B}$ = 2.7 ± 0.2 nm, γ($a_{2,B}$,$b_{2,B}$) = 71 ± 2°; γ($a_{2,B}$,d_1) = 6 ± 2°; γ($c_{2,B}$,d_1) = 90 ± 3°; (f) **3**; c = 10^{-5} M, V_S = −1.2 V, I_t = 10 pA; $a_{3,B}$ = 4.6 ± 0.2 nm, $b_{3,B}$ = 3.1 ± 0.2 nm, γ($a_{3,B}$,$b_{3,B}$) = 68 ± 2°; γ($a_{3,B}$,d_1) = 2 ± 2°; γ($c_{3,B}$,d_1) = 90 ± 3°). All image sizes are 32.7 × 32.7 nm^2. The red lines indicate the unit cells, $a_{n,m}$, $b_{n,m}$, γ($a_{n,m}$,$b_{n,m}$), the white and black lines indicate the HOPG main axis directions, d_1, d_2, d_3, and the blue arrows indicate the north–south axis directions of the backbones, $c_{n,m}$, n = 1, 2, 3; m = A, B. The dashed white arrows in (b), (e), and (f) point out packing faults. In particular, arrows A–C point out packing faults where the lines of macrocycles are shifted along the HOPG main axis direction d_1 by the length of one or more –CH$_2$– units. The STM image in (e) is adapted with permission from [22]. Copyright 2012 The Royal Society of Chemistry.

Figure 5: (a)–(e): Schematic structure of the shape-persistent macrocycle **1** (as a representative of the series of **1–3** that form the same patterns), its alterable side chain interaction schemes, and the resulting pattern geometries. (a) Eight alkoxy side chains are attached to four corners of the backbone. After adsorption, four side chains align along the crystallographic main axis direction d_1, and four alkoxy side chains align along directions d_2 and d_3. (b) Two alkoxy side chains of neighboring sides form an ABAB interdigitation motif along d_1 (more robust packing). (c) Two side chains of neighboring macrocycles align along directions d_2, and d_3, here denoted as AB packing motif (less robust packings). (d) Porous pattern (polymorph A) of macrocycles where all alkoxy side chains are adsorbed on the substrate. (e) Oblique packing (polymorph B) of the molecules where six of the eight alkoxy side chains (black solid and dash-double-dotted thin lines) of each molecule are adsorbed on the substrate, whereas two side chains of each molecule point towards the solution phase (black dots). The arrows in (b) define the HOPG crystallographic main axis directions d_1, d_2, and d_3. The backbones are shown as bold black and grey lines with alkoxy side chains that after adsorption align along d_1 (thin solid lines), d_2 (thin dash-dotted lines), and d_3 (thin dash-double-dotted lines). The red lines indicate the unit cell vectors $a_{n,m}$ and $b_{n,m}$; the blue arrows indicate the macrocycle north–south axis directions, $c_{n,m}$.

and for compound **3**: $a_{3,B} = 4.6 \pm 0.2$ nm, $b_{3,B} = 3.1 \pm 0.2$ nm, $\gamma(a_{3,B},b_{3,B}) = 68 \pm 2°$. This means that the unit cells vary slightly but significantly with respect to the experimental error for the three compounds. A further evaluation of the results requires a more detailed inspection of the packings. The alignment of the unit cell vectors $a_{n,B}$, $n = 1, 2, 3$, with respect to d is $\gamma(a_{1,B},d_1) = 1 \pm 2°$, $\gamma(a_{2,B},d_1) = 6 \pm 2°$, and $\gamma(a_{3,B},d_1) = 2 \pm 2°$ and thus identical for **1** and **3** within the experimental error, whereas it is slightly different for **2**. The orientation of the backbones $c_{n,B}$, $n = 1, 2, 3$, is again $\gamma(c_{n,B},d_1) = 90 \pm 3°$ relative to the HOPG main axis direction d_1. Five side chains of two adjacent macrocycles are aligned along the crystallographic main axis direction d_1 and form an ABABA interdigitation motif (Figure 5e) and give rise to a certain robustness of the latter. However, the binding motif of two side chains that align along

directions d_2 and d_3 between each two macrocycles, here denoted as an AB packing motif (and observed in polymorph A, Figure 4a–c, and schematically shown in Figure 5c) is no longer found in polymorph B.

In other words, at higher concentration the packing changes compared to the low-concentration polymorph can be described as following:

(i) The alkoxy side chains indicated as solid lines in Figure 5d and e have the same alignment in both polymorphs (robust packing);

(ii) two of the side chains of each macrocycle that stabilize the less robust packing motifs (which are indicated as dash-double-

dotted lines in Figure 3a as well as Figure 5d and e) alter between different alignment directions in both polymorphs, along d_3 in the porous pattern in Figure 5d and along d_1 in the dense pattern in Figure 5e; and

(iii) two side chains (which are indicated as dash-dotted lines in Figure 3a and Figure 5d) point towards the solution phase (and are represented as dots in Figure 5e).

Note that the alkyl chains that point towards to the solution phase may, in principle, interfere with the STM tip. However, the high flexibility, the low electric conductivity, and the low number of only two dangling alkyl chains per molecule allow a (rather) undisturbed STM imaging. In addition, the molecules are still fixed on the substrate by the remaining six adsorbed side chains and the dense packing.

The packing alters from the porous polymorph A, a highly symmetric hexagonal pattern of macrocycles (where all alkoxy side chains are adsorbed on the substrate which is similar to the pattern discussed for the molecular hexagons, Figure 2) to the dense polymorph B, an oblique packing. Thereby the coordination numbers of the molecules – defined as the directions along which the side chains stabilize the network [15] – are reduced from six in polymorph A (Figure 4a–c, Figure 5a–d) to two in polymorph B (Figure 4d–f, Figure 5e). Both supramolecular patterns are closely related to their backbone structures and substitution schemes.

While the lattice parameters of the porous packings (polymorph A) are identical for all compounds, **1**–**3**, the lattice parameters of the dense packings (polymorph B) vary slightly, depending on whether the cavity is empty (**1**), filled with an undecyl diether strand (**2**), or a tetraethylene glycol strand (**3**). In the porous polymorphs (of each compound), the alkoxy side chains maximize their overlap, and both lattice constants are a direct effect of the side chain lengths. In the dense polymorphs, the packing along lattice vector $a_{n,\mathrm{B}}$ ($n = 1, 2, 3$) is similarly a direct result of the side chain length. Contrary, the packing along the lattice vector $b_{n,\mathrm{B}}$ ($n = 1, 2, 3$) is a result of two effects:

(i) It results from the packing density of six interdigitating side chains, and the distance between each two neighboring chains is ca. 0.4 nm, as discussed above.

(ii) It is an effect of the steric requirement of the northeast and the southwest parts of neighboring macrocycle backbones. The backbone sizes of **1**–**3** vary slightly as an effect of the macrocycle interior, and are 25.1 Å for **1**, 24.5 Å for **2**, and 23.3 Å for **3** (cf. Figure 3c).

The angle $\gamma(a_{n,\mathrm{B}}, b_{n,\mathrm{B}})$ between the unit cell vectors a and b (for $n = 1, 2, 3$) is a result of the interlocking of the $-CH_2-$ units of alkoxy side chains neighboring macrocycles. The macrocycles can be shifted along the HOPG main axis direction d_1 by multiples of two $-CH_2-$ units. Examples for this behavior are also seen in the packing faults that are indicated by arrows A–C in Figure 4e and f. In other words, slight changes of the backbone sizes can lead to a different interlocking of the side chains of adjacent macrocycles and thus may affect the packing of the macrocycles to an extent quite above the threshold of the experimental resolution.

Contrary to the different robustness of the tubular aggregates (gels) from these macrocycles (where the intraannular strands come into close contact) [22], no stability changes and no packing scheme changes for the 2D surface patterns are observed. Similar patterns with alike (porous polymorph) and only slightly varying (dense polymorph) unit cell parameters for all three compounds are formed. This is a clear result of the driving force for the pattern formation, which is – at least for the porous polymorph – a combination of van der Waals interactions between the molecules and the underlying graphite and the alkyl chain interdigitation between neighbored macrocycles. This shows that it is possible to vary the functionality of the macrocycle interior and to keep the pattern constant, which is of great relevance for the tailored design of functionalized adsorbate layers. Moreover, the distances of the macrocycles **1**–**3** (cf. Figure 5a) are alterable in a (more) predictable fashion along a specific direction (that shows the weakest intermolecular van der Waals interaction strength) as compared to the rather unspecific denser polymorphs of the hexagonal molecules described earlier (Figure 2). This can be drawn back to two discrete stabilities of different binding motifs that occur along the directions d_1 as compared to d_2 and d_3.

Conclusion

STM investigations of three shape-persistent macrocycles with different cavity fillings demonstrate that the ring interior has (rather) no effect on the 2D supramolecular surface patterns. Hence, this approach opens a way towards the tailored design of adsorbate layers that can carry functional groups in their interior. The pattern geometry is steered by the periphery and backbone of the macrocycle, whereas the layer functionalization is provided by the specific interior. Furthermore, the packings are closely related to the backbone structures and substitution patterns, for both, porous and dense polymorphs, and are alterable by compound concentration changes. The future investigations will include the role of size and flexibility of the intraannular strands on the supramolecular assembly in one and two dimensions, a strategy to attach functional units that point away from the surface to the third dimension in a pillar-like

fashion, as well as the attachment of groups that selectively bind additional guest molecules that do not self-assemble without macrocycle template layers.

Experimental

The synthesis and characterization of the compounds has been reported before [22]. STM was performed at the solution/ solid interface under ambient conditions. 0.5 µL of a 10^{-5}–2×10^{-6} M solution of the respective substance in 1,2,4-trichlorobenzene (TCB) was dropped onto a piece of freshly cleaved HOPG at elevated temperature (70 °C), and the sample was allowed to cool to rt prior to STM imaging. All STM measurements were performed in situ (with the tip immersed into the liquid) and typically completed within 30 min after the sample preparation. Bias voltages between −1.0 V and −1.2 V and current setpoints between 5 pA and 30 pA were applied to image the molecular adlayers shown in this work. Mechanically cut Pt/Ir (80:20) tips were used and further modified in situ by applying short voltage pulses. All STM images were in situ calibrated by subsequent immediate acquisition of an additional image at reduced bias voltage, therefore the atomic lattice of the HOPG surface is visible, which is used as a calibration grid. Data processing, also for image calibration, was performed using the SPIP 5 (Image Metrology) software package.

Acknowledgements

References

1. Mali, K. S.; Adisoejoso, J.; De Cat, I.; Balandina, T.; Ghijsens, E.; Guo, Z.; Li, M.; Pillai, M. S.; Vanderlinden, W.; Xu, H.; De Feyter, S. Physisorption for Self-Assembly of Supramolecular Systems: A Scanning Tunneling Microscopy Perspective.. In *Supramolecular Chemistry: From Molecules to Nanomaterials;* Gale, P. A.; Steed, J. W., Eds.; John Wiley and Sons, 2012; Vol. 7, pp 3419–3443.

2. Plass, K. E.; Grzesiak, A. L.; Matzger, A. J. *Acc. Chem. Res.* **2007,** *40,* 287–293. doi:10.1021/ar0500158

3. Adisoejoso, J.; Tahara, K.; Okuhata, S.; Lei, S.; Tobe, Y.; De Feyter, S. *Angew. Chem.* **2009,** *121,* 7489–7493. doi:10.1002/ange.200900436 *Angew. Chem., Int. Ed.* **2009,** *48,* 7353–7357. doi:10.1002/anie.200900436

4. Jester, S.-S.; Sigmund, E.; Höger, S. *J. Am. Chem. Soc.* **2011,** *133,* 11062–11065. doi:10.1021/ja203536t

5. Pan, G.-B.; Cheng, X.-H.; Höger, S.; Freyland, W. *J. Am. Chem. Soc.* **2006,** *128,* 4218–4219. doi:10.1021/ja060469f

6. Chen, T.; Pan, G.-B.; Wettach, H.; Fritzsche, M.; Höger, S.; Wan, L.-J.; Yang, H.-B.; Northrop, B. H.; Stang, P. J. *J. Am. Chem. Soc.* **2010,** *132,* 1328–1333. doi:10.1021/ja907220f

7. Groszek, A. J. *Nature* **1964,** *204,* 680. doi:10.1038/204680a0

8. Rabe, J. P.; Buchholz, S. *Science* **1991,** *253,* 424–427. doi:10.1126/science.253.5018.424

9. Ilan, B.; Florio, G. M.; Hybertsen, M. S.; Berne, B. J.; Flynn, G. W. *Nano Lett.* **2008,** *8,* 3160–3165. doi:10.1021/nl8014186

10. Yang, T.; Berber, S.; Liu, J.-F.; Miller, G. P.; Tománek, D. *J. Chem. Phys.* **2008,** *128,* 124709. doi:10.1063/1.2841478

11. Liang, W.; Whangbo, M.-H.; Wawkuschewski, A.; Cantow, H.-J.; Magonov, S. N. *Adv. Mater.* **1993,** *5,* 817–821. doi:10.1002/adma.19930051106

12. Magonov, S. N.; Wawkuschewski, A.; Cantow, H.-J.; Liang, W.; Whangbo, M.-H. *Appl. Phys. A: Solids Surf.* **1994,** *59,* 119–133. doi:10.1007/BF00332204

13. Tahara, K.; Lei, S.; Adisoejoso, J.; De Feyter, S.; Tobe, Y. *Chem. Commun.* **2010,** *46,* 8507–8525. doi:10.1039/c0cc02780d

14. Tahara, K.; Furukawa, S.; Uji-i, H.; Uchino, T.; Ichikawa, T.; Zhang, J.; Mamdouh, W.; Sonoda, M.; De Schryver, F. C.; De Feyter, S.; Tobe, Y. *J. Am. Chem. Soc.* **2006,** *128,* 16613–16625. doi:10.1021/ja0655441

15. Jester, S.-S.; Sigmund, E.; Röck, L. M.; Höger, S. *Angew. Chem.* **2012,** *124,* 8683–8687. doi:10.1002/ange.201204006 *Angew. Chem., Int. Ed.* **2012,** *51,* 8555–8559. doi:10.1002/anie.201204006

16. Ito, S.; Wehmeier, M.; Brand, J. D.; Kübel, C.; Epsch, R.; Rabe, J. P.; Müllen, K. *Chem. – Eur. J.* **2000,** *6,* 4327–4342. doi:10.1002/1521-3765(20001201)6:23<4327::AID-CHEM4327>3.0.CO;2-7

17. Höger, S.; Bonrad, K.; Mourran, A.; Beginn, U.; Möller, M. *J. Am. Chem. Soc.* **2001,** *123,* 5651–5659. doi:10.1021/ja003990x

18. Coenen, M. J. J.; den Boer, D.; van den Bruele, F. J.; Habets, T.; Timmers, K. A. A. M.; van der Maas, M.; Khoury, T.; Panduwinata, D.; Crossley, M. J.; Reimers, J. R.; van Enckevort, W. J. P.; Hendriksen, B. L. M.; Elemans, J. A. A. W.; Speller, S. *Phys. Chem. Chem. Phys.* **2013,** *15,* 12451–12458. doi:10.1039/c3cp50829c

19. Lei, S.; Tahara, K.; De Schryver, F. C.; Van der Auweraer, M.; Tobe, Y.; De Feyter, S. *Angew. Chem.* **2008,** *120,* 3006–3010. doi:10.1002/ange.200705322 *Angew. Chem. Int. Ed.* **2008,** *47,* 2964–2968. doi:10.1002/anie.200705322

20. Tahara, K.; Okuhata, S.; Adisoejoso, J.; Lei, S.; Fujita, T.; De Feyter, S.; Tobe, Y. *J. Am. Chem. Soc.* **2009,** *131,* 17583–17590. doi:10.1021/ja904481j

21. Höger, S.; Morrison, D. L.; Enkelmann, V. *J. Am. Chem. Soc.* **2002,** *124,* 6734–6736. doi:10.1021/ja017628+

22. Vollmeyer, J.; Jester, S.-S.; Eberhagen, F.; Prangenberg, T.; Mader, W.; Höger, S. *Chem. Commun.* **2012,** *48,* 6547–6549. doi:10.1039/c2cc32804f

23. Lazzaroni, R.; Calderone, A.; Brédas, J. L.; Rabe, J. P. *J. Chem. Phys.* **1997,** *107,* 99–105. doi:10.1063/1.474356

Mono- and multilayers of molecular spoked carbazole wheels on graphite

Stefan-S. Jester[*], A. Vikas Aggarwal, Daniel Kalle and Sigurd Höger

Abstract

Self-assembled monolayers of a molecular spoked wheel (a shape-persistent macrocycle with an intraannular spoke/hub system) and its synthetic precursor are investigated by scanning tunneling microscopy (STM) at the liquid/solid interface of 1-octanoic acid and highly oriented pyrolytic graphite. The submolecularly resolved STM images reveal that the molecules indeed behave as more or less rigid objects of certain sizes and shapes – depending on their chemical structures. In addition, the images provide insight into the multilayer growth of the molecular spoked wheels (MSWs), where the first adlayer acts as a template for the commensurate adsorption of molecules in the second layer.

Introduction

Molecular spoked wheels (MSWs) have gained increasing interest as two-dimensional (2D) carbon-based objects of adjustable sizes [1-5]. They can be viewed as shape-persistent arylene–alkynylene macrocycles in which the intraannular spoke system increases the stiffness (persistence length) of the ring. They are non-collapsible monodisperse cyclooligomers with a fixed and predictable conformation, and their side-chain substitution guarantees their solubility in organic media. Our previous works on freely rotating chains of rigid rod segments and on shape-persistent macrocycles [6,7] have recently led us to a set of molecular polygons (macrocycles) of discrete sizes and symmetries, e.g., triangles, squares, pentagons, and hexa-

gons [8]. These represent basic building blocks for a supramolecular Archimedean surface tessellation system [9]. Thereby, the highly oriented pyrolytic graphite (HOPG) acts as a template along the main axis directions of which the alkyl/alkoxy side chains align [10,11], and consequently the superstructures can be viewed as commensurably aligned adlayers. Among a series of characteristic superstructures, a hexagonal pattern is observed for molecular hexagons that self-assemble at the liquid/solid interface of 1,2,4-trichlorobenzene (TCB) and HOPG, however, the molecules tend to collapse (by rotation around the single bonds of two corner units) in the presence of molecular squares [8]. Consequently, an increased under-
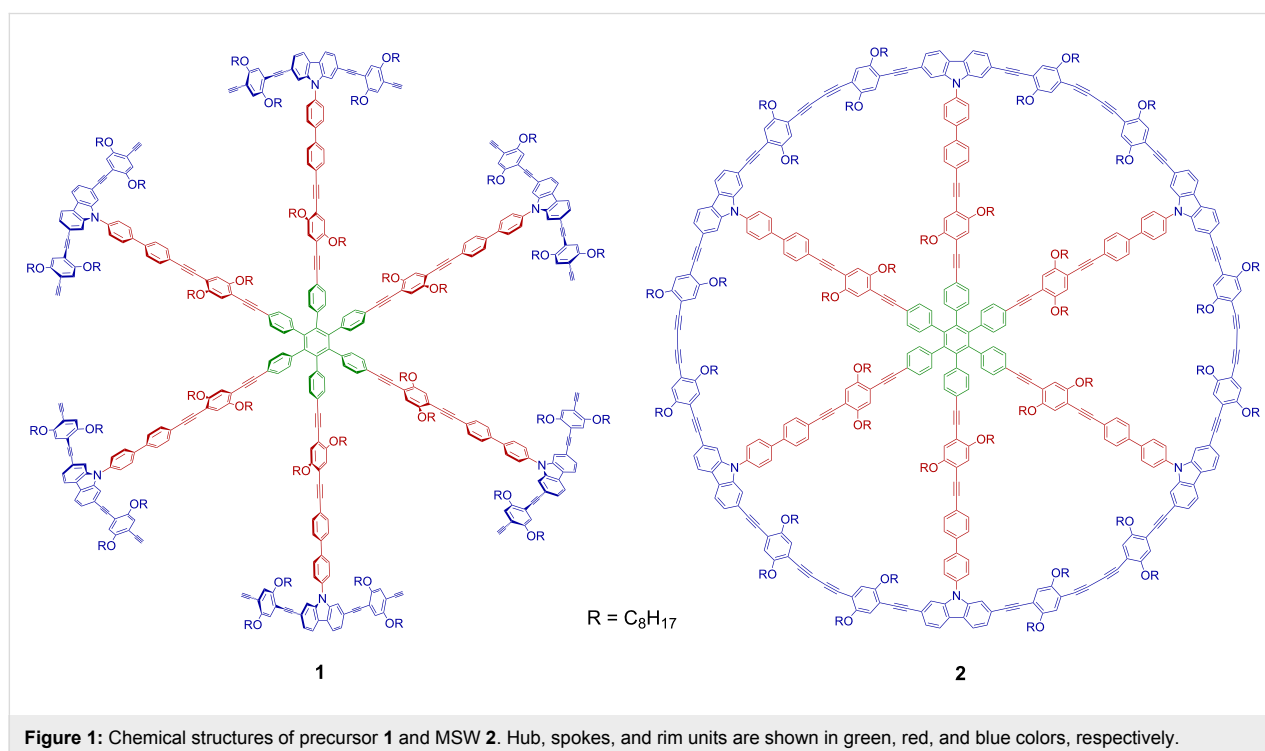
standing of the 2D self-assembly of MSWs on HOPG should nominally pave the way towards a suitable molecular design for (stiffened) hexagons that is compatible with our previous series and might form cocrystals with other polygons, thus patterns of increased complexity and larger lattice constants become feasible. Our MSW **2** and its precursor **1** were recently investigated by means of single-molecule photoluminescence spectroscopy as model compounds for conjugated oligomers commonly used in polymer light emitting diodes [12]. The chemical structures of both compounds are shown in Figure 1. Their synthesis and characterization has been reported before [11]. Here, we present scanning tunnelling microscopy (STM) investigations of both compounds, aiming at an extended description of the observed molecular geometries and their supramolecular monolayer and multilayer formation on HOPG.
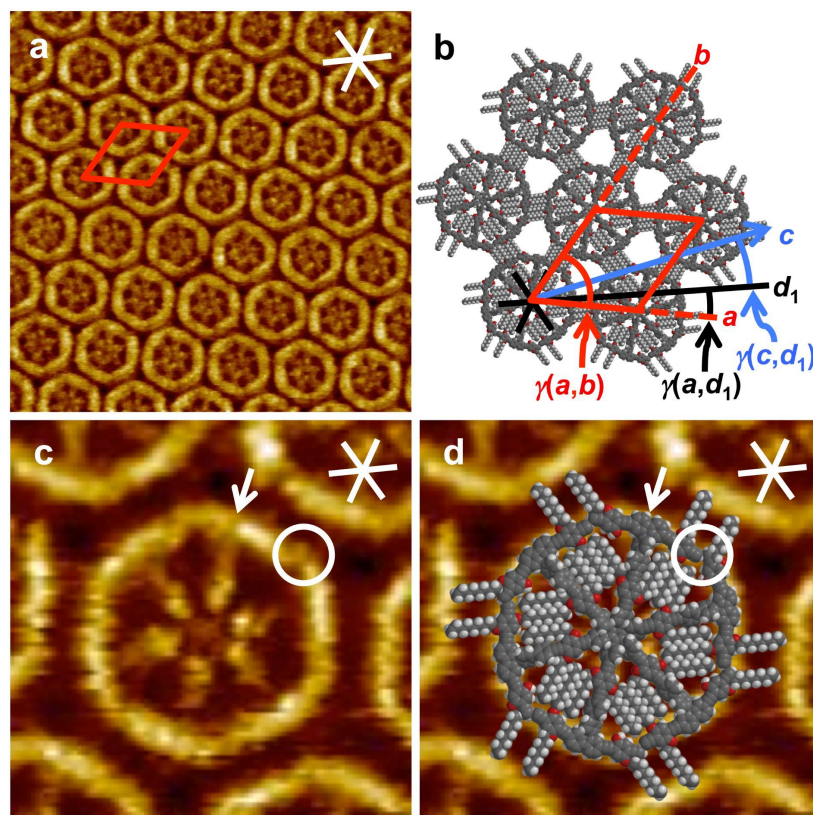
Results and Discussion

We started our STM investigations on the MSW **2** using TCB as a standard solvent for STM, but did not observe molecules, most probably because they do not adsorb to form two-dimensional (2D) supramolecular adlayers at the liquid/solid interface of TCB and HOPG. When using 1-phenyloctane, another commonly used solvent for STM measurements, we could acquire some images of the MSWs, but imaging was less stable (Supporting Information File 1). However, much better images of **2** were obtained using a third solvent, octanoic acid (OA), which has also previously been used for imaging MSWs [2,4]. We compared the so-obtained images of MSW **2** with its

precursor **1** under similar conditions. In all images, regions covered with conjugated backbones and alkoxy side chains are observed in bright and dark colors, related to high and low tunneling currents, respectively [13].

At the OA/HOPG interface **1** forms a 2D-crystalline monolayer (Figure 2a and b) for which a hexagonal unit cell of $a = b = 6.7 \pm 0.2$ nm, $\gamma(a,b) = 60 \pm 2°$ can be indexed. The unit cell vector a is oriented with $\gamma(a,d_1) = 9 \pm 2°$ relative to one of the HOPG main axes (and alkoxy side chain alignment directions) [10,11], d_1. A high resolution STM image is shown in Figure 2c, and a molecular model is superimposed to a copy of the image in Figure 2d. On a first sight, a bright hexagonal frameline (corresponding to the six rim segments) is observed, which is filled with a star-shaped (spoke) system and central darker spot (hub; cf. definition in Figure 1). In other words, the rim units appear (mostly) as a continuous line. The six rim segments contain central carbazole units (cf. chemical structure in Figure 1), so that they are only slightly curved (or bent; as seen in the molecular model in Figure 2c and d where one of the six carbazole units is marked by a white arrow). They are still not directly connected, but terminated with acetylene units. However, a gap can rarely be estimated from the brightness modulation (cf. circle in Figure 2c). Moreover, the six kinks that are seen in the STM images (one of which is marked by the white circle in Figure 2c and d) correspond (not to the carbazole units but) to the intersections of the terminal acetylenes of the rim segments.


Figure 1: Chemical structures of precursor **1** and MSW **2**. Hub, spokes, and rim units are shown in green, red, and blue colors, respectively.

R = C$_8$H$_{17}$

1   **2**

Figure 2: (a)–(d) STM images, a molecular, and a supramolecular model of **1** at the OA/HOPG interface. (a) STM image (40.9 × 40.9 nm², V_S = −1.6 V, I_t = 5 pA) and (b) supramolecular model: The MSW precursors self-assemble into a 2D-crystalline pattern of densely packed molecules. A hexagonal unit cell (red lines) of $a = b = 6.7 \pm 0.2$ nm, $\gamma(a,b) = 60 \pm 2°$ is indexed. The unit cell vector a is aligned relative to one of the three HOPG main axis directions (black, white lines), d_1, with $\gamma(a,d_1) = 9 \pm 2°$. The direction of the backbones, c, as defined by two spokes (and shown by the blue arrow), is $\gamma(c,d_1) = 12 \pm 2°$. (c) and (d): High-resolution STM image (9.3 × 9.3 nm², V_S = −1.6 V, I_t = 4 pA), (c) without and (d) with a superimposed molecular model. The white arrows indicate one representative carbazole unit that connects a rim segment with a spoke. The white circles indicate one representative kink of the brightly appearing hexagon, and the corresponding region in the molecular model where two adjacent rim segments meet. In other words, the kinks do not correspond to the carbazole units, but originate from adjacent rim segments that align in a characteristic fashion. Both STM images were acquired from a 2 × 10⁻⁶ M solution of **1** in OA, and the sample was thermally annealed for 30 s at 70 °C prior to imaging.

According to the space-filling model, only three of the four pseudo-intraannular alkoxy side chains fit (after adsorption) into the triangular cavity regions between each two spokes and the rim. Based on the observed intermolecular distances and an alignment of the alkoxy side chains along the HOPG main axis directions [10,11], an intermolecular side chain interdigitation scheme as shown in Figure 2b is proposed. Alternatively, it cannot be excluded that all intraannular alkoxy chains point to the solution phase. Due to the high flexibility and the weak electrical conductivity of the alkoxy chains, this commonly does (rather) not affect the image quality if the molecules are sufficiently strong bound to the substrate. Oppositely, the pseudo-extraannular side-groups are most probably adsorbed on the graphite surface and interdigitate, since the observed (regular) distance between the molecules fits perfect with the molecular model. Additionally, this assumption is supported

from the slight contrast undulation between the backbones in the STM image.

Opposed to **1**, MSW **2** self-assembles into a less ordered adlayer (Figure 3a). Throughout all STM images, the expected MSW-like shape of each of the molecular entities is clearly apparent. The conjugated rims appear brightly, but have a significantly more round and/or disturbed shape (Figure 3d) as compared to the precursor **1** (Figure 2c). The spoke units of the MSW (Figure 3a and d) appear – throughout all images – less brightly than the rim, which was not the case for precursor **1** (Figure 2a, c, d). The central hub does nearly show any (bright) tunneling current features. For the overall hexagonal packing a (nominal) unit cell of $a = b = 6.9 \pm 0.2$ nm, $\gamma(a,b) = 60 \pm 2°$ is approximated where both unit cell vectors are aligned along the HOPG main axis directions (Figure 3a). The centers of all
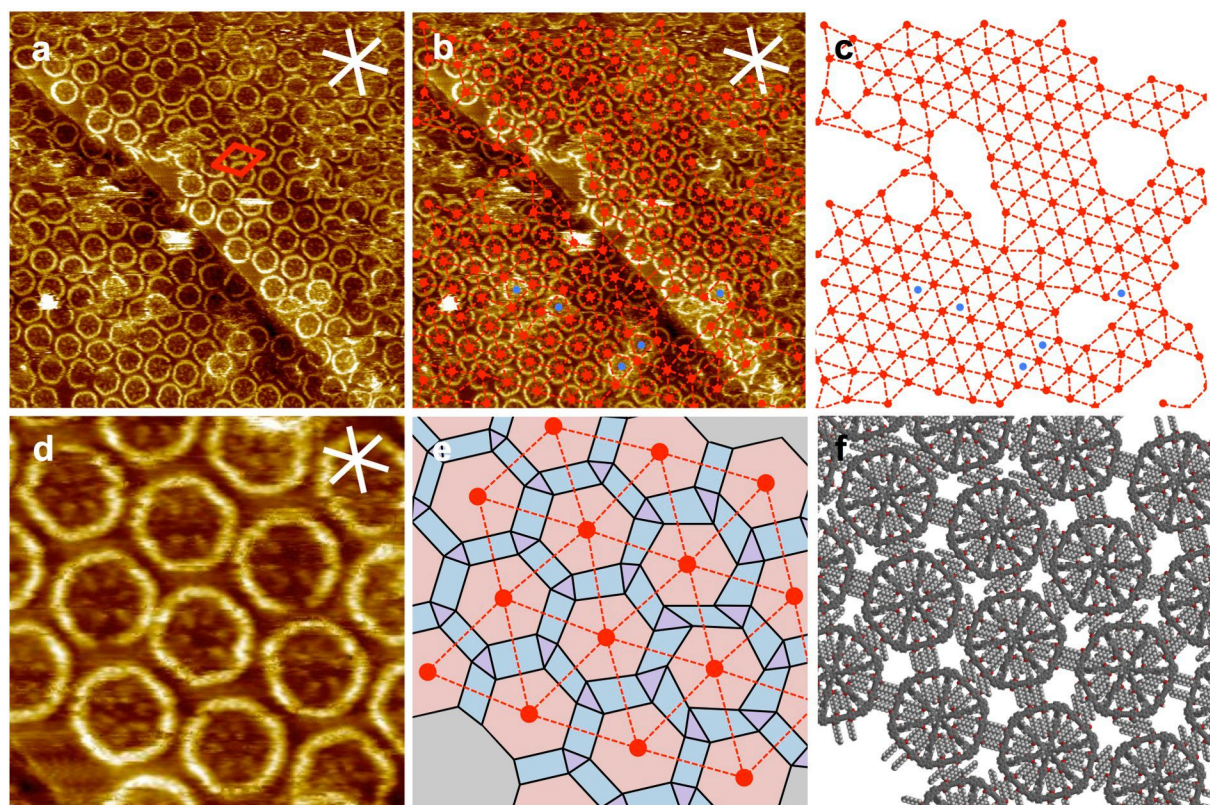
Figure 3: (a)–(f) STM images, mesh, polygon, and supramolecular models of MSW **2** at the OA/HOPG interface. (a) The overview STM image (88.6 × 88.6 nm^2, V_S = −1.5 V, I_t = 10 pA) shows an adlayer in which the circular shapes of the MSW rims and features of the central hub/spoke system are recognizable. A (nominal) unit cell of *a* = *b* = 6.9 ± 0.2 nm, γ(*a*,*b*) = 60 ± 2° (red lines) is approximated. (b) A copy of the STM image shown in (a), where the centers of all MSWs are marked by red dots, and dashed lines are drawn to connect all adjacent dots, so that a network structure results, which is shown without the STM image in (c). (d) A more detailed STM image (23.0 × 23.0 nm^2, V_S = −1.5 V, I_t = 10 pA) confirms the high variation of rim–rim distances. (e) A mesh model is drawn similar as in (b). The centers of equilateral hexagons are placed at the positions of the red dots, and the orientation of each hexagon is fitted to match the MSW orientation (by rotation). The corners of adjacent hexagons are connected by solid black lines to form triangles and tetragons, the variation of the shapes of which points out the high degree of disorder. (f) The data obtained in (d) and (e) is translated into a supramolecular model. The alkoxy side-chains are subsequently added to match the expected directions along the HOPG main axes [10,11], showing that the intermolecular interactions cannot be described by (only) one side-chain interdigitation motif. The MSWs were deposited from a 10^{-5} M solution, and the sample was thermally annealed for 30 s at 80 °C.

MSWs in the STM image in Figure 3b (which is a copy of the image shown in Figure 3a) are marked by red dots. All adjacent dots are connected by dashed lines, resulting in a mesh model of triangular tiles and sixfold vertices (Figure 3c). However, following the dashed lines along each of the six predominant directions shows a slight zig-zagged distortion. The mesh has a significantly lower degree of order than expected for a 2D-crystalline packing (that was observed for **1**). Some regions even do not allow a detailed interpretation (as shown as blank parts in Figure 3c).

A higher resolved STM image (shown in Figure 3d) shows that the MSW distances are not equal. The MSW centers are again marked by red dots and connected by dashed red lines (to form the red mesh shown in Figure 3e). The center of an equilateral hexagon is placed onto each of the red dots in Figure 3e, and the orientation of each hexagon is fitted (by rotation) to match the

orientation of each corresponding MSW observed in Figure 3d. In other words, the high-resolution STM image is transcribed into a polygon model. The corners of adjacent hexagons are connected with solid black lines. The resulting triangles and tetragons are far from having identical shapes that were expected for a crystalline pattern (for two hypothetical packings and corresponding tessellation patterns, see Supporting Information File 1). The STM image (shown in Figure 3d) and the mesh model (shown in Figure 3e) are transcribed into a supramolecular model (shown in Figure 3f) based on rigid (ideal) backbones and subsequently added alkoxy side chains, each aligned along the HOPG main axis direction it fits best to (cf. white lines in Figure 3d) [10,11]. The result confirms that the intermolecular interaction cannot be described by a single packing concept. Consequently, the packing must be interpreted as an effect of a variety of different intermolecular (and intramolecular) alkoxy side-chain interaction/interdigitation

motifs. The degrees of freedom of each MSW **2** are reduced (as compared to **1**), and the lower flexibility of the MSWs together with their large size and the resulting molecule–surface interaction decrease the ability to form a regular pattern, probably (also) due to a lower compound solubility. We observed a similar behavior for phenylene–ethynylene–butadiynylene macrocycles which we compared to their acyclic analoga of identical oligomerization degree [7].

Moreover, a strong tendency of **2** to stack into multilayers was observed, even if the first adlayer was not fully covered with MSWs (as seen in the overview STM image in Figure 4a). The more detailed STM image in Figure 4b shows that the MSWs in the second layer adsorb on top of the center between three first-layer MSWs (cf. arrows in Figure 4b, and the underlying molecular model in Figure 4c that represents the region marked by the dashed lines in Figure 4b). The central hub of the second-layer MSWs, which can for sterical reasons not planarize, fits perfectly into the intermolecular cavities formed by three adjacent molecules in the first layer. In addition, the MSWs in the second layer in the region marked by the white dashed lines in Figure 4b are rotated by ~30° relative to the MSWs in the first layer, as seen from the orientation of the rim segments, so that their pseudo-extraannular octyloxy side chains are (most probably) adsorbed on the HOPG substrate in the intermolecular pores of the first layer. The results clearly indicate that not only the HOPG acts as a template for the organization of the first molecular adlayer, but the adsorption pattern is transferred to the second layer. In other words, the first layer of MSWs in a template for the commensurate adsorption of the second MSW layer.

In STM experiments, the second adsorption layer is generally not observed due to the high mobility of the molecules therein with respect to the scanning STM tip, and the higher tunneling resistivity. Coadsorption on a (supra-)molecular template is rather an exception than a rule. However, when observed, it is often between electron-rich macrocycles that act as hosts for electron-deficient guest molecules (e.g., fullerenes, metallacycles) [14,15]. In the case here, the adlayer stability can be ascribed to a mechanical interlocking together with a high van der Waals interaction due to the large molecule size. It is worth to note that these investigations may also give insight into the spoked wheel organization in the bulk material.

Conclusion

Precursor **1** and MSW **2** self-assemble at the OA/HOPG interface into 2D adlayers. In both cases, the packing is determined by the molecular backbone shapes and the attached octyloxy side chains that tend to pack densely and align along the main axis directions of the HOPG substrate which acts as a template. The STM images of both, **1** and **2**, reveal the differences in the molecular structures that result in different adsorption behavior. While only 2D-crystalline monolayers were observed for the more flexible precursor **1**, MSW **2** forms less ordered patterns and tends to form multilayers. A characteristic stacking of the macrocycles in the second layer on top of three macrocycles of the first layer is observed, showing that the first molecule layer acts as a template for the second molecule layer.

Experimental

The synthesis and characterization of the compounds has been reported before [11]. STM was performed at the liquid/solid
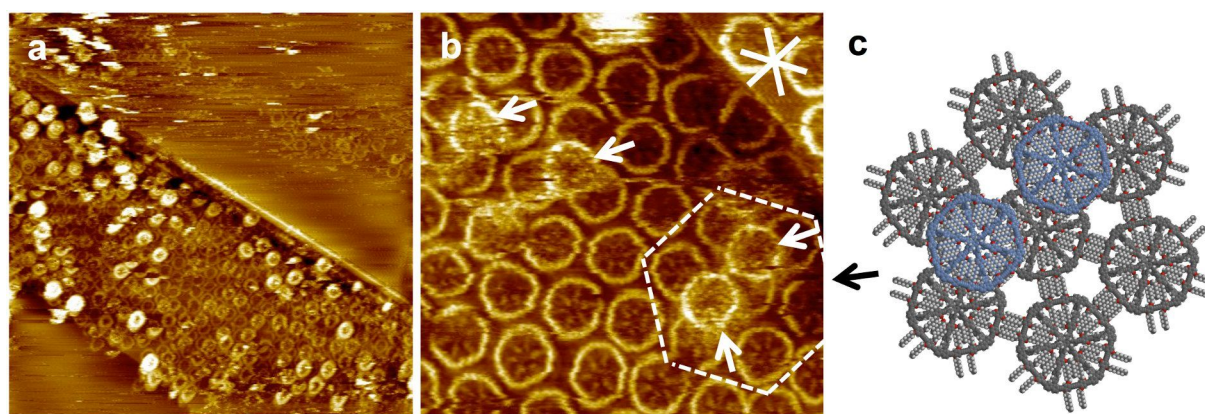
Figure 4: (a)–(c) STM images and a supramolecular model of MSW **2** at the OA/HOPG interface. (a) Overview STM image (200 × 200 nm^2 (internal scanner calibration), V_S = −1.4 V, I_t = 5 pA). A several 10 × 10 nm^2 large region is covered by a monolayer and (partly) a multilayer, whereas large parts remain uncovered. (b) The more detailed STM image (40.5 × 40.5 nm^2, V_S = −1.5 V, I_t = 10 pA) shows MSWs that are adsorbed in a second layer on top of the centers of three supporting molecules (and indicated by white arrows). (c) Supramolecular model of the region marked by white dashed lines in (b). The first MSW monolayer (on HOPG) is shown in grey color, whereas the molecules in the second layer are shown in blue color (and their pseudo-extraannular alkoxy side chains are not shown). The molecules were adsorbed from a 10^{-5} M solution, and the sample was thermally annealed for 30 s at 80 °C prior to imaging. The white asterisk in (b) indicates the HOPG main axis directions.

interface under ambient conditions. Typically, 0.5 µL of a 10^{-5}–10^{-6} M solution of the respective substance in OA was dropped onto a piece of freshly cleaved HOPG at elevated temperature (70–80 °C), and the sample was allowed to cool to rt prior to STM imaging. All STM measurements were performed in situ (with the tip immersed into the liquid) and typically completed within 30 min after the sample preparation. Bias voltages between −1.4 V and −1.6 V and current setpoints between 4 pA and 10 pA were applied to image the molecular adlayers shown in this work. Mechanically cut Pt/Ir (80:20) tips were used and further modified (while imaging) by applying short voltage pulses. All STM images were calibrated by subsequent immediate acquisition of an additional image at reduced bias voltage, therefore the atomic lattice of the HOPG surface is visible, which is used as a calibration grid. Data processing, also for image calibration, was performed using the SPIP 5 (Image Metrology) software package.

Supporting Information

Supporting Information File 1

Theoretical considerations on supramolecular pattern structures of **2** and additional STM images.
[http://www.beilstein-journals.org/bjoc/content/supplementary/1860-5397-10-295-S1.pdf]

Acknowledgements

References

1. Mössinger, D.; Hornung, J.; Lei, S.; De Feyter, S.; Höger, S. *Angew. Chem., Int. Ed.* **2007**, *46*, 6802–6806. doi:10.1002/anie.200701614
   Angew. Chem. **2007**, *119*, 6926-6930. doi:10.1002/ange.200701614
2. Lei, S.; Ver Heyen, A.; De Feyter, S.; Surin, M.; Lazzaroni, R.; Rosenfeldt, S.; Ballauff, M.; Lindner, P.; Mössinger, D.; Höger, S. *Chem. – Eur. J.* **2009**, *15*, 2518–2535. doi:10.1002/chem.200801939
3. Mössinger, D.; Chaudhury, D.; Kudernac, T.; Lei, S.; De Feyter, S.; Lupton, J. M.; Höger, S. *J. Am. Chem. Soc.* **2010**, *132*, 1410–1423. doi:10.1021/ja909229y
4. Aggarwal, A. V.; Jester, S.-S.; Taheri, S. M.; Förster, S.; Höger, S. *Chem. – Eur. J.* **2013**, *19*, 4480–4495. doi:10.1002/chem.201203444
5. O'Sullivan, M. C.; Sprafke, J. K.; Kondratuk, D. V.; Rinfray, C.; Claridge, T. D. W.; Saywell, A.; Blunt, M. O.; O'Shea, J. N.; Beton, P. H.; Malfois, M.; Anderson, H. L. *Nature* **2011**, *469*, 72–75. doi:10.1038/nature09683
6. Jester, S.-S.; Shabelina, N.; Le Blanc, S. M.; Höger, S. *Angew. Chem., Int. Ed.* **2010**, *49*, 6101–6105. doi:10.1002/anie.201001625
   Angew. Chem. **2010**, *122*, 6237–6241. doi:10.1002/ange.201001625
7. Jester, S.-S.; Idelson, A.; Schmitz, D.; Eberhagen, F.; Höger, S. *Langmuir* **2011**, *27*, 8205–8215. doi:10.1021/la201413h
8. Jester, S.-S.; Sigmund, E.; Höger, S. *J. Am. Chem. Soc.* **2011**, *133*, 11062–11065. doi:10.1021/ja203536t
9. Jester, S.-S.; Sigmund, E.; Röck, L. M.; Höger, S. *Angew. Chem., Int. Ed.* **2012**, *51*, 8555–8559. doi:10.1002/anie.201204006
   Angew. Chem. **2012**, *124*, 8683–8687. doi:10.1002/ange.201204006
10. Yang, T.; Berber, S.; Liu, J.-F.; Miller, G. P.; Tománek, D. *J. Chem. Phys.* **2008**, *128*, 124709. doi:10.1063/1.2841478
11. Ilan, B.; Florio, G. M.; Hybertsen, M. S.; Berne, B. J.; Flynn, G. W. *Nano Lett.* **2008**, *8*, 3160–3165. doi:10.1021/nl8014186
12. Aggarwal, A. V.; Thiessen, A.; Idelson, A.; Kalle, D.; Würsch, D.; Stangl, T.; Steiner, F.; Jester, S.-S.; Vogelsang, J.; Höger, S.; Lupton, J. M. *Nat. Chem.* **2013**, *5*, 964–970. doi:10.1038/nchem.1758
13. Lazzaroni, R.; Calderone, A.; Brédas, J. L.; Rabe, J. P. *J. Chem. Phys.* **1997**, *107*, 99. doi:10.1063/1.474356
14. Pan, G.-B.; Cheng, X.-H.; Höger, S.; Freyland, W. *J. Am. Chem. Soc.* **2006**, *128*, 4218–4219. doi:10.1021/ja060469f
15. Chen, T.; Pan, G.-B.; Wettach, H.; Fritzsche, M.; Höger, S.; Wan, L.-J.; Yang, H.-B.; Northrop, B. H.; Stang, P. J. *J. Am. Chem. Soc.* **2010**, *132*, 1328–1333. doi:10.1021/ja907220f

License and Terms